THE TOPOGRAPHICALLY ASYMMETRICAL ALASKA RANGE: MULTIPLE TECTONIC DRIVERS THROUGH SPACE AND TIME

By

Jeffrey Benowitz

RECOMMENDED:

Wesley K Wallace

Sarah Jawdy

Advisory Committee Chair

Sarah Jawdy

Chair, Department of Geology and Geophysics

APPROVED:

Dean, College of Natural Science and Mathematics

Dean of the Graduate School

August 17, 2011

Date

THE TOPOGRAPHICALLY ASYMMETRICAL ALASKA RANGE: MULTIPLE TECTONIC DRIVERS THROUGH SPACE AND TIME

A

DISSERTATION

Presented to the Faculty

of the University of Alaska Fairbanks

in Partial Fulfillment of the Requirements

for the Degree of

DOCTOR OF PHILOSOPHY

By

Jeffrey Benowitz, B.S., M.F.A.

Fairbanks, Alaska

August 2011

Abstract

The topographically segmented, ~700 km long Alaska Range evolved over the last ~50 Ma in response to both far-field driving mechanisms and near-field boundary conditions. The eastern Alaska Range follows the curve of the Denali Fault strike-slip system, forming a large arc of high topography across southern Alaska. The majority of the topography in the eastern Alaska Range lies north of the Fault. A region of low topography separates the eastern Alaska Range from the central Alaska Range, where most of the high topography lies south of the Denali Fault. To the west, there is a restraining bend in the Fault. Southwest of the bend, the north-south trending western Alaska Range takes an abrupt 90 degree turn away from the Denali Fault.

I applied $^{40}Ar/^{39}Ar$ thermochronology to over forty granitic samples to constrain the thermal history of the western and eastern Alaska Range. I combine the $^{40}Ar/^{39}Ar$ analyses with available apatite fission track and apatite (U-Th)/He dating. I then inferred the Alaska Range's exhumation history from the region's rates and patterns of rock cooling.

Periods of mountain building within the Alaska Range are related to Paleocene-Eocene ridge subduction and an associated slab window (~50 Ma to ~35 Ma), Neogene flat-slab subduction of the Yakutat microplate (~24 Ma to present), Yakutat microplate latitudinal variation in thickness (~6 Ma to present), block rotation/migration, and fault reorganization along the Denali Fault. However, it is

clear from basin, petrological and thermochronological constraints that not all of the far-field driving mechanisms affected every segment of the Alaska Range to the same degree or at the same time. Alaska Range tectonic reconstruction is also complicated by near-field structural controls on both the timing and extent of deformation. Fault geometry affects both the amount of exhumation (e.g., ~14 km in the Susitna Glacier region of the eastern Alaska Range) and location of topographic development (e.g., north or south of the Denali Fault). The topographic signature we see today is also in part the result of a pre-existing landscape modified by Plio-Quaternary (~3 Ma to present) surface processes.

Table of Contents

Page

Signature Page i

Title Page ii

Abstract iii

Table of Contents v

List of Figures xi

List of Tables xxi

Acknowledgements xxii

CHAPTER 1 SYNOPSIS 1

1.1 Document Format 1

1.2 Motivation 1

1.3 Research Objectives 5

1.4 Chapter Summaries 6

CHAPTER 2 SPATIAL VARIATIONS IN FOCUSED EXHUMATION ALONG A CONTINENTAL SCALE STRIKE-SLIP FAULT: THE DENALI FAULT OF THE EASTERN ALASKA RANGE 10

2.1 Abstract 10

2.2 Introduction 11

2.3 Geological Background 13

Page

2.3.1 Denali Fault 13

2.3.2 Uplift History of the Alaska Range 14

2.3.3 Physiography of the Eastern Alaska Range 14

2.4 Methods 15

2.4.1 Sampling and Analytical Techniques 15

2.4.2 The Geothermal Gradient and Closure Temperatures 16

2.5 Results 18

2.6 Discussion 19

2.6.1 Along-Strike Exhumation 19

2.6.2 Across-Strike Influence of the Denali Fault 22

2.6.3 Overall Depth of Exhumation Patterns in the Eastern Alaska Range 23

2.6.4 Role of Denali Fault Dip in Driving Exhumation 24

2.6.5 Climate and Exhumation Rate Trends in the Eastern Alaska Range 26

2.6.6 Driving Mechanisms of Neogene Exhumation in the Eastern Alaska Range 28

2.7 Conclusions 31

2.8 Acknowledgements 32

2.9 Figures 33

2.10 References 46

2.11 Repository Materials 54

Page

2.11.1 Summary of the $^{40}Ar/^{39}Ar$ Analysis 54

2.11.2 Minimum K-Spar Ages 56

2.11.3 MDD Models 56

2.11.4 Fission-track Analyses 57

2.11.5 Apatite (U-Th)/He and Fission-track Age Data 58

2.12 Repository Figures 60

2.13 Repostory Tables 102

2.14 Repository References 140

CHAPTER 3 PERSISTENT LONG-TERM (~24 MA) EXHUMATION IN THE EASTERN ALASKA RANGE CONSTRAINED BY STACKED THERMOCHRONOLOGY 143

3.1 Abstract 143

3.2 Introduction 144

3.3 Tectonics and Exhumation in Southern Alaska 147

3.3.1 Western Alaska Range 148

3.3.2 Central Alaska Range 148

3.3.3 Eastern Alaska Range 149

3.4 Methods and Stacked Thermochronology Approach 150

3.4.1 Analytical and Sampling Methods 150

Page

3.4.2 Lateral Edge of Range Front and Deeper Indicators of Crustal Exhumation....155

3.4.3 Stacked Multi-Domain Diffusion Modeling....155

3.5 Results....156

3.5.1 Mica $^{40}Ar/^{39}Ar$ Ages....156

3.5.2 K-spar $^{40}Ar/^{39}Ar$ MDD Thermal Models....157

3.5.3 Stacked K-spar $^{40}Ar/^{39}Ar$ MDD Thermal Models....157

3.6 Discussion....158

3.6.1 Background Exhumation Rate....160

3.6.2 Initiation of Rapid Exhumation....161

3.6.3 Standard Thermochronolgical Approach vs. the Veritcally Stacked Approach....162

3.6.4 A New View of Eastern Alaska Range Exhumation Rates....164

3.6.5 Mechanism for Spatially Varying Exhumation Patterns....165

3.6.6 Alaska Range Deformation in Response to the Yakutat Collision....166

3.7 Conclusions....170

3.8 Acknowledgements....171

3.9 Figures....172

3.10 Tables....184

3.11 References....185

Page

3.12 Repository Figures 194

3.13 Repository Tables 201

CHAPTER 4 CENOZOIC TECTONO-THERMAL HISTORY OF THE TORDRILLO MOUNTAINS, ALASKA: PALEO-EOCENE RIDGE-SUBDUCTION, DECREASING RELIEF, AND LATE NEOGENE FAULTING 207

4.1 Abstract 207

4.2 Introdcution 208

4.3 Tordrillo Mountains (Western Alaska Range) Physiography 209

4.4 Methods: Sampling and Analytical Techniques 211

4.5 Results 213

4.6 Discussion 214

4.6.1 Mechanisms for Rock Cooling in the Tordrillo Mountains 214

4.6.2 Tordrillo Mountains Eocene Regional Cooling Rates, Total Rock Uplift, Cooling Amount, and Depth of Emplacement 217

4.6.3 Tordrillo Mountains Block Boundaries Defined by KFAT Thermochronology Results 218

4.6.4 Tordrillo Mountains Age-elevation Relation Reconstruction and Block Model 219

4.6.5 $KFAT_{max}$ Negative Age-elevation Relationship 222

Page

4.6.6 Southern Alaska Paleocene-Eocene Tectonic Reconstruction: Ridge Subduction and Slab Window Migration 226

4.7 Conclusons 234

4.8 Acknowledgements 235

4.9 Figures 236

4.10 Tables 249

4.11 References 251

4.12 Repository Figures....259

4.13 Repository Tables....269

CHAPTER 5 CONCLUSION: OROGENIC HISTORY OF THE TOPOGRAPHICALLY SEGMENTED ALASKA RANGE 276

5.1 Introduction 276

5.2 Discussion....277

5.2.1 Eocene Slab Window 278

5.2.2 Neogene Yakutat Flab Slab Subduction....279

5.2.3 ~6 Ma: Fault Reorganization and Block Rotation....280

5.2.4 Near Field Boundary Conditions: The Geometry of the Denali Fault ..283

5.2.5 Late Cenozoic Climatic Forcing: Tecono-Glacial Interactions....284

5.3 Figures 285

5.4 References 287

List of Figures

Page

Figure 2.1: Tectonic map of southern Alaska 33

Figure 2.2: Colored digital elevation map of the eastern Alaska Range, showing sample locations and major faults 34

Figure 2.3: Colored digital elevation map of the eastern Alaska Range showing sample locations south of the Denali Fault 35

Figure 2.4: Integrated age versus plateau age for the entire $^{40}Ar/^{39}Ar$ hornblende, muscovite and biotite data set 36

Figure 2.5: Colored digital elevation map of the eastern Alaska Range showing major faults and sample locations for figures 2.6, 2.7, 2.8 and 2.9 37

Figure 2.6: $^{40}Ar/^{39}Ar$ age spectra for K-spar from sample 01PAN from Mount Panorama and sample 332AST from Schist Creek Pluton 38

Figure 2.7: $^{40}Ar/^{39}Ar$ age spectra for K-spar from sample 22DEB from the Mount Deborah transect 39

Figure 2.8: Monotonic multiple diffusion domain (MDD) thermal models for K-spar from samples 26BAL, 03RAP, 03BAL, 18BAL, 22DEB, and 32NEN 40

Figure 2.9: $^{40}Ar/^{39}Ar$ age spectra for K-spar for samples 311AST and 45RAP south of the Denali Fault 41

Page

Figure 2.10: Exhumation cooling ages versus (A) distance from the Denali Fault and (B) elevation above sea level for all samples from the three transects shown in figure 2.2 42

Figure 2.11: Regions (contours) of varying exhumation depth along the Denali Fault based on the current set of high temperature hornblende, muscovite, biotite, and K-spar minimum closure ages 43

Figure 2.12: Schematic model of variations in the dip of the Denali Fault plane at depth that may contribute to asymmetric topographic development along the Denali Fault 44

Figure 2.13: Time-averaged temperature paths for individual samples from north (A) and south (B) of the Denali Fault, based on multiple thermochronometers 45

Figure 2R.1: $^{40}Ar/^{39}Ar$ age spectra, K/Ca ratios and Cl/K ratios for sample 01PAN biotite analyses 60

Figure 2R.2: $^{40}Ar/^{39}Ar$ age spectra, K/Ca ratios and Cl/K ratios for sample 04NEN biotite analyses 61

Figure 2R.3: $^{40}Ar/^{39}Ar$ age spectra, K/Ca ratios and Cl/K ratios for sample 37NEN biotite analyses 62

Figure 2R.4: $^{40}Ar/^{39}Ar$ age spectra, K/Ca ratios and Cl/K ratios for sample 32NEN biotite analyses 63

Page

Figure 2R.5: $^{40}Ar/^{39}Ar$ age spectra, K/Ca ratios and Cl/K ratios for sample 02DEB biotite analyses 64

Figure 2R.6: $^{40}Ar/^{39}Ar$ age spectra, K/Ca ratios and Cl/K ratios for sample 24DEB biotite analyses 65

Figure 2R.7: $^{40}Ar/^{39}Ar$ age spectra, K/Ca ratios and Cl/K ratios for sample 07DEB biotite analyses 66

Figure 2R.8: $^{40}Ar/^{39}Ar$ age spectra, K/Ca ratios and Cl/K ratios for sample 03BAL biotite analyses 67

Figure 2R.9: $^{40}Ar/^{39}Ar$ age spectra, K/Ca ratios and Cl/K ratios for sample 18BAL biotite analyses 68

Figure 2R.10: $^{40}Ar/^{39}Ar$ age spectra, K/Ca ratios and Cl/K ratios for sample 19BAL biotite analyses 69

Figure 2R.11: $^{40}Ar/^{39}Ar$ age spectra, K/Ca ratios and Cl/K ratios for sample 30RAP biotite analyses. 70

Figure 2R.12: $^{40}Ar/^{39}Ar$ age spectra, K/Ca ratios and Cl/K ratios for sample 03RAP biotite analyses. 71

Figure 2R.13: $^{40}Ar/^{39}Ar$ age spectra, K/Ca ratios and Cl/K ratios for sample 45RAP biotite analyses. 72

Figure 2R.14: $^{40}Ar/^{39}Ar$ age spectra, K/Ca ratios and Cl/K ratios for sample 311AST biotite analyses. 73

Page

Figure 2R.15: $^{40}Ar/^{39}Ar$ age spectra, K/Ca ratios and Cl/K ratios for sample 05RAP biotite analyses 74

Figure 2R.16: $^{40}Ar/^{39}Ar$ age spectra, K/Ca ratios and Cl/K ratios for sample 09RAP biotite analyses 75

Figure 2R.17: $^{40}Ar/^{39}Ar$ age spectra, K/Ca ratios and Cl/K ratios for sample 45RAP muscovite analyses 76

Figure 2R.18: $^{40}Ar/^{39}Ar$ age spectra, K/Ca ratios and Cl/K ratios for sample 05RAP muscovite analyses 77

Figure 2R.19: $^{40}Ar/^{39}Ar$ age spectra, K/Ca ratios and Cl/K ratios for sample 311AST hornblende analyses 78

Figure 2R.20: $^{40}Ar/^{39}Ar$ age spectra and inverse isochron plots for 01PAN K-spar analyses 79

Figure 2R.21: $^{40}Ar/^{39}Ar$ age spectra and inverse isochron plots for 332AST K-spar analyses 80

Figure 2R.22: $^{40}Ar/^{39}Ar$ age spectra and inverse isochron plots for DT45 K-spar analyses 81

Figure 2R.23: $^{40}Ar/^{39}Ar$ age spectra and inverse isochron plots for 37NEN K-spar analyses 82

Page

Figure 2R.24: $^{40}Ar/^{39}Ar$ age spectra and inverse isochron plots for 32NEN K-spar analyses....83

Figure 2R.25: $^{40}Ar/^{39}Ar$ age spectra and inverse isochron plots for 02DEB K-spar analyses....84

Figure 2R.26: $^{40}Ar/^{39}Ar$ age spectra and inverse isochron plots for 24DEB K-spar analyses....85

Figure 2R.27: $^{40}Ar/^{39}Ar$ age spectra and inverse isochron plots for 22DEB K-spar analyses....86

Figure 2R.28: $^{40}Ar/^{39}Ar$ age spectra and inverse isochron plots for 03BAL K-spar analyses....87

Figure 2R.29: $^{40}Ar/^{39}Ar$ age spectra and inverse isochron plots for 26BAL K-spar analyses....88

Figure 2R.30: $^{40}Ar/^{39}Ar$ age spectra and inverse isochron plots for 18BAL K-spar analyses....89

Figure 2R.31: $^{40}Ar/^{39}Ar$ age spectra and inverse isochron plots for 03RAP K-spar analyses....90

Figure 2R.32: $^{40}Ar/^{39}Ar$ age spectra and inverse isochron plots for 45RAP K-spar analyses....91

Figure 2R.33: $^{40}Ar/^{39}Ar$ age spectra and inverse isochron plots for 311AST K-spar analyses....92

Page

Figure 2R.34: $^{40}Ar/^{39}Ar$ age spectra and inverse isochron plots for 05RAP K-spar analyses....93

Figure 2R.35: $^{40}Ar/^{39}Ar$ age spectra and inverse isochron plots for 09RAP K-spar analyses....94

Figure 2R.36: $^{40}Ar/^{39}Ar$ age spectra and inverse isochron plots for 23RAP K-spar analyses....95

Figure 2R.37: Arrhenius plot, measured, Cl corrected and modeled $^{40}Ar/^{39}Ar$ age spectra, monotonic multiple diffusion domain (MDD) thermal models generated for K-feldspar from sample 32NEN....96

Figure 2R.38: Arrhenius plot, measured, Cl corrected and modeled $^{40}Ar/^{39}Ar$ age spectra, monotonic multiple diffusion domain (MDD) thermal models generated for K-feldspar from sample 22DEB....97

Figure 2R.39: Arrhenius plot, measured, Cl corrected and modeled $^{40}Ar/^{39}Ar$ age spectra, monotonic multiple diffusion domain (MDD) thermal models generated for K-feldspar from sample 03BAL....98

Figure 2R.40: Arrhenius plot, measured, Cl corrected and modeled $^{40}Ar/^{39}Ar$ age spectra, monotonic multiple diffusion domain (MDD) thermal models generated for K-feldspar from sample 26BAL....99

Page

Figure 2R.41: Arrhenius plot, measured, Cl corrected and modeled $^{40}Ar/^{39}Ar$ age spectra, monotonic multiple diffusion domain (MDD) thermal models generated for K-feldspar from sample 18BAL 100

Figure 2R.42: Arrhenius plot, measured, Cl corrected and modeled $^{40}Ar/^{39}Ar$ age spectra, monotonic multiple diffusion domain (MDD) thermal models generated for K-feldspar from sample 03RAP 101

Figure 3.1: Tectonic map of southern Alaska 172

Figure 3.2: Colored digital elevation map of the eastern Alaska Range 173

Figure 3.3: Conceptual schematic illustration of the stacked thermochronology approach 174

Figure 3.4: Biotite $^{40}Ar/^{39}Ar$ age spectrum for sample 01KIM 175

Figure 3.5: Muscovite/biotite $^{40}Ar/^{39}Ar$ age spectra pairs for sample 26 and 28 RAP 176

Figure 3.6: Complexly down-stepping K-spar $^{40}Ar/^{39}Ar$ age spectra 177

Figure 3.7: Monotonic multiple diffusion domain (MD) thermal model 178

Figure 3.8: Monotonic multiple diffusion domain (MDD) thermal model 179

Figure 3.9: Example stacked MDD 90% confidence interval of the mean 180

Figure 3.10: Standard composite of the MDD 90% confidence interval of the mean 181

Page

Figure 3.11: Age of initiation of rapid cooling versus distance from the Denali fault and elevation above sea level....182

Figure 3.12: Summary figure....183

Figure 3.R1: Time-Temperature results....194

Figure 3.R2: $^{40}Ar/^{39}Ar$ age spectra for biotite from sample 01 KIM RAP....195

Figure 3R.3: $^{40}Ar/^{39}Ar$ age spectra for muscovite and biotite from sample 26 RAP....196

Figure 3R.4: $^{40}Ar/^{39}Ar$ age spectra for muscovite and biotite from sample 28 RAP....197

Figure 3R.5: Monotonic multiple diffusion domain (MDD) thermal models, measured, Cl corrected and modeled $^{40}Ar/^{39}Ar$ age spectra, and Arrhenius plot generated for K-spar from sample 01 KIM....198

Figure 3R.6: Monotonic multiple diffusion domain (MDD) thermal models, measured, Cl corrected and modeled $^{40}Ar/^{39}Ar$ age spectra, and Arrhenius plot generated for K-spar from sample 26 RAP....199

Figure 3R.7: Monotonic multiple diffusion domain (MDD) thermal models, measured, Cl corrected and modeled $^{40}Ar/^{39}Ar$ age spectra, and Arrhenius plot generated for K-spar from sample 19BAL....200

Figure 4.1: Digital elevation map of the topographically segmented Alaska Range flooded to 795 m to emphasis high topography....236

Page

Figure 4.2: Map of south central Alaska 237

Figure 4.3: Digital elevation map of Tordrillo Mountains of western Alaska 238

Figure 4.4: Age-elevation plot of AFT dates with two sigma errors. 239

Figure 4.5: $^{40}Ar/^{39}Ar$ age K-spar spectra for the ten Tordrillo Mountains samples 240

Figure 4.6: Probability plot of AFT ages 241

Figure 4.7: AFT and KFAT span ages plotted vs. elevation 242

Figure 4.8: $KFAT_{max}$ and AFT cooling ages plotted vs. elevation 243

Figure 4.9: Reconstructed AFT age-elevation relationship for Blocks B, C and D. 244

Figure 4.10: Block diagrams of the Tordrillo Mountains through time based on the AFT and 245

Figure 4.11: Conceptual cross section of the Tordrillo Mountains explaining the negative 246

Figure 4.12: Eocene slab window summary figure 247

Figure 4.13: Summary of the Cenozoic history of the Tordrillo Mountains 248

Figure 4R.1: $^{40}Ar/^{39}Ar$ age spectra for K-spar from Tordrillo Mountains sample 02PH322 259

Figure 4R.2: $^{40}Ar/^{39}Ar$ age spectra for K-spar from Tordrillo Mountains sample 01PH426A 260

Page

Figure 4R.3: $^{40}Ar/^{39}Ar$ age spectra for K-spar from Tordrillo Mountains sample 03PH408.....261

Figure 4R.4: $^{40}Ar/^{39}Ar$ age spectra for K-spar from Tordrillo Mountains sample 03PH407.....262

Figure 4R.5: $^{40}Ar/^{39}Ar$ age spectra for K-spar from Tordrillo Mountains sample 03PH406A.....263

Figure 4R.5: $^{40}Ar/^{39}Ar$ age spectra for K-spar from Tordrillo Mountains sample 03PH405A.....264

Figure 4R.7: $^{40}Ar/^{39}Ar$ age spectra for K-spar from Tordrillo Mountains sample 03PH404A.....265

Figure 4R.8: $^{40}Ar/^{39}Ar$ age spectra for K-spar from Tordrillo Mountains sample 03PH403A.....266

Figure 4R.9: $^{40}Ar/^{39}Ar$ age spectra for K-spar from Tordrillo Mountains sample 03PH402A.....267

Figure 4R.10: $^{40}Ar/^{39}Ar$ age spectra for K-spar from Tordrillo Mountains sample 03PH401.....268

Figure 5.1: Coastal relief model of southern Alaska.....285

Figure 5.2: Summary of timing and tectonic cause of surface uplift events in the Alaska Range since ~50 Ma to present. 286

List of Tables

Page

Table 2R.1: $^{40}Ar/^{39}Ar$ data from Potassium Feldspar, (F): furnace run, (L): laser run 102

Table 2R.2: $^{40}Ar/^{39}Ar$ and K-Ar data from biotite, muscovite and hornblende. 103

Table 2R.3: Apatite Fission Track Analysis 104

Table 2R.4: Apatite U-Th/He data 105

Table 2R.5: $^{40}Ar/^{39}Ar$ data for biotitie, muscovite, hornblende and K-spar. 106

Table 3.1: Sample location, rock type and age summary data for feldspars and micas 184

Table 3R.1: K-feldspar summary and model ages 201

Table 3R.2: $^{40}Ar/^{39}Ar$ data for step-heating analyses of micas 205

Table 4.1: Samples, locations, FT age summary 249

Table 4.2: Summary of K-Spar $^{40}Ar/^{39}Ar$ results 250

Table 4R.1: $^{40}Ar/^{39}Ar$ data for K-spar from the Tordrillo Mountains 269

Acknowledgements

Like a manuscript, a dissertation is not a solo project. My advisor, Paul Layer, was more than a mentor, educator, and geochronology guide. Paul allowed me to re-enter the world of science, as an adult, which I left in 1992, not so mature. Paul's trust in my abilities and capabilities helped me have them. My overall committee provided the perfect dash of limits and scientific freedom to allow me to completethis project. Peter Haeussler in many ways formed the direction of this project in one early summer phone call in 2006. During the conversation, Peter caught me up on 10 years of progress in thermochronology science and nudged me in the right direction as I pinballed around in my thoughts. The countless email exchanges between Peter and I over the last 5 years kept tapping me back on track. Wes Wallace taught me more about structural geology than I thought was possible. In particular Wes showed me that structural geology is the foundation to orogenesis thought. Though at times I abused Wes's open door policy, he always looked up to answer my inquiries. Sarah Fowell asked just the right questions to prod me along and to promote self-confidence. My collaborators on the NSF funded D.E.A.R.E. project acted like committee members from afar, providing both career and scientific advisement. Paul Fitzgerald responded positively to my out of the blue clunky email with more climbing than science references. Paul's mentoring in thermochronology has led me to oft quote him. Sarah Roeske, in one summer in the field, filled my head with petrology. Sarah was extra patient with this tutelage,

considering there was already a fair deal of lithology in my head. Paul O'Sullivan at meetings and through emails taught me how to thermally relax. Stephanie Perry, the fission ½ of the graduate students on the D.E.A.R.E. project, answered my endless apatite fission track 101 questions. The members of the Fairbanks geology community that contributed to my project are endless. In particular I would like to thank Jason Addison, Sean Bemis, Bob Gillis, Carla Tomsich, and Sam VanLaningham and Phil Armstrong at Fullerton for their contributions to this project. The project would not have been possible without funding from the American Alpine Club, the Mugs Stump Grant, the UAF Graduate Fellowship, the B.P. Foundation, the Geological Society of America Grant, the National Science Foundation, and the Alaska Geological Society scholarships. For every mg of biotite dated, 5 kg of rock were carried on the backs of my friends and colleagues. Matt Klick, Jed Brown, Anna Liljedahl, Sam Herreid, Robert Wing, Tim Cosick and the Andy Stern all assisted as unpaid field assistants. Andy's smile and "We got to get that rock" attitude is behind success of this project in many ways. My farther and mother, Arnold and Rochelle Benowitz, at an early age created the curiosity of "whence the mountains?" Anna Liljedahl, besides carrying rocks, held my hand through marriage, comprehensives and surgery. As we both leave this educational chapter behind I look forward to the next, non-educational chapter.

CHAPTER 1

SYNOPSIS

1.1 **Document Format**

This dissertation is presented in 5 chapters. Chapter 1 discusses motivation and background definitions, introduces the document, outlines the scientific objectives, provides a summary of the goals of this study, and summarizes key results. Chapters 2 and 3 focus on the eastern Alaska Range's Neogene tectonic history and provide background on the Alaska Range's known uplift history, the Denali Fault, and the Yakutat Microplate. Chapter 4 focuses on the western Alaska Range's Paleocene to present tectono-thermal history with the Tordrillo Mountain region the main area of study. It also provides background on the Paleocene-Eocene ridge subduction event in southern Alaska and how ridge-subduction related slab windows can be documented in the rock record. Chapter 5 is a conclusion chapter, tying the first 4 chapters together. Chapter 2, 3, and 4 are intended for separate publication. Supplementary data and all analytical work relevant to, but not included in, the main body of the text are in the repository at the end of each chapter.

1.2 **Motivation**

Mountains have played and continue to play a pivotal role in our mythology. Mount Olympus of Greek times was considered the home of the gods. Mount Sinai of Biblical times was the de facto peak of knowledge and law. During

the first half of the twentieth century, mountains like the Eiger of Switzerland were climbed for national prominence. In the nuclear age, we have investigated how mountains play an active role in many aspects of the natural world. Orogenic belts affect climate on both a regional and global scale. Basin formation is often linked to orogenesis. Evolution can be affected by the biological barrier mountain belts can create. The study of orogenesis is motivated in part by scientific pursuits in plate tectonic reconstruction, paleo-climatology, and resource development. The desire to unravel the history of an orogenic belt may also be primordially linked to our urge to climb mountains. The drive to see what is on the other side might have grown out of our evolutionary history along the rift mountains of eastern Africa.

There are many tools available for studying mountain building. Basin analysis, structural reconstruction, stable isotope examination, and palynology are just a few of the disciplines that have been applied to the study of orogenesis. I chose to use a discipline of geochronology known as thermochronology to further our understanding of the tectonic history of the Alaska Range. *Thermochronology* is a dating technique that associates an age with a blocking temperature. A closure age or *cooling age* is nominally the temperature below which a radiometric system starts to record an age. Different radiometric systems have different closure temperatures. By applying a broad range of thermochronometers, the history of a rock from crystallization to the Earth's surface can be investigated. K-feldspar $^{40}Ar/^{39}Ar$ thermochronology (KFAT) in particular is a powerful

thermochronometric tool because of the multi-domain nature of KFAT closure. KFAT can record both the history of a sample as it passes through the ~350 °C isotherm to the ~150 °C isotherm and any possible reheating events. Because of its potential to record protracted and complicated thermal histories and because there are numerous felsic plutons in the Alaska Range to sample from, I chose KFAT analysis as our main tool.

The exhumation history of rock is inferred from the rock's thermal history by evoking a geothermal gradient and assuming the geothermal gradient is both temporally and spatially consistent. There are modern computational tools to model paleo-geothermal gradients, but the application of such are nascent and beyond the scope of this research. In this study, instead of modeling the geothermal gradient through time and space, I look at general trends in cooling rates and try to avoid placing emphasis on rates of exhumation.

The closure or blocking temperature concept is considered nominal because there are numerous grain size, chemical, radiogenic and kinetic properties that can affect the true temperature of closure. A rock sample that has experienced a short period of reheating even at a relatively low temperature, such as a forest fire, can have inverse thermochronometric cooling ages. Inverse thermochronometric ages in the same sample can also be evidence of alteration ($^{40}Ar/^{39}Ar$ system) or a litany of problems with the thermochronometric system itself. Care must be taken when

applying (U-Th)/He dating in particular because it is common for the results to be a range of ages that may or may not be geologically meaningful.

The spatial pattern of cooling ages from both vertical profiles and horizontal transects and/or numerous cooling ages from a single sample can be used to infer a rock's history as it moves towards the surface. This rock path is known as *exhumation* and involves both erosion and rock uplift. Exhumation is the preferred term to uplift because it is not clear from the word uplift what the reference frame is. Uplift in relation to the surface has the extra complication of unknown paleo-surface elevations before the surface uplift event.

Complications still exist in terms of projecting the spatial extent of an inferred exhumation event from a single sample or even numerous samples. The caveat that the absence of evidence of exhumation is not necessarily evidence of the absence of an exhumation event adds to the difficulties in using thermochronology as a tectonic reconstruction tool. I prefer to apply numerous thermochronometric systems to each sample to better elucidate a rock's thermal history from crystallization to the surface. I also tried to sample both along and across major regional structures and performed both vertical profiles and horizontal transects to examine short and long wave trends in exhumation patterns.

The Alaska Range is a prominent orographic barrier that makes interior Alaska cold and dry. The continental climate of interior Alaska can lead to the bending of light, creating atmospheric illusions or mirages. Often the Alaska Range

appears flatter and wider than the Range actually is. Under other atmospheric conditions the Alaska Range can emerge tall and skinny on the horizon. The day to day changes in our observation of the Alaska Range is a fitting analog for the overall topographic development of the region through space and time.

1.3 **Research Objectives**

When this study was started there was limited thermochronological data published from the Alaska Range. Cooling age data from a small number of samples from two geographically limited regions (Tordrillo Mountains and Mount McKinley region) were used to decipher the ~700 km long Alaska Range's entire tectonic history. Thermochronology is a powerful tool for tectonic reconstruction. The question remains whether tectonic events constrained from a small sample set reflect actual tectonic events or sample biases. I set out to collect a large sample set and apply a broad range of thermochronological techniques to examine the uplift history of the Alaska Range. By applying a broad range of thermochronometers the time-temperature path of a rock towards the surface can be constrained. By collecting samples along and across the strike of the Alaska range I was also able, at times, to examine how major structures affected exhumation patterns.

The majority of the low-temperature (apatite fission track and apatite (U-Th)/He) for this project was produced by Stephanie Perry at Syracuse University. Ms. Perry's low-temperature data set from these samples will be published in her Ph.D dissertation and collaborative manuscripts.

The main questions of this study are:

1) How old is the Alaska Range?
2) What far-field plate-scale tectonic process led to the formation of the Alaska Range?
3) What near-field (~20 km proximity) boundary conditions affect topographic development in the Alaska Range?
4) What happened to long-term erosion rates in the Alaska Range after the introduction of valley glaciation after ~ 3 Ma?

These questions all fall under the umbrella questions: Did the Alaska Range rise synchronously, implying a singular tectonic mechanism? Did the eastern, central and western Alaska Ranges rise diachronously, implying different tectonic drivers through time and space? Or did the Alaska Range rise in a spatially and temporally progressive manner, implying the same far-field tectonic event with stresses disturbed by near-field boundary conditions such as translation through a restraining bend?

1.4 **Chapter Summaries**

Chapter 1 provides a philosophical introduction of why I care "whence the mountains?" The chapter introduces the reader to some key terms and concepts that will make the manuscript chapters more accessible. It also provides a description of the overall document format.

Chapter 2 focuses on the Neogene exhumation history of the eastern Alaska Range region. In particular the chapter discusses the relationship between exhumation in the eastern Alaska Range and the Denali Fault. A large range of $^{40}Ar/^{39}Ar$ thermochronometers are applied. In addition, apatite fission track and apatite (U-Th)/He cooling age data is provided by Stephanie Perry and Dr. Phil Armstrong at Fullerton College. It is clear from the cooling age data set that depth of exhumation varies both across and along the Denali Fault. It is also clear that rapid exhumation has been occurring in the eastern Alaska Range since ~24 Ma. The spatial focus of rapid exhumation varies with time in a general east to west pattern with the current focus in the Nenana Mountain region. There is also evidence of an increase in exhumation rates after ~3 Ma that is temporally correlated with increased erosional forcing due to glaciation. Surge-type glaciers are suggested to play a particularly important role in the rapid exhumation of the region after ~3 Ma. The Yakutat microplate collision/flat slab subduction is suggested as far-field plate-scale tectonic driver for Neogene exhumation. Chapter 2 has been published in the journal Geosphere.

Chapter 3 focuses on the question of what constitutes an exhumation event. Does cooling in one rock imply a change in plate-scale tectonic forcing? Can a single vertical transect constrain the orogenic history of entire mountain range? Is episodic exhumation a reflection of sampling biases or variations in tectonic forcing? To investigate these questions I examine the thermal history of the eastern

Alaska Range as a continuum and constrain persistent exhumation from ~24 Ma to present. By applying a new graphical approach, vertically stacked thermochronology, I view the thermal history of the region in a singular context. No single sample underwent rapid cooling for ~24 Ma, but as a sample collective, some region in the eastern Alaska Range experienced rapid cooling for a shorter period of time from ~24 Ma to present. With persistent exhumation documented, I then make a stronger case for flat slab subduction of the Yakutat microplate driving exhumation in the eastern Alaska Range. Chapter 3 is prepared for submission to the journal Tectonics.

Chapter 4 focuses on K-spar thermochronology in the Tordrillo Mountains of the western Alaska Range. The samples were previously analyzed for apatite-fission-track and (U-Th)/He by Peter Haeussler, Jim Spotila, Paul O'Sullivan and Aaron Berger. I applied K-spar thermochronology to examine the thermal and rock uplift history of the samples from a deeper crustal level than captured by the low-temperature thermochronometers. Clustering of the K-spar ages generally supports previous conclusions that the Tordrillo Mountains are probably dissected by faults. The K-spar analysis also captured the first evidence of rapid rock cooling during the early Eocene in the Alaska Range. I inferred the cooling was related to exhumation. The likely driver for the exhumation event is upwelling of the asthenosphere and magma injection into the upper plate because of a slab window related to the Kula-Resurrection ridge subduction event. I invoke a high geothermal

gradient (~50 °C/km) to explain the large (~200 °C) amount of recorded rock cooling during the Eocene in the Tordrillo Mountains. Regional thermochronology, basin history, and magmatism support the slab window interpretation. Chapter 4 is prepared for submission to Geochemistry, Geophysics, and Geosystems.

Chapter 5 is both a short discussion of orogenesis in general and a conclusion. The Alaska Range is topographically asymmetrical, raising questions as to whether the topographic signature of the Alaska Range is related to antecedent rivers or reflects variations in both far and near-field tectonic processes. It is clear from this research that different segments of the Alaska Range experienced rapid exhumation at different times. Within individual segments, the eastern Alaska Range in particular, exhumation patterns likely reflect near-field boundary conditions such as the dip of the Denali Fault. The western Alaska Range experienced rapid cooling from ~49 Ma to ~35 Ma due to a slab window event. The eastern and western Alaska Range experienced exhumation at ~24 Ma most likely related to the initial flat slab subduction of the Yakutat microplate. The eastern Alaska Range continued to experience rapid exhumation from ~24 Ma to present as the Yakutat Microplate drove the southern Alaska Block into the apex of the Denali Fault. At ~6 Ma the western and central Alaska Range experienced a marked increase in exhumation rates, probably due to the onset of southern Alaska block rotation. Block rotation was driven by convergence of the unsubductable outboard section of the Yakutat Microplate with the Fairweather fault system.

CHAPTER 2

SPATIAL VARIATIONS IN FOCUSED EXHUMATION ALONG A CONTINENTAL SCALE STRIKE-SLIP FAULT: THE DENALI FAULT OF THE EASTERN ALASKA RANGE[1]

2.1 Abstract

$^{40}Ar/^{39}Ar$, apatite fission-track and apatite (U-Th)/He thermochronological techniques were used to determine the Neogene exhumation history of the topographically asymmetric eastern Alaska Range. Exhumation cooling ages range from ~33 Ma to ~18 Ma for $^{40}Ar/^{39}Ar$ biotite, ~18 Ma to ~ 6 Ma for K-feldspar minimum closure ages, and ~15 Ma to ~1 Ma for apatite fission track ages. Apatite (U-Th)/He cooling ages range from ~4 Ma to ~ 1 Ma. There has been at least ~11 km of exhumation adjacent to the north side of Denali Fault during the Neogene inferred from biotite $^{40}Ar/^{39}Ar$ thermochronology. Variations in exhumation history along and across the strike of the fault are influenced by both far-field effects and local structural irregularities. We infer that deformation and rapid exhumation has been occurring in the eastern Alaska Range since at least ~22 Ma, most likely related to the continued collision of the Yakutat microplate with the North American plate. The Nenana Mountain region is the late Pleistocene to Holocene (past ~1 Ma) primary locus of tectonically driven exhumation in the eastern Alaska

[1]Benowitz, J.A., Layer, P.W., Armstrong, P., Perry, S.E., Haeussler, P.J., Fitzgerald, P.G., and VanLaningham, S., 2011, Spatial Variations in Focused Exhumation Along a Continental-Scale Strike-Slip Fault: the Denali Fault of the Eastern Alaska Range, *Geosphere,* v. 7; no. 2; p. 455-467; DOI: 10.1130/GES00589.1

Range, possibly related to variations in geometry. During the Pliocene, a marked increase in climatic instability and related global cooling is temporally correlated with an increase in exhumation rates in the eastern Alaska Range north of Denali Fault system.

2.2 **Introduction**

Regions of focused, rapid (>0.5 mm/yr) exhumation are a common occurrence along major strike-slip fault systems such as the Alpine Fault in New Zealand, the Denali fault in Alaska and the San Andreas fault in California (e.g., Little et al., 2005; Fitzgerald et al., 1995; Spotila et al., 1998). However, the cause of rapid exhumation along these faults is often complex, with near-field (<20 km) boundary conditions and far-field plate tectonic driving mechanisms contributing to exhumation patterns (e.g., Buscher and Spotila, 2007). Unexpectedly, the amount of exhumation along a strike-slip fault is not always correlative with the degree of obliquity of the plate motion vector with respect to the fault trace or the composition of the juxtaposed rocks (e.g. Roeske et al., 2007; Spotila et al., 2007). Climate change (Whipple, 2009), structural irregularities such as stepovers (Hilley and Arrowsmith, 2008), variations in master fault dip (Dair and Cooke, 2009) and changes in plate motion (e.g., Fitzgerald et al., 1995) all can play an important role in observed regional exhumation patterns. Given that many orogenic belts associated with strike-slip faults have heterogeneous exhumation patterns, there is a need for more case studies to examine how vertical motion is related to both near-

field boundary conditions and far-field driving mechanisms (Buscher and Spotila, 2007).

The Denali Fault, an active continental-scale strike-slip fault, has an asymmetric topographic signature (the Alaska Range) making the region an ideal location to examine the contribution of local and regional structures on strain partitioning and the timing of exhumation adjacent to the Fault. We employ $^{40}Ar/^{39}Ar$, apatite fission track (AFT), and apatite (U-Th)/He (AHe) thermochronology to document cooling, and thus exhumation patterns along the Denali Fault system in the eastern Alaska Range. We find that during the Neogene, rapid exhumation in the eastern Alaska Range was initiated by the early Miocene (~22 Ma). A major contributing factor to rapid exhumation in the eastern Alaska Range during the Neogene is most likely the far-field effects of the continuing collision of the Yakutat microplate with southern Alaska (North American plate).

Our data show that exhumation is greatest in a narrow wedge (<10 km wide) proximal to the Denali Fault and is partitioned across and along strike in relation to possible changes in fault geometry. Rapid ongoing exhumation in the eastern Alaska Range was possibly enhanced in the Late Pliocene by the transition to more efficient glacial erosion with the onset of the Northern Hemisphere glaciation (~3 Ma; Lisiecki and Raymo, 2005) and increased erosional forcing due to climatic instability (Clift, 2010).

2.3 **Geological Background**

2.3.1 **Denali Fault**

The Denali Fault system in central Alaska makes a broad arc through the extensively glaciated Alaska Range (Fig 2.1; St. Amand, 1957). It is a major intracontinental right-lateral strike-slip fault that is still active, as demonstrated by the 2002 **M**7.9 Denali Fault earthquake (Eberhart-Phillips et al., 2003). Neogene movement and deformation are driven by plate tectonic processes at the Alaska margin subduction zone 500 km to the south (e.g., Haeussler, 2008). Matmon et al. (2006) and Mériaux et al. (2009) date late Pleistocene moraines offset by the Denali Fault in the eastern Alaska Range and show that modern slip rates are higher to the east at ~12 mm/yr, decreasing to the west at ~7 mm/yr. This suggests that slip is partitioned between the Denali Fault and the Northern Foothills Thrust Belt and siphoned off the Denali fault system onto contractional structures south of the Denali fault (Figs. 2.1 and 2.2; Bemis and Wallace, 2007; Crone et al., 2004).

2.3.2 **Uplift History of the Alaska Range**

The ~650 km long Alaska Range follows the curve of the Denali Fault system. Areas of high peak elevation (e.g., 6194 m in the central Alaska Range and 4216 m in the eastern Alaska Range) are separated by broad regions of low topography (e.g., Broad Pass, ~700 m, separating the central Alaska Range from the eastern Alaska Range). The majority of thermochronometric data from the Alaska Range are from the central Alaska Range (Plafker et al., 1992; Fitzgerald et

al., 1993, 1995), including a 4 km vertical profile in the Mount McKinley region of the central Alaska Range (e.g., Fitzgerald et al., 1995), and from AFT work done in the western Alaska Range (Haeussler et al., 2008). These thermochronometric data sets indicate that the modern-day Alaska Range started to form ~6 Ma, although the western Alaska Range data set shows evidence of an earlier phase of rapid exhumation ~23 Ma.

With the available low-temperature data, it is logical to view the Alaska Range as a singular orogenic feature which experienced a region-wide exhumation pulse at ~6 Ma. However, in the western Alaska Range and central Alaska Range, all regions of high topography (e.g. Mt. McKinley) are south of the Denali Fault. This observation is in stark contrast to the eastern Alaska Range, where all of the high peaks are located north of the Denali Fault (Fig. 2.1). In addition, Ridgway et al. (2007), in an analysis of the Miocene Usibelli Group and Pliocene Nenana Gravel within the Tanana Basin, hypothesize development of significant topography in the eastern Alaska Range prior to the late Miocene. Thus, the spatial and temporal evolution of the Alaska Range may be more complex than the existing data suggest.

2.3.3 **Physiography of the Eastern Alaska Range**

Unlike the western and central Alaska Range, the high peaks of the eastern Alaska Range are sandwiched between the active McKinley strand of the Denali Fault and the presumed-to-be inactive Hines Creek strand (Wahrhaftig et al., 1975).

High topography (>3000 m) is limited to a narrow region (<20 km) along the north side of the Denali Fault. There are numerous identified reverse and thrust faults in the greater eastern Alaska Range region with many located in the northern foothills fold and thrust belt to the north of the Hines Creek Fault (Bemis and Wallace, 2007). Few active and inactive structures have been identified in the ice-covered high peak region of the eastern Alaska Range, with the exception of the Susitna Glacier thrust fault which was only recognized after it ruptured during the 2002 **M**7.9 Denali earthquake (Fig. 2.2; Crone et al., 2004).

Plutons north and south of the Susitna Glacier have ~70 Ma U-Pb emplacement ages (Aleinikoff et al., 2000). Nenana Mountain, Schist Creek and Panorama plutons are thought to have ~38 Ma emplacement ages based on K-Ar dating of biotite and hornblende (Csejtey et al., 1992). Both sides of the Denali Fault in the high-peak region of the eastern Alaska Range experience the same climatic regime (precipitation of ~1500 to ~2000 mm/yr; Manley and Daly, 2005).

2.4 **Methods**

2.4.1 **Sampling and Analytical Techniques**

We applied $^{40}Ar/^{39}Ar$, AFT and AHe thermochronology to 30 bedrock samples along and across the strike of the eastern Alaska Range proximal to the Denali Fault system in order to better constrain the timing and patterns of exhumation. Sampling was focused along three transects north of the Denali Fault: Nenana Mountain transect (NM), Mount Deborah transect (MD), and Mount

Balchen transect (MB) (Fig. 2.2). One transect was conducted south of the Denali Fault in the Meteor Peak region (Fig. 2.3), which is the largest expanse of high topography south of the Denali Fault in the eastern Alaska Range.

Eighteen samples were analyzed using $^{40}Ar/^{39}Ar$ thermochronology on potassium feldspar (K-spar) using either a laser or a resistance furnace (data repository table 2R.1). Six of the furnace-run samples were then modeled using a multi-domain diffusion modeling (MDD) approach (e.g., Lovera et al., 2002) to determine thermal histories and an associated closure temperature for the minimum isochron age grouping (K-spar minimum closure age). Unaltered biotite (16), muscovite (2) and hornblende (1) (data repository table 2R.2), when present, were also analyzed using $^{40}Ar/^{39}Ar$ laser step heating to supplement the time-temperature cooling trajectories of rocks in the Alaska Range.

Eight new AFT (data repository table 2R.3) and three new AHe ages (data repository table 2R.4) are presented for the eastern Alaska Range. Further details of the $^{40}Ar/^{39}Ar$, AFT, and AHe methods and closure temperatures are presented in the data repository text file and data repository table 2R.5.

2.4.2 **The Geothermal Gradient and Closure Temperatures**

Along the Denali Fault, maximum aftershock depths of ~11 km identify the brittle-ductile transition and suggest a regional geothermal gradient of ~30 °C/km (Fisher et al., 2004), which we use to estimate the depth to closure temperature (Tc) for the various thermochronologic systems. Approximately 30 °C/km is the same

standard regional geothermal gradient inferred by other thermochronology studies in Alaska (O'Sullivan and Currie, 1996; Haeussler et al., 2008; McAleer et al., 2009). For the purpose of constraining first-order estimates on exhumation during the Neogene, we assume that the gradient remained spatially and temporally uniform. Thus, we assume the same depth to closure isotherms across the region. We acknowledge that for the low-temperature AFT and AHe data, due to their lower closure temperatures, and hence shallower depths of closure, plus higher Pliocene-Quaternary exhumation rates, this assumption is a simplification and the resulting trends, an approximation. However, the majority of the data in this manuscript are from high-temperature thermochronometers with deep closure depths. These ages are less affected by high Quaternary exhumation rates and variation in isotherm depth related to surface topography (e.g., Braun et al., 2006). We first determine whether the higher temperature cooling ages are related to initial emplacement cooling or cooling related to exhumation before calculating depth of closure.

We use standard closure temperatures for $^{40}Ar/^{39}Ar$ dating of hornblende (550 °C), muscovite (Tc 400 °C) biotite (Tc 350 °C), K-spar (Tc 150 °C), and also for AFT (Tc 110°C) and AHe (Tc 65 °C) cooling ages (Harrison et al., 2009; Reiners and Ehlers, 2005; McDougall and Harrison, 1999). Precise spatial differences in exhumation rates and/or trends are not critical because the variations are large enough to be significant and are not artifacts of variations in geothermal

gradients. We also do not give quantitative rates of cooling, but instead discuss overall trends in cooling rates to avoid over interpreting time-averaged thermochronological constraints. In addition, the dip of the Denali Fault at depth is poorly constrained (see discussion below), but we assume general subvertical rock trajectories based on available structural work done in the region (Sherwood and Craddock, 1979). These assumptions about temperature, and hence depth of closure, allow us to examine near-field exhumation trends and patterns during the Neogene in the eastern Alaska Range.

2.5 **Results**

Most hornblende, muscovite, and biotite analyses from samples on both sides of the Denali Fault show well-defined $^{40}Ar/^{39}Ar$ age plateaus with simple spectra with little or no argon loss (Figures 2R.1 to 2R.19, Table 2R.2 and Table 2R.5 in data repository). This evidence of unaltered samples is demonstrated by the high concordance between integrated ages (whole gas) and plateau ages for the hornblende, muscovite, and biotite analyses (Fig. 2.4).

Along the Balchen transect, biotite cooling ages decrease southwards towards the Denali Fault from ~33.3 Ma to ~18.4 Ma (Fig. 2.2). Proximal Black Rapids, Mount Deborah and the far southeastern part of Nenana Mountain pluton have biotite cooling ages of ~32 Ma to ~18 Ma. The west part of the Nenana Mountain region, Schist Creek, and Panorama plutons have biotite ages of ~38 Ma.

The Mount Deborah sample, which is most distal from the Denali Fault, has a biotite age of ~68 Ma.

K-spar minimum closure ages for Nenana Mountain, Mount Deborah, Mount Balchen, and the north side of the Black Rapids Glacier regions range from ~18.6 Ma to ~6.0 Ma. K-spar minimum closure ages west of the Nenana Mountain region and also south of the Denali Fault (Figs. 2.2 and 2.3) are distinctly older (~28.6 to ~30.8 Ma). K-spar MDD modeling of six samples from the region north of the Denali Fault indicates that K-spar minimum ages represent cooling through the ~150°C isotherm. We interpret MDD models as indicating a diffuse pattern for the initiation of rapid cooling.

Approaching the Denali Fault from the north, AFT ages generally decrease from ~6.7 Ma to ~1.2 Ma with the youngest ages in the Nenana Mountain region. AHe ages north of the Denali Fault range from ~4.0 Ma to ~1.5 Ma. Near the south side of the Denali Fault, we report an AFT age of ~15.5 Ma and one AHe age of ~4.5 Ma (Figs. 2.2 and 2.3).

2.6 **Discussion**

2.6.1 **Along-Strike Exhumation**

A) North of the Denali Fault

Biotite ages of samples from the westernmost Nenana Mountain region have ages (~38.3 Ma to ~36.2 Ma; Fig. 2.2) concordant with the emplacement age of the pluton (~38 Ma) indicating postemplacement rapid cooling and not

exhumation related cooling. Schist Creek and Panorama plutons have biotite ages of ~38 Ma and are interpreted as being related to initial melt emplacement cooling as well.

Biotite ages of ~32 Ma to ~18 Ma from intrusions on the north side of the Black Rapids glacier and eastern edge of the Nenana Mountain pluton are interpreted as exhumation related cooling ages based on the respective emplacement ages of the plutons (~70 Ma; ~38 Ma). Because the emplacement age of the Balchen intrusion is ~70 Ma (Aleinikoff et al., 2000), the trend of younger biotite ages (~33.3 Ma to ~18.4 Ma) towards the Denali Fault demonstrates that the biotite ages are cooling ages related to exhumation, with exhumation increasing toward the Fault (Fig. 2.2). The Mount Deborah pluton, like the Balchen pluton, is assumed to have an ~70 Ma emplacement age based on the upper sample having a biotite age of ~68.4 Ma (Fig. 2.2). The Mount Deborah samples (proximal to the Denali Fault) have biotite cooling ages that are related to exhumation (~32 Ma to ~28 Ma).

The K-spar minimum ages (~30 Ma), the flat shape of the K-spar $^{40}Ar/^{39}Ar$ age spectra and biotite $^{40}Ar/^{39}Ar$ ages (~38 Ma) for the Panorama and Schist Creek plutons imply rapid post-emplacement cooling for both plutons through the minimum closure temperature for K-spar (Figs. 2.5 and 2.6). The downward-stepping K-spar $^{40}Ar/^{39}Ar$ age spectra and MDD modeling of furnace runs of samples from Nenana Mountain, Mount Deborah, Mount Balchen transects and the

Black Rapids Glacier regions north of the Denali Fault confirm that the minimum closure ages indicate rapid cooling due to exhumation through ~150 °C (Figs. 2.5, 2.7 and 2.8).

The MDD K-spar thermal models from north of the Denali Fault show relatively diverse cooling histories with rapid cooling occurring in individual samples between ~22 Ma and ~6 Ma (Fig. 2.8). These north side thermal models suggest heterogeneous exhumation along and across the strike of the Denali Fault. AFT ages range from ~6.7 Ma (Mount Balchen) to ~1.2 Ma (Nenana Mountain region) and AHe ages range from ~4 Ma to ~1.5 Ma (Mount Balchen). Combined with the biotite and K-spar data, the AFT and AHe ages indicate that Neogene rapid exhumation has been a long term (~22 Ma to present) phenomenon along the north side of the Denali Fault in the eastern Alaska Range.

B) South of the Denali Fault

In contrast to samples north of the fault, orthogneiss samples south of the Denali Fault have flat ~30 Ma K-spar age spectra that are concordant with $^{40}Ar/^{39}Ar$ hornblende, muscovite, and biotite ages (~35 Ma to ~31 Ma) from the same samples (Figs. 2.5 and 2.9). We interpret this rapid cooling event as a short-lived metamorphic event because the samples have a penetrative fabric and concordant $^{40}Ar/^{39}Ar$ cooling ages, which is in general agreement with past interpretations for the region (e.g. Nokleberg et al., 1992). Proximal to the Denali Fault, ~15.5 Ma AFT and ~4.5 Ma AHe ages on the south side of the Fault are older than AFT ~1.2

Ma AFT and ~1.5 Ma AHe ages on the north side of the Fault. These low-temperature data combined with the aforementioned $^{40}Ar/^{39}Ar$ thermochronology results indicate different exhumation histories for the north and south sides of the Denali Fault.

2.6.2 **Across-Strike Influence of the Denali Fault**

The trend of cooling ages decreasing towards the Denali Fault from the north is directly correlated with both elevation (Fig. 2.10A) and distance from the Fault (Fig. 2.10B) for all four thermochronometric systems. This relationship indicates that exhumation just north of the Denali Fault in the eastern Alaska Range has been focused there and persisted for at least the last ~20 Ma. Although cooling age is correlated with both elevation and distance from the Denali Fault, distance from the fault is more significant. A good example of this relationship is seen in the Mount Balchen transect K-spar minimum cooling age data where proximity to the Denali Fault has a stronger effect on cooling age than elevation (Fig. 2.10).

Thermochronometric data from the south side of the Denali Fault show no strong elevation or distance-from-fault trends. Muscovite, biotite, and K-spar minimum cooling ages are all concordant and suggest very rapid cooling at ~30 Ma throughout the area (Figs. 2.2 and 2.3). No graphical representation is presented because the cooling ages would simply overlap – biotite ages are all ~31 Ma, K-spar minimum ages are all ~29 Ma.

2.6.3 **Overall Depth of Exhumation Patterns in the Eastern Alaska Range**

In the eastern Alaska Range, the depth of Neogene exhumation varies dramatically across and along the Denali Fault, allowing for general contouring of Neogene minimum or maximum exhumation depths (Fig. 2.11). The difference in cooling ages across the Denali Fault defines a narrow (less than ~10km) wedge of deep Neogene exhumation in the eastern Alaska Range. It is also clear that the region south of the Denali Fault in the eastern Alaska Range experienced less total exhumation during the Neogene than the region immediately north of the fault.

Samples south of the Denali Fault have only been exhumed through the AFT closure system during the Neogene and experienced less than ~5 km of exhumation since ~28 Ma based on the assumed geothermal gradient of ~30 °C/km, the assumed Tc of ~150 °C for K-spar and the concordant muscovite, biotite and K-spar ages in the region. To the west, Panorama and Schist Creek plutons experienced less than ~5 km of exhumation based on concordance of the $^{40}Ar/^{39}Ar$ biotite and $^{40}Ar/^{39}Ar$ K-spar systems. Because $^{40}Ar/^{39}Ar$ biotite ages (Tc ~350 °C) from samples north of the Denali Fault between the Black Rapids Glacier and the southeast end of the Nenana Mountain pluton are exhumation-related closure ages, this region experienced sufficient unroofing to exhume rocks that have passed through the ~350 °C isotherm. Therefore, the region has undergone a minimum of ~11 km of exhumation. The region around the epicenter of the 23 October 2002 **M**6.7 Nenana Mountain earthquake has experienced at least ~5 km

of exhumation. This conclusion assumes that the K-spar minimum ages are exhumation related closure ages, but the $^{40}Ar/^{39}Ar$ biotite ages of these samples are concordant with the emplacement age of the pluton. This relationship limits the possible depth of exhumation for these samples to a maximum of ~11 km. The Nenana Mountain region is located at the western end of the high topography in the eastern Alaska Range, where we found the youngest AFT age (1.2 Ma) and where young cooling ages transition to older cooling ages farther to the west (Fig. 2.2).

Modern earthquake behavior also varies along strike. The Oct 23 2002 **M**6.7 Nenana Mountain earthquake had a westward propagating rupture (Lu et al., 2003). However, the 2002 **M**7.9 Denali Fault earthquake had an eastward propagating surface rupture (Eberhart-Phillips et. al., 2003) implying a possible change in fault behavior from east to west (Ratchkovski et al., 2004) in the Nenana Mountain region. This is the same region where we see young AFT cooling ages in samples that have not been exhumed deeply enough to have exhumation related biotite closure ages (Figs. 2.2 and 2.11), suggesting a possible Pleistocene increase in exhumation rates in the area.

2.6.4 **Role of Denali Fault Dip in Driving Exhumation**

Strike-slip faults by definition involve predominately lateral slip along a vertical to high-angle fault plane (e.g. Sylvester, 1988). Asymmetric basin development as seen in the North Anatolian Fault (Cormier et al., 2006) and variations in uplift rates along the San Andreas Fault (Dair and Cooke, 2009) have

recently been explained through models involving nonvertical fault planes. Variations in fault dip (both along strike and at depth) have been thoroughly documented for the Alpine Fault of New Zealand (e.g. Little et al., 2005) and may be applicable to many strike-slip fault systems.

The dip of the Denali Fault is near vertical along the Delta River corridor where the topography is low (Fisher et al., 2004). The measured surface dip of the Denali Fault is about 80° N in the region between the Balchen and Deborah transects (Haeussler et al., 2004), but it is not well constrained beneath the glaciers or at depth. If the dip of the Denali Fault plane (Fig. 2.12) varies along strike (east to west) from north dipping in parts of the eastern Alaska Range (Fig. 2.12C), to near-vertical (Fig. 2.12B) in areas of low elevation like Broad Pass, to south dipping in the central Alaska Range (Fig. 2.12A) then the change in fault geometry may partially or fully explain the variations in along- and across-strike variations in topography.

An alternative explanation for the high topography and/or deep exhumation north of the Denali Fault in the eastern Alaska Range is the fact that there may be unmapped, ice-covered structures splaying off the eastern Denali Fault system that are the results of partitioned strain. The along-strike (west to east) change from deep exhumation to shallow exhumation west of the Nenana Mountain transect occurs along a section of the Denali Fault that is straight. This relationship

indicates that variations in obliquity of convergence probably are not driving exhumation patterns in the eastern Alaska Range.

2.6.5 **Climate and Exhumation Rate Trends in the Eastern Alaska Range**

Increase in exhumation rates have been shown to correlate with climate change in tectonically active regions of Alaska (e.g., Berger et al., 2008a; McAleer et al., 2009) and in a variety of orogens globally (Clift, 2010). Our data show a temporal correlation with Late Neogene climatic fluctuations; however, distribution is not sufficient to fully evaluate the role of climate on Alaska Range orogenesis. When we compare the global $\delta^{18}O$ compilation (Zachos et al. 2001) with plots of closure temperature vs. age for different thermochronometers from the eastern Alaska Range, we see a temporal link between an increase in bedrock cooling rates on the north side of the Denali Fault (based on the kink in slope at ~3 Ma) and the onset of Northern Hemisphere glaciation (Fig. 2.13; Lisiecki and Raymo, 2005; Zachos et al., 2001). Exhumation data from the south side of the Denali Fault indicate a similar pattern, but at lower resolution and with slower cooling and less rapid exhumation rates. This temporal correlation by no means proves that climate is forcing exhumation. However, the similarity in timing between climate change and exhumation in the eastern Alaska Range, combined with the vast number of other orogens showing similar linkages (Clift, 2010), suggests that climate may play a role in driving exhumation in the Alaskan interior.

A possible mechanism for a climate related exhumation rate increase at ~3 Ma is the addition of glaciers in the Alaska Range (i.e., more efficient erosion processes [Hallet et al., 1996; Westgate et al., 1990]). It has been shown that glaciers and climatic instability in a tectonically active region have a greater effect on denudation processes than simple isostatic response to tectonic forces in a quasi-stable climate setting (Clift, 2010; Berger et al., 2008a; Berger et al., 2008b; Molnar and England, 1990). It has also been shown that periods of climatic instability when glaciers advance and retreat enhance erosion by allowing the erosive power of glaciers and the mass transport capabilities of fluvial systems to work in tandem (Owen et al., 2008; Shuster et al., 2005; Zhang et al., 2001). The Alaska Range has a documented Pleistocene glacial history of numerous advance and retreat cycles (e.g. Briner and Kaufman, 2008).

In addition, a large percentage of the glaciers along the Denali Fault System are rare surge-type glaciers (Echelmeyer et al., 1987; Post, 1969; St. Amand, 1957). Surge-type glaciers experience surge events, involving large increases in velocity and advancement at a fairly consistent recurrence interval of 10^2 to 10^3 years (Woodward et al., 2002; Raymond, 1987; Kamb et al., 1985), and present a unique case of glacier retreat and advance. Surge events are accompanied by an exponential increase in erosion relative to steady-state surge quiescence (Humphrey and Raymond, 1994; Smith, 1990). We feel it is important to point out that the subarctic eastern Alaska Range has modern glaciers with known high basal

velocities (Thomson et al., 2010). Thomson et al. (2010) demonstrate that low-velocity glacial cover can actually limit erosion rates. We make no claims on how long there have been surge-type glaciers along the Denali Fault, but it is clear that high-velocity surge-type glaciers are spatially correlated to the Denali Fault System and not simply a product of the region's current climatic regime (Manley and Daly, 2005; Raymond, 1987; Post, 1969). Based on our thermochronological analysis (Fig. 2.13) the Denali Fault System may have experienced climate-induced Pliocene exhumation rate increases. Thus we postulate that the combination of lateral fault strain accumulation with highly efficient episodic surge-type and nonsurge glacial erosion contribute to high exhumation rates adjacent to the Denali Fault during the late Cenozoic.

2.6.6 **Driving Mechanisms of Neogene Exhumation in the Eastern Alaska Range**

These new thermochronology data offer a long record of exhumation from the eastern Alaska Range. The first sign of rapid Neogene exhumation begins ~22 Ma and is consistent with early exhumation events in the western Alaska Range (~23 Ma; Haeussler et al., 2008). Our interpretation of the thermochronological data is consistent with the stratigraphic record of the Tanana basin, where Ridgway et al. (2007) reconstruct a transpressional foreland-basin system related to regional shortening of the Alaska Range, associated with strike-slip displacement along the Denali Fault system. We also see the continuance of rapid exhumation from ~22

Ma to the present. The absence of a region-wide exhumation rate change in the eastern Alaska Range at ~6 Ma is curious considering the strong evidence that the central Alaska Range (Mount McKinley region) and the western Alaska Range experienced a change in exhumation rate at ~6 Ma (Haeussler et al., 2008; Fitzgerald, et al., 1995). The central Alaska Range and western Alaska Range are located at the interface between the rotating southern Alaska block and the rotating Bering block (Cross and Freymueller, 2008; Fig. 2.1). The interactions between these tectonic entities likely have contributed to the complex patterns of exhumation occurring along the Alaska Range. More thermochronometric data with better spatial coverage across the entire Alaska Range will help constrain the near-field boundary conditions along the western Denali Fault and test whether there are spatially and temporally complex exhumation patterns resulting from the interactions among these (micro) plates.

Our exhumation data from the Alaska Range correlate well with the initial timing of rapid Neogene exhumation in the eastern Chugach-St Elias Mountains at ~ 20 Ma based on an AFT vertical profile on Mount Logan (~18 Ma; O'Sullivan and Currie, 1996) and a detrital zircon fission track study on glacial outwash sands (Enkelmann et al., 2008, ~20 Ma). Additionally, the still active Wrangell volcanic field first developed ~23 Ma (Richter et al., 1990), suggesting that the early Miocene was an important time in the tectonic development of southern margin of Alaska.

The overall Neogene tectonic history of Alaska is not well constrained, but there is growing evidence from thermochronologic studies of exhumation events initiated at ~23 Ma, ~22 Ma, ~20 Ma, ~16 Ma, ~11 Ma, ~6 Ma, 4 Ma and ~1 Ma (Spotila and Berger, 2010; Berger et al., 2008a; Berger et al., 2008b; Haeussler et al., 2008; Enklemann et al., 2008; O'Sullivan and Currie, 1996; Fitzgerald et al., 1995; this study). In addition, strata in regional basins suggest that pulses of enhanced exhumation occurred from the Miocene to present (Finzel et al., 2009; Haeussler et al. 2008; Ridgway et al., 2007; Lagoe et al., 1993). Though Alaska exhumation events since ~5 Ma have been correlated with climatic drivers by some researchers (e.g., Enkelmann et al., 2009, Berger et al. 2008a; Berger et al., 2008b), there is a general consensus that tectonic drivers have also been continual since the middle Miocene (e.g., Spotila and Berger 2010).

The ~22 Ma initiation of rapid exhumation in the eastern Alaska Range is roughly correlative with the arrival of the Yakutat microplate into the southern Alaska subduction zone (Plafker et al., 1994). The Yakutat microplate is thought to consist primarily of mafic oceanic plateau rocks (Plafker, 1987) between 15 and 35 km thick (Christeson et al., 2010; Eberhart-Phillips et al., 2006; Ferris et al., 2003). Although the timing of the arrival of the Yakutat microplate and the change from normal subduction to flat slab subduction and/or collision is poorly constrained, the longevity (~22 Ma to present) of rapid exhumation in the eastern Alaska Range and across south-central Alaska suggests that long term exhumation in the eastern

Alaska Range is recording the timing of "collision" and the effects of continuing collision. This interpretation does not discount the influence of block rotation (Haeussler et al., 2008) or climatic influences on exhumation history (Berger et al., 2008a; Berger et al., 2008b). That said, both rotation of the Southern Alaska Block and Quaternary tectonic/climate coupling are ultimately driven by tectonic processes at Alaska's southern margin subduction zone.

2.7 **Conclusions**

We applied $^{40}Ar/^{39}Ar$ (hornblende, muscovite, biotite, and K-spar), AFT, and AHe thermochronology to examine the asymmetric topographic signature of the Denali Fault in the eastern Alaska Range. We identified spatial variations in the amount of exhumation along and across strike and temporal variations in the focus of exhumation. Rapid exhumation has been occurring since ~22 Ma, with a zone of focused deep exhumation along, and on the north side of the Denali Fault. The youngest AFT ages (~1 Ma) were identified in the Nenana Mountain region where total Neogene exhumation is less than elsewhere in the region. We postulate that a segment of the Denali Fault has a north-dipping fault plane and the asperity is fixed onto the south side of the Denali Fault with the deforming edge currently in the Nenana Mountain region.

An exhumation rate increase in the Pliocene and Quaternary may be related to climate change. Coeval changes in exhumation and climate are most clearly expressed on the north side of the Denali Fault, whereas the south side of the

Denali Fault indicates a more suppressed Pliocene-Quaternary increase in exhumation. This apparent Pliocene-Quaternary exhumation gradient across the Fault could be due to a lack of data on the south side or weaker tectonic forcing. Although we discussed a unique glacial-tectonic exhumation feedback loop for ice covered strike-slip faults, more information is needed to conclusively link increases in Pliocene-Quaternary exhumation rates to climate in the Alaska Range.

The longevity of rapid exhumation in the eastern Alaska Range demands a long-term driving mechanism. We suggest that by at least ~22 Ma, the Yakutat microplate was not undergoing standard subduction, but instead either flat slab subduction or collision had initiated and continues today.

2.8 **Acknowledgements**

We would like to thank the Geological Society of America and the Geological Society of Alaska for supporting this research project through graduate research grants. We would also like to thank the American Alpine Club and Mugs Stump Climbing grant for field season funding. This manuscript benefited greatly from the constructive reviews of A. Berger, C. Sorlien and S. Gulick. This research was also made possible by support from National Science Foundation grants EAR 0952793 and EAR 0952800. We thank W. Nokleberg for his work in the region and the numerous other Alaska-based research projects that that were the foundation for this research. A special thanks to A. Sterns for field assistance.

2. 9 **Figures**

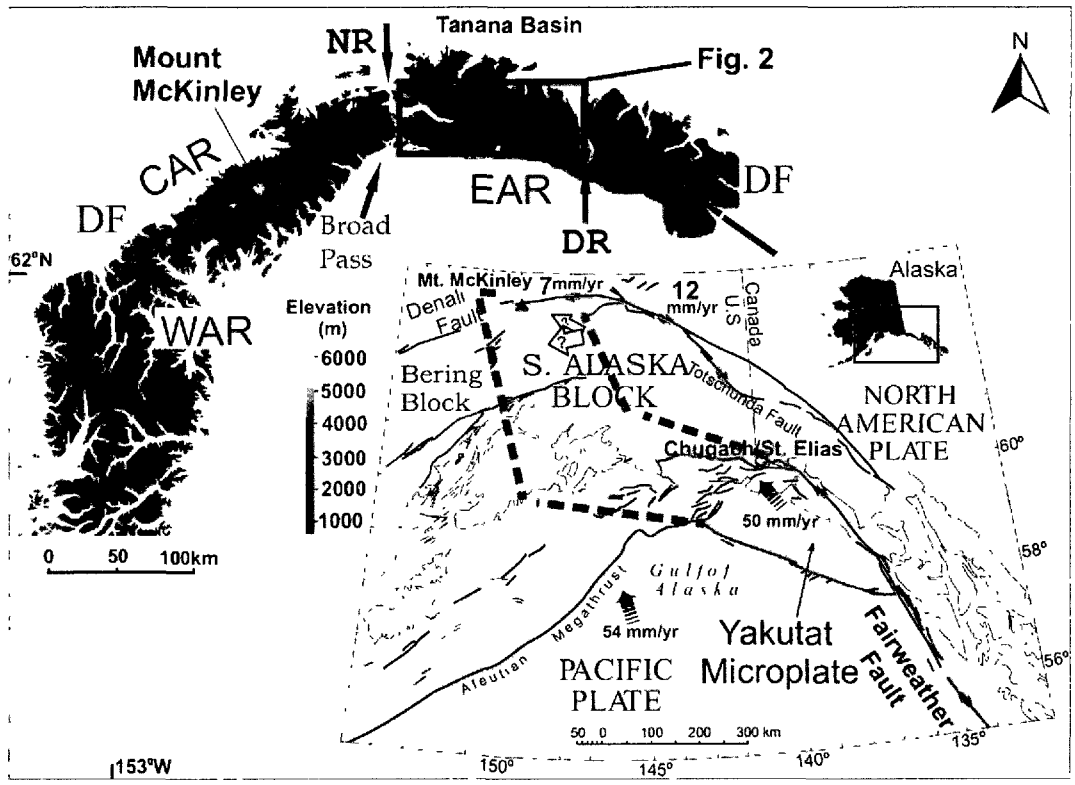

Figure 2.1: Tectonic map of southern Alaska. Modified from Haeussler et al. (2000), showing major faults, tectonic plates, and tectonic blocks. Decreasing westward Pleistocene Denali Fault slip rates are from Matmon et al. (2006) and Mériaux et al. (2009). Yakutat– North America plate motion (solid arrow on Yakutat Microplate) is from Elliott (2010). The open arrows on the Southern Alaska Block show the inferred movement of the Southern Alaska block with respect to North America. The western boundary of the southern Alaska block is poorly defined. The grey dashed line denotes the modern day location of the subducted Yakutat slab beneath the continental margin (after Eberhart-Phillips et al., 2006).
A detailed digital elevation model of the Alaska Range flooded to 1000 m elevation is used to emphasize higher topography. Most of the western and central Alaska Range are south of the Denali Fault. The eastern Alaska Range is mostly north of the Denali Fault. The rectangle delineates the study area in the eastern Alaska Range along the Denali Fault shown in Figure 2.2. WAR, western Alaska Range; CAR, central Alaska Range; EAR, eastern Alaska Range; DF, Denali Fault; NR, Nenana River; DR, Delta River.

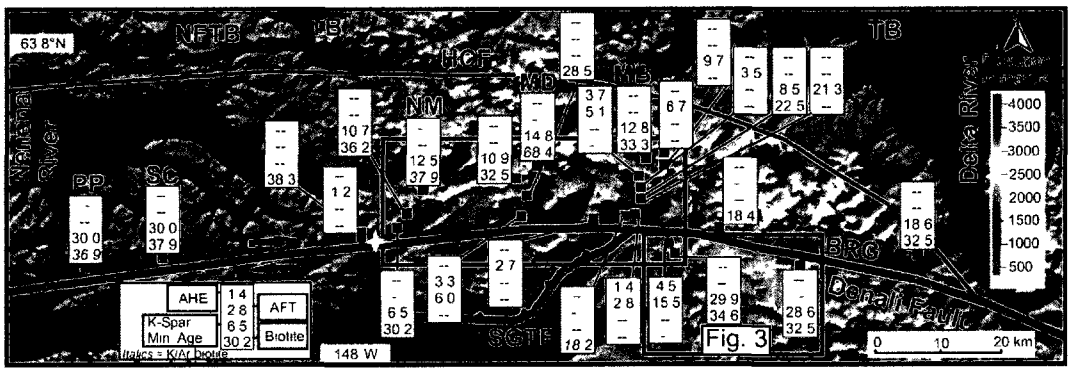

Figure 2.2: Colored digital elevation map of the eastern Alaska Range, showing sample locations and major faults. Sample labels show apatite helium (AHe), apatite fission track (AFT), K-spar minimum (K-spar) and biotite closure ages in descending order. Two hyphens (--) indicate no data. Italics refer to previous K-Ar work from Csejtey et al. (1992) or Nokleberg et al. (1992). The red cross shows the epicenter of the 2 November 2002 **M**7.9 Denali Fault earthquake; the yellow cross shows the epicenter of the 23 October 2002 **M**6.7 Nenana Mountain earthquake. NFTB, Northern Foothills Thrust Belt; HCF, Hines Creek Fault; SGTF, Susitna Glacier Thrust Fault; DF, Denali Fault; PP, Panorama Peak; SC, Schist Creek Pluton; NM, Nenana Mountain Transect; MD, Mount Deborah Transect; MB, Mount Balchen Transect; BRG, Black Rapids Glacier; MET, Meteor Peak Region. The rectangle delineates the study area in the eastern Alaska Range along the Denali Fault shown in Figure 2.3.

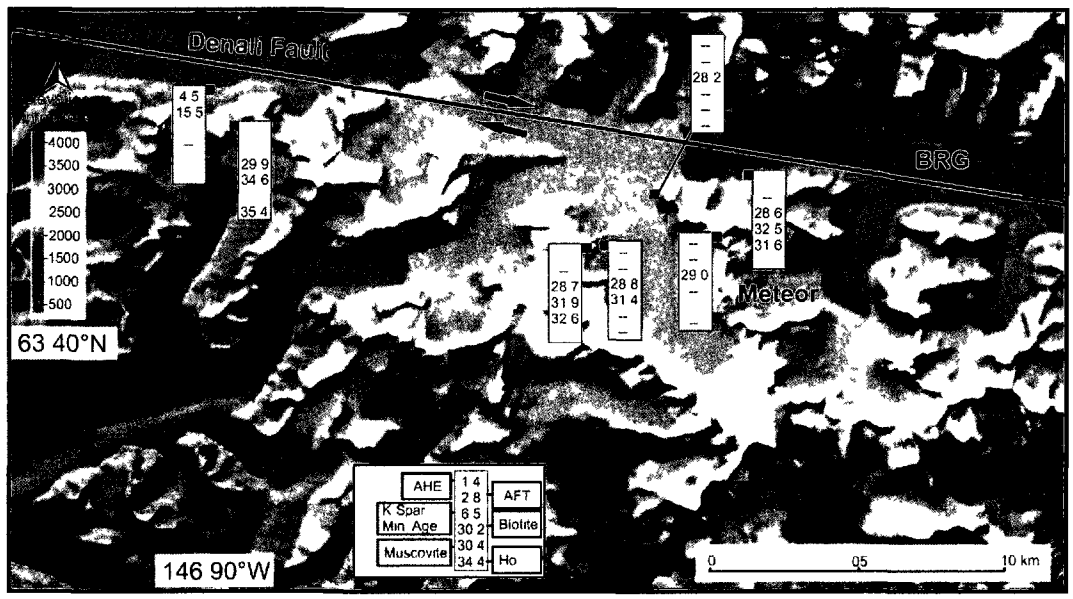

Figure 2.3: Colored digital elevation map of the eastern Alaska Range showing sample locations south of the Denali Fault. Sample labels show apatite helium (AHe), apatite fission track (AFT), K-spar minimum (K-spar), biotite, muscovite, and hornblende closure ages in descending order. Two hyphens (--) refer to no data. BRG, Black Rapids Glacier; Meteor, Meteor Peak Region.

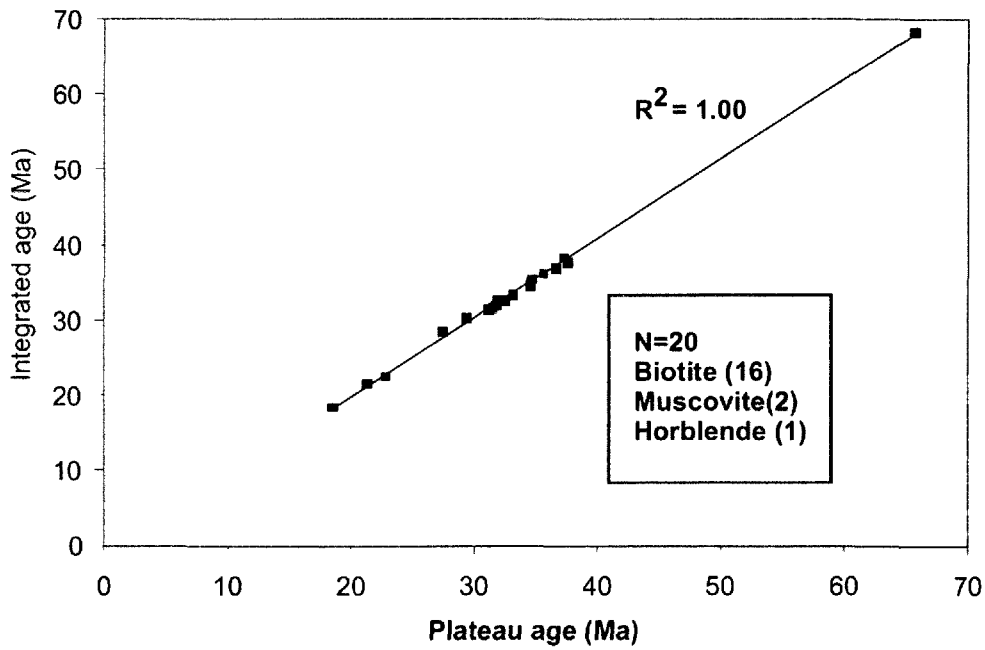

Figure 2.4: Integrated age versus plateau age for the entire $^{40}Ar/^{39}Ar$ hornblende, muscovite and biotite data set. The similarity between the two age determinations demonstrates little or no argon loss for the sample analyses.

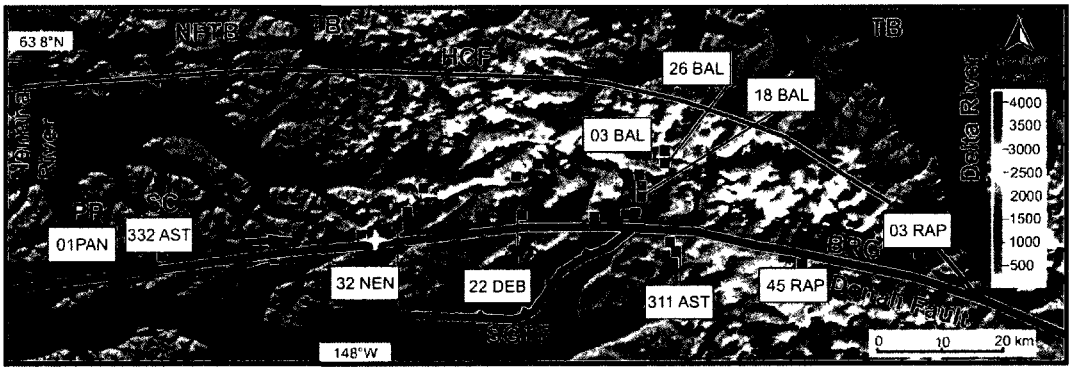

Figure 2.5: Colored digital elevation map of the eastern Alaska Range showing major faults and sample locations for those in figures 2.6, 2.7, 2.8, and 2.9. The red cross shows the epicenter of the 2 November 2002 **M**7.9 Denali Fault earthquake; the yellow cross indicates the epicenter of the 23 October 2002 **M**6.7 Nenana Mountain earthquake. NFTB, Northern Foothills Thrust Belt; HCF: Hines Creek Fault; SGTF; Susitna Glacier Thrust Fault (shown in blue); Denali Fault : Denali Fault; PP Panorama Peak; SC: Schist Creek Pluton; BRG: Black Rapids Glacier.

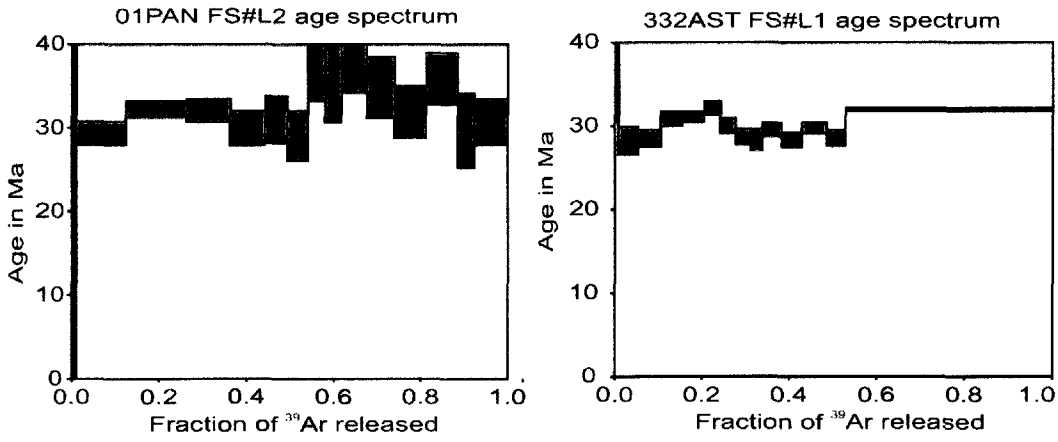

Figure 2.6: $^{40}Ar/^{39}Ar$ age spectra for K-spar from sample 01PAN from Mount Panorama and sample 332AST from Schist Creek Pluton. The general flat shape of the age spectra implies rapid postemplacement cooling. Sample locations are shown on figure 2.5.

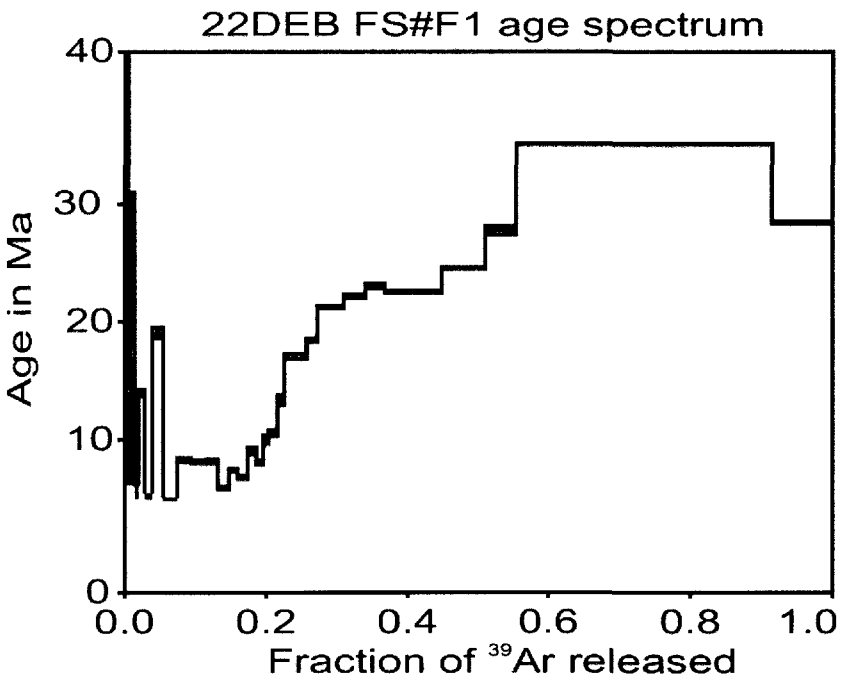

Figure 2.7: $^{40}Ar/^{39}Ar$ age spectra for K-spar from sample 22DEB from the Mount Deborah transect. The downstepping nature of the release indicates a prolonged and complicated thermal history. Sample location is shown on Figure 2.5. See data repository figures 2R.22 to 2R.31 for other samples.

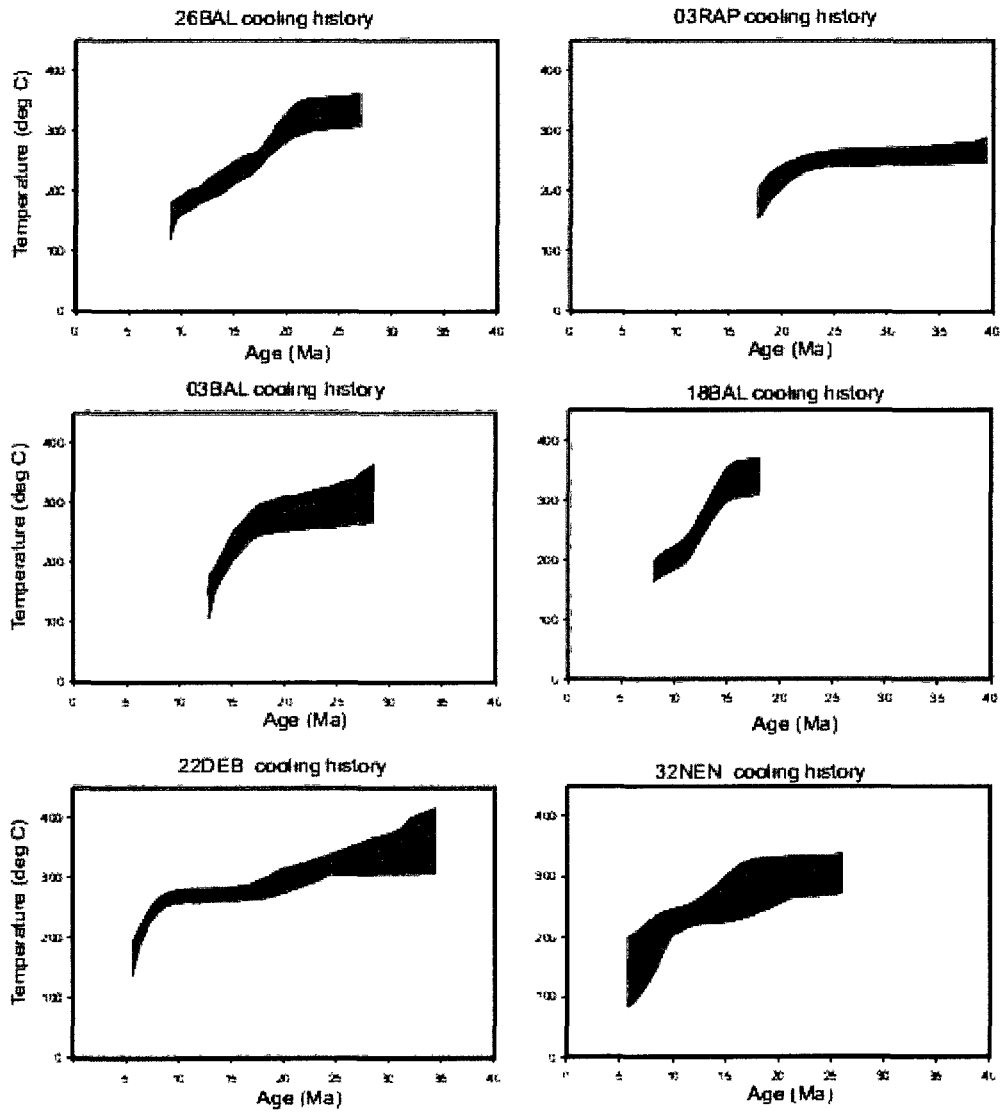

Figure 2.8: Monotonic multiple diffusion domain (MDD) thermal models for K-spar from samples 26BAL, 03RAP, 03 BAL, 18BAL, 22DEB, and 32NEN. The MDD magenta band is the 90% confidence interval of the mean and the purple band is the 90% confidence of the distribution. Sample locations are shown on Figure 2.5.

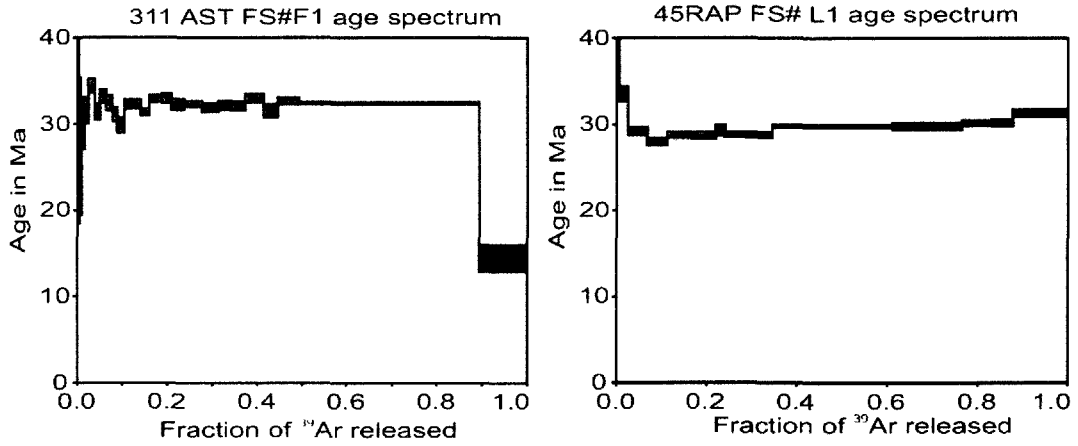

Figure 2.9: $^{40}Ar/^{39}Ar$ age spectra for K-spar for samples 311AST and 45RAP from south of the Denali Fault. The flat-shape of the age spectra implies rapid cooling, which we interpret as a short-lived metamorphic event based on rock fabric. Sample locations are shown on Figure 2.5.

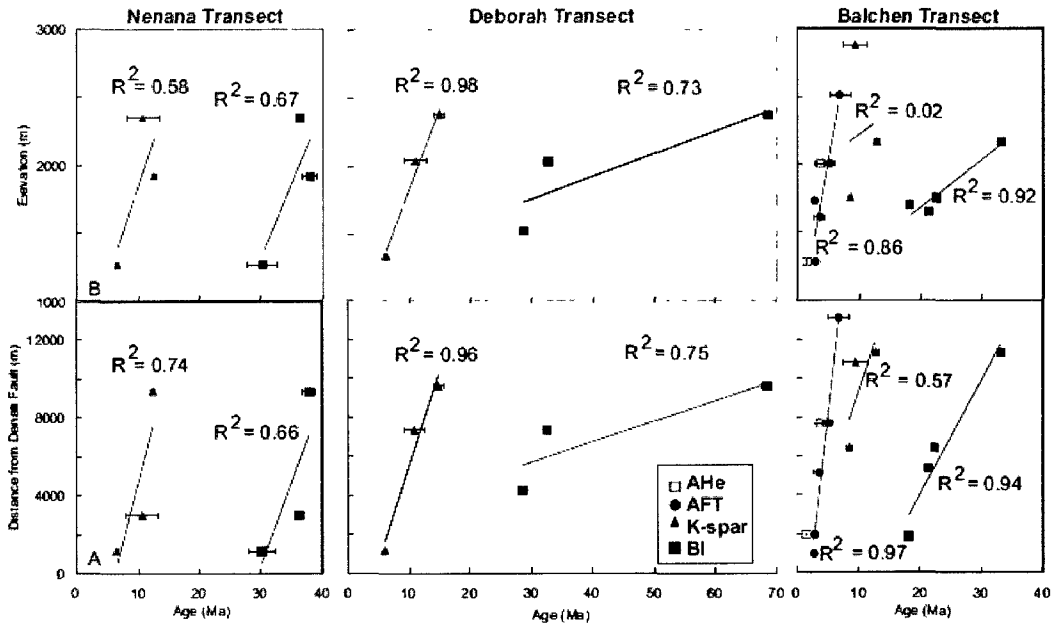

Figure 2.10: Exhumation cooling ages versus (A) distance from the Denali Fault and (B) elevation above sea level for all samples from the three transects shown in figure 2.2. The Denali Fault is interpreted as lying in the center of each glacier in the study area. Lines show best linear fit to data points of same thermochronology method. Correlation coefficient is shown next to the best-fit lines. Because there were only two AHe samples from near Mount Balchen, these AHe ages are shown without a trend line. Although cooling age in all systems correlates with both elevation and distance from the Denali Fault, distance from the fault is more significant. A good example of this relationship is seen in the Mount Balchen transect K-spar minimum age data, where proximity to the Denali Fault has a stronger effect on cooling age than elevation.

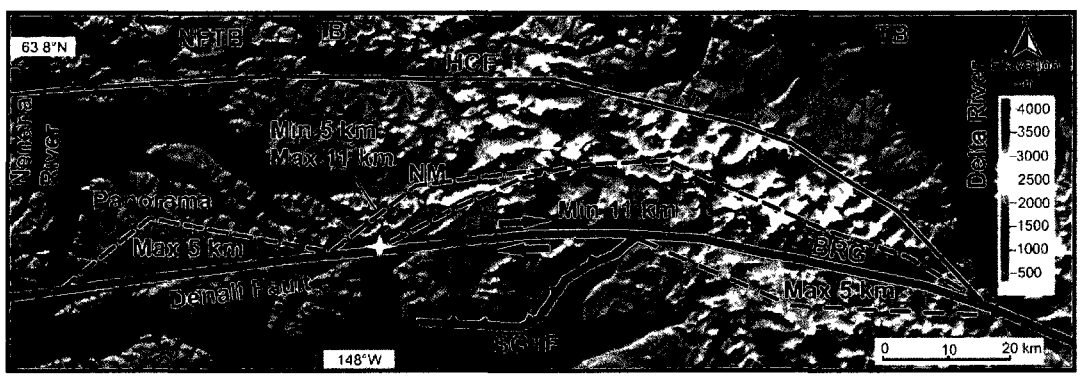

Figure 2.11: Regions (contours) of varying exhumation depth along the Denali Fault based on the current set of high temperature hornblende, muscovite, biotite, and K-spar minimum closure ages. The red cross shows the epicenter of the 2 November 2002 **M**7.9 Denali Fault earthquake; the yellow cross indicates the epicenter of the 23 October 2002 **M**6.7 Nenana Mountain earthquake. NFTB: Northern Foothills Thrust Belt; HCF: Hines Creek Fault; SGTF; Susitna Glacier Thrust Fault Denali Fault: Denali Fault; BRG: Black Rapids Glacier region; NM: Nenana Mountain region; Panorama: Panorama and Schist Creek plutons. The current locus of rapid exhumation is inferred to be near the epicenter (yellow cross) of the 23 October 2002 M6.7 Nenana Mountain earthquake and related to the edge of a segment of north-dipping fault plane.

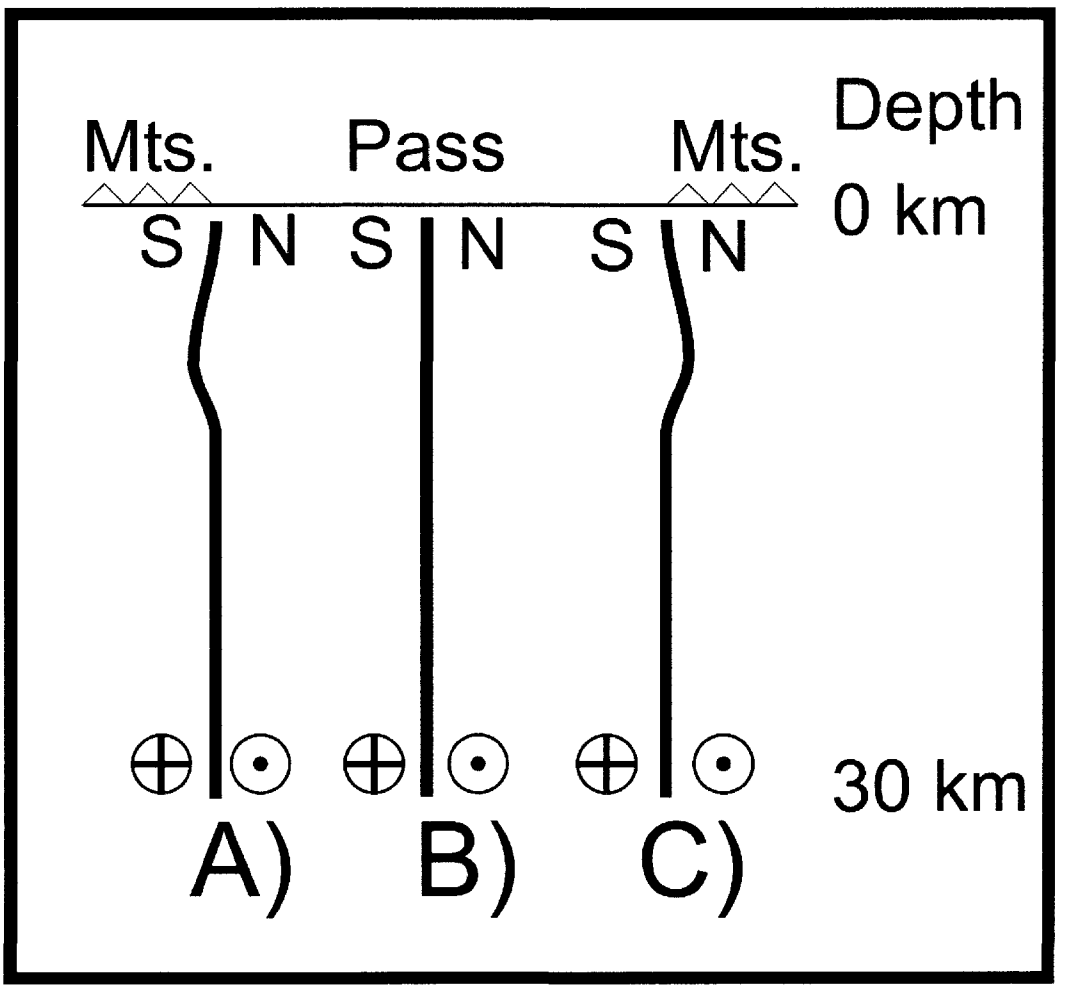

Figure 2.12: Schematic model of variations in the dip of the Denali Fault plane at depth that may contribute to asymmetric topographic development along the Denali Fault. View is along the fault plane looking westward. Note, the Denali fault in the central Alaska Range may dip south (A), the broad pass region may be vertical (B), and the Denali fault in the eastern Alaska Range may dip to the north (C) resulting in asymmetric topographic develop

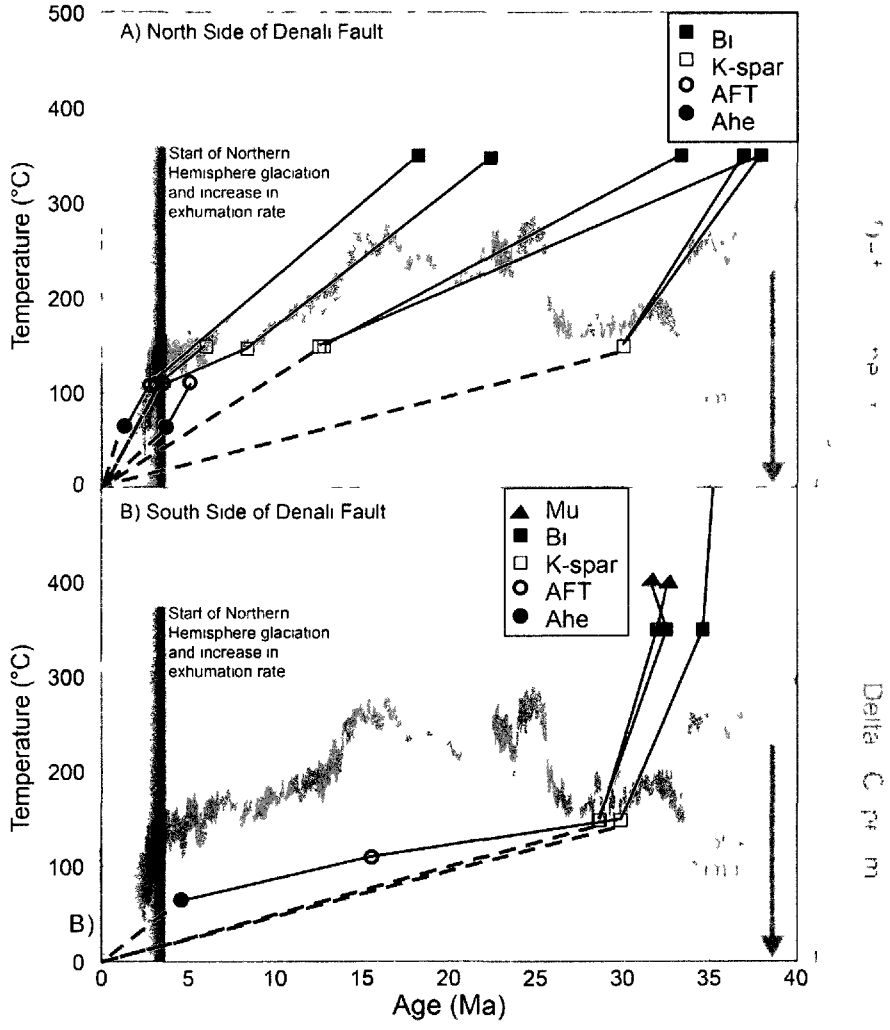

Figure 2.13: Time-averaged temperature paths for individual samples from north (A) and south (B) of the Denali Fault, based on multiple thermochronometers. Data include hornblende (550 °C; off graph), muscovite (Tc 400 °C; Mu) biotite (Tc 350 °C; Bi), K-spar (Tc 150 °C), AFT (Tc 110°C), and AHE (Tc 65 °C) ages (Reiners and Ehlers, 2005). Samples with multiple cooling ages are shown. All samples are within ~10 km of the Denali Fault. Cooling paths are assumed to be linear in between data points. $\delta^{18}O$ is modified from Zachos et al. (2001) and used as a proxy for world temperature trends. Samples north of the Denali Fault show a marked increase in cooling rate at ~3 Ma. Limited data from samples south of the Denali Fault show a marked increase in cooling rate at ~ 4-5 Ma.

2.10 **References**

Aleinikoff, J.N., Farmer, G.L., Rye, R.O., and Nokleberg, W.J,. 2000, Isotopic evidence for the sources of Cretaceous and Tertiary granitic rocks, east-central Alaska: implications for the tectonic evolution of the Yukon–Tanana terrane. Can. J. of Ear. Sci., 37: 945–956.

Bemis, S.P., and Wallace, W., 2007, Neotectonic framework of the north-central Alaska Range foothills, in Ridgway, K.D., Trop, J.M., Glen, J.M.G., and O'Neill, J.M., eds., Tectonic Growth of a Collisional Continental Margin: Crustal Evolution of Southern Alaska: Geological Society of America Special Paper 431, p. 549–572, doi: 10.1130/2007.2431(21).

Berger, A.L., Gulick, S.P.S., Spotila, J.A., Upton, P., Jaeger, J.M., Chapman, J.B., Worthington, L.A., Pavlis, T.L., Ridgway, K.D., Willems, B.A. and McAleer, R.J, 2008a, Quaternary tectonic response to intensified glacial erosion in an orogenic wedge. Nature Geoscience 1, 793–99.

Berger, A.L., Spotila, J.A., Chapman, J., Pavlis, T.L., Enkelmann, E., Ruppert, N.A., and Buscher, J.T., 2008b, Architecture, kinematics, and exhumation of a convergent orogenic wedge: A thermochronological investigation of tectonic-climatic interactions within the central St. Elias orogen, Alaska: Earth and Planetary Science Letters, v. 270, p. 13–24, doi: 10.1016/j.epsl.2008.02.034.

Braun, J., van der Beek, P., Batt, G., 2006, Quantitative Thermochronology: Cambridge, Cambridge University Press.

Briner, J.P., and Kaufman, D.S, 2008, Late Pleistocene mountain glaciation in Alaska: Key chronologies. Journal of Quaternary Science, v. 23, p. 659-670.

Buscher, J. T., and J. A. Spotila, 2007, Near-field response to transpression along the southern San Andreas Fault, based on exhumation of the northern San Gabriel Mountains, southern California, Tectonics, 26, TC5004, doi:10.1029/2006TC002017.

Christeson, G.L., Gulick, S.P.S., van Avendonk, H.J.A., Worthington, L., Reece, R.S. and Pavlis, T.L., 2010, The Yakutat terrane: Dramatic change in crustal thickness across the Transition fault, Alaska, Geology,v. 38, no. 10, p. 895-898. DOI: 10.1130/G31170.1.

Clift, P. D., 2010, Enhanced global continental erosion and exhumation driven by Oligo-Miocene climate change, Geophys. Res. Lett., 37, L09402, doi:10.1029/2010GL043067.

Cormier, M.H., Seeber, L., McHugh, C.M.G., Polonia, A., Cagatay, N., Emre, O., Gasperini, L., Gorur, N., Bortoluzzi, G., Bonatti, E., Ryan, W.B.F., Newman, K.R., 2006, North Anatolian Fault in the Gulf of Izmit (Turkey): Rapid vertical motion in response to minor bends of a nonvertical continental transform. J. Geophys. Res. 111 (B4) Art. No. B04102.

Crone, A., Personius, S., Craw, P., Haeussler, P., and Staft, L., 2004, The Susitna Glacier Thrust Fault—Characteristics of ruptures that initiated the 2002 Denali Fault earthquake, Bull. Seis. Soc. Amer., v. 94, no.6B, pp. S5-S22.

Cross, R. and Freymueller, J., 2008, Evidence for and implications of a Bering plate based on geodetic measurements from the Aleutians and western Alaska. Journal of Geophysical Research ,v. 113, B07405, doi: 10.1029/2007JB005136.

Csejtey, B., Jr., Mullen, M.W., Cox, D.P., and Stricker, G.D., 1992, Geology and geochronology of the Healy quadrangle, south-central Alaska: U.S. Geological Survey Miscellaneous Investigation Map I-1961, scale 1:250,000.

Dair, L., and Cooke, M.L., 2009, San Andreas fault geometry through the San Gorgonio Pass, California: Geology, v. 37, p. 119-122, doi: 10.1130/G25101A.1.

Eberhart-Phillips, D., Haeussler, P.J., Freymueller, J.T., Frankel, A.D., Rubin, C.M., Craw, P., Ratchkovski, N.A., Anderson, G., Carver, G.A., Crone, A.J., Dawson, T.E., Fletcher, H., Hansen, R., Harp, E.L., Harris, R.A., Hill, D.P., Hreinsdottir, S., Jibson, R.W., Jones, L.M., Kayen, R.E., Keefer, D.K., Larsen, C.F., Moran, S.C., Personius, S.F., Plafker, G., Sherrod, B.L., Sieh, K., Sitar, N., and Wallace, W.K., 2003, The 2002 Denali fault earthquake, Alaska: A large magnitude slip-partitioned event: Science, v. 300, p. 1113–1118.

Eberhart-Phillips, D., Christensen, D.H., Brocher, T.M., Hansen, R., Ruppert, N.A., Haeussler, P.J., and Abers, G.A., 2006, Imaging the transition from Aleutian subduction to Yakutat collision in central Alaska, with local earthquakes and active source data, Journal of Geophysical Research, 111, B11303.

Echelmeyer, K., Butterfield, R., and Cuillard, D., 1987, Some observations on a recent surge of Peters Glacier, Alaska, U.S.A. J. Glaciol., 33(115), 341–345.

Elliott, J. L., Larsen, C. F., Freymueller, J. T. and Motyka, R. J., 2010, Tectonic block motion and glacial isostatic adjustment in southeast Alaska and adjacent Canada constrained by GPS measurements, J. Geophys. Res., 115, B09407, doi:10.1029/2009JB007139.

Enklemann, E., Garver, J.I. Pavlis, T.L., 2008, Rapid exhumation of ice-covered rocks of the Chugach-St. Elias orogen, SE-Alaska. Geology, 36, no. 12; 915-918 doi:10.1130/G2252A.1.

Enkelmann, E., Zeitler, P. K., Pavlis, T. L., Garver, J. I. and Ridgway, K. D., 2009, Intense localized rock uplift and erosion in the St Elias orogen of Alaska, Nature Geoscience, 2, 360-363.

Ferris, A., Abers, G.A., Christensen, D.H., Veenstra, E., 2003, High resolution image of the subducted Pacific plate beneath central Alaska, 50-150km depth. Earth Planet. Sci. Lett. 214 (3-4), 575-588.

Finzel, E., Ridgway, K., Reifenstuhl, R., Blodgett, R., White, J., Decker, P., 2009, Stratigraphic framework and estuarine depositional environments of the Miocene Bear Lake Formation, Bristol Bay Basin, Alaska: Onshore equivalents to potential reservoir strata in a frontier gas-rich basin. American Association of Petroleum Geologists Bulletin, v. 93, no. 3, pp. 379–405.

Fisher, M.A., Ratchkovski, N.A., Nokleberg, W.J., Pellerin, L., and Glen, J.M.G., 2004, Geophysical data reveal the crustal structure of the Alaska Range orogen within the aftershock zone of the Mw 7.9 Denali Fault earthquake: Bull. Seis. Soc. Amer., v. 94, p. S107–S131, doi: 10.1785/0120040613.

Fitzgerald, P.G., Stump, E., Redfield, T.F., 1993, Late Cenozoic uplift of Denali and its relation to relative plate motion and fault morphology, Science, 259, pp. 497-499.

Fitzgerald, P.G., Sorkhabi, R., Redfield, T. Stump, E., 1995, Uplift and denudation of the central Alaska Range: a case study in the use of apatite fission track thermochronology to determine absolute uplift parameters, J. Geophys. Res., 100, pp. 20,175-20,191.

Haeussler, P.J., 2008, An overview of the neotectonics of interior Alaska; far-field deformation from the Yakutat Microplate collision. Geophysical Monograph 179: 83–108.

Haeussler, P.J., Bruhn, R.L, and Pratt, T.L., 2000, Potential seismic hazards and tectonics of the upper Cook Inlet basin, Alaska, based on analysis of Pliocene and younger deformation: Geol. Soc. Amer. Bull., v. 112, p. 1414–1429.

Haeussler, P.J., Schwartz, D.P., Dawson, T.E., Stenner, H.D., Lienkaemper, J.J., Cinti, F.,Montone, P., Sherrod, B., and Craw, P., 2004, Surface rupture of the 2002 Denali Fault, Alaska, Earthquake and comparison with other strike-slip ruptures: Earthquake Spectra, v. 20, p. 565–578.

Haeussler, P.J., O'Sullivan, P., Berger, A.L., and Spotila, J.A., 2008, Neogene exhumation of the Tordrillo Mountains, Alaska, and correlations with Denali (Mt. McKinley), in Freymueller, J.J., Haeussler, P.J., Wesson, R., and Ekstrom, G., Active Tectonics and Seismic Potential of Alaska: Washington, D.C., American Geophysical Union Monograph 179, p. 269–285.

Hallet, B., Hunter, L., and Bogen, J., 1996, Rates of erosion and sediment evacuation by glaciers: A review of field data and their implications, Global and Planetary Change, 12, 213-235.

Harrison, T.M., Celerier, J., Aikman, A.B., Hermann, J., Heizler, M.T., 2009, Diffusion of ^{40}Ar in muscovite, Geochemica et Cosmochimica Acta, Vol. 73, p. 1039-1051.

Harrison, W. D., and Post, A., 2003, How much do we really know about glacier surges?, Ann. Glaciol., 36, 1 – 6.

Hilley, G. and Arrowsmith, J., 2008, Geomorphic response to uplift along the Dragon's Back pressure ridge, Carrizo Plain, California, Geology 36 10.1130/G24517A.1.

Humphrey, N. F. and Raymond, C. F., 1994, Hydrology, erosion and sediment production in a surging glacier: Variegated Glacier, Alaska, 1982-83, J. Glaciol., 40(136), 539-552.

Kamb, B., Raymond, C., Harrison, W., Engelhardt, H., Echelmeyer, K., Humphrey, N., Brugman, M., and Pfeffer, T., 1985, Glacier surge mechanism: 1982–1983 surge of Variegated Glacier, Alaska, Science, 227, 469–479.

Lagoe, M.B., Eyles, C.H., Eyles, N., and Hale, C., 1993, Timing of late Cenozoic tidewater glaciation in the far North Pacific: Geological Society of America Bulletin, v. 105, p. 1542–1560, doi: 10.1130/0016– 7606.

Lisiecki, L.E. and Raymo, M.E., 2005, A Pliocene–Pleistocene stack of 57 globally distributed benthic $\delta^{18}O$ records. Paleoceanography 20, PA1003.

Little, T.A., Cox, S., Vry, J.K., and Batt, G., 2005, Variations in exhumation level and uplift rate along the oblique-slip Alpine fault, central Southern Alps, New Zealand: Geol. Soc. Amer. Bull., v. 117, p. 707–723.

Lovera O., Grove M., Harrison T., 2002, Systematic analysis of K-feldspar $^{40}Ar/^{39}Ar$ step heating results II: Relevance of laboratory argon diffusion properties to nature. Geochim Cosmochim Acta 66(7):1237- 1255.

Lu, Z., Wright, T., Wicks, C., 2003, Deformation of the 2002 Denali Fault Earthquakes, Mapped by Radarsat-1 Interferometry. Eos (Transactions, American Geophysical Union), Vol. 84, No. 41.

Manley W.F. and Daly, C., 2005, Alaska geospatial climate animations of monthly temperature and precipitation. Institute of Arctic and Alpine Research, University of Colorado. http://instaar.colorado.edu/QGISL/AGCA

Matmon, A., Schwartz, D., Haeussler, P. Finkel, R., Lienkaemper, J., Stenner, H., Dawson, T., 2006, Denali Fault slip rates and Holocene-late Pleistocene kinematics of central Alaska., Geology, 34, no. 8., pp. 645–648.

McAleer, R., Spotila, J., Enkelmann, E., Berger, A., 2009, Exhumation along the Fairweather fault, southeastern Alaska, based on low-temperature thermochronometry: Tectonics, 28, TC1007, doi:10.1029/2007TC002240.

McDougall, I. and Harrison, T.M., 1999, Geochronology and Thermochronology by the 40Ar/39Ar method-(2nd edition), New York, Oxford University Press, 269 p.

Mériaux, A.-S., Sieh, K., Finkel, R. C., Rubin, C. M., Taylor, M. H., Meltzner, A. J. and Ryerson, F. J., 2009, Kinematic behavior of southern Alaska constrained by westward decreasing postglacial slip rates on the Denali Fault, Alaska, J. Geophys. Res., 114, B03404, doi:10.1029/2007JB005053.

Molnar, P., and England, P., 1990, Late Cenozoic uplift of mountain ranges and global climate change: Chicken or egg? : Nature, v. 346, p. 29–34.

Nokleberg, W.J., Aleinikoff, J.N., Dutro, J.T., Jr., Lanphere, M.A., Silberling, N.J., Silva, S.R., Smith, T.E., and Turner, D.L., 1992, Map, tables, and summary of fossil and isotopic age data, Mount Hayes quadrangle, eastern Alaska Range, Alaska: U.S. Geological Survey Miscellaneous Field Studies Map 1996-D, scale 1:250,000.

O'Sullivan, P., and Currie, L, 1996, Thermotectonic history of Mt. Logan, Yukon Territory, Canada: Implications of multiple episodes of middle to late Cenozoic denudation, Earth and Planetary Sceince Letters, vol. 144, p. 251-261.

Owen, L.A., Thackray, G., Anderson, R.S., Briner, J.P., Kaufman, D., Roe, G., Pfeffer, W., Yi, C., 2008. Integrated mountain glacier research: current status, priorities and future prospects. Geomorphology 103, 158–171.

Plafker, G., 1987, Regional geology and petroleum potential of the northern Gulf of Alaska continental margin, *in* Scholl, D.W., et al., eds., Geology and resource potential of the continental margin of western North America and adjacent ocean basins: Circum-Pacific Council for Energy and Mineral Resources Earth Science Series, v. 6, p. 229–268.

Plafker G, Naeser, C.W., Zimmermann R.A., Lull J.S., Hudson, T. 1992, Cenozoic uplift history of the Mount McKinley area in the Central Alaska Range based on fission track dating. U.S. Geological Survey Bulletin 2041:202–12.

Plafker, G., Moore, J.C., and Winkler, G.R., 1994, Geology of the southern Alaska margin, *in* Plafker, G., and Berg, H.C., eds., The geology of Alaska: Boulder, Colorado, Geological Society of America, Geology of North America, v. G-1, p. 389–449.

Post, A., 1969, Distribution of surging glaciers in western North America, Journal of Glaciology 8, 229-240.

Ratchkovski, N.A., Wiemer, S., and Hansen, R.A., 2004, Seismotectonics of the Central Denali Fault, Alaska and the 2002 Denali Fault Earthquake Sequence, Bull. Seis. Soc. Am. 6B, S156-S174.

Raymond, C. F., 1987, How Do Glaciers Surge? A review: Journal of Geophysical Research, 644 v. 92, no. B9, 9121–9134, doi:10.1029/JB092iB09p09121.

Reiners, P.W. and Ehlers. T.A., eds. 2005, Low-Temperature Thermochronology: Techniques, Interpretations, Applications. Reviews in Mineralogy and Geochemistry, Vol. 58. Chantilly, VA: Mineral. Soc. Am., Geochem. Soc. pp. 622.

Ridgway, K., Thoms, E., Layer, P., Lesh, M., White, J., and Smith, S., 2007, Neogene transpressional foreland basin development on the north side of the central Alaska Range, Usibelli Group and Nenana Gravel, Tanana basin, in Ridgway, K.D., et al., Tectonic Growth 651 of a Collisional Continental Margin: Crustal Evolution of Southern Alaska: Geological Society of America Special Paper 431, p. 507–547, doi: 10.1130/2007.2431(20).

Richter, D.H., Smith, J.G., Lanphere, M.A., Dalrymple, G.B., Reed, B.L. and Shew, N., 1990. Age and progression of volcanism, Wrangell volcanic field, Alaska. Bulletin of Volcanology, vol. 53, p. 29-44.

Roeske, S., Till, A., Foster, D., and Sample, J., 2007, Introduction, *in* Till, A., Roeske, S., Foster,D., and Sample, J., eds., Uplift and Extension along Continental Strike-Slip Faults: Geological Society of America Special Paper 434, p. 15–33.

Sherwood, K.L., and Craddock, C., 1979, General geology of the central Alaska Range between the Nenana River and Mount Deborah: Alaska Division of Geological and Geophysical Surveys, Open-File Report AOF-116, scale 1:63,360, 3 sheets.

Shuster, D.L., Ehlers, T.A., Rusmore, M.E., and Farley, K.A., 2005, Rapid Glacial Erosion at 1.8 Ma Revealed by 4He/3He Thermochronometry: Science, v. 310, p. 1668-1670.

Smith, N. D., 1990, The effects of glacial surging on sedimentation in a modern ice-contact lake, Alaska. Geological Society of America, Bulletin, 102: 1393-1403.

Spotila, J. and Berger, A., 2010, Exhumation at orogenic indentor corners under long-term glacial conditions: Example of the St. Elias orogen, Southern Alaska, Tectonophysics, V. 490, pp. 241-256.

Spotila, J.A., Farley, K.A., Sieh, K., 1998, Uplift and erosion of the San Bernardino Mountains associated with transpression along the San Andreas fault, California, as constrained by radiogenic helium thermochronology, Tectonics, V. 17, p 360-378.

Spotila, J.A., Niemi, N., Brady, R., House, M., and Buscher, J., 2007, Long-term continental deformation associated with transpressive plate motion: The San Andreas fault: Geology, v. 35, p. 967–970, doi: 10.1130/G23816A.1.

St. Amand, P., 1957, Geological and geophysical synthesis of the tectonics of portions of British Columbia, the Yukon Territory, and Alaska: Geological Society of America Bulletin, v. 68, p. 1343–1370.

Sylvester, A.G., 1988, Strike-slip faults. Geol. Soc. Am. Bull. 100, 1666–1703.

Thomson, S.N., Brandon, M.T., Tomkin, J.H., Reiners, P.W., Vasquez, C., and Wilson, N.J., 2010, Glaciation as a destructive and constructive control on mountain building, Nature, v. 467, p. 313-317.

Wahrhaftig, C., Turner, D., Weber, F, Smith, T., 1975, Nature and timing of movement on Hines Creek strand of Denali Fault system, Alaska, Geology, 3(8), pp. 463-466.

Westgate, J.A., Stemper,B .A. and Pewe, T.L., 1990, A 3 Ma record of Pliocene Pleistocene loess in interior Alaska, Geology 18, 858-861.

Whipple, K., 2009, The influence of climate on the tectonic evolution of mountain belts. Nature Geoscience 2, p. 97 – 104.

Woodward, J., Carver, S., Kunzendorf, H. and Bennike, O., 2002, Observations of surge periodicity in East Greenland using molybdenum records from marine sediment cores. In: Dowdeswell J.A. and Ó Cofaigh, C. (eds): Glacier-influenced Sedimentation on High-latitude Continental Margins. The Geological Society of London Special Publications 203, p. 367–373.

Zachos, J., Pagani, M., Sloan, L., Thomas, E., and Billups, K., 2001, Trends, rhythms, and aberrations in global climate 65 Ma to present, Science, 292, p. 686-693.

Zhang, P.Z., Molnar, P., and Downs, W.R., 2001, Increased sedimentation rates and grain sizes 2–4 Myr ago due to the influence of climate change on erosion rates: Nature, v. 410, p. 891–897.

2.11 Repository Material

2.11.1 Summary of the $^{40}Ar/^{39}Ar$ Analysis

For $^{40}Ar/^{39}Ar$ analysis, samples were submitted to the Geochronology laboratory at UAF where they were crushed, sieved, washed and hand-picked for mineral phases. The monitor mineral MMhb-1 (Samson and Alexander, 1987) with an age of 513.9 Ma (Lanphere and Dalrymple, 2000) was used to monitor neutron flux (and calculate the irradiation parameter, J). The samples and standards were wrapped in aluminum foil and loaded into aluminum cans of 2.5 cm diameter and 6 cm height. The samples were irradiated in position 5c of the uranium enriched research reactor of McMaster University in Hamilton, Ontario, Canada for 30 megawatt-hours. Upon their return from the reactor, the samples and monitors were loaded into 2 mm diameter holes in a copper tray that was then loaded in an ultra-high vacuum extraction line. The monitors were fused, and samples heated, using a 6-watt argon-ion laser following the technique described in York et al. (1981), Layer et al. (1987) and Layer (2000).

Bulk furnace-run samples were loaded in aluminum packets and step-heated in a Modifications Ltd. low-blank furnace connected on-line to the mass spectrometer. Temperature is calibrated by means of a thermocouple and a maximum temperature in excess of 1,600°C is achievable. Duplicated isothermal step-heating schedules were conducted on K-feldspar in order to retrieve diffusion

characteristics, to apply diffusion models, and to calculate model thermal histories (Harrison et al., 1994; e.g. Lovera et al., 1993).

Argon purification was achieved using a liquid nitrogen cold trap and a SAES Zr-Al getter at 400C. The samples were analyzed in a VG-3600 mass spectrometer at the Geophysical Institute, University of Alaska Fairbanks. The argon isotopes measured were corrected for system blank and mass discrimination, as well as calcium, potassium and chlorine interference reactions following procedures outlined in McDougall and Harrision (1999). System blanks generally were $2x10^{-16}$ mol ^{40}Ar and $2x10^{-18}$ mol ^{36}Ar which are 10 to 50 times smaller than fraction volumes. Mass discrimination was monitored by running both calibrated air shots and a zero-age glass sample. These measurements were made on a weekly to monthly basis to check for changes in mass discrimination.

A summary of all the $^{40}Ar/^{39}Ar$ results is given in repository Table 2R.1, 2R.2, and 2R.5 with all ages quoted to the +/- 1 sigma level and calculated using the constants of Steiger and Jaeger (1977). The integrated age is the age given by the total gas measured and is equivalent to a potassium-argon (K-Ar) age. The spectrum provides a true plateau age if three or more consecutive gas fractions represent at least 50% of the total gas release and are within two standard deviations of each other (Mean Square Weighted Deviation less than ~2.7).

Isochron ages are obtained on an inverse isochron diagram of $^{36}Ar/^{40}Ar$ versus $^{39}Ar/^{40}Ar$ (Roddick, 1978; Roddick et al., 1980), which often allows

homogeneous excess components to be identified. Errors on age and intercept age include individual errors on each point and linear regression by York's (1969) method. The goodness of fit relative to individual errors is measured by mean square weighted deviation (MSWD).

2.11.2 **Minimum K-Spar Ages**

K-spar data is shown in table 2R.1. For most K-feldspars, plateau ages cannot be defined, but since we wish to compare and discuss a series of steps with similar ages we use minimum age isochron populations. This is similar to the minima potassium feldspar ages used in bulk analysis by Copeland and Harrison (1990) using minimum age spectra steps. A similar isochron approach was also used to examine deformation along the Karakorum Fault (Valli et al., 2007). We use the more robust isochron minimum population age, but show the pseudo simple-mean minimum age plateau for comparison. In summary, the youngest isochron age grouping derived from either single grain K-spar laser runs (3) or bulk furnace runs (10) were considered to be the age of closure for the smallest domain (e.g. McDougall and Harrison, 1999; Valli et al., 2007).

2.11.3 **MDD Models**

MDD data is shown in figures 2R.38 to 2R.43. MDD thermochronology has proven a useful tool to examine orogenic development because of the wide closure temperature window (~350 °C to ~150 °C) of the system (McDougall and Harrison, 1999). K-spar MDD thermochronology is also useful due to the deep depth for

closure (~5 km) of the system, minimizing the affect of topography influencing the temperature field of the upper crust (Ehlers, 2005).

MDD thermal models were created using software developed by Lovera et al. (1993). Low temperature steps were adjusted to account for the likely presence of fluid-inclusion hosted excess Ar leading to older apparent ages. In many cases, the first step of an isothermal duplicate yielded a significantly older age than the second step. Although this pattern is consistent with the presence of fluid-inclusion hosted excess Ar (Harrison et al., 1994)., corrections using the equations from Harrison et al. (1994) did not yield usable results as was the case for Sanders et al., (2006). We used the isothermal correction technique outlined in Sanders et al. (2006), whereas they took the average age of the step before and the step after an apparent old age as an estimate of the excess Ar correction. See, GSA Data Repository item 2006190 (Sanders et al., 2006) for a detailed and extensive discussion on MDD modeling.

2.11.4 **Fission-track Analyses**

Apatite fission-track (AFT) data are shown in 2.R3. All the fission-track ages were measured with external detector method in Armstrong's fission track lab at Cal State Fullerton. Apatite grains were mounted in epoxy and ground/polished to reveal internal parts of the grains. Apatite grain mounts were etched in 5 M HNO_3 for 20 s at 21 ^{o}C. Grain mounts were affixed with low-uranium muscovite micas and irradiated at the TRIGA reactor facility at Oregon State University. After

irradiation, track densities were measured at 1250x and track length and Dpar measured at 2000x. See Table 2R.3 for additional measurement parameters.

Between 18 and 40 grains were measured per sample. $P(\chi^2)$ is > 23% in all samples indicating that the individual grain ages show little age dispersion. Track lengths were difficult to find in these young samples, thus the length data may be statistically insignificant for most of the samples. Nonetheless, track lengths are ~12 – 14 μm. Dpar was measured on each age-dated grain. The average sample Dpar varies from 1.36 to 2.02 μm with the largest Dpar measured on the oldest AFT age sample. The highest Dpar value is on for the sample (05PH003A) with the largest AFT age indicating that the apatites in this sample may be more resistant to annealing and hence give a higher age. However, the Dpar difference between the samples (1.36 – 2.02 μm) is great enough to account for only a very small part of the 3- to 5-fold age difference between the samples.

2.11.5 **Apatite (U-Th)/He and Fission-track Age Data**

Methods and results

The apatites for this study were separated using standard mineral separation techniques including crushing, sieving, water table, magnetic separator, and heavy liquids.

(U-Th)/He analyses: AHe data is shown in Tabe A4. Euhedral, inclusion-free apatite crystals were hand-picked in alcohol under cross-polars at 110x. Grain dimensions were measured for a-emission correction (Farley et al., 1996) and each

grain was individually loaded into Pt tube for He extraction. Samples were outgassed under a laser at 1100°C. After spiking with 3He, the 4He/3He ratio was measured on a quadrapole mass spectometer. Grains were then dissolved in nitric acid and analyzed for Th, U, and Sm isotope ratios by ICPMS. All analytical work was completed at in Ken Farley's lab at Caltech.

Analytical uncertainties on individual (U-Th)/He age is ~2%. However, the actual age uncertainty based on replicate analyses of individual grains from same samples is higher. In three of the samples, three individual grain ages were determined per sample (Table 2R.4); in these replicate samples, the average standard error is about 12% of the mean (at 1 sigma). In the sample with only one grain age (PH-06A), the mean uncertainty of 12% is used.

AHe/AFT closure temperatures

The AHe ages represent the time since the samples cooled through a closure temperature of 60-70 °C (Farley, 2000). The AFT ages represent the time since the samples cooled through a closure temperatures of about 100 – 120 °C (e.g., Ketcham et al., 1999) for typical apatites and monotonic cooling at rates typical of active mountain belts (Reiners and Brandon, 2006).

2.12 Repository Figures

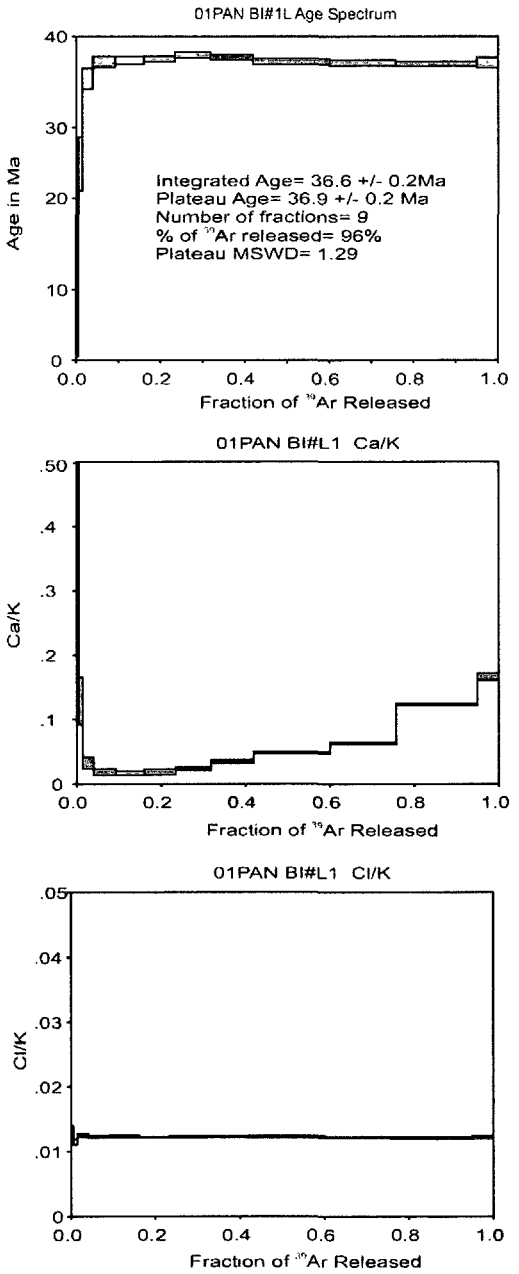

Figure 2R.1: $^{40}Ar/^{39}Ar$ age spectra, K/Ca ratios and Cl/K ratios for sample 01PAN biotite analyses.

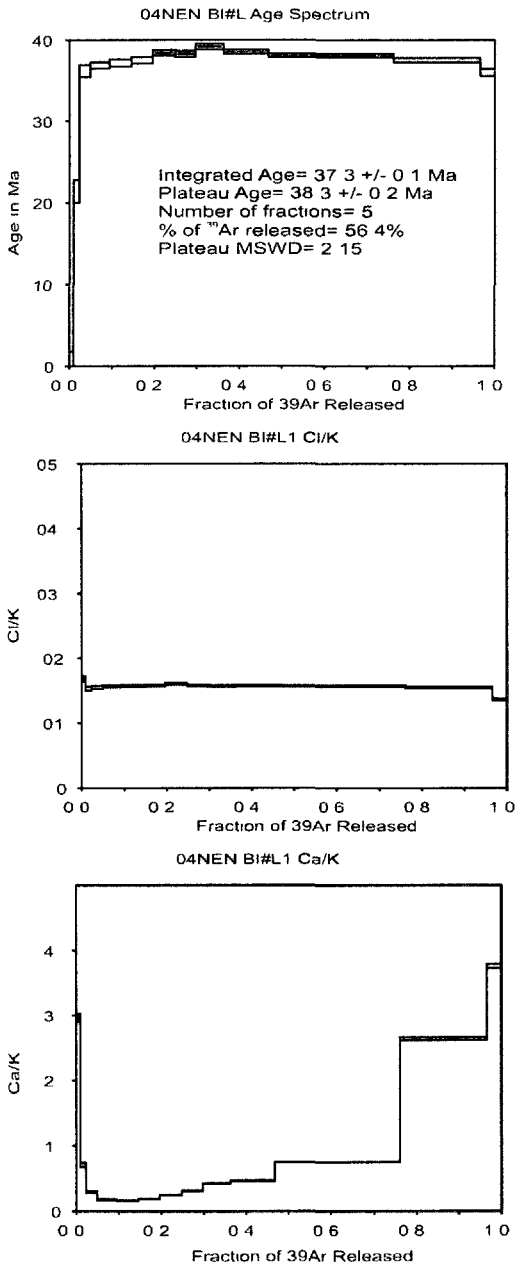

Figure 2R.2: $^{40}Ar/^{39}Ar$ age spectra, K/Ca ratios and Cl/K ratios for sample 04NEN biotite analyses.

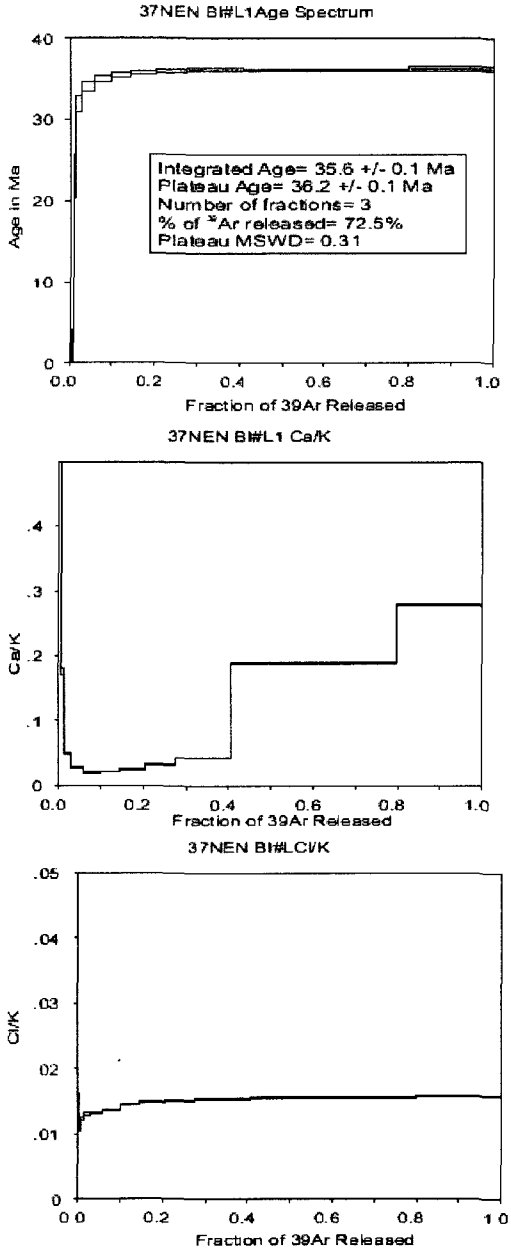

Figure 2R.3: $^{40}Ar/^{39}Ar$ age spectra, K/Ca ratios and Cl/K ratios for sample 37NEN biotite analyses.

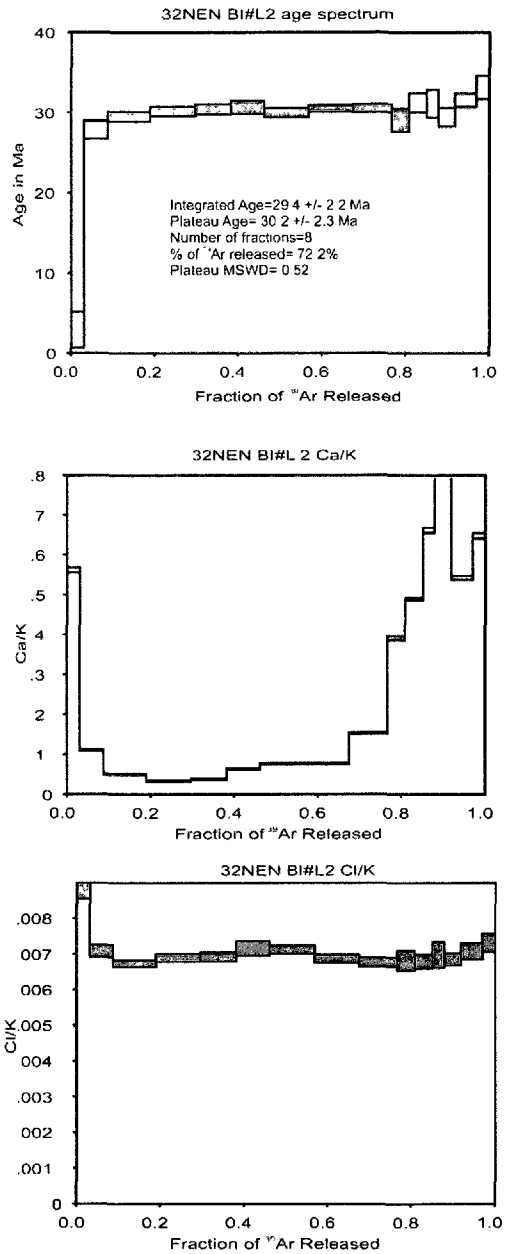

Figure 2R.4: $^{40}Ar/^{39}Ar$ age spectra, K/Ca ratios and Cl/K ratios for sample 32NEN biotite analyses.

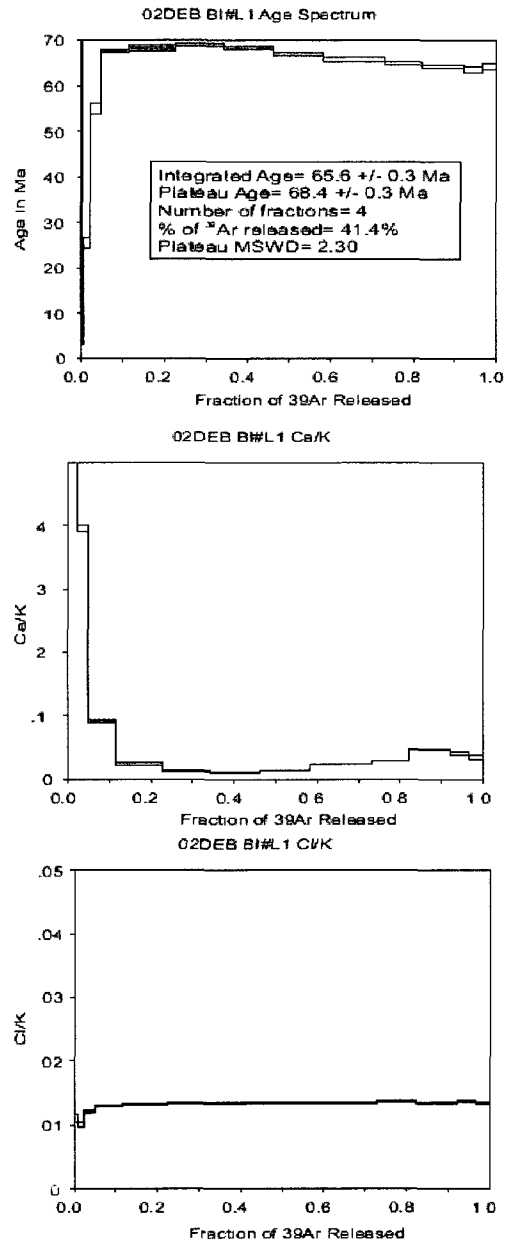

Figure 2R.5: $^{40}Ar/^{39}Ar$ age spectra, K/Ca ratios and Cl/K ratios for sample 02DEB biotite analyses.

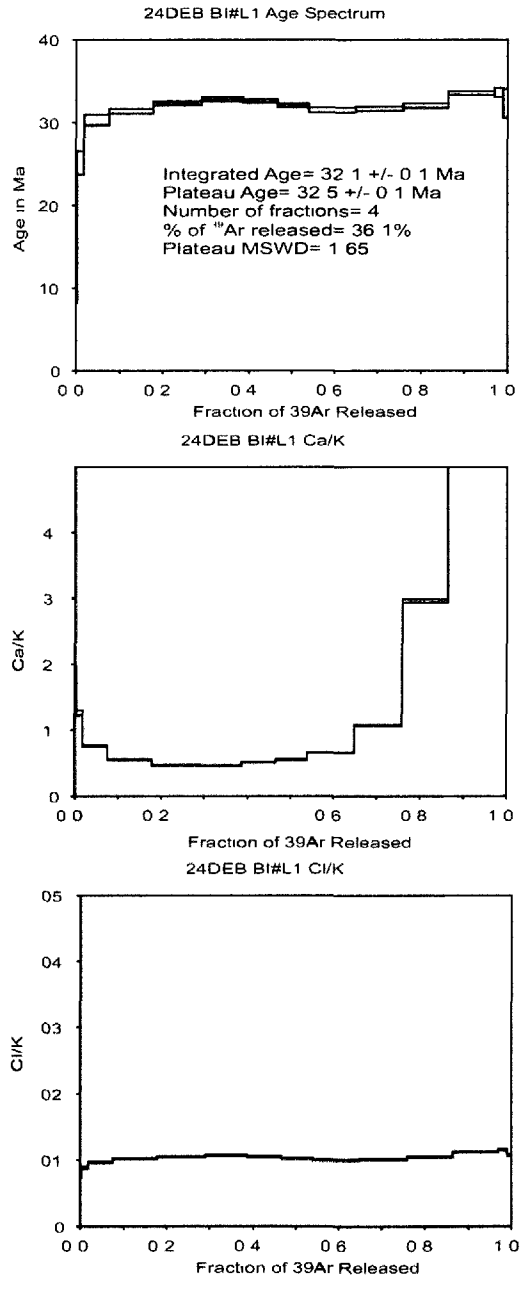

Figure 2R.6: $^{40}Ar/^{39}Ar$ age spectra, K/Ca ratios and Cl/K ratios for sample 24DEB biotite analyses.

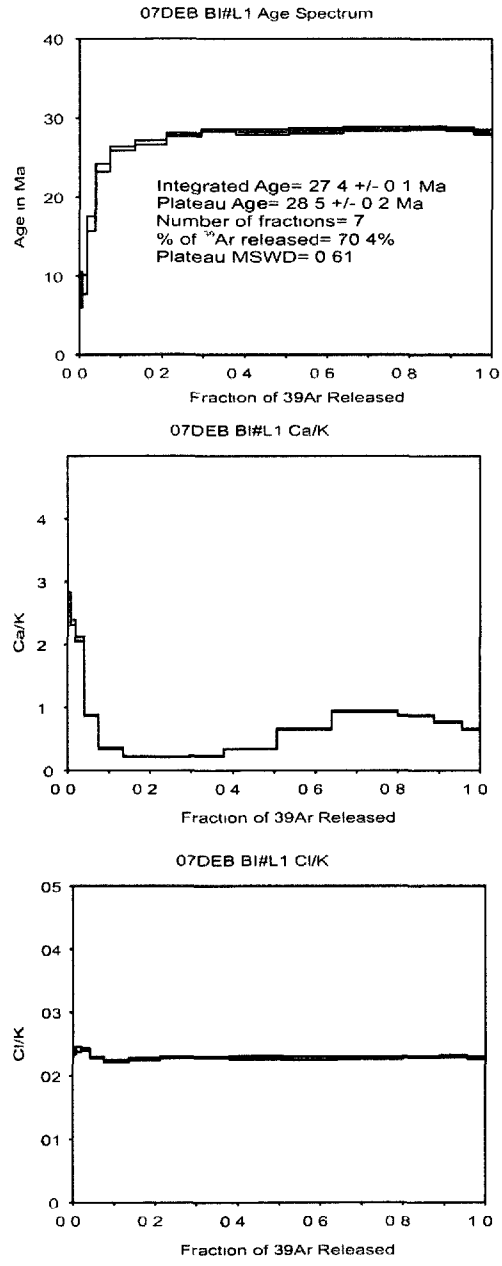

Figure 2R.7: $^{40}Ar/^{39}Ar$ age spectra, K/Ca ratios and Cl/K ratios for sample 07DEB biotite analyses.

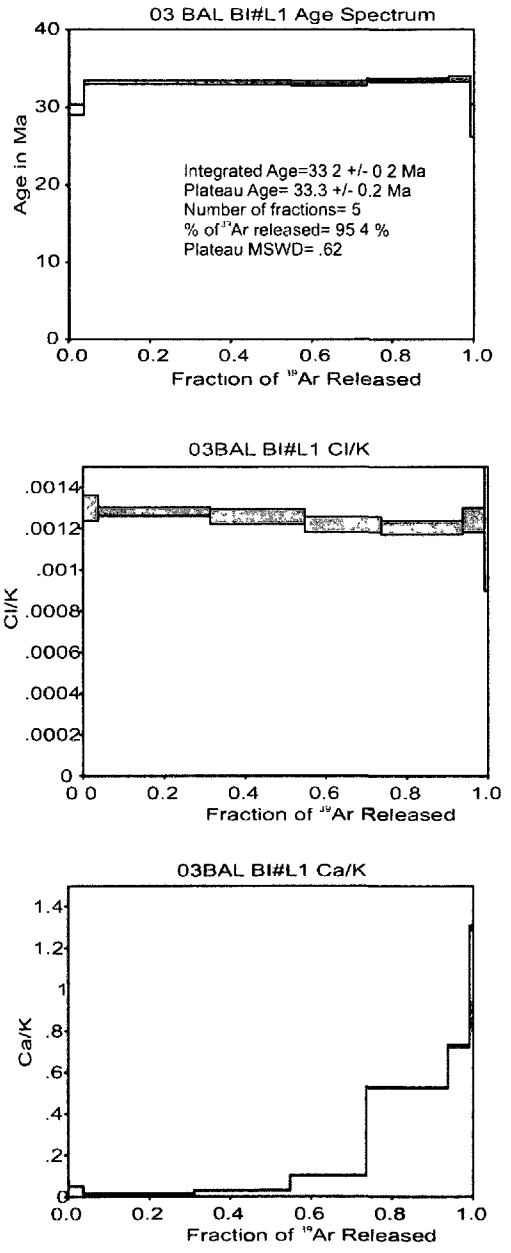

Figure 2R.8: $^{40}Ar/^{39}Ar$ age spectra, K/Ca ratios and Cl/K ratios for sample 03BAL biotite analyses.

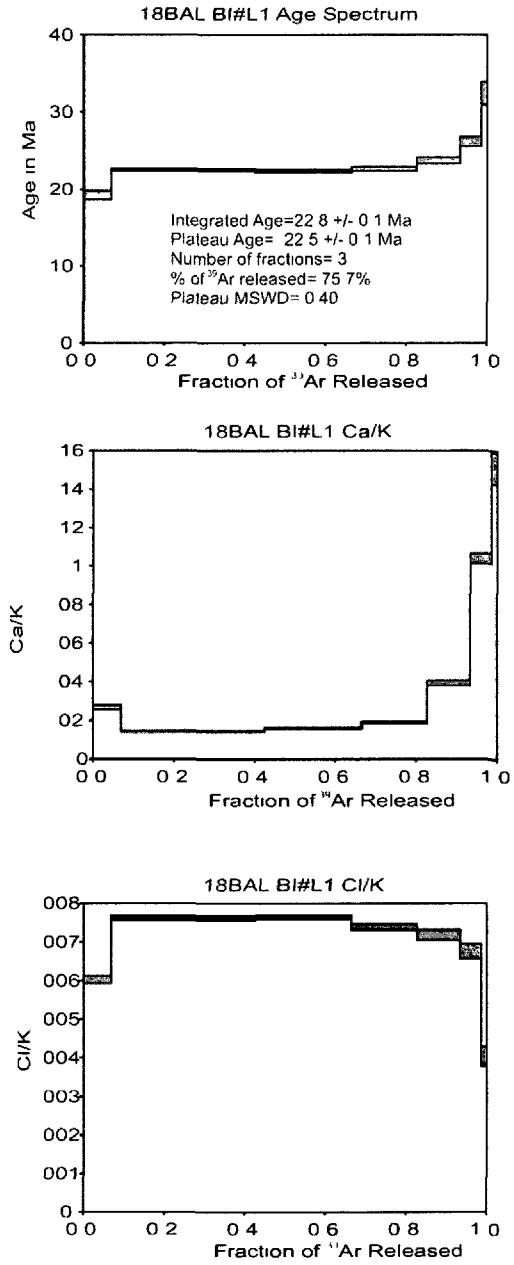

Figure 2R.9: $^{40}Ar/^{39}Ar$ age spectra, K/Ca ratios and Cl/K ratios for sample 18BAL biotite analyses.

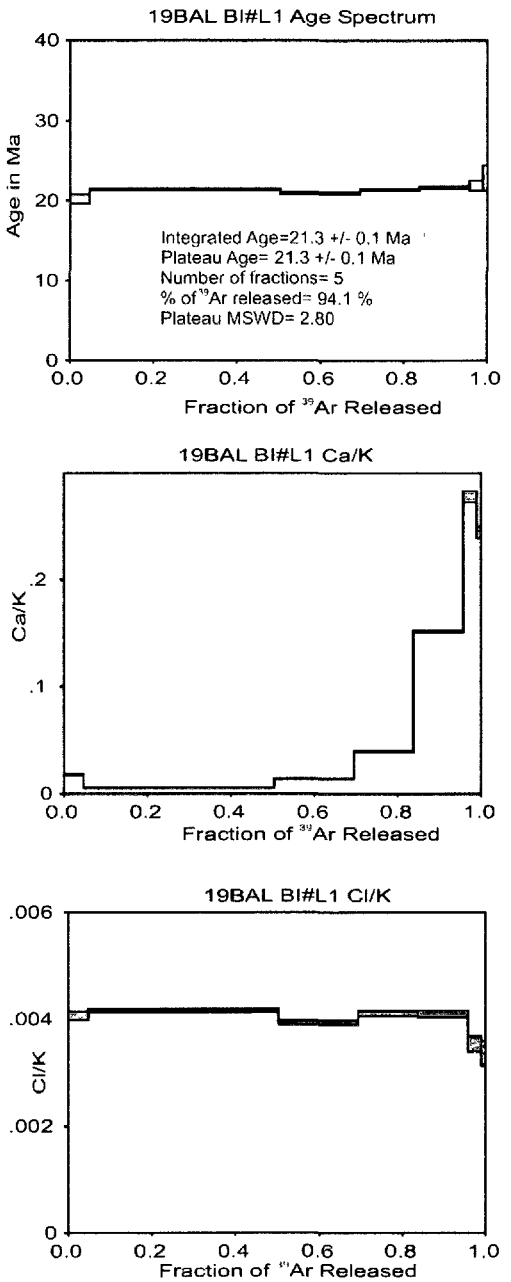

Figure 2R.10: $^{40}Ar/^{39}Ar$ age spectra, K/Ca ratios and Cl/K ratios for sample 19BAL biotite analyses.

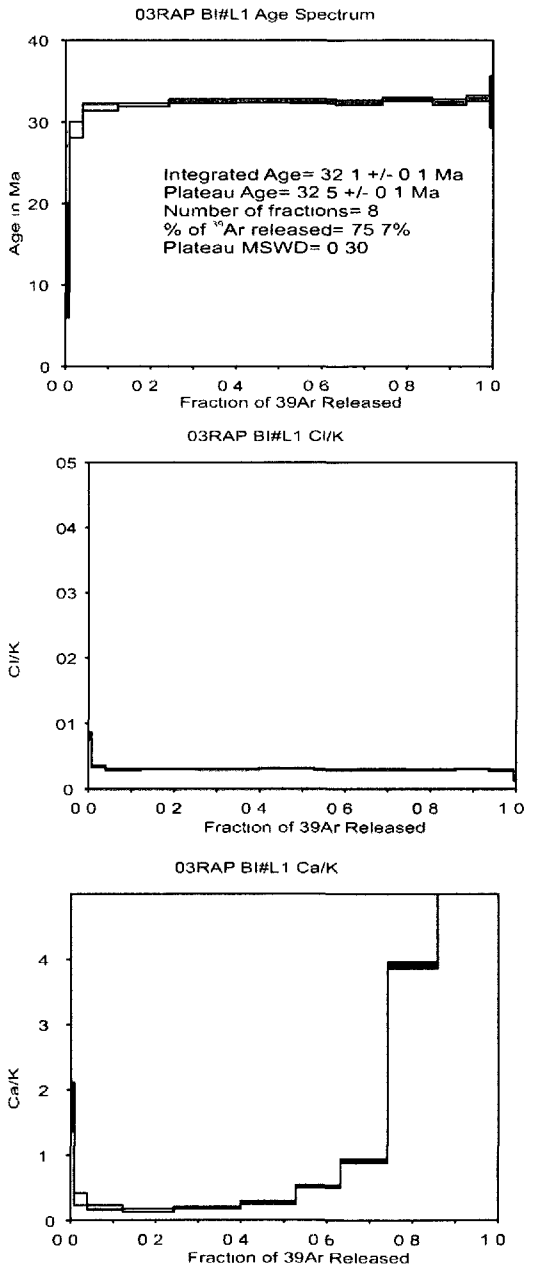

Figure 2R.11: $^{40}Ar/^{39}Ar$ age spectra, K/Ca ratios and Cl/K ratios for sample 30RAP biotite analyses.

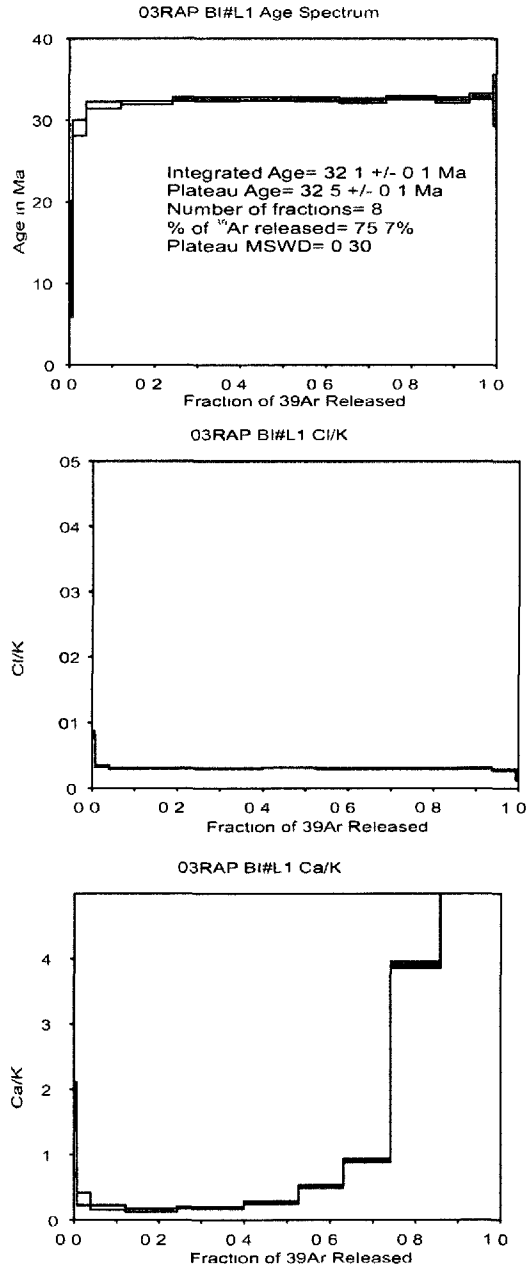

Figure 2R.12: $^{40}Ar/^{39}Ar$ age spectra, K/Ca ratios and Cl/K ratios for sample 03RAP biotite analyses.

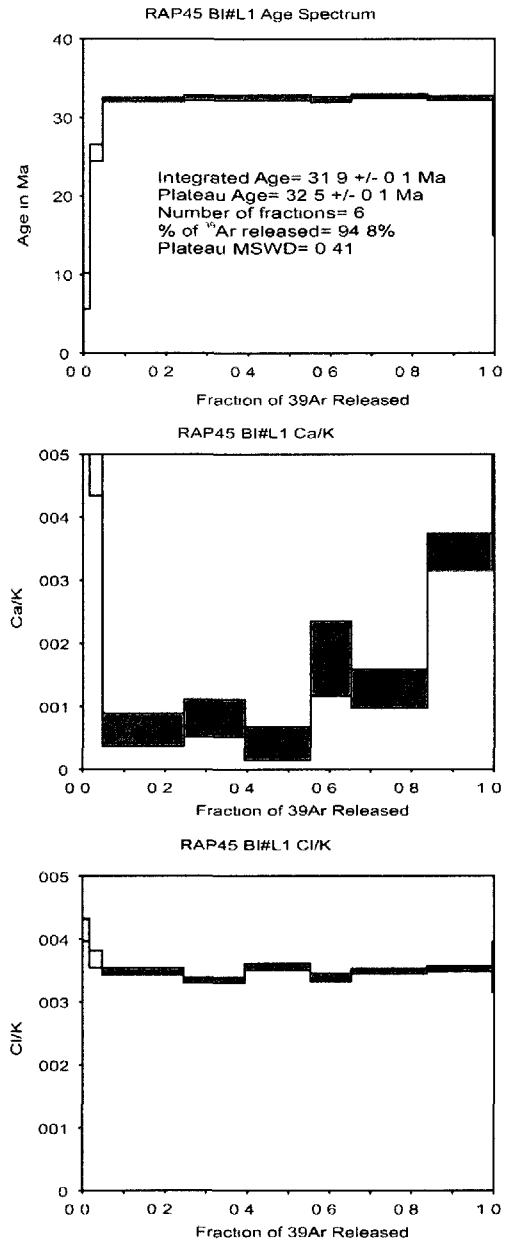

Figure 2R.13: $^{40}Ar/^{39}Ar$ age spectra, K/Ca ratios and Cl/K ratios for sample 45RAP biotite analyses.

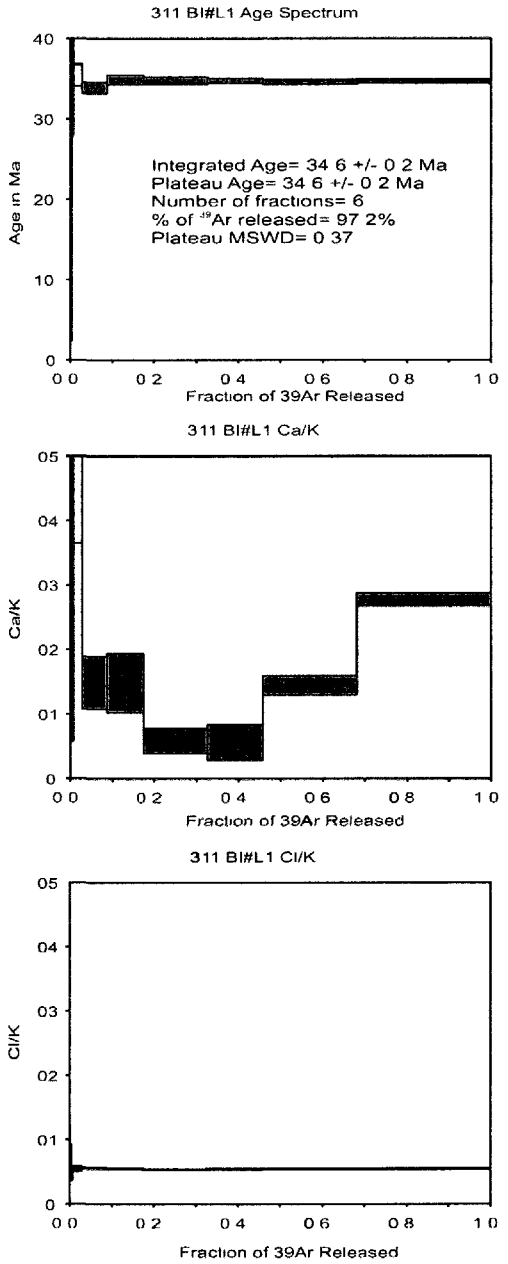

Figure 2R.14: $^{40}Ar/^{39}Ar$ age spectra, K/Ca ratios and Cl/K ratios for sample 311AST biotite analyses.

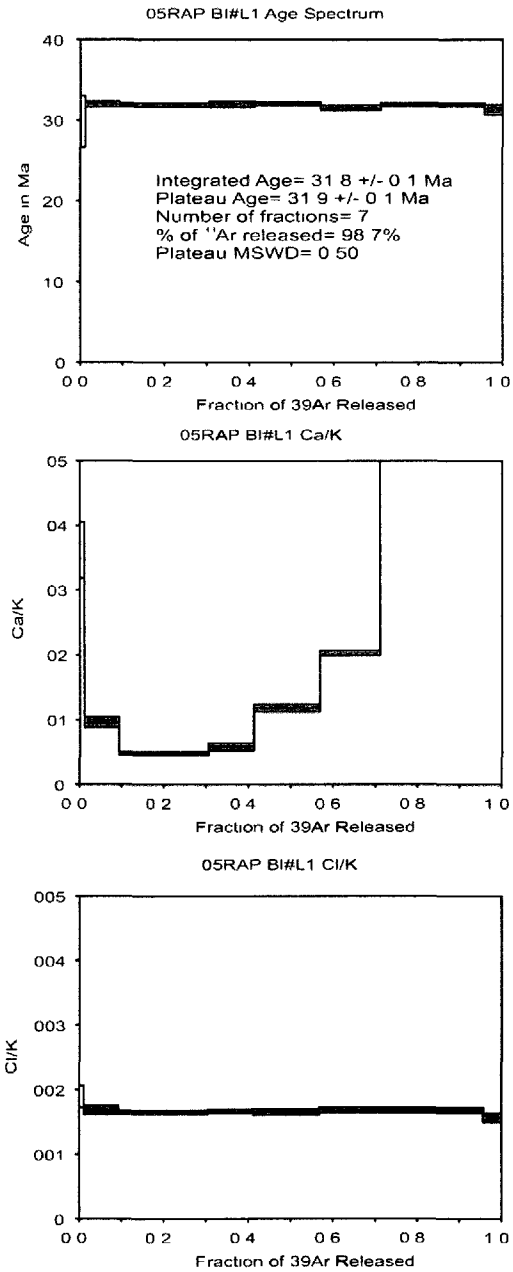

Figure 2R.15: $^{40}Ar/^{39}Ar$ age spectra, K/Ca ratios and Cl/K ratios for sample 05RAP biotite analyses.

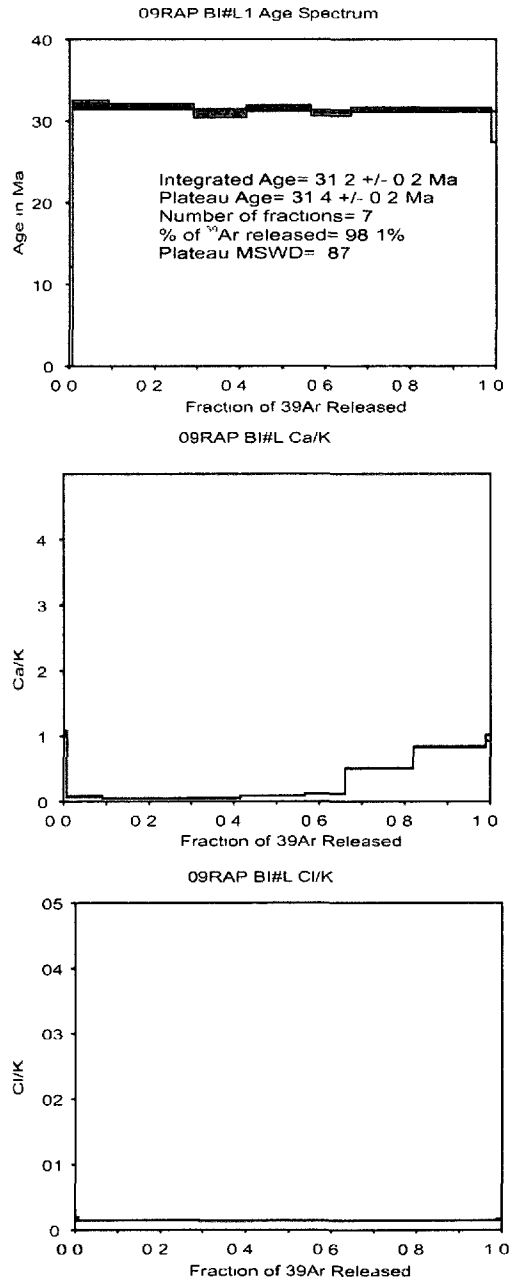

Figure 2R.16: $^{40}Ar/^{39}Ar$ age spectra, K/Ca ratios and Cl/K ratios for sample 09RAP biotite analyses.

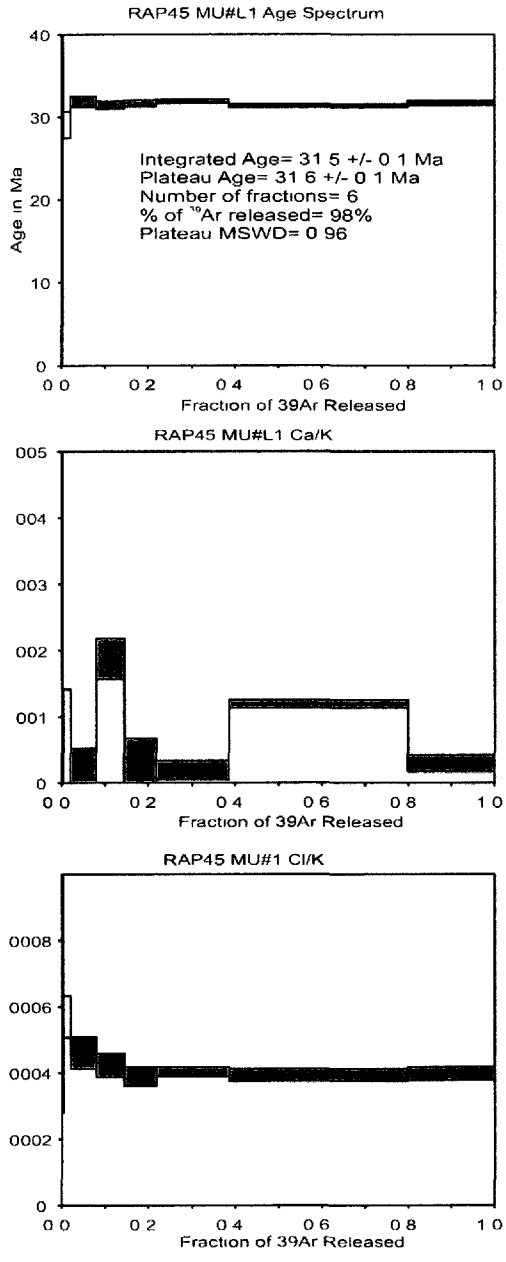

Figure 2R.17: $^{40}Ar/^{39}Ar$ age spectra, K/Ca ratios and Cl/K ratios for sample 45RAP muscovite analyses.

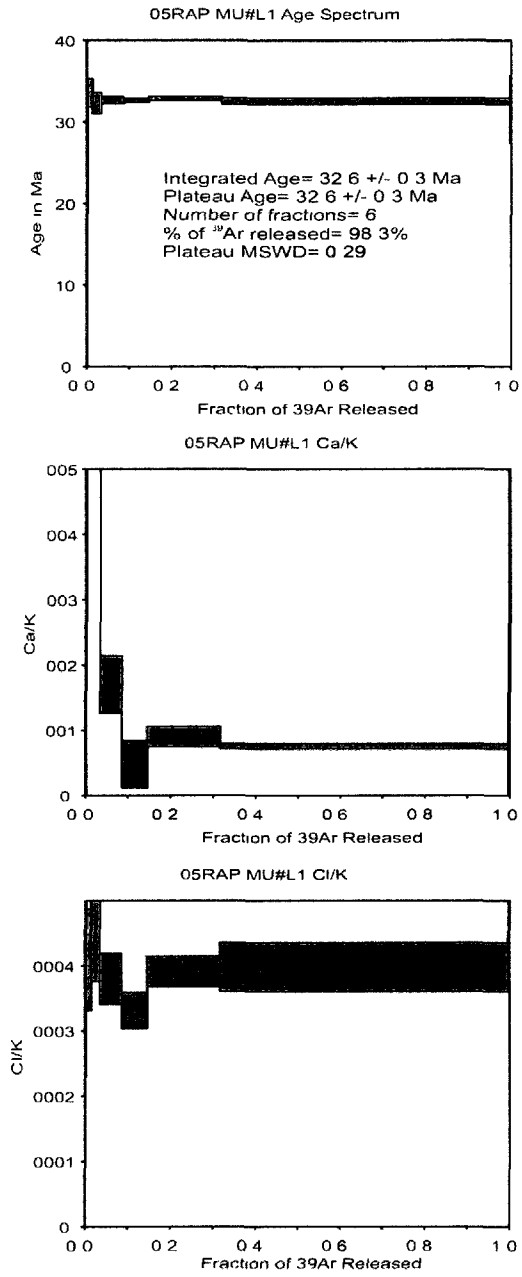

Figure 2R.18: $^{40}Ar/^{39}Ar$ age spectra, K/Ca ratios and Cl/K ratios for sample 05RAP muscovite analyses.

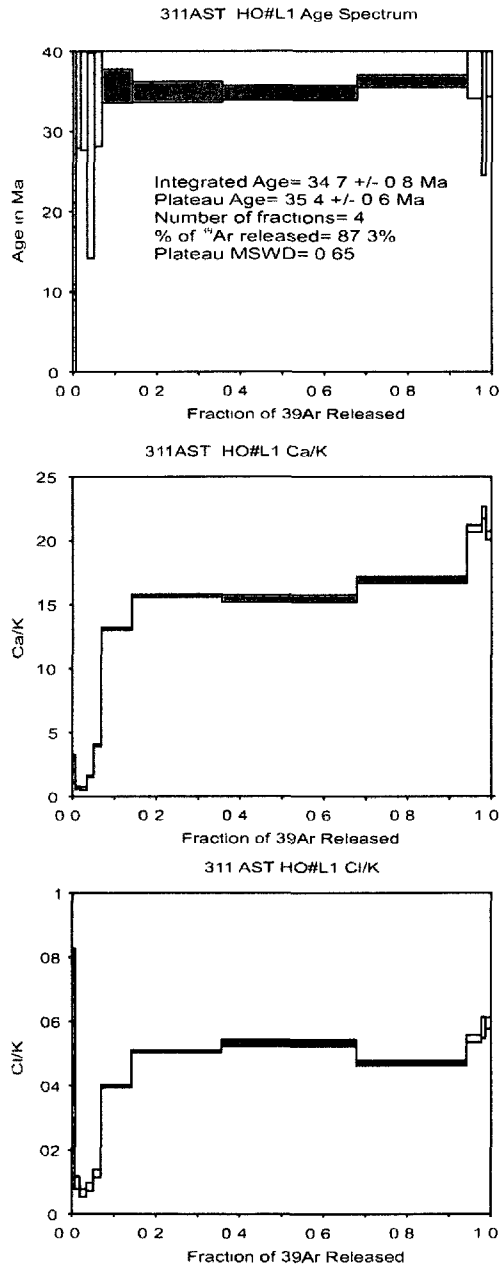

Figure 2R.19: $^{40}Ar/^{39}Ar$ age spectra, K/Ca ratios and Cl/K ratios for sample 311AST hornblende analyses.

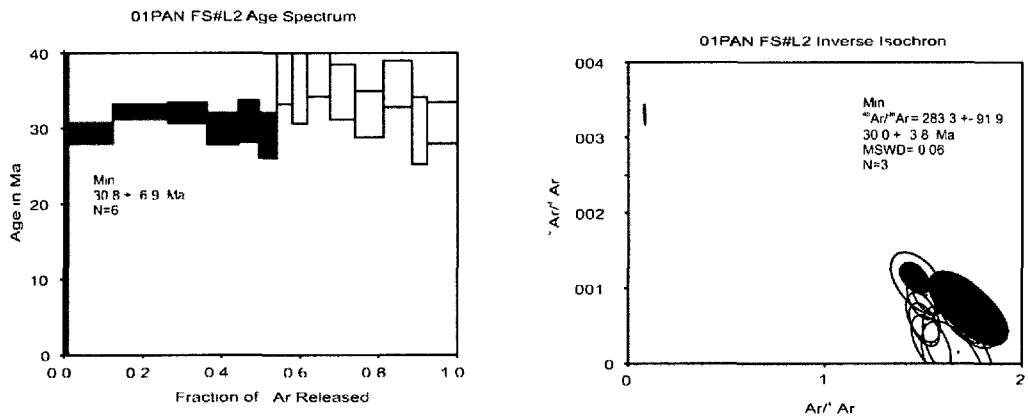

Figure 2R.20: $^{40}Ar/^{39}Ar$ age spectra and inverse isochron plots for 01PAN K-spar analyses.

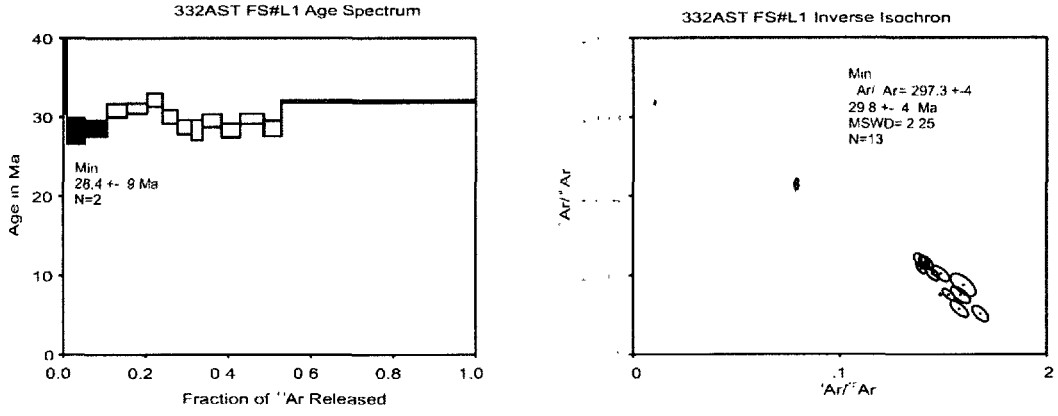

Figure 2R.21: $^{40}Ar/^{39}Ar$ age spectra and inverse isochron plots for 332AST K-spar analyses.

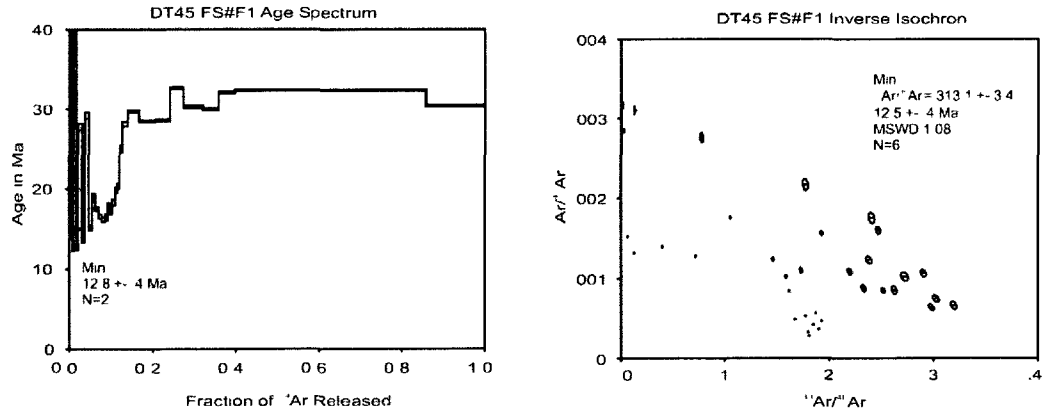

Figure 2R.22: $^{40}Ar/^{39}Ar$ age spectra and inverse isochron plots for DT45 K-spar analyses.

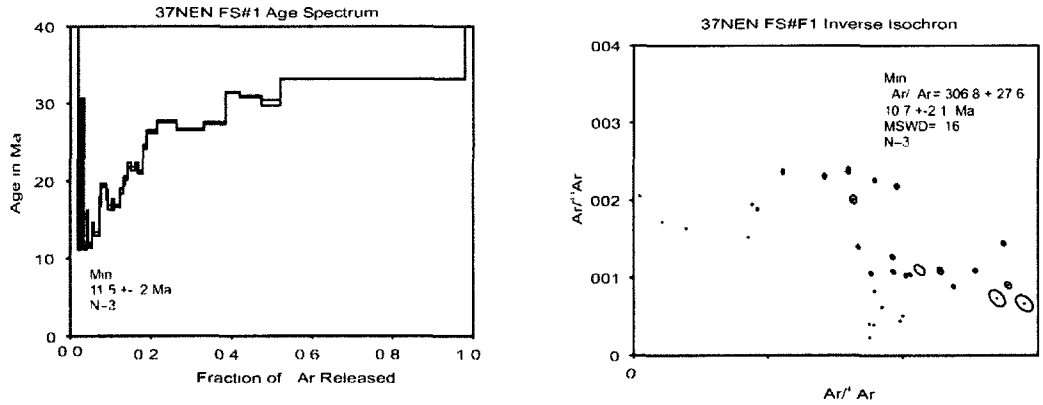

Figure 2R.23: $^{40}Ar/^{39}Ar$ age spectra and inverse isochron plots for 37NEN K-spar analyses.

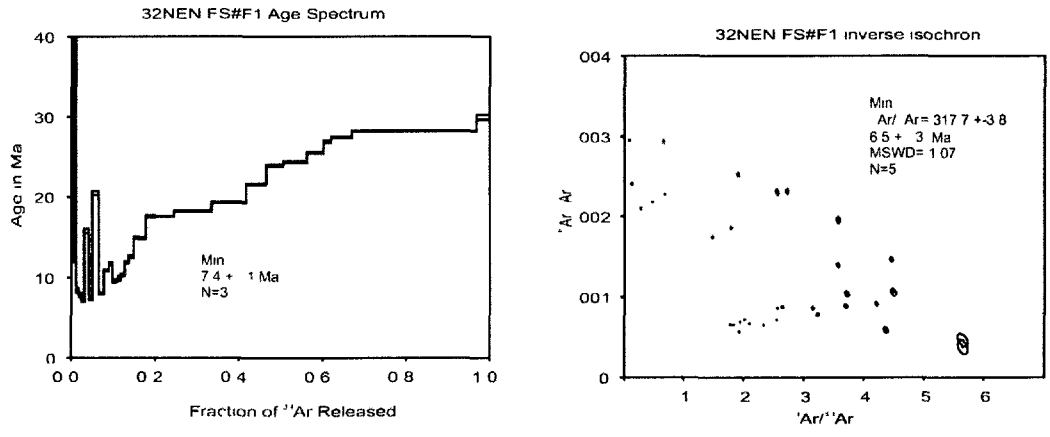

Figure 2R.24: $^{40}Ar/^{39}Ar$ age spectra and inverse isochron plots for 32NEN K-spar analyses.

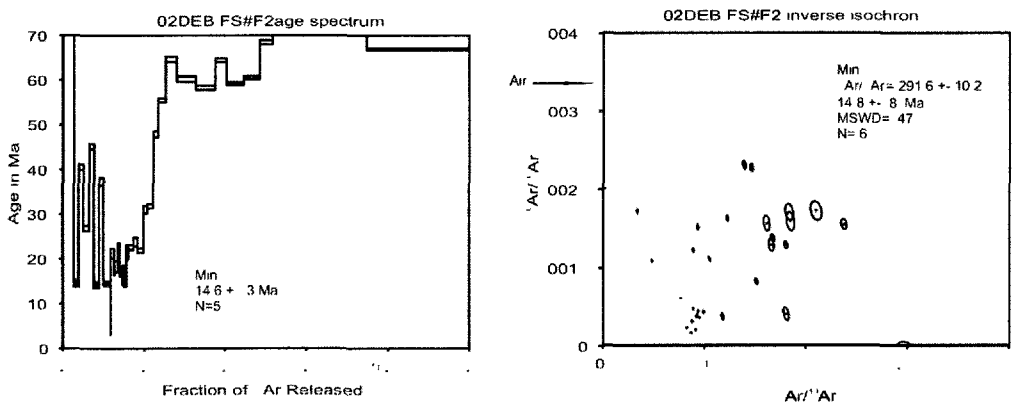

Figure 2R:25: $^{40}Ar/^{39}Ar$ age spectra and inverse isochron plots for 02DEB K-spar analyses.

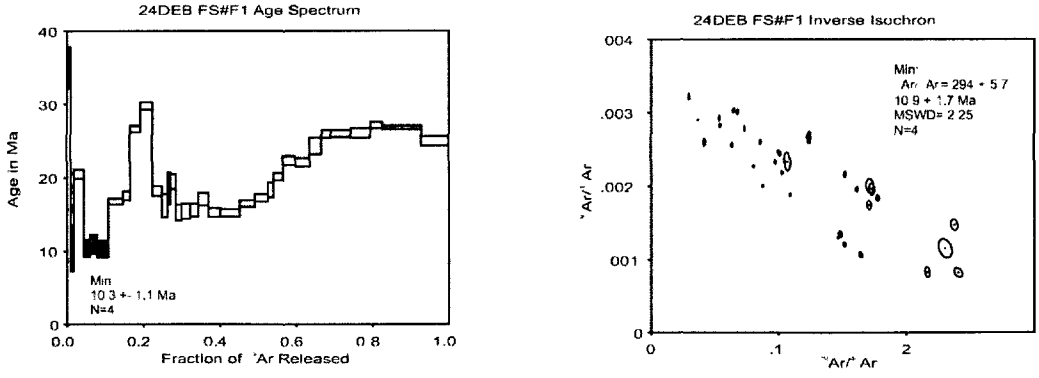

Figure 2R.26: $^{40}Ar/^{39}Ar$ age spectra and inverse isochron plots for 24DEB K-spar analyses.

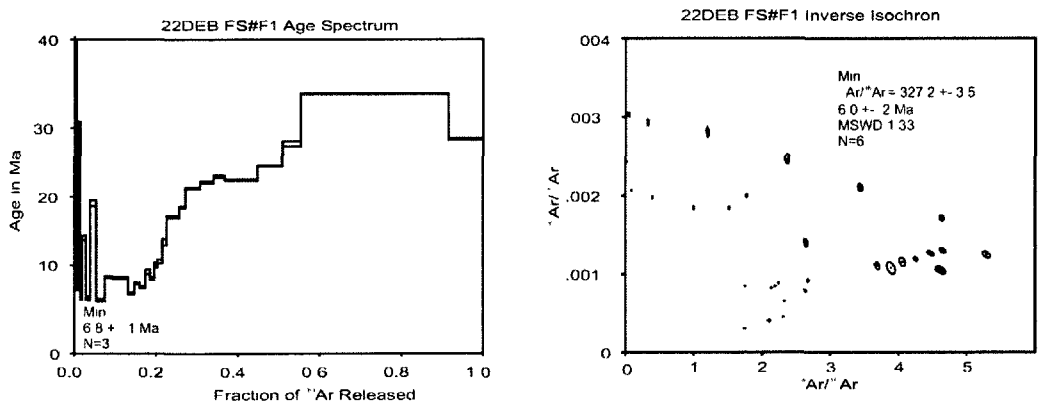

Figure 2R.27: $^{40}Ar/^{39}Ar$ age spectra and inverse isochron plots for 22DEB K-spar analyses.

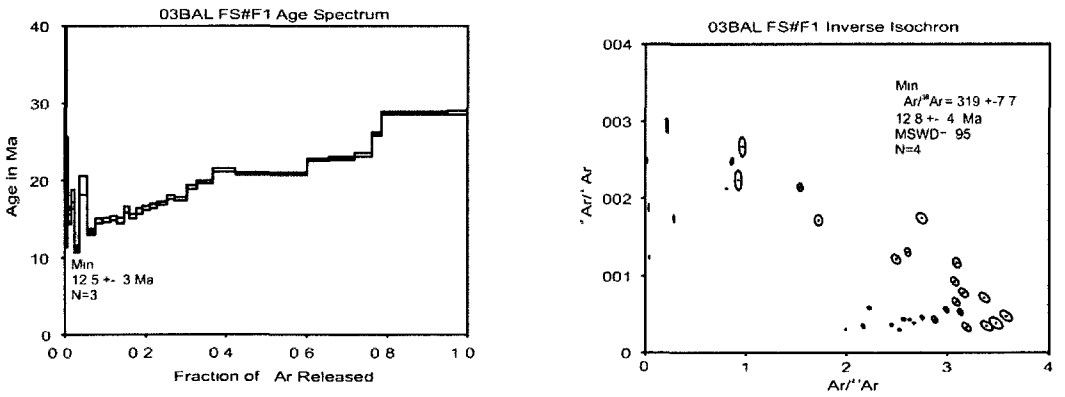

Figure 2R.28: $^{40}Ar/^{39}Ar$ age spectra and inverse isochron plots for 03BAL K-spar analyses.

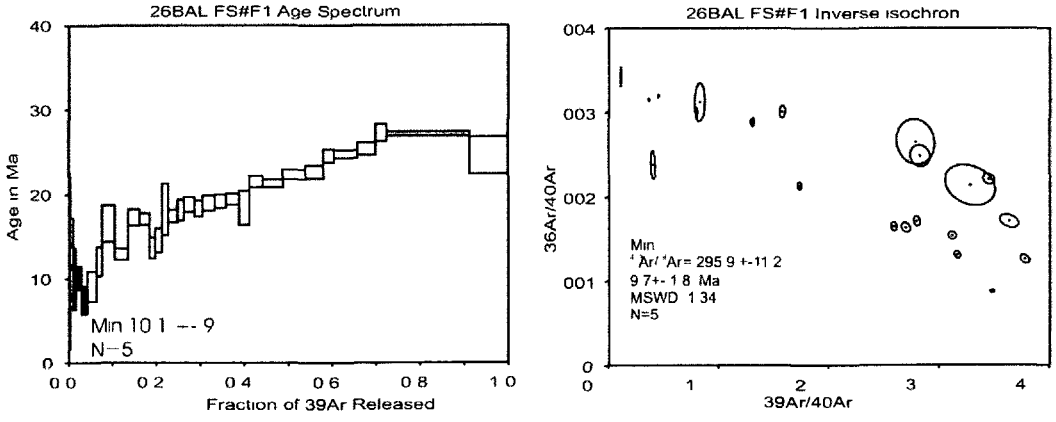

Figure 2R.29: $^{40}Ar/^{39}Ar$ age spectra and inverse isochron plots for 26BAL K-spar analyses.

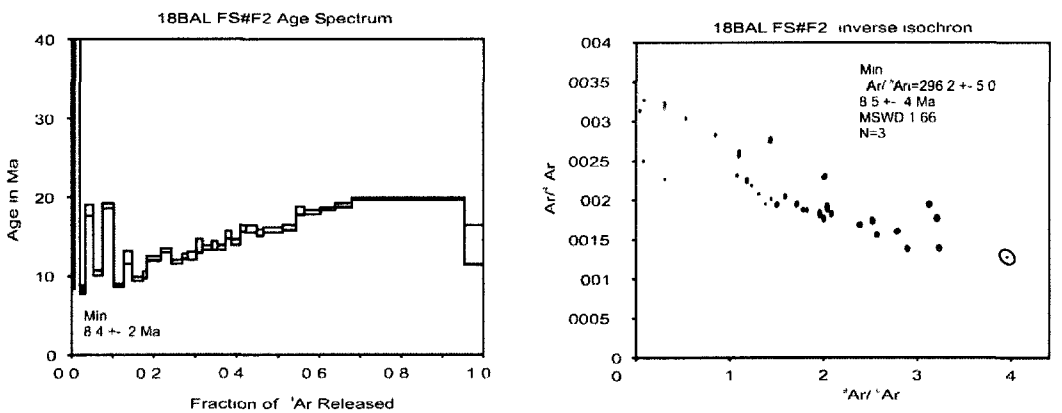

Figure 2R.30: $^{40}Ar/^{39}Ar$ age spectra and inverse isochron plots for 18BAL K-spar analyses.

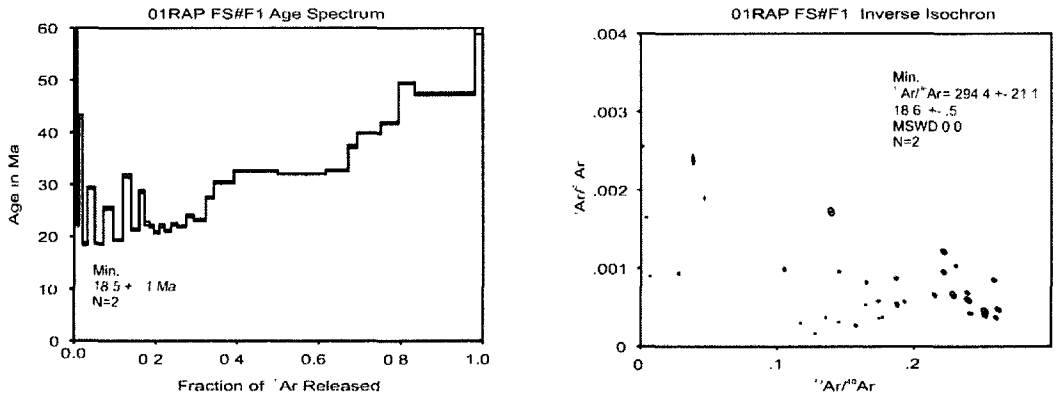

Figure 2R.31: $^{40}Ar/^{39}Ar$ age spectra and inverse isochron plots for 03RAP K-spar analyses.

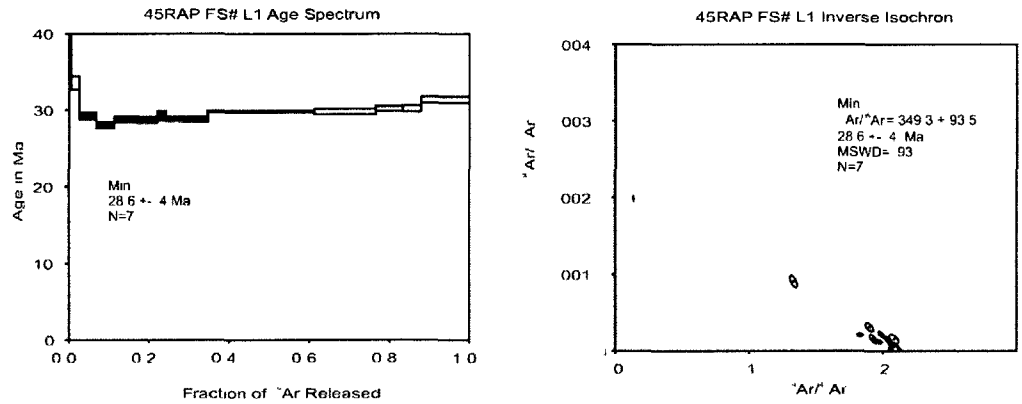

Figure 2R.32: $^{40}Ar/^{39}Ar$ age spectra and inverse isochron plots for 45RAP K-spar analyses.

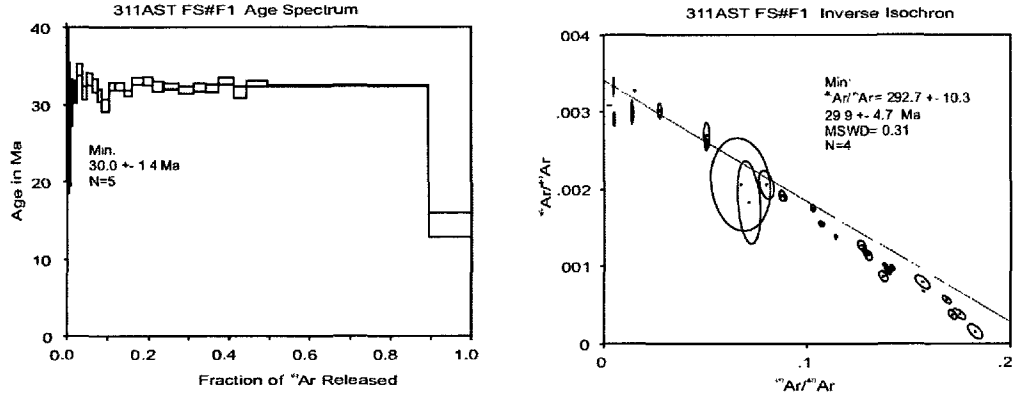

Figure 2R.33: $^{40}Ar/^{39}Ar$ age spectra and inverse isochron plots for 311AST K-spar analyses.

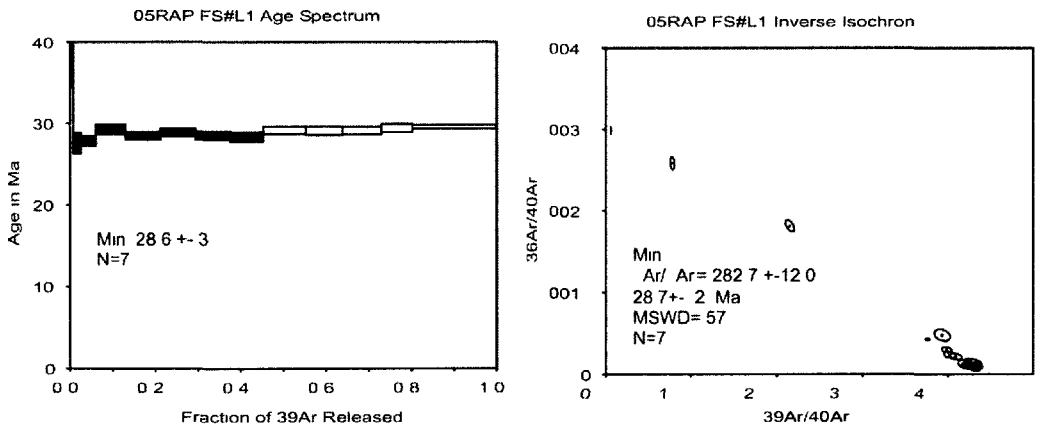

Figure 2R.34: $^{40}Ar/^{39}Ar$ age spectra and inverse isochron plots for 05RAP K-spar analyses.

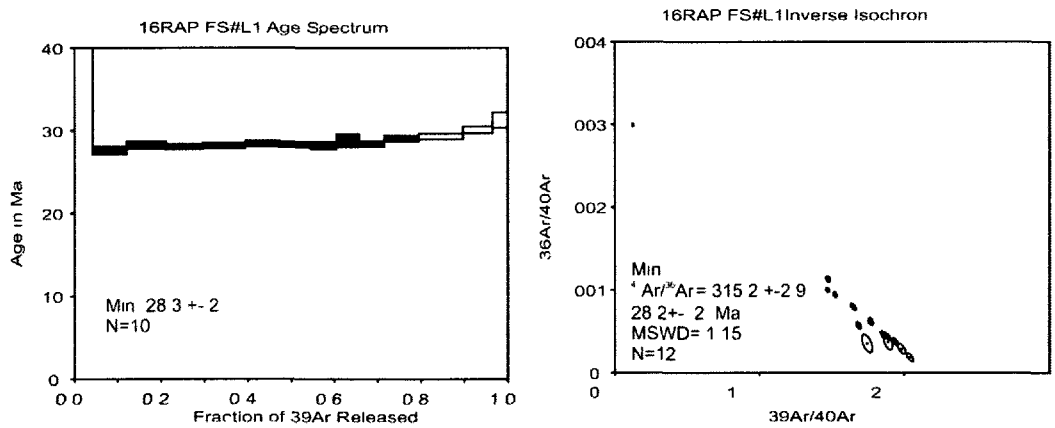

Figure 2R.35: $^{40}Ar/^{39}Ar$ age spectra and inverse isochron plots for 09RAP K-spar analyses.

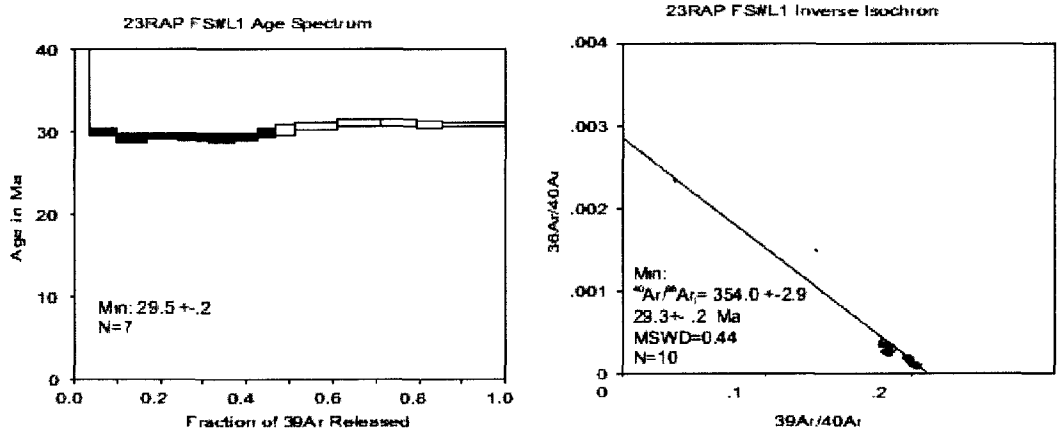

Figure 2R.36: $^{40}Ar/^{39}Ar$ age spectra and inverse isochron plots for 23RAP K-spar analyses.

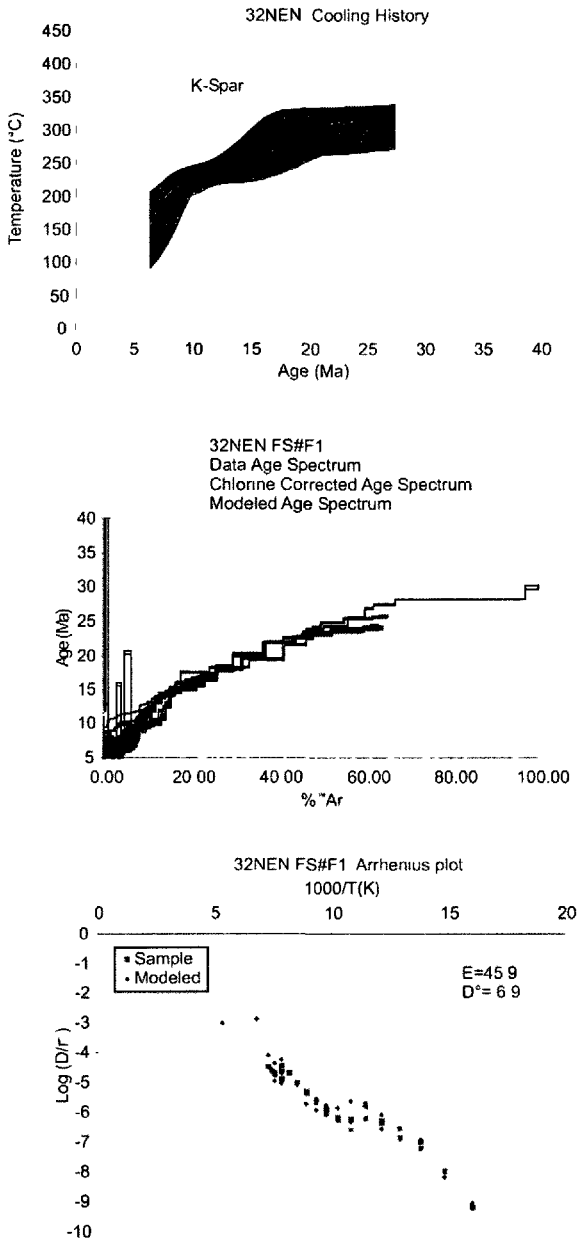

Figure 2R.37: Arrhenius plot, measured, Cl corrected and modeled $^{40}Ar/^{39}Ar$ age spectra, monotonic multiple diffusion domain (MDD) thermal models generated for K-feldspar from sample 32NEN.

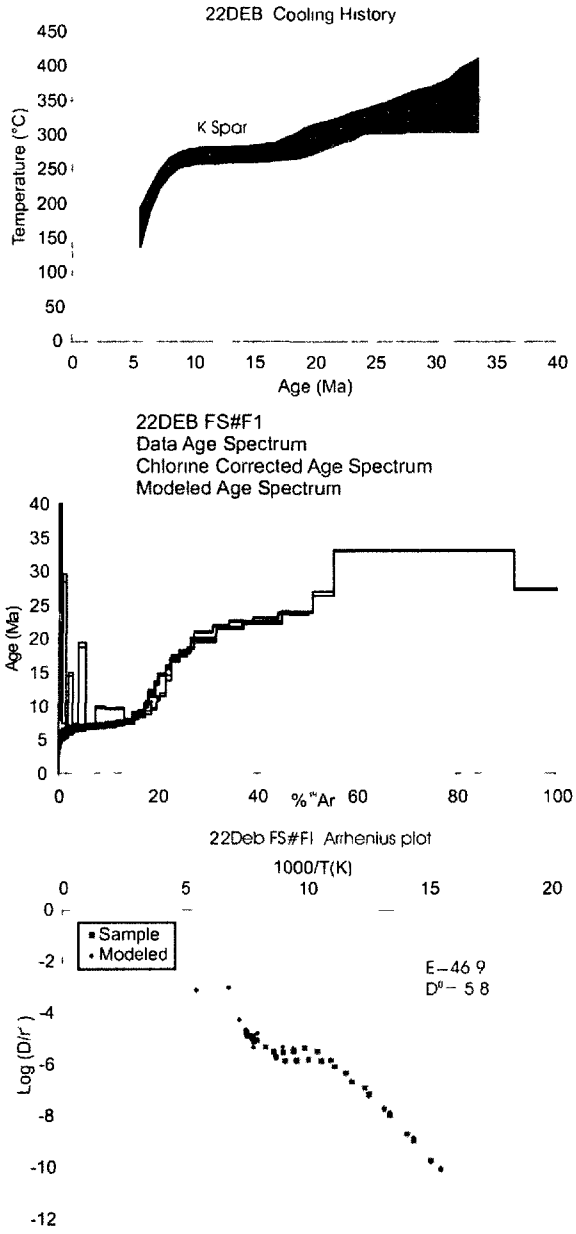

Figure 2R.38: Arrhenius plot, measured, Cl corrected and modeled $^{40}Ar/^{39}Ar$ age spectra, monotonic multiple diffusion domain (MDD) thermal models generated for K-feldspar from sample 22DEB.

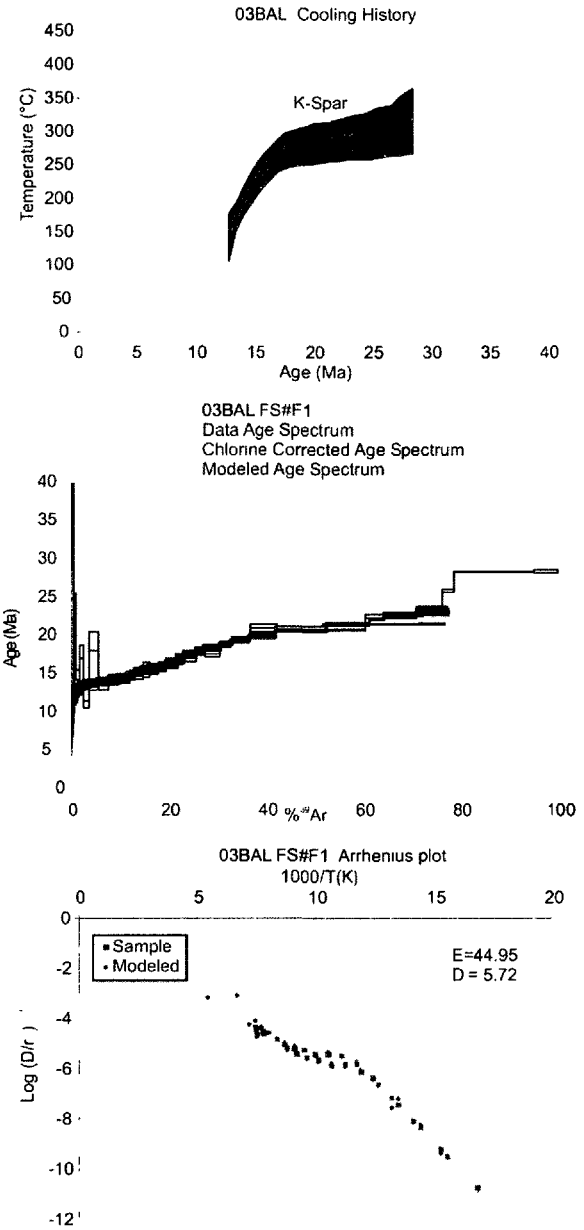

Figure 2R.39: Arrhenius plot, measured, Cl corrected and modeled $^{40}Ar/^{39}Ar$ age spectra, monotonic multiple diffusion domain (MDD) thermal models generated for K-feldspar from sample 03BAL.

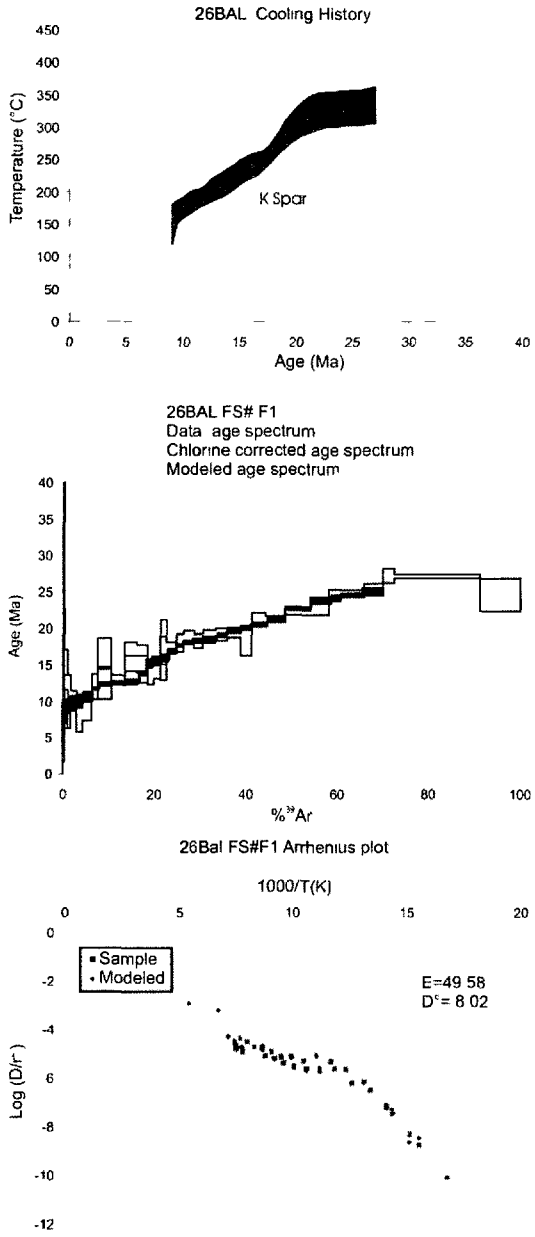

Figure 2R.40: Arrhenius plot, measured, Cl corrected and modeled $^{40}Ar/^{39}Ar$ age spectra, monotonic multiple diffusion domain (MDD) thermal models generated for K-feldspar from sample 26BAL.

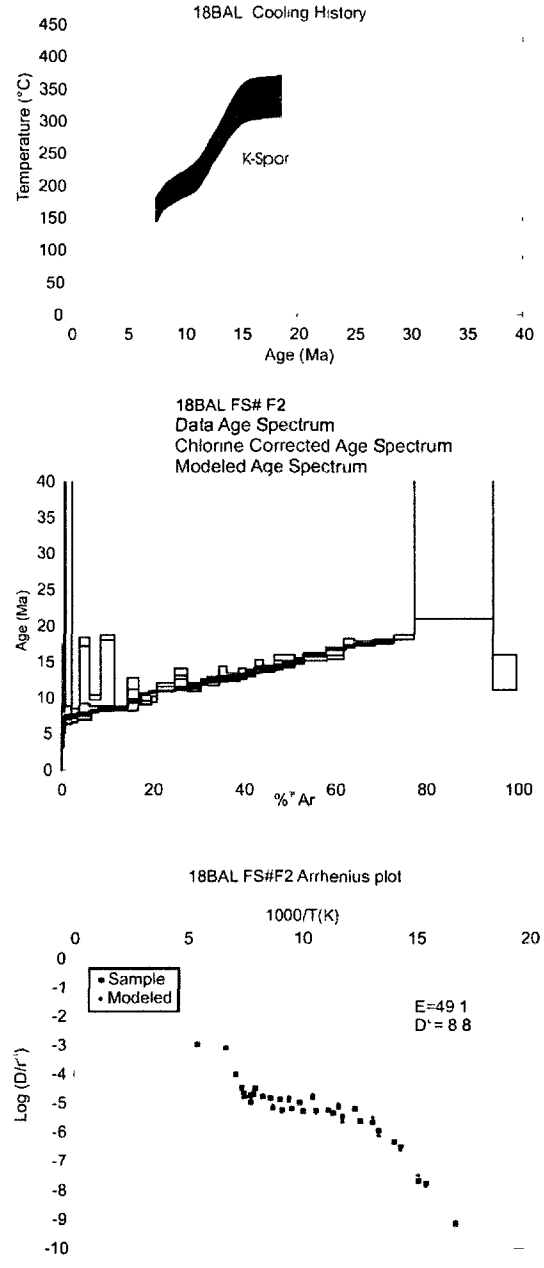

Figure 2R.41: Arrhenius plot, measured, Cl corrected and modeled $^{40}Ar/^{39}Ar$ age spectra, monotonic multiple diffusion domain (MDD) thermal models generated for K-feldspar from sample 18BAL.

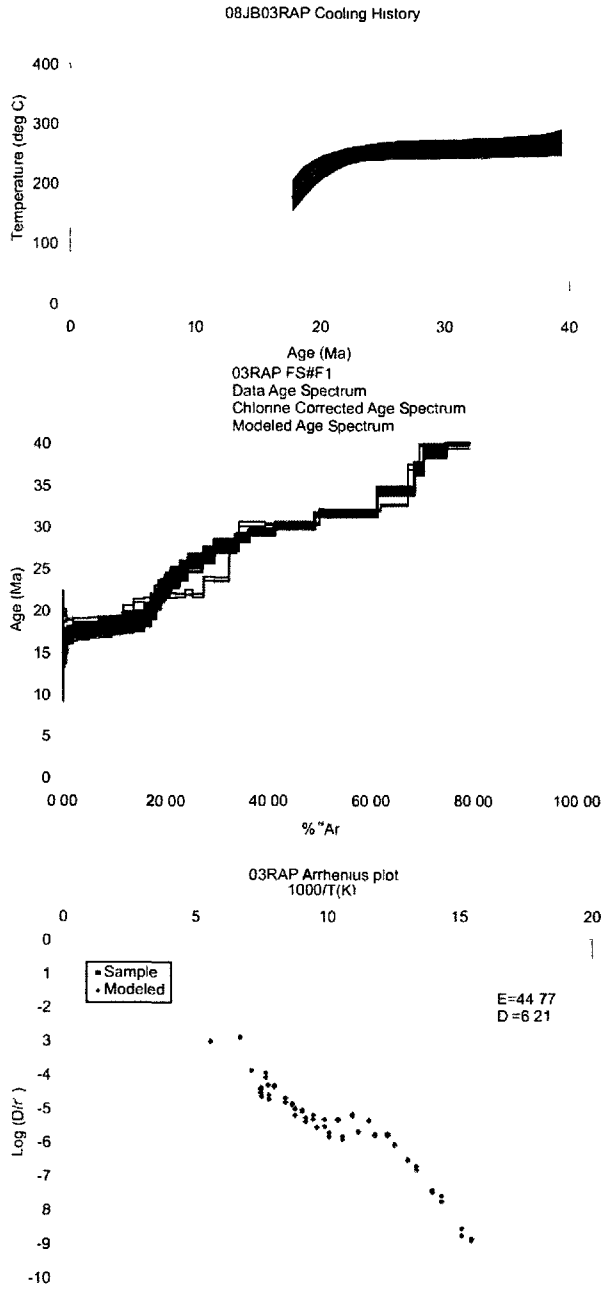

Figure 2R.42: Arrhenius plot, measured, Cl corrected and modeled $^{40}Ar/^{39}Ar$ age spectra, monotonic multiple diffusion domain (MDD) thermal models generated for K-feldspar from sample 03RAP.

2.13 Repository Tables

Table 2R.1: $^{40}Ar/^{39}Ar$ data from Potassium Feldspar, (F): furnace run, (L): laser run

Sample # and rock type	Lat (°N) Lon (°W)	Elev (m)	$^{40}Ar/^{39}Ar$ ave min age (Ma) ± 1σ	# steps in ave	Isochron min age (Ma) ± 1σ	$^{40}Ar/^{36}Ar_i$	MSWD	# isoc steps
North of Denali Fault								
01PAN (L) granite	63 4670 148 7350	1011	30 8 ± 6 9	6	30 ± 3 8	283 3 ± 91 9	0 06	3
332AST (L) granite	63 4810 148 4880	1324	28 4 ± 0 9	2	29 8 ± 0 4	297 3 ± 0 4	2 25	13
DT45 (F) granodiorite	63 5800 147 6460	1920	12 8 ± 0 4	2	12 5 ± 0 4	313 1 ± 3 4	1 08	6
37NEN (F) granodiorite	63 5440 147 6970	2347	11 5 ± 0 2	3	10 7 ± 2 1	306 8 ± 27 6	0 16	3
32NEN (F) granodiorite	63 5130 147 7270	1271	7 4 ± 0 1	3	6 5 ± 0 3	317 7 ± 3 8	1 07	5
02DEB (F) tonalite	63 6126 147 2770	2268	14 6 ± 0 3	5	14 8 ± 0 8	291 6 ± 10 2	0 47	6
24DEB (F) tonalite	63 5957 147 3449	2042	10 3 ± 1 1	4	10 9 ± 1 7	294 0 ± 5 7	2 25	4
22DEB (F) granitoid	63 5391 147 3237	1341	6 8 ± 0 1	3	6 0 ± 0 2	327 2 ± 3 5	1 33	6
03BAL (F) granite	63 6224 146 9251	2164	12 5 ± 0 3	3	12 8 ± 0 4	319 0 ± 7 7	0 95	4
26BAL (F) granite	63 6139 146 8696	2846	10 1 ± 0 9	5	9 7 ± 1 8	295 9 ± 11 2	1 34	5
18BAL (F) granite	63 5808 146 9405	1750	8 4 ± 0 2	2	8 5 ± 0 4	296 2 ± 5 0	1 66	3
03RAP (F) granite	63 4827 146 0428	2041	18 5 ± 0 1	2	18 6 ± 0 5	294 4 ± 21 1	0	2
South of Denali Fault								
45RAP (L) orthogneiss	63 4723 146 4310	1635	28 6 ± 0 4	7	28 6 ± 0 4	349 3 ± 93 5	0 93	7
311AST (F) orthogneiss	63 4881 146 8292	1905	30 0 ± 1 4	5	29 9 ± 4 7	292 7 ± 10 3	0 31	4
05RAP (L) orthogneiss	63 4337 146 5411	2111	28 6 ± 0 3	7	28 7± 0 2	282 7 ± 12 0	0 57	7
09RAP (L) orthogneiss	63 4345 146 5277	1918	29 2 ± 0 3	9	28 8 ± 0 2	319 0± 2 6	0 87	11
16RAP (L) orthogneiss	63 4635 146 5028	1748	28 3 ± 0 2	10	28 2 ± 0 2	315 2 ± 2 9	1 15	12
23RAP (L) orthogneiss	63 4492 146 4516	2458	29 5 ± 0 2	7	29 3 ± 0 2	354 0 ± 2 9	0 44	10

Table 2R.2: $^{40}Ar/^{39}Ar$ and K-Ar data from biotite, muscovite and hornblende

Sample # and rock type	Lat (°N) Lon (°W)	Elev (m)	$^{40}Ar/^{39}Ar$ integrated or K-Ar Age (Ma) ± 1σ	$^{40}Ar/^{39}Ar$ plateau Age (Ma) ± 1σ	Plateau information (or K-Ar reference)
Biotite North of Denali Fault					
01PAN granite	63 4670 148 7350	1011	36 6 ± 0 2	36 9 ± 0 2	9 steps MSWD = 1 29
AST332 granite	63 4810 148 4880	1324	37 9 ± 1 1 (K-Ar)	-	Csejtey, 1992
04NEN granite	63 5160 147 8477	1859	37 3 ± 0 1	38 3 ± 0 2	5 steps MSWD = 2 11
DT45 granodiorite	63 5800 147 6460	1920	37 9 ±1 1 (K-Ar)	-	Csejtey et al , 1992
37NEN granodiorite	63 5440 147 6970	2347	35 6 ± 0 1	36 2 ± 0 1	3 steps MSWD = 0 31
32NEN granodiorite	63 5130 147 7270	1271	29 4 ± 2 2	30 2 ± 2 3	8 steps MSWD = 0 52
02DEB tonalite	63 6126 147 2770	2268	65 6 ± 0 3	68 4 ± 0 3	4 steps MSWD = 2 30
24DEB tonalite	63 5957 147 3449	2042	32 0 ± 0 1	32 5 ± 0 1	4 steps MSWD = 1 65
07DEB tonalite	63 5699 147 2897	1524	27 4 ± 0 1	28 5 ± 0 2	7 steps MSWD = 0 61
03BAL granite	63 6224 146 9251	2164	33 2 ± 0 2	33 3 ± 0 2	5 steps MSWD = 0 62
18BAL granite	63 5808 146 9405	1750	22 8 ± 0 1	22 5 ± 0 1	3 steps MSWD = 0 40
19BAL granite	63 5713 146 9481	1615	21 3 ± 0 1	21 3 ± 0 1	5 steps MSWD = 2 80
ANK28 metagranite	63 5380 146 9710	1694	18 2 ± 0 6 (K-Ar)	-	Nokleberg et al , 1992
30RAP granite	63 5160 146 6847	1719	18 5 ± 0 1	18 4 ± 0 1	8 steps MSWD = 1 29
03RAP granite	63 4827 146 0428	2041	32 1 ± 0 1	32 5 ± 0 1	8 steps MSWD = 0 30
Biotite South of Denali Fault					
45RAP orthogneiss	63 4723 146 4310	1635	31 9 ± 0 1	32 5 ± 0 1	6 steps MSWD = 0 41
311AST orthogneiss	63 4881 146 8292	1905	34 6 ± 0 2	34 6 ± 0 2	6 steps MSWD = 0 37
05RAP orthogneiss	63 4337 146 5411	2111	31 8 ± 0 1	31 9 ± 0 1	7 steps MSWD = 0 50
09RAP orthogneiss	63 4345 146 5277	1918	31 2 ± 0 2	31 4 ± 0 2	7 steps MSWD = 0 87
Muscovite South of Denali Fault					
45RAP orthogneiss	63 4723 146 4310	1635	31 5 ± 0 1	31 6 ± 0 1	6 steps MSWD = 0 96
05RAP orthogneiss	63 4337 146 5411	2111	32 6 ± 0 3	32 6 ± 0 3	6 steps MSWD = 0 29
Hornblende North of Denali Fault					
DT45 granodiorite	63 5800 147 6460	1920	39 6 ± 1 1 (K-Ar)	-	Csejtey, 1992
Hornblende South of Denali Fault					
311AST orthogneiss	63 4881 146 8292	1905	34 7 ± 0 8	35 4 ± 0 6	4 steps MSWD = 0 65

Table 2R.3: Apatite Fission Track Analysis

	Lat (°N) Lon (°W)	Elev (m)	n	ρ_s	N_s	ρ_i	N_i	$P(X^2)$ (%)	ρ_D	N_D	**Age (Ma) ± 2σ**	Mean lengths (μm)	n	Dpar (μm)
North of Denali Fault														
01BAL Granite	63 6326 146 8637	2499	11	0 051	19	1 690	631	6 7	1 262	2038	**6.7 ± 1.6**	12 4	1	1 99
05PH001A Tonalite	63 5952 146 9522	2003	37	0 021	45	1 797	2141	74 5	1 334	3334	**5.1 ± 0.8**	11 79 ± 0 66	7	1 52
05PH002A Granite	63 5730 146 9507	1607	16	0 030	18	2 058	1253	29 6	1 330	3325	**3.5 ± 0.8**	none	--	1 83
05PH005A Diorite	63 5291 147 0158	1282	40	0 014	28	1 245	2443	75 1	1 323	3308	**2.8 ± 0.5**	13 86	1	--
05PH005B Aplite	63 5291 147 0158	1282	40	0 010	28	0 795	2289	98	1 320	3299	**2.9 ± 0.6**	12 5 ± 0 74	13	1 50
05PH006A Granodiorite	63 5386 147 0736	1730	40	0 046	128	4 035	11217	23 1	1 294	3235	**2.7 ± 0.2**	none	--	1 36
05NEN Granodiorite	63 5098 147 8443	1640	30	0 030	20	5 680	3842	24	1 315	2124	**1.2 ± 0.3**	13 9 ± 1 40	18	2 06
22DEB Granitoid	63 5391 147 3237	1341	30	0 013	42	3 220	3135	<1	1 395	2254	**3.3 ± 0.5**	12 2 ± 0 70	8	1 99
South of Denali Fault														
05PH003A Tonalite	63 5043 146 8302	1358	20	0 269	157	4 001	2449	99 5	1 327	3316	**15.5 ± 1.3**	11 94 ± 0 28	24	2 02

Notes: Track densities (ρ) are x 10^6 tracks cm^{-2}. s: spontaneous, i: induced, D: dosimeter; n: number of grains counted for age or length determination. All analyses are by the External Detector Method using 0.5 for the geometry correction factor. Apatite ages calculated using dosimeter glass CN5 and zeta = 364.0 ± 6.3 (± 1σ). Apatite ages for three samples (01BAL, 05NEN, and 22DEB) were calculated using a zeta = 349.0 ± 5.1 (± 1σ). Age standards include Fish Canyon Tuff, Durango and Mount Dromedary apatites. $P(\chi^2)$ is the probability of obtaining χ^2 value for v degrees of freedom (where v is the number of crystals -1) (Galbraith, 1981); pooled ρs/ρi ratio is used to calculate age and uncertainty where $P(\chi^2)$ >5%; mean ρs/ρi ratio is used for samples where $P(\chi^2)$ <5% and for which Central ages (Galbraith and Laslett, 1993) are calculated. Apatite grain mounts were etched in 5 M HNO3 for 20 s at 21 deg. C.

Table 2R.4: Apatite U-Th/He data

Sample # And rock type	Lat (°N) Lon (°W)	Elev (m)	U (ppm)	Th (ppm)	He (nmol/g)	Sm (ppm)	Mass (mg)	Ft	Radius (mm)	Corrected age (Ma)	Mean age (Ma)	Std error (Ma)
North of Denali Fault												
05PH001A	63 5952	2003	3 09	5 27	0 05	70 27	6 16	0 78	62 25	2 59	**3 65**	0 78
hb tonalite	146 9522		8 90	9 17	0 14	111 16	1 88	0 70	45 60	3 19		
			84 99	219 04	2 75	584 24	2 10	0 71	54 00	5 17		
05PH005A	63 5291	1282	4 74	4 63	0 04	86 26	4 76	0 78	68 90	1 53	**1 41**	0 06
diorite	147 0158		5 57	5 24	0 04	69 98	4 17	0 76	57 45	1 38		
			6 09	5 19	0 04	67 88	5 93	0 78	62 25	1 31		
South of Denali Fault												
05PH003A	63 5043	1358	21 66	27 50	0 58	144 86	6 21	0 76	55 00	4 94	**4.54**	0 46
hb tonalite	146 8302		31 19	32 52	0 74	112 60	2 11	0 69	41 55	5 04		
			15 11	19 77	0 27	89 11	1 59	0 69	45 50	3 63		

Notes

1. Ft is fraction of total a particles retained (Farley et al., 1996)
2. Standard error for single grain sample (PH-06) is the average standard error for other samples with 3 grains each.

Table 2R.5: $^{40}Ar/^{39}Ar$ data for biotitie, muscovite, hornblende and K-spar.

BIOTITE

L=Laser Run F=Furnace Run

North of Denali Fault

01PAN BI#L1 FIGURE 2R 1

Weighted average of J from standards = 3 571e-03 +/- 1 656e-05

Laser Power (mW)	Cumulative 39Ar	40Ar/39Ar measured	+/-	37Ar/39Ar measured	+/-	36Ar/39Ar measured	+/-	% Atmospheric 40Ar	Ca/K	+/-	Cl/K	+/-	40*/39K	+/-	Age (Ma)	+/- (Ma)
400	0 01	86 92	0 74	0 26	0 0283	0 29	0 0038	98 86	0 48	0 05	0 01	0 0008	0 99	0 92	6 38	5 88
600	0 01	11 69	0 10	0 07	0 0198	0 03	0 0018	67 57	0 13	0 04	0 01	0 0004	3 78	0 52	24 21	3 29
800	0 04	6 90	0 07	0 02	0 0047	0 00	0 0007	20 77	0 03	0 01	0 01	0 0002	5 44	0 20	34 74	1 26
1000	0 09	6 22	0 03	0 01	0 0026	0 00	0 0003	6 69	0 02	0 00	0 01	0 0002	5 78	0 10	36 86	0 66
1250	0 16	5 99	0 02	0 01	0 0017	0 00	0 0003	2 63	0 02	0 00	0 01	0 0002	5 80	0 08	37 01	0 49
1500	0 23	5 95	0 02	0 01	0 0021	0 00	0 0002	1 45	0 02	0 00	0 01	0 0001	5 83	0 05	37 20	0 32
1750	0 32	5 94	0 02	0 01	0 0012	0 00	0 0002	-0 18	0 02	0 00	0 01	0 0001	5 92	0 06	37 73	0 36
2000	0 42	5 91	0 02	0 02	0 0012	0 00	0 0001	0 22	0 03	0 00	0 01	0 0001	5 87	0 04	37 40	0 27
2500	0 60	5 83	0 05	0 03	0 0009	0 00	0 0001	0 29	0 05	0 00	0 01	0 0001	5 78	0 05	36 86	0 34
3000	0 76	5 77	0 05	0 03	0 0009	0 00	0 0001	-0 23	0 06	0 00	0 01	0 0001	5 76	0 05	36 71	0 34
5000	0 95	5 76	0 04	0 07	0 0008	0 00	0 0001	-0 06	0 12	0 00	0 01	0 0001	5 74	0 05	36 59	0 29
9000	1 00	5 83	0 02	0 09	0 0027	0 00	0 0003	0 67	0 17	0 00	0 01	0 0002	5 76	0 10	36 75	0 63
Integrated		6 39	0 02	0 04	0 0005	0 00	0 0001	9 76	0 06	0 00	0 01	0 0000	5 74	0 02	36 61	0 22

04NEN BI#L1 FIGURE 2R 2

Weighted average of J from standards = 3 297e-03 +/- 8 602e-06

Laser Power (mW)	Cumulative 39Ar	40Ar/39Ar measured	+/-	37Ar/39Ar measured	+/-	36Ar/39Ar measured	+/-	% Atmospheric 40Ar	Ca/K	+/-	Cl/K	+/-	40*/39K	+/-	Age (Ma)	+/- (Ma)

Table 2R 5
continued

300	0 01	43 47	0 41	0 16	0 0033	0 15
500	0 02	19 55	0 11	0 04	0 0017	0 05
650	0 05	10 18	0 08	0 02	0 0008	0 01
800	0 09	7 64	0 05	0 01	0 0003	0 00
950	0 15	7 86	0 05	0 01	0 0004	0 01
1100	0 20	7 69	0 04	0 01	0 0004	0 00
1300	0 25	7 45	0 04	0 01	0 0004	0 00
1500	0 30	7 34	0 04	0 02	0 0003	0 00
1800	0 36	7 41	0 04	0 02	0 0004	0 00
2200	0 47	7 25	0 04	0 03	0 0004	0 00
3000	0 76	6 79	0 04	0 04	0 0003	0 00
5000	0 97	6 49	0 04	0 14	0 0011	0 00
9000	1 00	6 20	0 03	0 20	0 0019	0 00
Integrated		7 60	0 02	0 06	0 0002	0 00

37NEN BI#LI FIGURE 2R 3

Weighted average of J from standards = 3 493e-03 +/- 6 366e-06

Laser Power (mW)	Cumulative 39Ar	40Ar/39Ar measured	+/-	37Ar/39Ar measured	+/-	36Ar/39Ar measured	+/-
400	0 00	62 64	0 69	0 59	0 0133	0 21	
600	0 00	6 96	0 05	0 65	0 0081	0 03	
800	0 01	9 93	0 07	0 46	0 0071	0 03	
1000	0 01	14 78	0 12	0 10	0 0028	0 04	
1250	0 03	8 56	0 07	0 03	0 0010	0 01	
1500	0 06	6 99	0 04	0 01	0 0005	0 01	
1750	0 10	6 41	0 03	0 01	0 0004	0 00	
2000	0 14	6 26	0 02	0 01	0 0003	0 00	

0 0021	100 55	0 30	0 01	0 02	0 0004	-0 24	0 53	-1 43	3 17
0 0008	81 44	0 07	0 00	0 02	0 0003	3 62	0 24	21 41	1 40
0 0004	39 50	0 03	0 00	0 02	0 0003	6 14	0 13	36 16	0 75
0 0002	17 68	0 02	0 00	0 02	0 0002	6 26	0 07	36 87	0 38
0 0002	19 35	0 02	0 00	0 02	0 0002	6 32	0 07	37 18	0 43
0 0002	16 89	0 02	0 00	0 02	0 0002	6 37	0 07	37 49	0 42
0 0002	12 01	0 03	0 00	0 02	0 0002	6 53	0 06	38 43	0 35
0 0002	10 99	0 03	0 00	0 02	0 0001	6 51	0 07	38 28	0 39
0 0002	9 70	0 04	0 00	0 02	0 0001	6 66	0 06	39 19	0 34
0 0001	9 35	0 05	0 00	0 02	0 0001	6 55	0 05	38 54	0 27
0 0000	4 30	0 07	0 00	0 02	0 0001	6 47	0 04	38 05	0 23
0 0000	1 42	0 26	0 00	0 02	0 0001	6 37	0 04	37 49	0 25
0 0002	0 90	0 38	0 00	0 01	0 0002	6 12	0 08	36 02	0 44
0 0000	16 33	0 11	0 00	0 02	0 0001	6 33	0 02	37 26	0 15

% Atmospheric 40Ar		Ca/K	+/-	Cl/K	+/-	40*/39K	+/-	Age (Ma)	+/- (Ma)
0 0076	97 61	1 08	0 02	0 01	0 0015	1 50	2 16	9 40	13 56
0 0027	110 03	1 19	0 01	0 01	0 0007	-0 70	0 79	-4 39	5 02
0 0022	99 71	0 84	0 01	0 01	0 0004	0 03	0 63	0 18	3 99
0 0015	75 11	0 18	0 01	0 01	0 0003	3 67	0 43	22 98	2 68
0 0005	40 03	0 05	0 00	0 01	0 0002	5 11	0 15	31 94	0 95
0 0002	21 64	0 03	0 00	0 01	0 0002	5 46	0 08	34 06	0 49
0 0002	12 17	0 02	0 00	0 01	0 0001	5 61	0 07	34 99	0 40
0 0001	8 55	0 02	0 00	0 01	0 0001	5 70	0 04	35 54	0 25

Table 2R 5
continued

2500	0 20	6 16	0 02	0 01	0 0003	0 00
3000	0 27	6 07	0 02	0 02	0 0002	0 00
4000	0 41	6 03	0 04	0 02	0 0002	0 00
6000	0 80	5 92	0 02	0 10	0 0006	0 00
8000	1 00	5 94	0 03	0 15	0 0011	0 00
Integrated		6 20	0 01	0 08	0 0003	0 00
5000	0 99	5 48	0 03	0 40	0 0034	0 00
9000	1 00	5 64	0 03	0 71	0 0053	0 00
Integrated		5 56	0 02	0 10	0 0003	0 00

32NEN B1#L2 FIGURE 2R 4

Weighted average of J from standards = 3 493e-03 +/- 6 366e-06

Laser Power (mW)	Cumulative 39Ar	40Ar/39Ar measured	+/-	37Ar/39Ar measured	+/-	36Ar/39Ar measured	+/-
400	0 03	18 32	0 12	0 31	0 0035	0 06	
600	0 09	10 33	0 05	0 06	0 0009	0 02	
800	0 19	6 12	0 03	0 03	0 0009	0 00	
1000	0 30	5 94	0 03	0 02	0 0006	0 00	
1250	0 38	5 97	0 02	0 02	0 0012	0 00	
1500	0 46	6 23	0 02	0 03	0 0009	0 00	
1750	0 57	5 94	0 02	0 04	0 0008	0 00	
2000	0 68	5 55	0 01	0 04	0 0007	0 00	
2500	0 77	5 44	0 01	0 08	0 0011	0 00	
3000	0 81	5 38	0 02	0 21	0 0028	0 00	
3750	0 85	5 45	0 03	0 27	0 0020	0 00	
4500	0 88	5 41	0 04	0 36	0 0036	0 00	

0 0001	6 27	0 02	0 00	0 01	0 0001	5 74	0 03	35 83	0 18
0 0001	4 44	0 03	0 00	0 02	0 0001	5 77	0 03	36 00	0 17
0 0000	3 14	0 04	0 00	0 02	0 0001	5 81	0 04	36 23	0 22
0 0000	1 85	0 19	0 00	0 02	0 0001	5 79	0 02	36 10	0 13
0 0000	1 65	0 28	0 00	0 02	0 0001	5 81	0 03	36 27	0 21
0 0000	7 55	0 15	0 00	0 02	0 0001	5 71	0 01	35 60	0 11
0 0002	1 46	0 73	0 01	0 00	0 0001	5 37	0 06	33 69	0 37
0 0011	19 55	1 30	0 01	0 00	0 0003	4 51	0 34	28 34	2 09
0 0000	4 43	0 19	0 00	0 00	0 0000	5 29	0 02	33 15	0 19

	% Atmospheric 40Ar	Ca/K	+/-	Cl/K	+/-	40*/39K	+/-	Age (Ma)	+/- (Ma)
0 0012	97 47	0 56	0 01	0 01	0 0003	0 46	0 35	2 91	2 22
0 0006	56 73	0 11	0 00	0 01	0 0002	4 46	0 18	27 87	1 12
0 0003	22 42	0 05	0 00	0 01	0 0001	4 72	0 10	29 52	0 61
0 0003	18 35	0 03	0 00	0 01	0 0001	4 82	0 09	30 15	0 58
0 0004	18 17	0 04	0 00	0 01	0 0001	4 86	0 11	30 39	0 66
0 0004	20 84	0 06	0 00	0 01	0 0002	4 91	0 13	30 65	0 79
0 0003	18 84	0 08	0 00	0 01	0 0001	4 80	0 09	30 00	0 56
0 0002	11 54	0 08	0 00	0 01	0 0001	4 88	0 06	30 50	0 39
0 0003	9 69	0 15	0 00	0 01	0 0001	4 89	0 08	30 53	0 51
0 0008	13 22	0 39	0 01	0 01	0 0003	4 65	0 23	29 04	1 43
0 0006	7 79	0 49	0 00	0 01	0 0002	5 00	0 19	31 22	1 18
0 0009	7 52	0 66	0 01	0 01	0 0004	4 98	0 28	31 11	1 74

Table 2R 5
continued

5500	0 92	5 42	0 03	0 44	0 0038	0 00
6500	0 97	5 56	0 02	0 30	0 0025	0 00
8000	1 00	5 70	0 03	0 35	0 0038	0 00
Integrated		6 42	0 01	0 11	0 0004	0 01

02DEB BI#L1 FIGURE 2R 5

Weighted average of J from standards = 3 579e-03 +/- 1 276e-05

Laser Power (mW)	Cumulative 39Ar	40Ar/39Ar measured	+/-	37Ar/39Ar measured	+/-	36Ar/39Ar measured	+/-
400	0 00	78 65	1 24	0 18	0 0419	0 15	
600	0 01	7 03	0 08	0 37	0 0109	0 02	
800	0 02	8 66	0 09	0 45	0 0083	0 02	
1000	0 05	13 35	0 09	0 22	0 0031	0 02	
1250	0 12	12 44	0 04	0 05	0 0009	0 01	
1500	0 23	11 61	0 08	0 01	0 0007	0 00	
1750	0 34	11 30	0 05	0 01	0 0005	0 00	
2000	0 46	11 09	0 06	0 01	0 0004	0 00	
2500	0 58	10 83	0 05	0 01	0 0004	0 00	
3000	0 73	10 55	0 09	0 01	0 0004	0 00	
3500	0 82	10 52	0 03	0 02	0 0005	0 00	
4500	0 92	10 38	0 03	0 03	0 0006	0 00	
6000	0 97	10 42	0 07	0 02	0 0013	0 00	
8000	1 00	10 48	0 08	0 02	0 0014	0 00	
Integrated		11 07	0 02	0 03	0 0002	0 00	

24DEB BI#L1 FIGURE 2R 6

0 0006	12 63	0 80	0 01	0 01	0 0002	4 71	0 19	29 45	1 17
0 0004	8 72	0 54	0 00	0 01	0 0002	5 05	0 13	31 53	0 82
0 0008	6 47	0 65	0 01	0 01	0 0003	5 30	0 24	33 11	1 46
0 0001	26 33	0 20	0 00	0 01	0 0000	4 70	0 03	29 41	0 22

% Atmospheric 40Ar	Ca/K	+/-	Cl/K	+/-	40*/39K	+/-	Age (Ma)	+/- (Ma)
0 0106	57 08	0 33	0 08	0 02	0 0020	33 75	3 12	205 74	17 95
0 0016	86 25	0 68	0 02	0 01	0 0005	0 96	0 48	6 20	3 06
0 0006	53 82	0 83	0 02	0 01	0 0003	3 99	0 17	25 56	1 08
0 0006	35 10	0 40	0 01	0 01	0 0002	8 64	0 18	54 97	1 14
0 0002	14 07	0 09	0 00	0 01	0 0001	10 66	0 07	67 58	0 42
0 0002	6 88	0 02	0 00	0 01	0 0001	10 78	0 10	68 31	0 64
0 0001	3 25	0 01	0 00	0 01	0 0001	10 90	0 06	69 08	0 40
0 0001	2 56	0 01	0 00	0 01	0 0001	10 77	0 06	68 27	0 40
0 0001	2 04	0 01	0 00	0 01	0 0001	10 58	0 06	67 06	0 36
0 0001	1 53	0 02	0 00	0 01	0 0001	10 36	0 09	65 67	0 55
0 0001	2 29	0 03	0 00	0 01	0 0001	10 25	0 05	65 00	0 30
0 0001	2 11	0 05	0 00	0 01	0 0001	10 13	0 05	64 26	0 28
0 0002	3 50	0 04	0 00	0 01	0 0001	10 03	0 10	63 62	0 62
0 0003	3 01	0 03	0 00	0 01	0 0002	10 13	0 11	64 28	0 68
0 0001	6 27	0 05	0 00	0 01	0 0000	10 34	0 02	65 59	0 28

Table 2R 5
continued
Weighted average of J from standards = 3 493e-03 +/- 6 366e-06

Laser Power (mW)	Cumulative 39Ar	40Ar/39Ar measured	+/-	37Ar/39Ar measured	+/-	36Ar/39Ar measured	+/-
400	0 00	101 44	0 81	0 10	0 0061	0 34	
600	0 02	21 78	0 08	0 07	0 0020	0 06	
800	0 08	13 11	0 07	0 04	0 0006	0 03	
1000	0 18	7 47	0 04	0 03	0 0004	0 01	
1250	0 29	6 12	0 04	0 03	0 0003	0 00	
1500	0 39	5 86	0 04	0 02	0 0005	0 00	
1750	0 47	5 75	0 03	0 03	0 0004	0 00	
2000	0 54	5 73	0 02	0 03	0 0003	0 00	
2500	0 65	5 76	0 04	0 04	0 0004	0 00	
3000	0 76	5 78	0 04	0 06	0 0005	0 00	
3500	0 86	5 94	0 04	0 16	0 0013	0 00	
4500	0 97	6 17	0 03	0 40	0 0023	0 00	
6000	0 99	6 16	0 02	0 49	0 0046	0 00	
8000	1 00	6 11	0 03	0 40	0 0036	0 00	
Integrated		7 02	0 01	0 10	0 0003	0 01	

07DEB BI#1 FIGURE 2R 7

Weighted average of J from standards = 3 579e-03 +/- 1 276e-05

Laser Power (mW)	Cumulative 39Ar	40Ar/39Ar measured	+/-	37Ar/39Ar measured	+/-	36Ar/39Ar measured	+/-
400	0 01	19 46	0 18	0 15	0 0030	0 06	
600	0 02	7 93	0 11	0 13	0 0022	0 02	
800	0 04	9 31	0 06	0 11	0 0018	0 02	

	% Atmospheric 40Ar		Ca/K	+/-	Cl/K	+/-	40*/39K	+/-	Age (Ma)	+/- (Ma)
0 0034		97 92	0 19	0 01	0 01	0 0007	2 11	0 79	13 22	4 94
0 0008		81 49	0 13	0 00	0 01	0 0002	4 03	0 23	25 19	1 43
0 0003		62 89	0 08	0 00	0 01	0 0001	4 86	0 10	30 34	0 63
0 0001		32 42	0 05	0 00	0 01	0 0001	5 03	0 05	31 40	0 29
0 0001		15 02	0 05	0 00	0 01	0 0001	5 18	0 04	32 32	0 25
0 0001		9 92	0 05	0 00	0 01	0 0001	5 26	0 05	32 82	0 29
0 0001		8 71	0 05	0 00	0 01	0 0001	5 22	0 03	32 61	0 20
0 0001		9 88	0 06	0 00	0 01	0 0001	5 14	0 04	32 08	0 24
0 0001		11 89	0 07	0 00	0 01	0 0001	5 05	0 04	31 56	0 27
0 0001		11 77	0 11	0 00	0 01	0 0001	5 08	0 04	31 71	0 26
0 0001		13 09	0 30	0 00	0 01	0 0001	5 13	0 04	32 07	0 28
0 0001		12 32	0 73	0 00	0 01	0 0001	5 38	0 04	33 60	0 22
0 0003		12 10	0 89	0 01	0 01	0 0001	5 39	0 09	33 67	0 53
0 0010		14 88	0 73	0 01	0 01	0 0002	5 18	0 28	32 33	1 74
0 0000		26 78	0 18	0 00	0 01	0 0000	5 12	0 01	31 99	0 11

	% Atmospheric 40Ar		Ca/K	+/-	Cl/K	+/-	40*/39K	+/-	Age (Ma)	+/- (Ma)
0 0012		93 38	0 28	0 01	0 02	0 0003	1 29	0 35	8 29	2 27
0 0006		82 33	0 24	0 00	0 02	0 0004	1 40	0 19	8 99	1 21
0 0005		72 03	0 21	0 00	0 02	0 0002	2 60	0 14	16 68	0 91

Table 2R 5
continued

1000	0 07	8 19	0 03	0 05	0 0005	0 02
1250	0 13	5 68	0 03	0 02	0 0006	0 01
1500	0 21	5 08	0 03	0 01	0 0003	0 00
1750	0 30	4 93	0 02	0 01	0 0003	0 00
2000	0 38	4 97	0 02	0 01	0 0003	0 00
2500	0 51	5 05	0 05	0 02	0 0003	0 00
3000	0 64	5 06	0 05	0 04	0 0005	0 00
3500	0 80	5 07	0 04	0 05	0 0005	0 00
4500	0 89	5 07	0 02	0 05	0 0004	0 00
6000	0 96	5 04	0 02	0 04	0 0005	0 00
8000	1 00	4 99	0 03	0 04	0 0006	0 00
Integrated		5 40	0 01	0 03	0 0001	0 00

03BAL BI#L1 FIGURE 2R 8

Weighted average of J from standards = 3 507e-03 +/- 1 639e-05

Laser Power (mW)	Cumulative 39Ar	40Ar/39Ar measured	+/-	37Ar/39Ar measured	+/-	36Ar/39Ar measured	+/-
400	0 04	7 63	0 05	0 03	0 0007	0 01	
1000	0 31	5 57	0 03	0 01	0 0002	0 00	
1500	0 55	5 45	0 04	0 02	0 0002	0 00	
2000	0 74	5 40	0 04	0 06	0 0005	0 00	
3000	0 94	5 46	0 03	0 29	0 0013	0 00	
5000	0 99	5 48	0 03	0 40	0 0034	0 00	
9000	1 00	5 64	0 03	0 71	0 0053	0 00	
Integrated		5 56	0 02	0 10	0 0003	0 00	

0 0003	54 67	0 09	0 00	0 02	0 0002	3 70	0 08	23 74	0 50
0 0001	27 70	0 04	0 00	0 02	0 0002	4 08	0 04	26 18	0 28
0 0001	16 82	0 02	0 00	0 02	0 0002	4 20	0 04	26 93	0 29
0 0001	11 08	0 02	0 00	0 02	0 0002	4 36	0 03	27 93	0 19
0 0001	10 01	0 02	0 00	0 02	0 0001	4 44	0 03	28 47	0 20
0 0001	12 15	0 03	0 00	0 02	0 0003	4 41	0 05	28 26	0 34
0 0000	11 84	0 07	0 00	0 02	0 0003	4 43	0 05	28 40	0 33
0 0001	11 24	0 09	0 00	0 02	0 0002	4 47	0 04	28 65	0 26
0 0001	10 86	0 09	0 00	0 02	0 0001	4 49	0 03	28 76	0 21
0 0001	10 77	0 08	0 00	0 02	0 0002	4 47	0 03	28 66	0 20
0 0001	11 01	0 07	0 00	0 02	0 0002	4 41	0 05	28 28	0 30
0 0000	20 33	0 06	0 00	0 02	0 0001	4 28	0 01	27 42	0 13

% Atmospheric 40Ar	Ca/K	+/-	Cl/K	+/-	40*/39K	+/-	Age (Ma)	+/- (Ma)
0 0004	37 76	0 05	0 00	0 00	0 0001	4 73	0 11	29 70	0 68
0 0001	4 29	0 02	0 00	0 00	0 0000	5 31	0 04	33 26	0 22
0 0001	2 08	0 03	0 00	0 00	0 0000	5 30	0 04	33 25	0 25
0 0001	1 47	0 10	0 00	0 00	0 0000	5 29	0 05	33 17	0 29
0 0000	1 55	0 53	0 00	0 00	0 0000	5 35	0 03	33 54	0 21
0 0002	1 46	0 73	0 01	0 00	0 0001	5 37	0 06	33 69	0 37
0 0011	19 55	1 30	0 01	0 00	0 0003	4 51	0 34	28 34	2 09
0 0000	4 43	0 19	0 00	0 00	0 0000	5 29	0 02	33 15	0 19

Table 2R 5
continued

18BAL BI#L1 FIGURE 2R 9

Weighted average of J from standards = 3 507e-03 +/- 1 639e-05

Laser Power (mW)	Cumulative 39Ar	40Ar/39Ar measured	+/-	37Ar/39Ar measured	+/-	36Ar/39Ar measured	+/-
400	0 07	6 98	0 04	0 01	0 0006	0 01	
1000	0 42	3 95	0 02	0 01	0 0001	0 00	
1500	0 67	3 70	0 02	0 01	0 0002	0 00	
2000	0 83	3 77	0 03	0 01	0 0003	0 00	
3000	0 93	3 92	0 06	0 02	0 0007	0 00	
5000	0 99	4 38	0 08	0 06	0 0014	0 00	
9000	1 00	6 15	0 07	0 08	0 0045	0 00	
Integrated		4 12	0 01	0 01	0 0002	0 00	

19BAL BI#L1 FIGURE 2R 10

Weighted average of J from standards = 3 507e-03 +/- 1 639e-05

Laser Power (mW)	Cumulative 39Ar	40Ar/39Ar measured	+/-	37Ar/39Ar measured	+/-	36Ar/39Ar measured	+/-
400	0 05	10 18	0 03	0 01	0 0004	0 02	
1000	0 50	3 55	0 02	0 00	0 0001	0 00	
1500	0 69	3 44	0 02	0 01	0 0001	0 00	
2000	0 84	3 46	0 01	0 02	0 0003	0 00	
3000	0 96	3 52	0 02	0 08	0 0006	0 00	
5000	0 99	3 59	0 06	0 15	0 0028	0 00	
9000	1 00	3 71	0 06	0 13	0 0029	0 00	
Integrated		3 84	0 01	0 02	0 0001	0 00	

% Atmospheric 40Ar	Ca/K	+/-	Cl/K	+/-	40*/39K	+/-	Age (Ma)	+/- (Ma)
0 0003	56 04	0 03	0 00	0 01	0 0001	3 06	0 09	19 24	0 53
0 0000	8 40	0 01	0 00	0 01	0 0001	3 59	0 02	22 55	0 15
0 0001	2 86	0 02	0 00	0 01	0 0001	3 56	0 03	22 40	0 17
0 0001	3 75	0 02	0 00	0 01	0 0001	3 60	0 04	22 65	0 26
0 0001	2 97	0 04	0 00	0 01	0 0001	3 78	0 07	23 75	0 41
0 0002	4 21	0 10	0 00	0 01	0 0002	4 17	0 10	26 20	0 61
0 0008	15 46	0 15	0 01	0 00	0 0003	5 17	0 24	32 43	1 48
0 0000	11 48	0 03	0 00	0 01	0 0000	3 62	0 02	22 77	0 15

% Atmospheric 40Ar	Ca/K	+/-	Cl/K	+/-	40*/39K	+/-	Age (Ma)	+/- (Ma)
0 0003	68 39	0 02	0 00	0 00	0 0001	3 21	0 09	20 19	0 57
0 0000	3 38	0 01	0 00	0 00	0 0000	3 40	0 02	21 39	0 13
0 0000	2 44	0 01	0 00	0 00	0 0000	3 33	0 02	20 94	0 15
0 0001	1 01	0 04	0 00	0 00	0 0000	3 39	0 02	21 35	0 12
0 0001	1 24	0 15	0 00	0 00	0 0001	3 45	0 03	21 67	0 18
0 0003	2 19	0 28	0 01	0 00	0 0001	3 48	0 10	21 90	0 63
0 0008	1 07	0 24	0 01	0 00	0 0002	3 64	0 25	22 88	1 56
0 0000	11 03	0 04	0 00	0 00	0 0000	3 39	0 01	21 31	0 13

Table 2R 5
continued

30RAP BI#1 FIGURE 2R 11

Weighted average of J from standards = 3 411e-03 +/- 1 051e-05

Laser Power (mW)	Cumulative 39Ar	40Ar/39Ar measured	+/-	37Ar/39Ar measured	+/-	36Ar/39Ar measured	+/-
250	0 01	38 10	0 30	0 02	0 0041	0 12	
400	0 08	4 17	0 01	0 01	0 0005	0 00	
550	0 27	3 21	0 02	0 00	0 0002	0 00	
700	0 41	3 14	0 04	0 01	0 0003	0 00	
850	0 49	3 12	0 04	0 01	0 0006	0 00	
1000	0 57	3 10	0 03	0 01	0 0006	0 00	
1250	0 71	3 13	0 03	0 01	0 0003	0 00	
1500	0 84	3 11	0 03	0 00	0 0002	0 00	
1750	0 92	3 12	0 05	0 01	0 0004	0 00	
2000	0 95	3 21	0 06	0 03	0 0011	0 00	
2500	0 96	3 28	0 05	0 06	0 0032	0 00	
3000	0 98	3 19	0 05	0 04	0 0029	0 00	
5000	1 00	3 17	0 06	0 04	0 0025	0 00	
9000	1 00	3 52	0 11	0 04	0 0066	0 00	
Integrated		3 56	0 01	0 01	0 0002	0 00	

03RAP BI#L1 FIGURE 2R 12

Weighted average of J from standards = 3 571e-03 +/- 1 656e-05

Laser Power (mW)	Cumulative 39Ar	40Ar/39Ar measured	+/-	37Ar/39Ar measured	+/-	36Ar/39Ar measured	+/-
400	0 01	157 74	0 99	0 09	0 0201	0 53	
600	0 04	9 15	0 04	0 02	0 0051	0 02	

	% Atmospheric 40Ar	Ca/K	+/-	Cl/K	+/-	40*/39K	+/-	Age (Ma)	+/- (Ma)
0 0027	91 37	0 03	0 01	0 01	0 0006	3 29	0 75	20 11	4 54
0 0002	26 76	0 01	0 00	0 01	0 0001	3 03	0 06	18 55	0 37
0 0001	3 82	0 01	0 00	0 01	0 0001	3 06	0 04	18 75	0 23
0 0001	3 17	0 01	0 00	0 01	0 0001	3 02	0 05	18 47	0 29
0 0002	4 31	0 03	0 00	0 01	0 0002	2 95	0 06	18 08	0 35
0 0002	7 17	0 02	0 00	0 01	0 0002	2 85	0 08	17 44	0 47
0 0001	3 84	0 01	0 00	0 01	0 0001	2 98	0 05	18 26	0 29
0 0002	1 11	0 01	0 00	0 01	0 0002	3 05	0 06	18 67	0 35
0 0002	0 30	0 01	0 00	0 01	0 0002	3 08	0 07	18 86	0 45
0 0005	-0 25	0 05	0 00	0 01	0 0003	3 19	0 15	19 54	0 92
0 0011	5 47	0 11	0 01	0 01	0 0003	3 07	0 33	18 81	2 01
0 0013	5 96	0 07	0 01	0 01	0 0004	2 97	0 37	18 20	2 28
0 0008	6 32	0 06	0 00	0 01	0 0003	2 94	0 25	18 00	1 53
0 0056	17 47	0 06	0 01	0 01	0 0013	2 88	1 66	17 63	10 13
0 0001	14 54	0 02	0 00	0 01	0 0001	3 02	0 02	18 48	0 15

	% Atmospheric 40Ar	Ca/K	+/-	Cl/K	+/-	40*/39K	+/-	Age (Ma)	+/- (Ma)
0 0045	98 72	0 17	0 04	0 01	0 0006	2 02	1 10	13 00	7 05
0 0005	50 14	0 03	0 01	0 00	0 0002	4 55	0 16	29 07	0 98

Table 2R 5
continued

800	0 12	5 58	0 04	0 01	0 0018	0 00
1000	0 24	5 22	0 02	0 01	0 0012	0 00
1250	0 40	5 17	0 03	0 01	0 0008	0 00
1500	0 53	5 18	0 02	0 01	0 0011	0 00
1750	0 63	5 17	0 02	0 03	0 0012	0 00
2000	0 74	5 15	0 02	0 05	0 0014	0 00
2500	0 86	5 18	0 02	0 21	0 0026	0 00
3000	0 94	5 17	0 02	0 36	0 0034	0 00
5000	0 99	5 20	0 02	0 70	0 0064	0 00
9000	1 00	5 17	0 06	0 98	0 0284	0 00
Integrated		6 54	0 01	0 11	0 0007	0 01

South of Denali Fault

45RAP Bl#L1 FIGURE 2R 13

Weighted average of J from standards = 7 125e-03 +/- 1 903e-05

Laser Power (mW)	Cumulative 39Ar	40Ar/39Ar measured	+/-	37Ar/39Ar measured	+/-	36Ar/39Ar measured	+/-
400	0 02	3 94	0 02	0 01	0 0017	0 01	
600	0 05	3 19	0 01	0 00	0 0009	0 00	
1000	0 24	3 00	0 02	0 00	0 0001	0 00	
1250	0 39	2 68	0 02	0 00	0 0002	0 00	
1750	0 55	2 65	0 02	0 00	0 0001	0 00	
2000	0 65	2 66	0 02	0 00	0 0003	0 00	
3000	0 84	2 66	0 01	0 00	0 0002	0 00	
6000	0 99	2 66	0 01	0 00	0 0002	0 00	
9000	1 00	2 74	0 03	0 02	0 0052	0 00	

0 0002	10 25	0 02	0 00	0 00	0 0001	4 98	0 07	31 82	0 42
0 0001	3 11	0 02	0 00	0 00	0 0000	5 03	0 03	32 12	0 19
0 0001	0 77	0 02	0 00	0 00	0 0001	5 10	0 04	32 58	0 25
0 0001	0 71	0 03	0 00	0 00	0 0001	5 11	0 04	32 63	0 24
0 0001	0 65	0 05	0 00	0 00	0 0001	5 11	0 04	32 59	0 25
0 0001	0 97	0 09	0 00	0 00	0 0001	5 07	0 04	32 40	0 28
0 0001	0 29	0 39	0 00	0 00	0 0001	5 13	0 03	32 76	0 21
0 0002	1 21	0 66	0 01	0 00	0 0001	5 08	0 05	32 46	0 34
0 0002	0 32	1 28	0 01	0 00	0 0001	5 16	0 06	32 93	0 35
0 0017	1 05	1 80	0 05	0 00	0 0004	5 09	0 50	32 49	3 16
0 0001	22 55	0 21	0 00	0 00	0 0000	5 05	0 02	32 22	0 18

% Atmospheric 40Ar		Ca/K	+/-	Cl/K	+/-	40*/39K	+/-	Age (Ma)	+/- (Ma)
0 0006	84 28	0 01	0 00	0 00	0 0002	0 62	0 18	7 89	2 28
0 0003	36 91	0 01	0 00	0 00	0 0001	2 00	0 08	25 48	1 06
0 0000	14 54	0 00	0 00	0 00	0 0001	2 54	0 02	32 30	0 25
0 0001	3 62	0 00	0 00	0 00	0 0000	2 55	0 02	32 52	0 30
0 0001	2 46	0 00	0 00	0 00	0 0001	2 55	0 02	32 54	0 29
0 0001	3 36	0 00	0 00	0 00	0 0001	2 54	0 03	32 35	0 33
0 0001	2 34	0 00	0 00	0 00	0 0000	2 57	0 02	32 77	0 25
0 0001	2 88	0 00	0 00	0 00	0 0000	2 55	0 02	32 49	0 25
0 0017	38 39	0 03	0 01	0 00	0 0004	1 67	0 50	21 34	6 32

Table 2R 5
continued

Integrated	2 76	0 01	0 00	0 0001	0 00

AST311 BI#L1 FIGURE 2R 14

Weighted average of J from standards = 3 571e-03 +/- 1 656e-05

Laser Power (mW)	Cumulative 39Ar	40Ar/39Ar measured	+/-	37Ar/39Ar measured	+/-	36Ar/39Ar measured	+/-
400	0 00	384 60	31 02	0 30		0 3726	1 30
600	0 00	129 85	18 00	0 32		0 4791	0 47
800	0 00	141 07	10 41	0 26		0 2528	0 46
1000	0 00	29 42	0 93	0 23		0 1299	0 08
1250	0 01	15 73	0 21	0 05		0 0444	0 03
1500	0 03	8 02	0 05	0 03		0 0074	0 01
1750	0 09	6 03	0 03	0 01		0 0022	0 00
2000	0 17	5 64	0 02	0 01		0 0025	0 00
2500	0 33	5 54	0 03	0 00		0 0010	0 00
3000	0 46	5 51	0 02	0 00		0 0015	0 00
5000	0 68	5 53	0 02	0 01		0 0008	0 00
9000	1 00	5 48	0 03	0 02		0 0005	0 00
Integrated		5 99	0 01	0 01		0 0006	0 00

05RAP BI#L1 FIGURE 2R 15

Weighted average of J from standards = 7 125e-03 +/- 1 903e-05

Laser Power (mW)	Cumulative 39Ar	40Ar/39Ar measured	+/-	37Ar/39Ar measured	+/-	36Ar/39Ar measured	+/-
400	0 01	7 16	0 03	0 02		0 0024	0 02
600	0 09	2 84	0 02	0 01		0 0004	0 00

0 0000	8 57	0 00	0 00	0 00	0 0000	2 50	0 01	31 85	0 15

	% Atmospheric 40Ar	Ca/K	+/-	Cl/K	+/-	40*/39K	+/-	Age (Ma)	+/- (Ma)
0 1140	100 03	0 55	0 68	0 01	0 0096	-0 13	13 16	-0 85	84 85
0 0816	106 92	0 58	0 88	0 02	0 0130	-8 98	14 63	-58 81	97 36
0 0460	95 86	0 48	0 46	0 02	0 0069	5 84	9 26	37 21	58 46
0 0146	84 40	0 42	0 24	0 01	0 0027	4 59	4 24	29 31	26 87
0 0046	63 73	0 09	0 08	0 00	0 0011	5 69	1 35	36 31	8 50
0 0007	30 45	0 05	0 01	0 01	0 0004	5 55	0 21	35 43	1 35
0 0003	11 60	0 01	0 00	0 01	0 0001	5 30	0 10	33 86	0 66
0 0003	2 58	0 01	0 00	0 01	0 0001	5 46	0 09	34 86	0 57
0 0002	1 16	0 01	0 00	0 01	0 0001	5 45	0 07	34 78	0 41
0 0002	0 67	0 01	0 00	0 01	0 0001	5 45	0 05	34 75	0 30
0 0001	1 45	0 01	0 00	0 01	0 0001	5 42	0 04	34 60	0 27
0 0001	0 38	0 03	0 00	0 01	0 0001	5 43	0 04	34 67	0 23
0 0001	8 99	0 02	0 00	0 01	0 0000	5 43	0 03	34 62	0 23

	% Atmospheric 40Ar	Ca/K	+/-	Cl/K	+/-	40*/39K	+/-	Age (Ma)	+/- (Ma)
0 0009	67 20	0 04	0 00	0 00	0 0002	2 34	0 25	29 80	3 19
0 0001	10 59	0 01	0 00	0 00	0 0001	2 51	0 03	32 00	0 36

Table 2R 5
continued

1000	0 31	2 58	0 01	0 00	0 0001	0 00
1250	0 41	2 58	0 02	0 00	0 0003	0 00
1750	0 57	2 58	0 02	0 01	0 0003	0 00
2000	0 71	2 55	0 02	0 01	0 0002	0 00
3000	0 96	2 57	0 01	0 07	0 0006	0 00
6000	1 00	2 58	0 04	0 27	0 0045	0 00
9000	1 00	2 90	0 12	0 15	0 0202	0 01
Integrated		2 65	0 01	0 03	0 0002	0 00

09RAP BI#L1 FIGURE 2R 16

Weighted average of J from standards = 7 125e-03 +/- 1 903e-05

Laser Power (mW)	Cumulative 39Ar	40Ar/39Ar measured	+/-	37Ar/39Ar measured	+/-	36Ar/39Ar measured	+/-
400	0 01	50 93	0 21	0 06	0 0024	0 17	
600	0 09	4 02	0 01	0 00	0 0002	0 01	
1000	0 29	2 88	0 02	0 00	0 0001	0 00	
1250	0 42	2 67	0 02	0 00	0 0001	0 00	
1750	0 57	2 64	0 02	0 00	0 0001	0 00	
2000	0 66	2 60	0 01	0 01	0 0002	0 00	
3000	0 82	2 59	0 02	0 03	0 0003	0 00	
6000	0 99	2 55	0 02	0 05	0 0004	0 00	
9000	1 00	2 56	0 04	0 05	0 0025	0 00	
Integrated		3 15	0 01	0 02	0 0001	0 00	

MUSCOVITE

L=Laser Run F=Furnace Run

0 0000	1 73	0 00	0 00	0 00	0 0000	2 50	0 02	31 91	0 22
0 0001	1 47	0 01	0 00	0 00	0 0000	2 51	0 03	31 99	0 35
0 0000	1 35	0 01	0 00	0 00	0 0000	2 51	0 02	32 02	0 22
0 0001	1 92	0 02	0 00	0 00	0 0000	2 48	0 02	31 56	0 28
0 0000	1 08	0 14	0 00	0 00	0 0000	2 51	0 02	31 96	0 19
0 0001	3 63	0 49	0 01	0 00	0 0001	2 46	0 05	31 32	0 63
0 0056	115 36	0 27	0 04	0 00	0 0022	-0 44	1 66	-5 68	21 37
0 0000	4 67	0 06	0 00	0 00	0 0000	2 50	0 01	31 80	0 14

% Atmospheric 40Ar		Ca/K	+/-	Cl/K	+/-	40*/39K	+/-	Age (Ma)	+/- (Ma)
0 0018	99 10	0 10	0 00	0 00	0 0003	0 46	0 49	5 89	6 28
0 0001	37 06	0 01	0 00	0 00	0 0000	2 51	0 04	32 00	0 52
0 0001	12 48	0 00	0 00	0 00	0 0000	2 49	0 02	31 76	0 31
0 0001	8 18	0 01	0 00	0 00	0 0000	2 43	0 04	30 94	0 51
0 0001	5 21	0 01	0 00	0 00	0 0000	2 48	0 03	31 58	0 34
0 0001	5 56	0 01	0 00	0 00	0 0000	2 43	0 03	30 96	0 37
0 0000	3 76	0 05	0 00	0 00	0 0000	2 46	0 02	31 40	0 28
0 0000	2 24	0 08	0 00	0 00	0 0000	2 46	0 02	31 35	0 25
0 0005	9 12	0 10	0 00	0 00	0 0001	2 30	0 15	29 29	1 90
0 0000	21 41	0 03	0 00	0 00	0 0000	2 45	0 01	31 22	0 16

Table 2R 5 continued

South of Denali Fault

45RAP MU#L1 FIGURE 2R 17

Weighted average of J from standards = 7 125e-03 +/- 1 903e-05

Laser Power (mW)	Cumulative 39Ar	40Ar/39Ar measured	+/-	37Ar/39Ar measured	+/-	36Ar/39Ar measured	+/-
400	0 00	33 33	0 50	-0 01	0 0088	0 11	
600	0 00	7 96	0 13	-0 02	0 0086	0 01	
1000	0 02	4 19	0 03	0 00	0 0007	0 01	
1250	0 08	2 62	0 02	0 00	0 0003	0 00	
1750	0 14	3 00	0 02	0 00	0 0002	0 00	
2000	0 22	2 58	0 02	0 00	0 0002	0 00	
3000	0 39	2 58	0 01	0 00	0 0001	0 00	
6000	0 80	2 73	0 01	0 00	0 0000	0 00	
9000	1 00	2 56	0 02	0 00	0 0001	0 00	
Integrated		2 74	0 01	0 00	0 0000	0 00	

05RAP MU#1 FIGURE 2R 18

Weighted average of J from standards = 7 125e-03 +/- 1 903e-05

Laser Power (mW)	Cumulative 39Ar	40Ar/39Ar measured	+/-	37Ar/39Ar measured	+/-	36Ar/39Ar measured	+/-
400	0 00	119 80	0 96	0 03	0 0122	0 41	
600	0 00	7 93	0 07	0 00	0 0100	0 02	
1000	0 01	5 22	0 04	0 00	0 0013	0 01	
1250	0 03	4 14	0 05	0 01	0 0006	0 01	
1750	0 09	3 02	0 02	0 00	0 0002	0 00	

	% Atmospheric 40Ar	Ca/K	+/-	Cl/K	+/-	40*/39K	+/-	Age (Ma)	+/- (Ma)
0 0046	97 17	-0 01	0 02	0 00	0 0009	0 94	1 29	12 08	16 47
0 0033	51 46	-0 04	0 02	0 00	0 0006	3 85	0 97	48 81	12 18
0 0004	45 20	0 00	0 00	0 00	0 0001	2 28	0 13	29 04	1 60
0 0002	3 63	0 00	0 00	0 00	0 0001	2 50	0 05	31 85	0 61
0 0001	16 86	0 00	0 00	0 00	0 0000	2 47	0 04	31 45	0 46
0 0001	2 76	0 00	0 00	0 00	0 0000	2 48	0 03	31 64	0 38
0 0000	1 76	0 00	0 00	0 00	0 0000	2 51	0 02	31 92	0 21
0 0000	8 84	0 00	0 00	0 00	0 0000	2 46	0 01	31 35	0 18
0 0000	1 56	0 00	0 00	0 00	0 0000	2 49	0 02	31 69	0 24
0 0000	8 66	0 00	0 00	0 00	0 0000	2 48	0 01	31 54	0 14

	% Atmospheric 40Ar	Ca/K	+/-	Cl/K	+/-	40*/39K	+/-	Age (Ma)	+/- (Ma)
0 0092	101 11	0 06	0 02	0 00	0 0011	-1 32	2 55	-17 10	33 04
0 0033	79 23	0 00	0 02	0 00	0 0007	1 64	0 96	20 97	12 25
0 0004	49 17	0 01	0 00	0 00	0 0001	2 64	0 14	33 58	1 71
0 0003	38 27	0 01	0 00	0 00	0 0001	2 54	0 10	32 31	1 28
0 0001	14 16	0 00	0 00	0 00	0 0000	2 57	0 03	32 68	0 39

Table 2R 5
continued

2000	0 15	2 88	0 01	0 00	0 0002	0 00
3000	0 32	2 79	0 02	0 00	0 0001	0 00
6000	1 00	2 72	0 03	0 00	0 0000	0 00
9000	1 00	2 82	0 04	0 00	0 0033	0 00
Integrated		2 94	0 02	0 00	0 0000	0 00

HORNBLENDE

L=Laser Run F=Furnace Run

South of Denali Fault

311AST HO#L1 FIGURE 2R 19

Weighted average of J from standards = 3 571e-03 +/- 1 656e-05

Laser Power (mW)	Cumulative 39Ar	40Ar/39Ar measured	+/-	37Ar/39Ar measured	+/-	36Ar/39Ar measured	+/-
500	0 01	1839 56	39 29	1 68	0 0995	6 28	
750	0 02	59 53	0 70	0 38	0 0531	0 18	
1000	0 03	32 43	0 29	0 35	0 0517	0 09	
1250	0 05	64 72	0 97	0 85	0 0473	0 20	
1500	0 07	20 69	0 23	2 17	0 0597	0 05	
2000	0 14	18 95	0 14	7 11	0 0551	0 05	
2500	0 36	12 06	0 08	8 50	0 0663	0 02	
3000	0 68	6 64	0 11	8 39	0 1456	0 01	
4000	0 94	6 30	0 06	9 17	0 1243	0 00	
5000	0 98	6 57	0 08	11 33	0 1417	0 01	
6000	0 99	7 31	0 15	12 01	0 2590	0 01	
9000	1 00	7 43	0 11	11 03	0 1866	0 00	

0 0001	10 31	0 00	0 00	0 00	0 0000	2 56	0 02	32 62	0 23
0 0000	6 56	0 00	0 00	0 00	0 0000	2 58	0 02	32 88	0 24
0 0000	4 78	0 00	0 00	0 00	0 0000	2 56	0 03	32 58	0 38
0 0011	11 12	0 01	0 01	0 00	0 0002	2 48	0 33	31 58	4 11
0 0000	12 05	0 00	0 00	0 00	0 0000	2 56	0 02	32 58	0 28

	% Atmospheric 40Ar	Ca/K	+/-	Cl/K	+/-	40*/39K	+/-	Age (Ma)	+/- (Ma)
0 1379	100 89	3 08	0 18	0 08	0 0049	-16 32	11 77	-108 32	80 53
0 0060	89 83	0 69	0 10	0 01	0 0020	6 05	1 68	38 57	10 59
0 0056	81 59	0 63	0 09	0 01	0 0012	5 97	1 64	38 04	10 36
0 0075	93 48	1 57	0 09	0 01	0 0014	4 22	2 02	27 01	12 84
0 0041	72 97	3 99	0 11	0 01	0 0012	5 59	1 19	35 69	7 53
0 0012	70 59	13 11	0 10	0 04	0 0005	5 59	0 33	35 68	2 11
0 0007	54 76	15 69	0 12	0 05	0 0004	5 47	0 20	34 93	1 27
0 0003	17 95	15 48	0 27	0 05	0 0010	5 46	0 14	34 82	0 86
0 0004	9 94	16 94	0 23	0 05	0 0007	5 69	0 12	36 27	0 77
0 0023	8 63	20 96	0 26	0 05	0 0011	6 03	0 68	38 41	4 30
0 0079	15 72	22 22	0 48	0 06	0 0032	6 19	2 37	39 47	14 92
0 0072	-0 66	20 40	0 35	0 06	0 0018	7 51	2 14	47 76	13 43

Table 2R 5
continued

Integrated	22 59	0 12	8 20	0 0582	0 06

k-FELDSPAR

North of the Denali Fault

01PAN FS#L2 FIGURE 2R 20

Weighted average of J from standards = 3 571e-03 +/- 1 656e-05

Laser Power (mW)	Cumulative 39Ar	40Ar/39Ar measured	+/-	37Ar/39Ar measured	+/-	36Ar/39Ar measured	+/-
400	0 01	121 65	2 59	0 02	0 1269	0 40	
600	0 12	6 91	0 02	0 07	0 0093	0 01	
800	0 26	5 90	0 02	0 09	0 0070	0 00	
1000	0 36	5 83	0 02	0 12	0 0095	0 00	
1300	0 44	5 89	0 03	0 17	0 0118	0 00	
1600	0 49	5 83	0 03	0 22	0 0192	0 00	
2000	0 54	5 81	0 04	0 14	0 0193	0 00	
2500	0 58	6 04	0 06	0 09	0 0160	0 00	
3000	0 62	5 99	0 04	0 06	0 0250	0 00	
4000	0 68	6 52	0 04	0 04	0 0109	0 00	
5000	0 74	6 70	0 03	0 04	0 0146	0 00	
6000	0 81	6 73	0 03	0 04	0 0101	0 01	
9000	0 89	6 67	0 03	0 05	0 0095	0 00	
5001	0 92	6 80	0 06	0 01	0 0277	0 01	
9001	1 00	6 62	0 03	0 02	0 0108	0 01	
Integrated		7 53	0 01	0 08	0 0036	0 01	

322AST FS#L1 FIGURE 2R 21

0 0005	76 02	15 14	0 11	0 05	0 0004	5 44	0 13	34 73	0 81

	% Atmospheric 40Ar	Ca/K	+/-	Cl/K	+/-	40*/39K	+/-	Age (Ma)	+/- (Ma)
0 0193	97 64	0 03	0 23	0 01	0 0033	2 86	5 10	18 36	32 54
0 0007	33 18	0 13	0 02	0 00	0 0002	4 59	0 22	29 36	1 39
0 0005	13 99	0 16	0 01	0 00	0 0001	5 05	0 15	32 24	0 98
0 0007	13 43	0 21	0 02	0 00	0 0002	5 03	0 22	32 09	1 39
0 0011	19 98	0 32	0 02	0 00	0 0002	4 69	0 33	29 96	2 07
0 0015	16 42	0 40	0 04	0 00	0 0004	4 85	0 44	30 98	2 80
0 0016	21 29	0 27	0 04	0 00	0 0005	4 55	0 47	29 06	2 98
0 0031	-1 68	0 16	0 03	0 00	0 0006	6 12	0 91	38 98	5 76
0 0030	4 50	0 11	0 05	0 00	0 0008	5 69	0 89	36 31	5 63
0 0021	7 96	0 07	0 02	0 00	0 0004	5 97	0 61	38 07	3 83
0 0020	18 13	0 07	0 03	0 00	0 0004	5 46	0 58	34 84	3 65
0 0017	25 48	0 08	0 02	0 00	0 0004	4 99	0 49	31 89	3 09
0 0016	15 26	0 09	0 02	0 00	0 0004	5 63	0 49	35 91	3 07
0 0024	31 44	0 03	0 05	0 00	0 0006	4 64	0 70	29 67	4 45
0 0015	27 01	0 03	0 02	0 00	0 0003	4 81	0 43	30 73	2 75
0 0004	32 55	0 15	0 01	0 00	0 0001	5 06	0 12	32 32	0 80

Table 2R 5 continued

Weighted average of J from standards = 3 411e-03 +/- 1 051e-05

Laser Power (mW)	Cumulative 39Ar	40Ar/39Ar measured	+/-	37Ar/39Ar measured	+/-	36Ar/39Ar measured	+/-
400	0 01	96 20	0 59	0 06	0 0050	0 31	
600	0 05	12 65	0 03	0 05	0 0009	0 03	
800	0 11	7 14	0 03	0 02	0 0009	0 01	
1000	0 15	5 99	0 03	0 01	0 0006	0 00	
1300	0 20	6 59	0 03	0 01	0 0006	0 00	
1600	0 24	6 37	0 04	0 01	0 0010	0 00	
2000	0 28	6 35	0 04	0 01	0 0030	0 00	
2500	0 31	6 76	0 05	0 01	0 0014	0 01	
3000	0 34	6 30	0 06	0 02	0 0017	0 01	
4000	0 38	6 94	0 03	0 02	0 0013	0 01	
5000	0 43	7 08	0 04	0 02	0 0013	0 01	
6000	0 49	7 21	0 02	0 02	0 0008	0 01	
9000	0 53	7 23	0 04	0 01	0 0013	0 01	
9001	1 00	6 76	0 03	0 01	0 0002	0 01	
Integrated		7 74	0 02	0 01	0 0002	0 01	

DT45 FS#F1 FIGURE 2R 22

Weighted average of J from standards = 3 571e-03 +/- 1 656e-05

Temp (deg C)	Cumulative 39Ar	40Ar/39Ar measured	+/-	37Ar/39Ar measured	+/-	36Ar/39Ar measured	+/-
300	0 00	740 53	13 58	0 01	0 0292	2 34	
300	0 00	386 69	6 09	0 04	0 0362	1 10	
350	0 00	161 01	1 57	0 01	0 0124	0 25	

	% Atmospheric 40Ar	Ca/K	+/-	Cl/K	+/-	40*/39K	+/-	Age (Ma)	+/- (Ma)
0 0032	93 97	0 11	0 01	0 00	0 0006	5 80	0 80	35 37	4 85
0 0009	63 32	0 08	0 00	0 00	0 0001	4 63	0 27	28 26	1 62
0 0006	34 25	0 04	0 00	0 00	0 0001	4 68	0 16	28 56	0 99
0 0005	15 14	0 02	0 00	0 00	0 0001	5 06	0 14	30 86	0 85
0 0003	22 31	0 02	0 00	0 00	0 0001	5 10	0 10	31 10	0 62
0 0005	16 88	0 02	0 00	0 00	0 0002	5 27	0 14	32 16	0 84
0 0005	22 10	0 03	0 01	0 00	0 0002	4 92	0 15	30 04	0 89
0 0005	30 08	0 02	0 00	0 00	0 0002	4 70	0 15	28 72	0 89
0 0007	25 88	0 03	0 00	0 00	0 0002	4 65	0 21	28 36	1 25
0 0004	29 92	0 03	0 00	0 00	0 0001	4 84	0 13	29 55	0 81
0 0005	34 17	0 03	0 00	0 00	0 0002	4 64	0 14	28 32	0 85
0 0004	32 06	0 03	0 00	0 00	0 0001	4 88	0 11	29 78	0 64
0 0005	35 02	0 02	0 00	0 00	0 0001	4 68	0 16	28 57	0 97
0 0001	22 24	0 02	0 00	0 00	0 0000	5 24	0 03	31 94	0 18
0 0001	34 69	0 03	0 00	0 00	0 0000	5 04	0 03	30 73	0 20

	% Atmospheric 40Ar	Ca/K	+/-	Cl/K	+/-	40*/39K	+/-	Age (Ma)	+/- (Ma)
0 0488	93 57	0 02	0 05	0 02	0 0018	47 63	9 70	283 43	53 41
0 0200	84 18	0 07	0 07	0 02	0 0009	61 17	3 54	356 47	18 74
0 0034	45 02	0 01	0 02	0 03	0 0006	88 50	1 45	495 47	7 08

Table 2R 5
continued

350	0 00	78 26	0 85	0 02	0 0454	0 24	0 0052
400	0 00	77 94	0 42	0 02	0 0048	0 10	0 0015
400	0 00	12 95	0 08	0 01	0 0052	0 04	0 0008
450	0 01	25 14	0 13	0 01	0 0028	0 04	0 0006
450	0 01	5 68	0 02	0 02	0 0024	0 01	0 0004
500	0 02	13 88	0 07	0 02	0 0010	0 02	0 0003
500	0 02	4 19	0 01	0 02	0 0027	0 01	0 0003
550	0 03	6 87	0 03	0 03	0 0011	0 01	0 0002
550	0 04	4 08	0 02	0 04	0 0020	0 01	0 0002
600	0 05	9 53	0 05	0 04	0 0012	0 02	0 0002
600	0 05	3 48	0 02	0 05	0 0014	0 00	0 0001
650	0 06	4 01	0 01	0 04	0 0011	0 00	0 0001
650	0 07	3 39	0 01	0 02	0 0013	0 00	0 0001
700	0 08	3 34	0 02	0 02	0 0010	0 00	0 0001
700	0 09	3 16	0 01	0 02	0 0009	0 00	0 0001
750	0 09	3 70	0 03	0 01	0 0011	0 00	0 0002
750	0 10	5 22	0 02	0 01	0 0010	0 01	0 0002
800	0 10	4 23	0 02	0 01	0 0016	0 01	0 0002
800	0 11	3 84	0 02	0 01	0 0011	0 00	0 0002
850	0 12	4 59	0 02	0 02	0 0026	0 00	0 0002
850	0 12	4 32	0 01	0 01	0 0017	0 00	0 0002
900	0 13	5 81	0 02	0 01	0 0010	0 01	0 0002
950	0 14	6 33	0 04	0 01	0 0009	0 01	0 0001
1000	0 17	6 22	0 01	0 01	0 0004	0 01	0 0001
1000	0 21	5 38	0 01	0 01	0 0003	0 00	0 0000
1000	0 24	5 22	0 01	0 01	0 0003	0 00	0 0000
1050	0 27	6 01	0 02	0 01	0 0003	0 00	0 0000
1050	0 32	5 45	0 02	0 01	0 0002	0 00	0 0000
1050	0 36	5 30	0 01	0 01	0 0003	0 00	0 0000

91 69	0 03	0 08	0 00	0 0008	6 50	1 41	41 41	8 85
39 01	0 03	0 01	0 02	0 0002	47 52	0 52	282 79	2 86
81 53	0 02	0 01	0 00	0 0002	2 39	0 24	15 31	1 54
41 25	0 02	0 01	0 01	0 0001	14 75	0 19	92 61	1 19
64 06	0 03	0 00	0 00	0 0001	2 03	0 11	13 03	0 73
37 78	0 03	0 00	0 00	0 0000	8 61	0 10	54 67	0 60
51 82	0 04	0 00	0 00	0 0001	2 00	0 08	12 87	0 48
36 57	0 05	0 00	0 00	0 0001	4 34	0 06	27 75	0 40
47 33	0 07	0 00	0 00	0 0000	2 14	0 06	13 70	0 36
51 94	0 08	0 00	0 00	0 0000	4 56	0 07	29 17	0 41
31 43	0 08	0 00	0 00	0 0001	2 36	0 04	15 16	0 28
25 07	0 07	0 00	0 00	0 0000	2 98	0 04	19 09	0 24
18 85	0 03	0 00	0 00	0 0000	2 72	0 03	17 46	0 21
22 05	0 03	0 00	0 00	0 0001	2 58	0 04	16 53	0 25
19 57	0 03	0 00	0 00	0 0000	2 52	0 04	16 15	0 26
30 20	0 03	0 00	0 00	0 0000	2 57	0 06	16 45	0 37
46 19	0 02	0 00	0 00	0 0000	2 79	0 05	17 91	0 29
36 32	0 03	0 00	0 00	0 0001	2 68	0 05	17 16	0 35
25 23	0 02	0 00	0 00	0 0000	2 85	0 06	18 28	0 36
32 09	0 03	0 00	0 00	0 0001	3 09	0 05	19 82	0 32
26 00	0 02	0 00	0 00	0 0001	3 18	0 05	20 35	0 30
32 39	0 02	0 00	0 00	0 0000	3 91	0 06	25 00	0 39
30 20	0 02	0 00	0 00	0 0000	4 40	0 05	28 11	0 29
24 83	0 01	0 00	0 00	0 0000	4 65	0 02	29 72	0 14
16 72	0 01	0 00	0 00	0 0000	4 45	0 02	28 46	0 11
13 82	0 01	0 00	0 00	0 0000	4 47	0 02	28 57	0 10
14 41	0 01	0 00	0 00	0 0000	5 11	0 02	32 66	0 11
12 46	0 01	0 00	0 00	0 0000	4 74	0 02	30 30	0 12
10 78	0 01	0 00	0 00	0 0000	4 70	0 02	30 02	0 10

Table 2R 5
continued

1100	0 40	5 59	0 01	0 01	0 0002	0 00
1200	0 86	5 56	0 01	0 00	0 0000	0 00
1600	1 00	5 67	0 01	0 00	0 0001	0 00
Integrated		6 09	0 00	0 01	0 0001	0 00

37NEN FS#F1 FIGUREA23

Weighted average of J from standards = 3 493e-03 +/- 6 366e-06

Temp (deg C)	Cumulative 39Ar	40Ar/39Ar measured	+/-	37Ar/39Ar measured	+/-	36Ar/39Ar measured	+/-
300	0 00	223 20	0 77	0 00	0 0086	0 46	
300	0 01	47 02	0 15	0 01	0 0045	0 08	
350	0 02	25 50	0 09	0 01	0 0015	0 04	
350	0 03	6 29	0 03	0 03	0 0023	0 01	
400	0 03	10 88	0 07	0 03	0 0028	0 02	
400	0 04	5 15	0 02	0 05	0 0022	0 01	
450	0 04	6 15	0 06	0 06	0 0055	0 01	
450	0 05	5 61	0 02	0 05	0 0017	0 01	
500	0 06	7 07	0 03	0 06	0 0035	0 02	
500	*0 07*	*3 67*	*0 01*	*0 04*	*0 0024*	*0 01*	
550	0 08	3 48	0 03	0 02	0 0087	0 00	
550	0 09	4 24	0 02	0 02	0 0015	0 00	
600	0 09	3 74	0 03	0 02	0 0049	0 00	
600	0 10	3 63	0 02	0 03	0 0033	0 00	
650	0 11	9 02	0 04	0 03	0 0026	0 02	
650	0 12	3 97	0 02	0 03	0 0014	0 00	
700	0 13	4 42	0 02	0 02	0 0022	0 00	
750	0 13	4 74	0 04	0 01	0 0124	0 01	

0 0000	9 73	0 01	0 00	0 00	0 0000	5 02	0 02	32 07	0 10
0 0000	8 36	0 01	0 00	0 00	0 0000	5 07	0 01	32 36	0 04
0 0000	15 65	0 01	0 00	0 00	0 0000	4 76	0 01	30 39	0 08
0 0000	19 04	0 01	0 00	0 00	0 0000	4 90	0 00	31 32	0 15

% Atmospheric 40Ar		Ca/K	+/-	Cl/K	+/-	40*/39K	+/-	Age (Ma)	+/- (Ma)
0 0035	60 65	-0 01	0 02	0 02	0 0004	87 81	0 98	482 60	4 75
0 0005	50 70	0 02	0 01	0 01	0 0001	23 16	0 14	140 35	0 82
0 0002	48 27	0 02	0 00	0 00	0 0001	13 18	0 07	81 17	0 43
0 0003	70 43	0 05	0 00	0 00	0 0001	1 85	0 09	11 63	0 55
0 0003	55 68	0 06	0 01	0 00	0 0001	4 81	0 09	30 05	0 56
0 0002	64 45	0 09	0 00	0 00	0 0000	1 82	0 05	11 43	0 32
0 0003	59 26	0 10	0 01	0 00	0 0001	2 49	0 10	15 63	0 61
0 0002	66 67	0 10	0 00	0 00	0 0000	1 86	0 05	11 68	0 31
0 0003	68 15	0 11	0 01	0 00	0 0001	2 24	0 08	14 07	0 51
0 0001	*42 51*	*0 07*	*0 00*	*0 00*	*0 0000*	*2 09*	*0 03*	*13 14*	*0 20*
0 0003	19 77	0 04	0 02	0 00	0 0001	2 77	0 10	17 35	0 60
0 0001	26 23	0 05	0 00	0 00	0 0000	3 10	0 03	19 46	0 19
0 0003	21 71	0 04	0 01	0 00	0 0001	2 90	0 11	18 19	0 66
0 0001	26 72	0 05	0 01	0 00	0 0000	2 64	0 04	16 53	0 26
0 0004	69 92	0 05	0 00	0 00	0 0001	2 70	0 11	16 96	0 70
0 0001	32 21	0 05	0 00	0 00	0 0000	2 67	0 03	16 76	0 19
0 0002	32 21	0 03	0 00	0 00	0 0001	2 98	0 05	18 66	0 34
0 0002	32 53	0 03	0 02	0 00	0 0001	3 18	0 08	19 90	0 48

Table 2R 5
continued

750	0 14	5 23	0 02	0 01	0 0031	0 01
800	0 15	6 02	0 03	0 02	0 0021	0 01
800	0 16	4 97	0 02	0 01	0 0019	0 01
850	0 17	5 21	0 02	0 02	0 0042	0 01
850	0 18	4 90	0 02	0 02	0 0021	0 01
900	0 19	5 70	0 03	0 02	0 0019	0 01
950	0 21	5 61	0 02	0 02	0 0010	0 00
1000	0 26	5 44	0 02	0 01	0 0004	0 00
1000	0 33	5 03	0 02	0 01	0 0002	0 00
1000	0 38	5 08	0 02	0 01	0 0003	0 00
1050	0 42	5 74	0 01	0 01	0 0008	0 00
1050	0 47	5 63	0 02	0 01	0 0003	0 00
1050	0 52	11 33	0 06	0 01	0 0003	0 02
1200	0 98	5 73	0 01	0 01	0 0001	0 00
1600	1 00	11 72	0 03	0 12	0 0013	0 02
Integrated		6 77	0 00	0 01	0 0001	0 01

32NEN FS#F1 FIGURE 2R 24

Weighted average of J from standards = 3 493e-03 +/- 6 366e-06

Step	T (C)	t (min)	39Ar (mol)	+/-	Cum 39Ar	Age (Ma)	+/-
1	350 00	12 00	0 00	0 00	0 0726	90 07	
2	350 00	40 00	0 00	0 00	0 1767	139 26	
3	400 00	12 00	0 00	0 00	0 3580	84 99	
4	400 00	40 00	0 00	0 00	0 5694	12 76	
5	450 00	12 00	0 00	0 00	1 1829	46 95	
6	450 00	40 00	0 00	0 00	1 7471	8 40	
7	500 00	12 00	0 00	0 00	2 4027	7 84	

0 0001	37 47	0 02	0 01	0 00	0 0000	3 25	0 04	20 37	0 27
0 0002	41 18	0 03	0 00	0 00	0 0000	3 52	0 05	22 07	0 31
0 0001	30 39	0 02	0 00	0 00	0 0000	3 44	0 04	21 55	0 24
0 0001	31 81	0 03	0 01	0 00	0 0000	3 53	0 04	22 12	0 22
0 0001	30 76	0 03	0 00	0 00	0 0000	3 37	0 03	21 13	0 17
0 0001	31 25	0 04	0 00	0 00	0 0000	3 90	0 04	24 39	0 28
0 0001	24 50	0 03	0 00	0 00	0 0000	4 22	0 03	26 37	0 17
0 0000	18 36	0 02	0 00	0 00	0 0000	4 42	0 02	27 65	0 13
0 0000	14 98	0 02	0 00	0 00	0 0000	4 25	0 02	26 59	0 10
0 0000	13 06	0 01	0 00	0 00	0 0000	4 39	0 02	27 45	0 12
0 0000	11 87	0 02	0 00	0 00	0 0000	5 03	0 01	31 44	0 09
0 0000	11 66	0 02	0 00	0 00	0 0000	4 95	0 02	30 92	0 11
0 0002	57 43	0 02	0 00	0 00	0 0000	4 81	0 06	30 07	0 35
0 0000	6 70	0 01	0 00	0 00	0 0000	5 32	0 01	33 21	0 04
0 0001	44 88	0 21	0 00	0 00	0 0000	6 45	0 03	40 17	0 20
0 0000	25 46	0 03	0 00	0 00	0 0000	5 02	0 01	31 36	0 07

Model Age	Cl age	+/-
3 6600	3 66	7 28	3 66
3 4800	3 48	7 28	3 48
1 6200	1 62	7 28	1 62
0 8500	0 85	7 28	0 85
0 4200	0 42	7 28	0 42
0 2900	0 29	7 28	0 29
0 2900	0 29	7 28	0 29

Table 2R 5
continued

8	500 00	40 00	0 00	0 00	3 1005	7 28	0 2400
9	550 00	12 00	0 00	0 00	4 1263	15 79	0 2500
10	550 00	40 00	0 00	0 00	5 0050	7 45	0 2200
11	600 00	12 00	0 00	0 00	6 5598	20 53	0 2400
12	600 00	40 00	0 00	0 00	7 7467	8 01	0 1200
13	650 00	12 00	0 00	0 00	8 9962	10 91	0 1100
14	650 00	40 00	0 00	0 00	9 7627	11 73	0 1700
15	700 00	12 00	0 00	0 00	10 3926	9 59	0 2200
16	700 00	40 00	0 00	0 00	11 1267	9 63	0 1600
17	750 00	12 00	0 00	0 00	11 7868	9 88	0 2700
18	750 00	40 00	0 00	0 00	12 7606	10 34	0 1500
19	800 00	12 00	0 00	0 00	13 6988	11 88	0 1500
20	800 00	40 00	0 00	0 00	14 9349	12 54	0 1400
21	850 00	12 00	0 00	0 00	16 1319	14 92	0 1300
22	850 00	40 00	0 00	0 00	17 8026	14 87	0 1500
23	900 00	12 00	0 00	0 00	19 8026	17 58	0 1300
24	950 00	12 00	0 00	0 00	24 4570	17 55	0 0600
25	1000 00	12 00	0 00	0 00	33 4985	18 25	0 0900
26	1000 00	40 00	0 00	0 00	41 6534	19 31	0 0800
27	1000 00	60 00	0 00	0 00	46 5471	21 61	0 0900
28	1050 00	12 00	0 00	0 00	50 6085	23 89	0 1100
29	1050 00	40 00	0 00	0 00	56 2124	24 34	0 1100
30	1050 00	60 00	0 00	0 00	60 1605	25 52	0 1000
31	1075 00	12 00	0 00	0 00	62 0542	26 91	0 1400
32	1100 00	12 00	0 00	0 00	67 0002	27 47	0 1000
33	1200 00	12 00	0 00	0 00	96 8531	28 25	0 0300
34	1600 00	40 00	0 00	0 00	99 9900	29 97	0 2700

FIGURE 2R 25

0 24	7 28	0 24
0 25	7 37	0 25
0 22	7 45	0 22
0 24	7 73	0 24
0 12	8 01	0 12
0 11	8 88	0 11
0 17	8 88	0 17
0 22	9 59	0 22
0 16	9 63	0 16
0 27	9 88	0 27
0 15	10 34	0 15
0 15	11 88	0 15
0 14	12 54	0 14
0 13	14 92	0 13
0 15	14 92	0 15
0 13	17 58	0 13
0 06	17 58	0 06
0 09	18 25	0 09
0 08	19 31	0 08
0 09	21 61	0 09
0 11	23 89	0 11
0 11	24 34	0 11
0 10	25 52	0 10
0 14	26 91	0 14
0 10	27 47	0 10
0 03	28 25	0 03
0 27	29 97	0 27

Table 2R 5
continued
Weighted average of J from standards = 3 579e-03 +/- 1 276e-05

Temp (deg C)	Cumulative 39Ar	40Ar/39Ar measured	+/-	37Ar/39Ar measured	+/-	36Ar/39Ar measured	+/-
300	0 01	418 01	3 08	0 05	0 0333	0 84	
300	0 01	29 10	0 20	0 12	0 0169	0 05	
350	0 03	20 47	0 16	0 42	0 0140	0 02	
350	0 04	7 22	0 04	0 70	0 0155	0 02	
400	0 05	9 50	0 04	1 12	0 0161	0 01	
400	0 06	8 15	0 04	1 32	0 0184	0 01	
450	0 08	11 15	0 04	1 87	0 0220	0 01	
450	0 09	6 86	0 03	1 37	0 0209	0 02	
500	0 10	10 64	0 05	0 44	0 0209	0 02	
500	0 12	4 24	0 02	0 05	0 0102	0 01	
550	0 12	-2 14	0 10	-0 11	0 1281	-0 01	
550	0 13	6 21	0 04	0 00	0 0222	0 01	
600	0 13	1 60	0 05	-0 04	0 0664	0 00	
600	0 14	5 43	0 04	0 00	0 0255	0 01	
650	0 14	3 31	0 04	-0 01	0 0313	0 00	
650	0 15	5 47	0 04	-0 01	0 0231	0 01	
700	0 15	0 98	0 06	0 07	0 0566	-0 01	
700	0 16	4 79	0 05	0 00	0 0310	0 01	
750	0 16	3 08	0 06	0 01	0 0391	0 00	
750	0 17	6 00	0 02	0 00	0 0113	0 01	
800	0 18	6 05	0 04	0 02	0 0196	0 01	
800	0 20	5 57	0 02	0 01	0 0111	0 01	
850	0 21	5 56	0 03	0 04	0 0161	0 00	
850	0 22	6 63	0 03	0 00	0 0127	0 01	
900	0 23	8 49	0 04	0 01	0 0172	0 00	
950	0 25	10 06	0 04	0 00	0 0114	0 00	

	% Atmospheric 40Ar	Ca/K	+/-	Cl/K	+/-	40*/39K	+/-	Age (Ma)	+/- (Ma)
0 0078	59 68	0 09	0 06	0 03	0 0005	168 55	1 89	851 64	7 62
0 0010	50 97	0 21	0 03	0 00	0 0001	14 25	0 33	89 76	2 02
0 0004	32 32	0 78	0 03	0 00	0 0001	13 84	0 16	87 22	1 01
0 0004	68 53	1 28	0 03	0 00	0 0001	2 26	0 12	14 56	0 78
0 0003	32 93	2 06	0 03	0 00	0 0001	6 36	0 10	40 58	0 63
0 0003	48 34	2 43	0 03	0 00	0 0001	4 20	0 09	26 90	0 59
0 0003	36 29	3 44	0 04	0 00	0 0001	7 09	0 09	45 22	0 58
0 0004	67 55	2 51	0 04	0 00	0 0001	2 22	0 11	14 28	0 67
0 0004	45 04	0 80	0 04	0 00	0 0001	5 83	0 13	37 29	0 83
0 0003	46 09	0 09	0 02	0 00	0 0001	2 27	0 08	14 59	0 51
0 0030	162 95	-0 20	0 24	0 00	0 0005	1 36	0 88	8 78	5 65
0 0006	46 47	0 00	0 04	0 00	0 0001	3 31	0 18	21 25	1 12
0 0014	-89 78	-0 07	0 12	0 00	0 0003	2 99	0 42	19 18	2 66
0 0006	47 06	-0 01	0 05	0 00	0 0001	2 86	0 18	18 37	1 17
0 0007	-6 19	-0 01	0 06	0 00	0 0002	3 48	0 20	22 32	1 29
0 0005	50 62	-0 01	0 04	0 00	0 0001	2 68	0 16	17 25	1 03
0 0011	-170 08	0 13	0 10	0 00	0 0002	2 56	0 34	16 44	2 15
0 0005	51 13	0 00	0 06	0 00	0 0001	2 32	0 17	14 95	1 06
0 0008	-10 09	0 02	0 07	0 00	0 0002	3 36	0 25	21 54	1 56
0 0003	40 91	0 01	0 02	0 00	0 0001	3 53	0 08	22 64	0 53
0 0005	38 21	0 03	0 04	0 00	0 0001	3 72	0 14	23 86	0 91
0 0002	38 29	0 02	0 02	0 00	0 0001	3 42	0 07	21 95	0 47
0 0004	12 16	0 08	0 03	0 00	0 0001	4 86	0 13	31 10	0 80
0 0002	24 62	-0 01	0 02	0 00	0 0001	4 98	0 08	31 86	0 48
0 0004	11 25	0 02	0 03	0 00	0 0001	7 51	0 11	47 82	0 68
0 0002	12 99	-0 01	0 02	0 00	0 0001	8 73	0 07	55 52	0 41

Table 2R 5
continued

1000	0 28	11 30	0 07	-0 01	0 0065	0 00
1000	0 33	10 73	0 05	0 00	0 0036	0 00
1000	0 38	10 60	0 06	0 01	0 0080	0 00
1050	0 40	10 87	0 05	0 00	0 0050	0 00
1050	0 45	10 48	0 05	0 00	0 0036	0 00
1050	0 49	11 15	0 05	-0 01	0 0045	0 01
1100	0 52	11 42	0 06	-0 01	0 0051	0 00
1200	0 75	12 02	0 03	0 00	0 0006	0 00
1600	1 00	12 95	0 03	0 00	0 0006	0 01
Integrated		13 41	0 01	0 09	0 0011	0 01

24DEB FS#F1 FIGURE 2R 26

Weighted average of J from standards = 3 571e-03 +/- 1 656e-05

Temp (deg C)	Cumulative 39Ar	40Ar/39Ar measured	+/-	37Ar/39Ar measured	+/-	36Ar/39Ar measured	+/-
350	0 01	23 69	0 41	0 03	0 0057	0 06	
350	0 02	33 72	0 20	0 03	0 0073	0 11	
400	0 04	10 30	0 04	0 05	0 0026	0 02	
400	0 06	14 78	0 08	0 04	0 0033	0 04	
450	0 08	8 10	0 04	0 05	0 0021	0 02	
450	0 11	15 49	0 12	0 06	0 0016	0 05	
500	0 15	6 23	0 03	0 07	0 0029	0 01	
500	0 16	9 90	0 06	0 05	0 0025	0 02	
550	0 19	6 12	0 03	0 03	0 0017	0 01	
550	0 22	11 45	0 06	0 03	0 0017	0 02	
600	0 25	5 89	0 03	0 07	0 0031	0 01	
600	0 26	18 74	0 10	0 05	0 0044	0 05	

0 0002	9 48	-0 01	0 01	0 00	0 0001	10 20	0 09	64 68	0 55
0 0003	11 41	0 00	0 01	0 00	0 0000	9 48	0 10	60 22	0 61
0 0002	13 26	0 01	0 01	0 00	0 0001	9 17	0 08	58 26	0 48
0 0001	6 25	-0 01	0 01	0 00	0 0000	10 16	0 06	64 46	0 40
0 0001	10 82	-0 01	0 01	0 00	0 0000	9 32	0 05	59 17	0 31
0 0001	14 26	-0 01	0 01	0 00	0 0000	9 54	0 06	60 55	0 35
0 0001	5 06	-0 02	0 01	0 00	0 0001	10 81	0 07	68 51	0 46
0 0000	6 95	0 00	0 00	0 00	0 0000	11 15	0 03	70 62	0 16
0 0001	18 26	0 00	0 00	0 00	0 0000	10 56	0 03	66 93	0 19
0 0000	24 68	0 17	0 00	0 00	0 0000	10 08	0 02	63 92	0 25

% Atmospheric 40Ar	Ca/K	+/-	Cl/K	+/-	40*/39K	+/-	Age (Ma)	+/- (Ma)
0 0012	76 81	0 06	0 01	0 00	0 0002	5 49	0 44	35 02	2 75
0 0017	95 17	0 06	0 01	0 00	0 0001	1 63	0 49	10 45	3 13
0 0003	68 82	0 09	0 00	0 00	0 0001	3 20	0 10	20 52	0 62
0 0006	89 02	0 08	0 01	0 00	0 0001	1 62	0 18	10 41	1 17
0 0007	78 84	0 10	0 00	0 00	0 0001	1 71	0 20	10 97	1 28
0 0006	89 64	0 10	0 00	0 00	0 0001	1 60	0 17	10 30	1 11
0 0002	57 86	0 13	0 01	0 00	0 0000	2 61	0 06	16 76	0 40
0 0003	72 25	0 08	0 00	0 00	0 0001	2 74	0 10	17 56	0 63
0 0002	31 59	0 06	0 00	0 00	0 0001	4 17	0 07	26 64	0 42
0 0002	59 18	0 05	0 00	0 00	0 0001	4 66	0 08	29 78	0 49
0 0004	51 54	0 13	0 01	0 00	0 0001	2 84	0 11	18 20	0 67
0 0008	86 50	0 10	0 01	0 00	0 0001	2 53	0 25	16 20	1 58

Table 2R 5
continued

650	0 27	9 38	0 11	0 05	0 0077	0 02
650	0 28	18 52	0 08	0 04	0 0048	0 05
700	0 30	5 87	0 05	0 04	0 0046	0 01
700	0 32	13 70	0 05	0 03	0 0028	0 04
750	0 34	5 82	0 03	0 03	0 0029	0 01
750	0 37	11 65	0 04	0 03	0 0015	0 03
800	0 40	4 24	0 02	0 03	0 0018	0 01
800	0 45	6 61	0 04	0 02	0 0009	0 01
850	0 49	5 66	0 03	0 03	0 0011	0 01
850	0 53	10 01	0 04	0 03	0 0017	0 02
900	0 54	4 37	0 04	0 05	0 0051	0 01
950	0 56	4 19	0 03	0 05	0 0025	0 00
1000	0 60	4 65	0 02	0 05	0 0018	0 00
1000	0 64	9 78	0 06	0 04	0 0019	0 02
1000	0 67	15 71	0 12	0 04	0 0042	0 04
1050	0 69	6 77	0 03	0 03	0 0023	0 01
1050	0 74	9 21	0 07	0 03	0 0013	0 02
1050	0 79	12 47	0 06	0 03	0 0018	0 03
1100	0 83	6 63	0 03	0 03	0 0015	0 01
1200	0 93	6 84	0 03	0 03	0 0007	0 01
1600	1 00	27 19	0 07	0 04	0 0011	0 08
Integrated		10 51	0 01	0 04	0 0004	0 02

22DEB FS#F1 FIGURE 2R 27

Weighted average of J from standards = 3 571e-03 +/- 1 656e-05

Step	T (C)	t (mm)	39Ar (mol)	+/-	Cum 39Ar	Age (Ma)	+/-
1	388 00	14 00	0 00	0 00	0 0421	800 33	

0 0012	69 07	0 09	0 01	0 00	0 0002	2 89	0 35	18 54	2 22
0 0005	83 54	0 07	0 01	0 00	0 0001	3 04	0 16	19 50	1 03
0 0005	59 31	0 07	0 01	0 00	0 0001	2 38	0 17	15 24	1 07
0 0006	82 39	0 05	0 01	0 00	0 0001	2 41	0 16	15 44	1 05
0 0005	57 93	0 06	0 01	0 00	0 0001	2 43	0 14	15 62	0 88
0 0005	77 05	0 05	0 00	0 00	0 0001	2 67	0 13	17 09	0 86
0 0003	43 48	0 05	0 00	0 00	0 0001	2 38	0 09	15 28	0 60
0 0003	63 95	0 03	0 00	0 00	0 0000	2 37	0 08	15 22	0 52
0 0002	54 40	0 06	0 00	0 00	0 0000	2 57	0 07	16 48	0 45
0 0003	73 01	0 06	0 00	0 00	0 0000	2 69	0 08	17 27	0 52
0 0005	34 03	0 09	0 01	0 00	0 0001	2 87	0 16	18 37	0 99
0 0002	24 38	0 10	0 00	0 00	0 0001	3 14	0 08	20 15	0 48
0 0003	24 53	0 08	0 00	0 00	0 0001	3 49	0 09	22 34	0 60
0 0003	64 58	0 07	0 00	0 00	0 0001	3 45	0 09	22 11	0 55
0 0006	75 75	0 07	0 01	0 00	0 0001	3 80	0 18	24 34	1 14
0 0003	39 81	0 06	0 00	0 00	0 0001	4 06	0 08	25 95	0 53
0 0002	55 68	0 06	0 00	0 00	0 0000	4 07	0 07	26 02	0 46
0 0003	67 21	0 05	0 00	0 00	0 0001	4 08	0 10	26 10	0 64
0 0002	35 63	0 05	0 00	0 00	0 0001	4 25	0 06	27 16	0 41
0 0001	38 41	0 06	0 00	0 00	0 0000	4 20	0 03	26 84	0 21
0 0004	85 60	0 08	0 00	0 00	0 0000	3 91	0 10	25 03	0 63
0 0001	68 64	0 07	0 00	0 00	0 0000	3 29	0 02	21 06	0 16

	Model Age	Cl age	+/-
10 7900	10 79	6 85	10 79

Table 2R 5
continued

2	371 00	41 00	0 00	0 00	0 0691	159 65	16 1500
3	435 00	13 00	0 00	0 00	0 1567	269 91	3 9800
4	421 00	40 00	0 00	0 00	0 2619	26 77	2 8200
5	485 00	13 00	0 00	0 00	0 5272	66 64	1 2300
6	471 00	40 00	0 00	0 00	0 8400	9 16	1 0800
7	535 00	13 00	0 00	0 00	1 4225	29 00	0 5800
8	522 00	40 00	0 00	0 00	1 9737	7 36	0 4800
9	588 00	12 00	0 00	0 00	2 8952	14 76	0 2700
10	571 00	40 00	0 00	0 00	3 9694	7 07	0 2600
11	637 00	12 00	0 00	0 00	5 4505	19 21	0 3800
12	623 00	40 00	0 00	0 00	7 4160	6 85	0 1500
13	685 00	13 00	0 00	0 00	9 4076	9 79	0 1200
14	671 00	40 00	0 00	0 00	11 6049	9 64	0 1100
15	736 00	12 00	0 00	0 00	13 1675	9 67	0 1300
16	721 00	40 00	0 00	0 00	14 7610	7 68	0 1300
17	783 00	12 00	0 00	0 00	16 0041	9 02	0 1000
18	770 00	40 00	0 00	0 00	17 4461	8 52	0 1200
19	834 00	12 00	0 00	0 00	18 6284	10 43	0 2600
20	824 00	40 00	0 00	0 00	19 6292	9 59	0 1600
21	883 00	12 00	0 00	0 00	20 3617	11 26	0 3300
22	870 00	40 00	0 00	0 00	21 5865	11 73	0 2200
23	931 00	12 00	0 00	0 00	22 6121	14 23	0 4000
24	980 00	12 00	0 00	0 00	25 7339	17 44	0 1800
25	1015 00	12 00	0 00	0 00	27 2675	18 65	0 1300
26	1008 00	40 00	0 00	0 00	30 9644	21 07	0 1100
27	1006 00	60 00	0 00	0 00	34 0756	21 89	0 1300
28	1061 00	12 00	0 00	0 00	36 7647	22 64	0 1600
29	1056 00	40 00	0 00	0 00	44 8164	22 20	0 0700
30	1056 00	60 00	0 00	0 00	50 9240	23 96	0 0700

16 15	6 85	16 15
3 98	6 85	3 98
2 82	6 85	2 82
1 23	6 85	1 23
1 08	6 85	1 08
0 58	6 85	0 58
0 48	6 85	0 48
0 27	6 85	0 27
0 26	6 85	0 26
0 38	6 85	0 38
0 15	6 85	0 15
0 12	7 27	0 12
0 11	7 27	0 11
0 13	7 27	0 13
0 13	7 68	0 13
0 10	8 10	0 10
0 12	8 52	0 12
0 26	9 06	0 26
0 16	9 59	0 16
0 33	11 26	0 33
0 22	11 73	0 22
0 40	14 23	0 40
0 18	17 44	0 18
0 13	18 65	0 13
0 11	21 07	0 11
0 13	21 89	0 13
0 16	22 64	0 16
0 07	22 64	0 07
0 07	23 96	0 07

Table 2R 5
continued

31	1111 00	12 00	0 00	0 00	55 3437	26 75
32	1200 00	12 00	0 00	0 00	91 4722	33 12
33	1553 00	60 00	0 00	0 00	99 9900	27 31

03BAL FS#F1 FIGURE 2R 28

Weighted average of J from standards = 3 507e-03 +/- 1 639e-05

Step	T (C)	t (min)	39Ar (mol)	+/-	Cum 39Ar	Age (Ma)	+/-
1	321 00	41 00	0 00	0 00	0 0223	701 83	
2	382 00	14 00	0 00	0 00	0 0720	790 34	
3	370 00	41 00	0 00	0 00	0 1201	37 21	
4	436 00	12 00	0 00	0 00	0 2903	104 31	
5	421 00	40 00	0 00	0 00	0 5107	13 73	
6	485 00	13 00	0 00	0 00	0 7370	22 99	
7	469 00	40 00	0 00	0 00	1 5646	15 01	
8	534 00	12 00	0 00	0 00	2 4430	18 01	
9	520 00	40 00	0 00	0 00	3 5615	11 14	
10	582 00	12 00	0 00	0 00	5 5224	19 38	
11	569 00	40 00	0 00	0 00	7 5852	13 36	
12	631 00	12 00	0 00	0 00	9 2937	14 77	
13	619 00	40 00	0 00	0 00	11 1685	14 88	
14	679 00	12 00	0 00	0 00	12 8640	15 13	
15	667 00	40 00	0 00	0 00	14 7306	14 85	
16	729 00	12 00	0 00	0 00	15 9633	16 23	
17	718 00	40 00	0 00	0 00	17 7256	15 36	
18	778 00	12 00	0 00	0 00	19 2560	16 06	
19	766 00	40 00	0 00	0 00	21 1849	16 44	
20	828 00	12 00	0 00	0 00	22 8402	16 69	
21	816 00	40 00	0 00	0 00	25 5365	17 01	

0 3000	0 30	26 75	0 30
0 0400	0 04	33 12	0 04
0 1000	0 10	33 12	0 10

Model Age		Cl age	+/-
22 0000	22 00	13 36	0 36
10 3500	10 35	13 36	0 36
8 4900	8 49	13 36	0 36
3 7700	3 77	13 36	0 36
2 3900	2 39	13 36	0 36
2 6600	2 66	13 36	0 36
0 6400	0 64	13 36	0 36
0 8300	0 83	13 36	0 36
0 4500	0 45	13 36	0 36
1 1900	1 19	13 36	0 36
0 3600	0 36	13 36	0 36
0 3000	0 30	14 77	0 30
0 3000	0 30	14 88	0 30
0 3000	0 30	15 13	0 30
0 3700	0 37	14 85	0 37
0 4100	0 41	15 11	0 41
0 3000	0 30	15 36	0 30
0 3500	0 35	16 06	0 35
0 2600	0 26	16 44	0 26
0 3000	0 30	16 69	0 30
0 2200	0 22	17 01	0 22

Table 2R 5
continued

22	877 00	12 00	0 00	0 00	27 4078	17 82
23	867 00	40 00	0 00	0 00	30 4014	17 58
24	925 00	12 00	0 00	0 00	32 7991	19 12
25	976 00	12 00	0 00	0 00	36 6839	19 78
26	1028 00	12 00	0 00	0 00	42 2753	21 36
27	1015 00	40 00	0 00	0 00	51 3528	20 89
28	1011 00	60 00	0 00	0 00	60 2379	20 90
29	1071 00	12 00	0 00	0 00	65 5696	22 71
30	1064 00	40 00	0 00	0 00	71 9592	22 93
31	1061 00	60 00	0 00	0 00	76 1928	23 35
32	1123 00	12 00	0 00	0 00	78 5363	26 04
33	1226 00	12 00	0 00	0 00	95 0496	28 49
34	1567 00	60 00	0 00	0 00	99 9900	28 53

26BAL FS#F1 FIGURE 2R 29

Weighted average of J from standards = 7 125e-03 +/- 1 903e-05

Step	T (C)	t (min)	39Ar (mol)	+/-	Cum 39Ar	Age (Ma)	+/-
1	324 00	42 00	0 00	0 00	0 0492	-13 83	
2	389 00	14 00	0 00	0 00	0 1606	92 37	
3	371 00	41 00	0 00	0 00	0 3597	12 12	
4	437 00	14 00	0 00	0 00	0 9835	14 40	
5	423 00	41 00	0 00	0 00	1 5759	9 98	
6	489 00	13 00	0 00	0 00	2 9637	10 07	
7	473 00	41 00	0 00	0 00	4 2610	7 46	
8	537 00	13 00	0 00	0 00	6 3103	9 08	
9	522 00	41 00	0 00	0 00	7 5293	12 05	
10	585 00	13 00	0 00	0 00	10 5271	16 52	
11	572 00	41 00	0 00	0 00	13 5305	12 90	

0 2600	0 26	17 82	0 26
0 2100	0 21	17 58	0 21
0 2600	0 26	19 12	0 26
0 1900	0 19	19 78	0 19
0 2200	0 22	21 36	0 22
0 1300	0 13	20 89	0 13
0 1300	0 13	20 90	0 13
0 1700	0 17	22 71	0 17
0 2000	0 20	22 93	0 20
0 2500	0 25	23 35	0 25
0 2200	0 22	26 04	0 22
0 0800	0 08	28 49	0 08
0 2000	0 20	28 53	0 20

Model Age	Cl age	+/-	
42 1900	42 19	9 98	3 63
15 4400	15 44	9 98	3 63
10 4400	10 44	9 98	3 63
2 7300	2 73	9 98	3 63
3 6300	3 63	9 98	3 63
1 3300	1 33	10 07	1 33
1 6800	1 68	7 46	1 68
1 7700	1 77	9 08	1 77
1 7100	1 71	12 05	1 71
2 1800	2 18	12 48	2 18
0 6800	0 68	12 90	0 68

Table 2R 5
continued

12	635 00	13 00	0 00	0 00	16 0924	17 28
13	622 00	40 00	0 00	0 00	18 3961	17 05
14	684 00	13 00	0 00	0 00	19 7322	13 59
15	671 00	41 00	0 00	0 00	21 2628	14 52
16	736 00	12 00	0 00	0 00	22 5988	18 20
17	721 00	40 00	0 00	0 00	24 6764	17 43
18	785 00	13 00	0 00	0 00	26 1999	18 11
19	772 00	41 00	0 00	0 00	28 6713	18 81
20	834 00	13 00	0 00	0 00	30 4223	18 32
21	821 00	41 00	0 00	0 00	33 2646	18 94
22	885 00	12 00	0 00	0 00	35 8384	19 19
23	870 00	40 00	0 00	0 00	38 7695	19 42
24	935 00	13 00	0 00	0 00	41 1054	18 39
25	984 00	12 00	0 00	0 00	44 1825	21 51
26	1035 00	12 00	0 00	0 00	48 6177	21 29
27	1019 00	40 00	0 00	0 00	54 0435	22 37
28	1013 00	60 00	0 00	0 00	58 0735	22 65
29	1080 00	13 00	0 00	0 00	60 6320	24 55
30	1068 00	40 00	0 00	0 00	65 7610	24 77
31	1063 00	60 00	0 00	0 00	69 9369	25 39
32	1132 00	12 00	0 00	0 00	72 4514	27 25
33	1219 00	13 00	0 00	0 00	91 2301	27 15
34	1576 00	40 00	0 00	0 00	99 9900	24 60

18BAL FS#F2 FIGURE 2R 30

Weighted average of J from standards = 3 507e-03 +/- 1 639e-05

Step	T (C)	t (mn)	39Ar (mol)	+/-	Cum 39Ar	Age (Ma)	+/-
1	323 00	41 00	0 00	0 00	0 1536	109 77	

0 9400	0 94	13 25	0 94
0 6900	0 69	13 25	0 69
1 2500	1 25	13 59	1 25
1 4200	1 42	14 52	1 42
3 0400	3 04	15 98	3 04
0 7600	0 76	17 43	0 76
1 2400	1 24	18 11	1 24
0 8600	0 86	18 81	0 86
0 9600	0 96	18 32	0 96
0 9200	0 92	18 94	0 92
0 8000	0 80	19 19	0 80
0 6500	0 65	19 42	0 65
2 0400	2 04	18 39	2 04
0 6700	0 67	21 51	0 67
0 4800	0 48	21 29	0 48
0 5600	0 56	22 37	0 56
0 7900	0 79	22 65	0 79
0 7800	0 78	24 55	0 78
0 4800	0 48	24 77	0 48
0 7600	0 76	25 39	0 76
1 0100	1 01	27 25	1 01
0 2500	0 25	27 15	0 25
2 2400	2 24	24 60	2 24

	Model Age	Cl age	+/-
9 3500	9 35	8 06	9 35

Table 2R 5 continued

2	387 00	13 00	0 00	0 00	0 4914	206 39	4 8300
3	373 00	41 00	0 00	0 00	0 8904	11 06	2 9100
4	437 00	13 00	0 00	0 00	2 3231	66 92	0 9300
5	424 00	40 00	0 00	0 00	3 9168	8 06	0 5100
6	488 00	13 00	0 00	0 00	6 1337	17 87	0 6600
7	473 00	40 00	0 00	0 00	8 5621	10 11	0 3400
8	537 00	12 00	0 00	0 00	11 6724	18 42	0 3300
9	523 00	40 00	0 00	0 00	14 5208	8 58	0 2100
10	588 00	13 00	0 00	0 00	16 9074	12 03	0 8100
11	574 00	40 00	0 00	0 00	19 8465	9 39	0 2400
12	605 00	12 00	0 00	0 00	20 9035	9 91	0 4300
13	621 00	40 00	0 00	0 00	24 8574	11 90	0 2400
14	680 00	12 00	0 00	0 00	27 6609	12 88	0 2300
15	668 00	41 00	0 00	0 00	30 6401	11 48	0 2300
16	733 00	12 00	0 00	0 00	32 2314	12 17	0 3100
17	720 00	40 00	0 00	0 00	34 6724	12 22	0 5200
18	783 00	12 00	0 00	0 00	36 3179	13 46	0 8800
19	770 00	40 00	0 00	0 00	38 9770	13 22	0 2700
20	832 00	12 00	0 00	0 00	40 5207	13 49	0 5300
21	819 00	40 00	0 00	0 00	42 6905	13 24	0 3100
22	886 00	12 00	0 00	0 00	44 2883	14 81	0 4900
23	871 00	40 00	0 00	0 00	46 6458	13 91	0 3500
24	934 00	12 00	0 00	0 00	48 3047	15 63	0 4100
25	982 00	12 00	0 00	0 00	51 3386	15 58	0 4500
26	992 00	12 00	0 00	0 00	53 1073	15 08	0 3900
27	1015 00	40 00	0 00	0 00	58 3101	15 43	0 2800
28	1013 00	60 00	0 00	0 00	62 0920	15 72	0 3300
29	1081 00	12 00	0 00	0 00	64 3925	17 82	0 4900
30	1065 00	40 00	0 00	0 00	68 8270	17 63	0 2900

4 83	8 06	4 83
2 91	8 06	2 91
0 93	8 06	0 93
0 51	8 06	0 51
0 66	8 58	0 66
0 34	8 58	0 34
0 33	8 58	0 33
0 21	8 58	0 21
0 81	9 04	0 81
0 24	9 39	0 24
0 43	9 91	0 43
0 24	11 90	0 24
0 23	12 88	1 23
0 23	11 48	0 63
0 31	12 17	0 31
0 52	12 22	0 52
0 88	13 46	0 88
0 27	13 22	0 27
0 53	13 49	0 53
0 31	13 24	0 31
0 49	14 81	0 49
0 35	13 91	0 35
0 41	15 63	0 41
0 45	15 58	0 45
0 39	15 08	0 39
0 28	15 43	0 28
0 33	15 72	0 33
0 49	17 82	0 49
0 29	17 63	0 29

Table 2R 5
continued

31	1061 00	60 00	0 00	0 00	73 1116	18 02	0 2000
32	1130 00	12 00	0 00	0 00	77 5489	18 50	0 2600
33	1226 00	12 00	0 00	0 00	94 7572	35 19	14 1000
34	1567 00	40 00	0 00	0 00	99 9900	13 57	2 4300
Integrated		12 26	0 01	0 03	0 0002	0 03	0 0001

03RAP FS#F1 FIGURE 2R 31

Weighted average of J from standards = 3 571e-03 +/- 1 656e-05

Step	T (C)	t (min)	39Ar (mol)	+/-	Cum 39Ar	Age (Ma)	+/-	Model A
1	389 00	14 00	0 00	0 00	0 1316	600 99	4 0200	
2	374 00	41 00	0 00	0 00	0 2428	44 94	3 8400	
3	443 00	13 00	0 00	0 00	0 6169	158 71	1 8700	
4	426 00	40 00	0 00	0 00	1 0653	21 76	0 8100	
5	494 00	13 00	0 00	0 00	1 9726	42 50	0 4900	
6	476 00	40 00	0 00	0 00	3 0847	18 25	0 3300	
7	543 00	13 00	0 00	0 00	4 9062	29 13	0 2400	
8	525 00	40 00	0 00	0 00	6 9400	18 42	0 1800	
9	592 00	13 00	0 00	0 00	9 4028	25 29	0 2500	
10	575 00	40 00	0 00	0 00	11 6958	19 18	0 1600	
11	642 00	12 00	0 00	0 00	13 7661	31 43	0 3200	
12	625 00	40 00	0 00	0 00	15 8000	21 15	0 2100	
13	690 00	13 00	0 00	0 00	17 0794	28 37	0 3300	
14	674 00	40 00	0 00	0 00	18 2879	22 20	0 3600	
15	739 00	12 00	0 00	0 00	19 3664	21 67	0 3200	
16	723 00	40 00	0 00	0 00	20 7372	20 48	0 2700	
17	788 00	12 00	0 00	0 00	21 9701	21 74	0 3400	
18	771 00	40 00	0 00	0 00	23 6427	20 83	0 2200	

0 20	18 02	0 20						
0 26	18 50	0 26						
14 10	35 19	14 10						
2 43	13 57	2 43						
77 90	0 06	0 00	0 00	0 0000	2 70	0 02	17 02	0 15

Age	Cl age	+/-
4 02	18 25	4 02
3 84	18 25	3 84
1 87	18 25	1 87
0 81	18 25	0 81
0 49	18 25	0 49
0 33	18 25	0 33
0 24	18 34	0 24
0 18	18 42	0 18
0 25	18 80	0 25
0 16	19 18	0 16
0 32	20 17	0 32
0 21	21 15	0 21
0 33	21 15	0 33
0 36	21 41	0 36
0 32	21 67	0 32
0 27	21 67	0 27
0 34	21 74	0 34
0 22	21 74	0 22

Table 2R 5
continued

19	836 00	12 00	0 00	0 00	25 1950	22 15
20	821 00	40 00	0 00	0 00	27 3770	21 78
21	884 00	12 00	0 00	0 00	29 3113	23 74
22	870 00	40 00	0 00	0 00	32 1655	23 06
23	921 00	12 00	0 00	0 00	34 1069	27 31
24	982 00	12 00	0 00	0 00	39 0805	30 30
25	1036 00	12 00	0 00	0 00	49 8104	32 55
26	1023 00	40 00	0 00	0 00	61 6587	31 99
27	1016 00	60 00	0 00	0 00	67 1037	32 62
28	1069 00	12 00	0 00	0 00	69 2830	37 09
29	1070 00	40 00	0 00	0 00	74 9559	39 77
30	1067 00	60 00	0 00	0 00	79 2536	41 72
31	1137 00	12 00	0 00	0 00	83 3098	49 36
32	1229 00	12 00	0 00	0 00	98 0110	47 31
33	1531 00	40 00	0 00	0 00	99 9900	59 34

South of the Denali Fault

45RAP FS#L1 FIGURE 2R 32

Weighted average of J from standards = 3 411e-03 +/- 1 051e-05

Laser Power (mW)	Cumulative 39Ar	40Ar/39Ar measured	+/-	37Ar/39Ar measured	+/-	36Ar/39Ar measured	+/-
400	0 01	73 45	1 10	0 01	0 0040	0 15	
600	0 03	7 54	0 04	0 00	0 0013	0 01	
800	0 07	5 30	0 04	0 00	0 0005	0 00	
1000	0 11	4 83	0 04	0 01	0 0005	0 00	
1300	0 17	5 05	0 04	0 01	0 0005	0 00	
1600	0 22	4 92	0 04	0 01	0 0004	0 00	

0 2800	0 28	22 15	0 28
0 1900	0 19	21 78	0 19
0 2600	0 26	23 74	0 26
0 2100	0 21	23 74	0 21
0 1900	0 19	27 31	0 19
0 2500	0 25	30 30	0 25
0 1100	0 11	30 30	0 11
0 1100	0 11	31 99	0 11
0 1100	0 11	32 62	0 11
0 3000	0 30	37 09	0 30
0 1200	0 12	39 77	0 12
0 1500	0 15	41 72	0 15
0 1400	0 14	49 36	0 14
0 2100	0 21	49 36	0 21
0 7800	0 78	59 34	0 78

% Atmospheric 40Ar	Ca/K	+/-	Cl/K	+/-	40*/39K	+/-	Age (Ma)	+/- (Ma)
0 0030	58 73	0 02	0 01	0 01	0 0004	30 30	1 12	177 45	6 26
0 0005	26 70	0 00	0 00	0 00	0 0001	5 51	0 14	33 56	0 87
0 0002	9 10	0 01	0 00	0 00	0 0000	4 79	0 07	29 24	0 43
0 0002	4 55	0 01	0 00	0 00	0 0001	4 59	0 07	28 00	0 41
0 0002	6 16	0 01	0 00	0 00	0 0001	4 72	0 06	28 78	0 36
0 0002	3 85	0 02	0 00	0 00	0 0001	4 70	0 07	28 71	0 40

Table 2R 5
continued

2000	0 24	4 76	0 02	0 01	0 0009	0 00
2500	0 29	4 82	0 02	0 01	0 0005	0 00
3000	0 35	4 89	0 03	0 01	0 0004	0 00
4000	0 61	5 12	0 02	0 00	0 0001	0 00
5000	0 77	5 10	0 05	0 01	0 0002	0 00
6000	0 83	5 19	0 04	0 01	0 0003	0 00
9000	0 88	5 22	0 03	0 01	0 0006	0 00
9001	1 00	5 50	0 07	0 01	0 0002	0 00
Integrated		5 52	0 01	0 01	0 0001	0 00

311ASTFS#F1 FIGURE 2R 33

Weighted average of J from standards = 3 571e-03 +/- 1 656e-05

Temp (deg C)	Cumulative 39Ar	40Ar/39Ar measured	+/-	37Ar/39Ar measured	+/-	36Ar/39Ar measured	+/-
400	0 00	204 29	4 19	0 22	0 1469	0 59	
400	0 00	219 83	5 77	0 42	0 1855	0 73	
450	0 00	14 86	0 50	0 02	0 1115	0 03	
450	0 00	72 97	1 50	0 10	0 0699	0 22	
500	0 00	14 03	0 17	0 07	0 0375	0 03	
500	0 00	36 37	0 44	0 12	0 0410	0 11	
550	0 01	12 52	0 11	0 08	0 0199	0 03	
550	0 01	19 71	0 15	0 08	0 0158	0 05	
600	0 01	19 79	0 15	0 08	0 0087	0 05	
600	0 02	11 43	0 07	0 06	0 0063	0 02	
650	0 04	7 28	0 04	0 06	0 0032	0 01	
650	0 05	7 91	0 05	0 04	0 0049	0 01	
700	0 06	5 50	0 03	0 03	0 0032	0 00	

0 0003	-1 26	0 02	0 00	0 00	0 0001	4 79	0 10	29 26	0 60
0 0002	1 51	0 02	0 00	0 00	0 0001	4 72	0 05	28 83	0 29
0 0001	2 83	0 02	0 00	0 00	0 0001	4 72	0 05	28 81	0 29
0 0000	4 06	0 01	0 00	0 00	0 0000	4 89	0 02	29 81	0 13
0 0001	3 55	0 01	0 00	0 00	0 0000	4 89	0 06	29 82	0 35
0 0001	4 13	*0 01*	*0 00*	*0 00*	*0 0001*	4 95	*0 06*	30 21	*0 33*
0 0002	4 62	0 01	0 00	0 00	0 0001	4 95	0 06	30 19	0 38
0 0001	6 09	0 01	0 00	0 00	0 0001	5 14	0 07	31 34	0 41
0 0000	8 72	0 01	0 00	0 00	0 0000	5 01	0 02	30 58	0 14

	% Atmospheric 40Ar	Ca/K	+/-	Cl/K	+/-	40*/39K	+/-	Age (Ma)	+/- (Ma)
0 0226	85 77	0 41	0 27	0 02	0 0025	29 07	5 79	178 21	33 80
0 0332	97 97	0 78	0 34	0 01	0 0054	4 46	8 14	28 54	51 63
0 0079	60 79	0 03	0 20	0 00	0 0033	5 81	2 35	37 07	14 81
0 0120	88 31	0 17	0 13	0 00	0 0022	8 53	3 32	54 11	20 74
0 0074	53 96	0 13	0 07	0 00	0 0010	6 45	2 17	41 07	13 69
0 0039	89 06	0 22	0 08	0 00	0 0008	3 97	1 09	25 43	6 96
0 0022	60 71	0 15	0 04	0 00	0 0003	4 91	0 64	31 35	4 08
0 0033	79 57	0 15	0 03	0 00	0 0004	4 02	0 97	25 72	6 19
0 0016	76 11	0 14	0 02	0 00	0 0002	4 72	0 48	30 17	3 03
0 0007	56 58	0 12	0 01	0 00	0 0002	4 95	0 23	31 62	1 43
0 0004	25 50	0 11	0 01	0 00	0 0001	5 41	0 13	34 49	0 79
0 0005	37 48	0 08	0 01	0 00	0 0001	4 92	0 14	31 45	0 92
0 0004	4 61	0 06	0 01	0 00	0 0001	5 22	0 12	33 29	0 79

Table 2R 5
continued

700	0 08	7 72	0 04	0 04	0 0033	0 01
750	0 09	6 40	0 05	0 05	0 0047	0 01
750	0 10	9 75	0 04	0 07	0 0038	0 02
800	0 12	5 74	0 02	0 03	0 0029	0 00
800	0 14	7 79	0 04	0 03	0 0018	0 01
850	0 16	5 95	0 03	0 03	0 0025	0 00
850	0 19	7 15	0 03	0 03	0 0022	0 01
900	0 21	5 85	0 02	0 06	0 0033	0 00
950	0 24	9 39	0 05	0 13	0 0033	0 01
1000	0 28	7 27	0 04	0 17	0 0021	0 01
1000	0 31	7 83	0 03	0 13	0 0018	0 01
1000	0 34	9 32	0 05	0 11	0 0039	0 01
1050	0 37	7 09	0 03	0 09	0 0018	0 01
1050	0 41	8 79	0 03	0 08	0 0012	0 01
1050	0 44	11 21	0 03	0 07	0 0021	0 02
1100	0 49	7 23	0 03	0 04	0 0008	0 01
1200	0 89	6 37	0 02	0 02	0 0002	0 00
1600	1 00	66 87	0 18	0 12	0 0013	0 22
Integrated		13 90	0 02	0 06	0 0004	0 03

05RAPFS#L1 FIGURE 2R 34

Weighted average of J from standards = 7 125e-03 +/- 1 903e-05

Laser Power	Cumulative	40Ar/39Ar	+/-	37Ar/39Ar	+/-	36Ar/39Ar	+/-
(mW)	39Ar	measured		measured		measured	
400	0 00	182 50	3 30	0 03	0 0079	0 55	
600	0 01	12 81	0 19	0 02	0 0033	0 03	

0 0004	33 78	0 07	0 01	0 00	0 0001	5 09	0 13	32 50	0 85
0 0004	23 39	0 09	0 01	0 00	0 0001	4 88	0 12	31 17	0 79
0 0004	51 82	0 12	0 01	0 00	0 0001	4 68	0 13	29 92	0 82
0 0003	11 27	0 06	0 01	0 00	0 0001	5 07	0 08	32 35	0 53
0 0003	34 70	0 05	0 00	0 00	0 0001	5 07	0 08	32 35	0 51
0 0002	16 78	0 05	0 00	0 00	0 0001	4 93	0 06	31 48	0 41
0 0002	27 34	0 05	0 00	0 00	0 0001	5 17	0 06	33 03	0 40
0 0003	11 10	0 12	0 01	0 00	0 0001	5 17	0 09	33 03	0 55
0 0003	45 91	0 24	0 01	0 00	0 0001	5 06	0 09	32 33	0 59
0 0001	29 96	0 31	0 00	0 00	0 0001	5 07	0 05	32 36	0 33
0 0002	35 88	0 24	0 00	0 00	0 0000	5 00	0 07	31 94	0 46
0 0002	45 70	0 20	0 01	0 00	0 0001	5 04	0 08	32 21	0 49
0 0003	28 72	0 17	0 00	0 00	0 0001	5 03	0 08	32 12	0 51
0 0002	40 96	0 15	0 00	0 00	0 0001	5 17	0 07	33 02	0 44
0 0004	55 76	0 14	0 00	0 00	0 0001	4 95	0 12	31 59	0 75
0 0002	28 72	0 08	0 00	0 00	0 0000	5 13	0 06	32 75	0 39
0 0000	19 94	0 03	0 00	0 00	0 0000	5 08	0 02	32 43	0 11
0 0010	96 63	0 23	0 00	0 00	0 0001	2 25	0 24	14 43	1 55
0 0001	65 57	0 11	0 00	0 00	0 0000	4 78	0 03	30 51	0 23

% Atmospheric 40Ar		Ca/K	+/-	Cl/K	+/-	40*/39K	+/-	Age (Ma)	+/- (Ma)
0 0112	88 26	0 06	0 01	0 02	0 0018	21 42	2 78	256 27	30 95
0 0010	76 34	0 03	0 01	0 00	0 0002	3 02	0 31	38 45	3 88

Table 2R 5
continued

800	0 02	4 68	0 07	0 02	0 0010	0 01
1000	0 06	2 57	0 04	0 02	0 0005	0 00
1300	0 13	2 41	0 04	0 03	0 0006	0 00
1600	0 21	2 37	0 04	0 03	0 0005	0 00
2000	0 29	2 35	0 03	0 03	0 0004	0 00
2500	0 38	2 34	0 03	0 02	0 0004	0 00
3000	0 45	2 34	0 04	0 02	0 0004	0 00
4000	0 55	2 40	0 03	0 02	0 0004	0 00
5000	0 64	2 47	0 04	0 02	0 0004	0 00
6000	0 73	2 54	0 03	0 02	0 0004	0 00
9000	0 80	2 51	0 04	0 02	0 0003	0 00
9001	1 00	2 69	0 02	0 01	0 0001	0 00
Integrated		2 81	0 01	0 02	0 0001	0 00

09RAP FS#L1 FIGURE 2R 35

Weighted average of J from standards = 7 125e-03 +/- 1 903e-05

Laser Power	Cumulative	40Ar/39Ar	+/-	37Ar/39Ar	+/-	36Ar/39Ar	+/-
(mW)	39Ar	measured		measured		measured	
400	0 00	575 18	12 43	-0 06	0 0390	1 81	
600	0 00	153 96	3 14	-0 01	0 0150	0 39	
800	0 01	29 09	0 35	0 00	0 0013	0 08	
1000	0 04	7 60	0 10	0 00	0 0005	0 02	
1300	0 11	3 82	0 05	0 00	0 0004	0 00	
1600	0 19	2 61	0 03	0 00	0 0002	0 00	
2000	0 29	2 44	0 03	0 00	0 0002	0 00	
2500	0 40	2 47	0 02	0 00	0 0001	0 00	
3000	0 49	2 56	0 03	0 00	0 0002	0 00	

0 0003	53 54	0 03	0 00	0 00	0 0001	2 16	0 10	27 55	1 28
0 0001	14 10	0 04	0 00	0 00	0 0001	2 18	0 05	27 85	0 62
0 0001	3 61	0 05	0 00	0 00	0 0001	2 30	0 05	29 27	0 60
0 0001	4 65	0 05	0 00	0 00	0 0001	2 23	0 04	28 48	0 48
0 0001	2 29	0 05	0 00	0 00	0 0000	2 27	0 04	28 88	0 49
0 0001	3 02	0 04	0 00	0 00	0 0001	2 24	0 04	28 52	0 50
0 0001	3 79	0 03	0 00	0 00	0 0001	2 22	0 05	28 36	0 58
0 0001	3 27	0 03	0 00	0 00	0 0000	2 29	0 04	29 20	0 45
0 0001	6 45	0 04	0 00	0 00	0 0001	2 28	0 04	29 11	0 51
0 0001	8 93	0 04	0 00	0 00	0 0000	2 28	0 04	29 12	0 46
0 0001	7 03	0 03	0 00	0 00	0 0001	2 31	0 04	29 45	0 52
0 0000	12 59	0 02	0 00	0 00	0 0000	2 32	0 02	29 60	0 23
0 0000	17 12	0 04	0 00	0 00	0 0000	2 30	0 01	29 38	0 17

% Atmospheric 40Ar		Ca/K	+/-	Cl/K	+/-	40*/39K	+/-	Age (Ma)	+/- (Ma)
0 0402	92 86	-0 10	0 07	0 06	0 0021	41 07	4 96	463 08	49 36
0 0097	73 92	-0 01	0 03	0 04	0 0015	40 14	2 70	453 78	26 95
0 0009	77 84	0 00	0 00	0 01	0 0002	6 44	0 31	80 93	3 85
0 0003	62 94	0 01	0 00	0 00	0 0001	2 81	0 10	35 72	1 30
0 0001	37 11	0 00	0 00	0 00	0 0000	2 39	0 05	30 40	0 69
0 0001	11 66	0 00	0 00	0 00	0 0001	2 28	0 04	29 07	0 47
0 0001	4 85	0 00	0 00	0 00	0 0000	2 30	0 03	29 29	0 41
0 0001	7 27	0 00	0 00	0 00	0 0000	2 26	0 03	28 84	0 38
0 0001	12 86	0 00	0 00	0 00	0 0000	2 21	0 04	28 17	0 51

Table 2R 5
continued

4000	0 57	2 41	0 03	0 00	0 0001	0 00
5000	0 63	2 36	0 03	0 00	0 0003	0 00
6000	0 68	2 39	0 02	0 00	0 0003	0 00
9000	0 72	2 43	0 02	0 00	0 0004	0 00
9001	1 00	2 66	0 01	0 00	0 0001	0 00
Integrated		3 61	0 01	0 00	0 0001	0 00

16RAPFS#L1 FIGURE 2R 36

Weighted average of J from standards = 3 411e-03 +/- 1 051e-05

Laser Power (mW)	Cumulative 39Ar	40Ar/39Ar measured	+/-	37Ar/39Ar measured	+/-	36Ar/39Ar measured	+/-
400	0 04	81 86	0 42	0 01	0 0009	0 24	
600	0 12	6 81	0 04	0 01	0 0004	0 01	
800	0 21	5 68	0 02	0 01	0 0005	0 00	
1000	0 30	5 19	0 01	0 01	0 0003	0 00	
1300	0 39	5 34	0 02	0 01	0 0003	0 00	
1600	0 47	5 42	0 02	0 01	0 0005	0 00	
2000	0 54	4 93	0 02	0 01	0 0005	0 00	
2500	0 61	5 07	0 02	0 01	0 0004	0 00	
3000	0 66	5 32	0 02	0 02	0 0008	0 00	
4000	0 71	6 10	0 02	0 03	0 0006	0 00	
5000	0 79	6 60	0 03	0 03	0 0005	0 01	
6000	0 90	6 83	0 04	0 02	0 0003	0 01	
9000	0 96	5 96	0 02	0 01	0 0005	0 00	
9001	1 00	5 76	0 02	0 01	0 0008	0 00	
Integrated		9 06	0 01	0 01	0 0001	0 01	

0 0001	5 04	0 00	0 00	0 00	0 0000	2 26	0 04	28 84	0 46
0 0001	2 66	0 00	0 00	0 00	0 0001	2 27	0 05	28 89	0 57
0 0002	2 85	0 00	0 00	0 00	0 0001	2 30	0 05	29 28	0 65
0 0002	6 42	0 00	0 00	0 00	0 0000	2 24	0 06	28 61	0 80
0 0000	11 47	0 00	0 00	0 00	0 0000	2 33	0 01	29 72	0 19
0 0000	32 37	0 00	0 00	0 00	0 0000	2 42	0 01	30 86	0 17

% Atmospheric 40Ar		Ca/K	+/-	Cl/K	+/-	40*/39K	+/-	Age (Ma)	+/- (Ma)
0 0025	88 42	0 02	0 00	0 00	0 0002	9 48	0 66	57 39	3 91
0 0002	33 30	0 02	0 00	0 00	0 0001	4 52	0 07	27 62	0 45
0 0002	18 24	0 02	0 00	0 00	0 0001	4 62	0 07	28 22	0 44
0 0002	11 09	0 02	0 00	0 00	0 0001	4 59	0 05	28 03	0 31
0 0002	12 95	0 02	0 00	0 00	0 0001	4 62	0 05	28 22	0 32
0 0002	13 52	0 02	0 00	0 00	0 0001	4 66	0 06	28 45	0 36
0 0002	5 56	0 02	0 00	0 00	0 0001	4 63	0 05	28 27	0 31
0 0002	8 52	0 02	0 00	0 00	0 0001	4 61	0 07	28 17	0 43
0 0004	10 97	0 03	0 00	0 00	0 0001	4 71	0 13	28 78	0 78
0 0002	23 50	0 05	0 00	0 00	0 0001	4 64	0 05	28 35	0 32
0 0002	27 75	0 05	0 00	0 00	0 0001	4 75	0 06	28 97	0 34
0 0002	29 44	0 03	0 00	0 00	0 0001	4 80	0 06	29 29	0 34
0 0002	16 85	0 01	0 00	0 00	0 0001	4 93	0 07	30 09	0 41
0 0005	10 44	0 01	0 00	0 00	0 0001	5 13	0 15	31 31	0 92
0 0001	45 78	0 02	0 00	0 00	0 0000	4 90	0 03	29 87	0 22

Table 2R 5
continued
23RAP FS#L1

FIGURE 2R 37

Weighted average of J from standards = 3 411e-03 +/- 1 051e-05

Laser Power (mW)	Cumulative 39Ar	40Ar/39Ar measured	+/-	37Ar/39Ar measured	+/-	36Ar/39Ar measured	+/-
400	0 03	27 13	0 15	0 01	0 0004	0 06	
600	0 10	5 46	0 07	0 02	0 0005	0 00	
800	0 17	5 07	0 07	0 02	0 0003	0 00	
1000	0 24	5 03	0 07	0 02	0 0003	0 00	
1300	0 31	4 99	0 07	0 02	0 0003	0 00	
1600	0 37	4 95	0 08	0 02	0 0004	0 00	
2000	0 42	5 09	0 08	0 02	0 0005	0 00	
2500	0 47	5 40	0 08	0 01	0 0006	0 00	
3000	0 51	5 55	0 08	0 01	0 0004	0 00	
4000	0 61	5 60	0 06	0 01	0 0002	0 00	
5000	0 71	5 54	0 06	0 00	0 0002	0 00	
6000	0 79	5 52	0 07	0 00	0 0002	0 00	
9000	0 85	5 47	0 08	0 00	0 0003	0 00	
9001	1 00	5 47	0 03	0 00	0 0001	0 00	
Integrated		6 07	0 02	0 01	0 0001	0 00	

	% Atmospheric 40Ar	Ca/K	+/-	Cl/K	+/-	40*/39K	+/-	Age (Ma)	+/- (Ma)
0 0005	68 76	0 02	0 00	0 00	0 0001	8 47	0 16	51 36	0 97
0 0001	9 60	0 03	0 00	0 00	0 0001	4 91	0 08	29 94	0 47
0 0002	4 98	0 03	0 00	0 00	0 0001	4 79	0 08	29 21	0 48
0 0001	3 58	0 03	0 00	0 00	0 0001	4 82	0 07	29 40	0 41
0 0001	3 08	0 03	0 00	0 00	0 0001	4 80	0 07	29 32	0 44
0 0001	2 67	0 03	0 00	0 00	0 0001	4 79	0 09	29 24	0 52
0 0002	5 13	0 03	0 00	0 00	0 0000	4 80	0 09	29 30	0 53
0 0002	8 88	0 03	0 00	0 00	0 0001	4 90	0 09	29 88	0 57
0 0002	10 47	0 03	0 00	0 00	0 0001	4 94	0 10	30 15	0 59
0 0001	9 92	0 02	0 00	0 00	0 0001	5 02	0 07	30 63	0 43
0 0001	7 45	0 01	0 00	0 00	0 0000	5 10	0 06	31 09	0 36
0 0001	7 43	0 01	0 00	0 00	0 0001	5 08	0 08	30 98	0 46
0 0001	7 12	0 01	0 00	0 00	0 0001	5 06	0 08	30 85	0 50
0 0001	7 31	0 00	0 00	0 00	0 0000	5 05	0 03	30 79	0 21
0 0000	16 17	0 02	0 00	0 00	0 0000	5 07	0 02	30 91	0 15

2.14 **Repository References:**

Copeland, P., Harrison, T.M., 1990, Episodic rapid uplift in the Himalaya revealed by $^{40}Ar/^{39}Ar$ analysis of detrtial K-feldspar and muscovite, Bengal fan: Geology, v. 18, p. 354-357.

Ehlers T (2005), Crustal thermal processes and the interpretation of thermochronometer data. Rev Mineral Geochem 58:315-350

Farley, K.A., 2000, Helium diffusion from apatite: General behavior as illustrated by Durango apatite: Journal of Geophysical Research, v. 105, p. 2903–2914, doi: 10.1029/1999JB900348.

Farley, K.A., R.A. Wolf, and L.T. Silver, 1996, The effects of long alpha-stopping distances on (U-Th)/He ages, Geochimica et Cosmochimica Acta, 60, 4223-4229.

Galbraith, R.F., 1981, On statistical methods of fission track counts, Mathematical Geology, 13, 471-478.

Galbraith, R.F., and G.M. Laslett, 1993, Statistical models for mixed fission track ages, Nuclear Tracks and Radiation Measurements, 21, 459-470.

Harrison, T.M., M.T. Heizler, O.M. Lovera, Wenji Chen, and M.A. Grove (1994), Chlorine disinfectant for excess argon released from K-feldspar during step heating, Earth Planet. Sci. Lett., 123, 95-104.

Ketcham, R.A., Donelick, R.A., Carlson, W.D., 1999, Variability of apatite fission-track annealing kinetics. III. Extrapolation to geological time scales, American Mineralogist, v. 84, 1235-1255.

Lanphere, M.A., and Dalrymple, G.B., 2000, First-principles calibration of ^{38}Ar tracers: Implications for the ages of $^{40}Ar/^{39}Ar$ fluence monitors, U.S. Geological Survey Professional Paper 1621, 10 p.

Layer, P.W., 2000, Argon-40/argon-39 age of the El'gygytgyn impact event, Chukotka, Russia, Meteroitics and Planatary Science, v. 35, 591-599.

Layer, P.W., Hall, C.M. & York, D., 1987. The derivation of $^{40}Ar/^{39}Ar$ age spectra of single grains of hornblende and biotite by laser step heating, Geophys. Res. Lett., 14, 757-760.

Lovera, O.M., Heizler, M.T., and Harrison, T.M., 1993, Argon diffusion domains in K-feldspar 11: Kinetic properties of MH-10: Contributions to Mineralogy and Petrology, v. 1 13, p. 381-393.

McDougall, I. and Harrison, T.M., 1999, Geochronology and Thermochronology by the 40Ar/39Ar method-2nd ed, Oxford University Press, New York, 269pp.

Reiners, P.W., Brandon, M.T., 2006, Using thermochronology to understand orogenic erosion, Annual Review of Earth and Planetary Science, v. 34, 419-466.

Roddick, J. C. (1978), The application of isochron diagrams in 40Ar_39Ar dating, a discussion, Earth Planet. Sci. Lett., 41, 233 – 244.

Roddick, J. C., R. A. Cliff, and D. C. Rex (1980), The evolution of excess argon in alpine biotites, a 40Ar/39Ar analysis, Earth Planet. Sci. Lett., 48, 185 – 208

Samson S. D., and Alexander E. C. (1987) Calibration of the interlaboratory 40Ar/39Ar dating standard, MMhb1. Chem. Geol. **66**, 27-34.

Sanders, R.E., Heizler, M.T., and Goodwin, L.B., 2006, 40Ar/39Ar thermochronology constraints on the timing of Proterozoic basement exhumation and fault ancestry, southern Sangre de Cristo Range, New Mexico: Geological Society of America Bulletin, v. 118, no. 11–12, p. 1489–1506, doi: 10.1130/B25857.1.

Steiger, R.H. and Jaeger, E., 1977, Subcommission on geochronology: Convention on the use of decay constants in geo and cosmochronology, Earth and Planet Science Letters, v. 36, p. 359-362.

Spotila, J.A., Niemi, N., Brady, R., House, M., and Buscher, J., 2007, Long-term continental deformation associated with transpressive plate motion: The San Andreas fault: Geology, v. 35, p. 967–970, doi: 10.1130/G23816A.1.

Valli, F., Arnaud, N., Leloup, P., Sobel, E., Mahéo, G., Lacassin, R., Guillot, S., Li, H., Tapponnier, P., and Xu, Z., 2007, Twenty million years of continuous deformation along the Karakorum fault, western Tibet: a thermochronological analysis, Tectonics 26 10.1029/2005TC001913.

York, D. (1969), Least squares fitting of a straight line with correlated errors, Earth Planet. Sci. Lett., 5, 320 – 324.

York, D., Hall, C.M., Yanase, Y., Hanes, J.A. & Kenyon, W.J., 1981. $^{40}Ar/^{39}Ar$ dating of terrestrial minerals with a continuous laser, Geophys. Res. Lett., 8, 1136-1138.

CHAPTER 3

PERSISTENT LONG-TERM (~24 MA) EXHUMATION IN THE EASTERN ALASKA RANGE CONSTRAINED BY STACKED THERMOCHRONOLOGY[1]

3.1 Abstract

Thermochronology studies commonly project the results from a spatially limited sampling approach to an entire mountain range even though the exhumation history of a mountain range usually varies along and across strike. This can lead to incorrect assumptions regarding the start of regional exhumation and the episodic nature of exhumation. To address these problems, we introduce a new graphical procedure that vertically stacks spatially diverse K-feldspar $^{40}Ar/^{39}Ar$ multi-domain diffusion (MDD) models from the length of the ~100 km long high-peak region of the eastern Alaska Range (EAR). The vertically stacked thermal models provide a comprehensive spatial-temporal view of the region's complex exhumation history. We supply additional constraints with $^{40}Ar/^{39}Ar$ mica dating because the higher closure-temperature-window places limits on the initiation of rapid EAR exhumation. We find that rapid and persistent (non-episodic) exhumation has occurred in the EAR since ~24 Ma at a long-term rate of ~0.9 km/Ma, but that the spatial focus of this rapid exhumation moves through time (i.e., spatially variable).

[1]Benowitz, J.A., Layer, P.W., VanLaningham, S., Persistent long-term (~24 Ma) exhumation in the eastern Alaska Range constrained by stacked thermochronology, prepared for submission to *Tectonics*.

Onset of exhumation is coincident with the initiation of rapid exhumation in southwestern Alaska, the western Alaska Range and the Chugach-St. Elias Range at ~24 Ma, implying a region-wide deformational response to a change in tectonic forcing. The collision of the Yakutat microplate is likely responsible for this rapid exhumation in southern Alaska. Our results show that vertical stacking of thermal models facilitates a more complete analysis of the Neogene deformation history of southern Alaska and should be applicable to other orogenic belts.

3.2 **Introduction**

Thermochronology has now been used for over 30 years [see *Reiners et al.*, 2005] to study orogenic development. Many data interpretation methods regarding orogenic tectono-thermal histories have been standardized, including the time-averaged time-temperature (T-t) plots of one sample or one vertical transect using numerous samples from one mountain. Typically, any significant changes in time-averaged cooling rates (i.e., breaks in slope) based on these results are interpreted to indicate changes in exhumation rate. These changes in exhumation rate, also known as "events" or "episodes", are usually interpreted to reflect either large-scale changes in tectonic forcing or variations in near-field conditions that may influence exhumation (climate, fault geometry, rheology, etc.). Yet, tectonic processes (e.g., continental collisions) produce exhumation that can occur over long timescales (10 Ma to 50 Ma) and great distances (100's to 1000's of km). In addition, along-strike variations in the focus of exhumation are seen across the world [*Little et al.*, 2005;

Yin, 2006; *Tricart et al.*, 2007; *Seeber et al.*, 2010]. Thus, orogen-scale interpretations of tectonic processes based on thermochronological analyses of a single vertical transect [*Fitzgerald et al.*, 1993; *O'Sullivan and Currie*, 1996] or a single rock sample [*Richter et al.*, 1990] may not capture the spatial and temporal variability inherent to orogenesis. Although spatially restricted sampling for thermochronology can provide first-order windows into timing of orogenesis, can the total exhumation history of an orogen be constrained by such a practice?

One approach for capturing along- and across-strike variations in deformation response in complicated tectonic settings is to apply a "shotgun" sampling strategy [*Spotila*, 2005]. Deconvolving constrained lateral variations in initiation of rapid exhumation from a shotgun sampling strategy into episodic or persistent exhumation is critical to correlating an orogen's exhumation history to far-field tectonic processes. Thus, a need remains for developing approaches that capture the "big-picture" tectonic development of orogens that have experienced sub-regional variations in exhumation history.

We have investigated these orogenic development/plate-tectonic reconstruction difficulties along the continental-scale transpressional Denali fault in the topographically high eastern Alaska Range and propose a graphical procedure to view an orogen's exhumation history through time and space (Figures 3.1 and 3.2). Thermochronological research on the Neogene tectonic history of southern Alaska has led to the interpretation of exhumation pulses at ~23 Ma, ~20 Ma, ~18 Ma, ~16

Ma, ~11 Ma, ~6 Ma, ~4 Ma and ~1 Ma [*Plafker et al.*, 1992; *Fitzgerald et al.*, 1995; *O'Sullivan and Currie*, 1996; *Berger et al.*, 2008; *Enkleman et al.*, 2008; *Haeussler et al.*, 2008; *Spotila and Berger*, 2010]. Paleo-environmental analysis of Alaska sedimentary basins also suggests that pulses of exhumation occurred during the Miocene to present [*Lagoe et al.*, 1993; *Thoms*, 2000; *Ridgway et al.*, 2007; *Haeussler et al.*, 2008; *Finzel et al.*, 2009]. What is still not clear is whether the Neogene exhumation history of southern Alaska is a series of discrete events or part of a continuum related to on-going long-term tectonic processes such as the progressive collision of the Yakutat microplate (Figure 3.1).

To address the continuous vs. episodic nature of exhumation in southern Alaska, we employ $^{40}Ar/^{39}Ar$ K-feldspar (K-spar) thermochronology combined with $^{40}Ar/^{39}Ar$ muscovite and $^{40}Ar/^{39}Ar$ biotite analysis from six different areas of the eastern Alaska Range. These thermochronometers span a closure temperature range of ~400 °C to ~150 °C. Muscovite, biotite and K-spar record exhumation from a broad range of crustal depths, thereby providing a large time-temperature window to allow us to assess whether orogenesis is persistent or episodic. We graphically vertically stack numerous best-fit K-spar multi-domain diffusion thermal models (MDD) [*Lovera et al.*, 2002] (herein referred to as "vertical stacking" or "stacked thermochronology") to account for spatial variations in the focus of exhumation of an orogen. We believe the eastern Alaska Range is an ideal location to derive a long-term, spatially robust history of deformation in southern

Alaska. Numerous K-spar bearing plutons are in the region, allowing us to minimize spatial biases in sampling. The eastern Alaska Range is also at the apex of the curvilinear Denali fault and has an associated Neogene foreland basin [*Ridgway et al.*, 2007] recording a long history of regional exhumation.

We show that rapid exhumation in the eastern Alaska Range began by the late Oligocene and that it continues to the present. At the regional scale, our data indicate that at any snapshot in time, rapid exhumation was occurring somewhere in the orogen throughout the Neogene at a relatively consistent rate of ~0.9 km/Ma. However, at the local scale the timing of rapid exhumation varied, depending on location. We infer that deformation and exhumation have been occurring in southern Alaska for at least ~24 million years and are related to the progressive collision of the Yakutat microplate with North America. Because our stacked $^{40}Ar/^{39}Ar$ thermochronology approach accounts for variations in exhumation focus along and across strike, it could be useful for establishing a more complete history of exhumation in other active or ancient orogens. The graphical procedure presented here can also be used in conjunction with other thermochronology techniques [e.g., HeFTy, *Ketcham*, 2005].

3.3 **Tectonics and Exhumation in Southern Alaska**

The Alaska Range lies along the continental-scale, dextral strike-slip Deanli fault (Figures 3.1 and 3.2). This intra-plate range is located ca. 500 km inboard from the active subduction zone of southern Alaska. Suggested drivers for Neogene

deformation in the Alaska Range are changes in Pacific plate motion relative to stable North America [*Fitzgerald et al.*, 1995; *Enkelmann et al.*, 2008], microplate collision in the Gulf of Alaska [*Plafker et al.*, 1992], and block rotation associated with the Yakutat microplate collision (Figure 3.1) [*Haeussler et al.*, 2008; *Cross and Freymeuller*, 2008]. A variety of studies have used thermochronology to examine the possibility of these as drivers of Alaska Range exhumation, and we summarize them to provide context for the debate about continuous vs. episodic exhumation. We discuss them in terms of the western, central, and eastern parts of the Alaska Range (Figure 3.1).

3.3.1 **Western Alaska Range**

The Tordrillo Mountains are the area of high peaks in the western Alaska Range (Figure 3.1). Rocks there preserve evidence of rapid exhumation at ~23 Ma and ~6 Ma based on apatite fission track (AFT) thermochronology [*Haeussler et al.*, 2008]. The 23 Ma exhumation pulse is thought to be controlled by regional uplift and is corroborated by the high-energy depositional environment of the early Miocene Tyonek Formation of Cook Inlet [*Stricker and Flores*, 1996]. The ~6 Ma exhumation pulse is also thought to be controlled by regional uplift and is corroborated by the clastic Pliocene Sterling Formation [*Haeussler et al.*, 2008].

3.3.2 **Central Alaska Range**

The central Alaska Range is defined by the Mt. McKinley region (Figure 3.1) and is the site of one of the landmark vertical-transect AFT studies [*Fitzgerald*

et al., 1993]. The results clearly indicate a change in exhumation rate at ~6 Ma, which is interpreted as the beginning of uplift of the central Alaska Range. The exhumation event is correlated with the inferred depositional age of the 1000 m thick Nenana Gravel of the Tanana Basin, located ~150 km to the east [*Wahrhaftig et al.*, 1994]. The question remains whether the limited spatial scope of the study (restricted to Mt. McKinley, with no samples in the vicinity of the Denali fault) was sufficient to capture the full exhumation history of the region considering the large variation in exhumation patterns found in other regions [e.g., *Little et al.*, 2005; *Yin, 2006*; *Tricart et al.*, 2007] and along and across the Denali fault farther to the east [*Benowitz et al.*, 2011].

3.3.3 **Eastern Alaska Range**

The eastern Alaska Range as defined here spans the area between the Nenana River in the west and the Tok River valley in the east (Figures 3.1 and 3.2). Uranium-lead emplacement ages for plutons in the Black Rapids Glacier part of the eastern Alaska Range are ~70 Ma [*Aleinikoff et al.*, 2000]. Plutons in the Mount Nenana region of the western part of the eastern Alaska Range are thought to have ~38 Ma emplacement ages based on K-Ar and $^{40}Ar/^{39}Ar$ dating of biotite and hornblende [*Csejtey et al.*, 1992; *Benowitz et al.*, 2011]. The plutons around Mount Kimball along the easternmost edge of the eastern Alaska Range have inferred emplacement ages of ~100 Ma based on K/Ar dating of hornblende [*Nokleberg et al.*, 1992]. Knowing the ages of pluton emplacement in the eastern Alaska Range

allows distinction between post-emplacement cooling and cooling related to exhumation.

Young apatite fission track and (U-Th/He) apatite (AHe) ages in the eastern Alaska Range [<~3 Ma, *Armstrong et al.*, 2007; *Benowitz et al.*, 2011], as well as active seismicity including the 2002 **M**7.9 Denali fault earthquake [*Eberhart-Phillips et al.*, 2003] indicate that the region is tectonically active. Deformation and uplift of the eastern Alaska Range has recently been correlated with the Neogene Usibelli Group of the Tanana Basin, which is interpreted to contain a long-term record of a transpressional foreland basin system related to regional shortening in the Alaska Range along the Denali fault system [*Ridgway et al.*, 2007]. This Neogene basin association makes the region a prime location to investigate long-term exhumation patterns and thus the far-field drivers of exhumation in southern Alaska.

3.4 **Methods and Stacked Thermochronology Approach**

3.4.1 **Analytical and Sampling Methods**

We collected four new bedrock samples from granitic plutons along and across the strike of the eastern Alaska Range, proximal to the north side of the Denali fault system, in order to better constrain the initiation of rapid Neogene exhumation, the long-term exhumation history in the eastern Alaska Range, and the spatial pattern of exhumation (Table 3.1 and Figure 3.2). These samples are from

Mount Kimball (KIM) and the Black Rapids Glacier (RAP) and Mount Balchen (BAL) regions.

For $^{40}Ar/^{39}Ar$ analysis, samples were processed at the geochronology laboratory at the University of Alaska Fairbanks (UAF), where samples were crushed, sieved (250 micron to 1000 micron fraction), washed, paper-shaked and hand-picked for mica mineral phases. A Franz magnetic separator and a variable density liquid (sodium-polytungstate and deionized water) were used to separate out K-spar grains. Aliquots of K-spar separates derived from the heavy liquid separation were analyzed at UAF using a Panalytical wavelength dispersive Axios X-ray fluorometer (XRF) to confirm mineral identification and purity.

The mineral standard MMhb-1 [*Samson and Alexander*, 1987], with an age of 513.9 Ma [*Lanphere and Dalrymple*, 2000], was used to monitor neutron fluence (and calculate the irradiation parameter, J). The samples and standards were wrapped in aluminum foil and loaded into aluminum cans of 2.5 cm diameter and 6 cm height. The samples were irradiated in position 5c of the uranium-enriched research reactor of McMaster University in Hamilton, Ontario, Canada for 30 megawatt-hours. Upon their return from the reactor, the samples and monitors were loaded into 2 mm diameter holes in a copper tray that was then loaded in an ultra-high vacuum extraction line. The monitors were fused and samples were heated using a 6-watt argon-ion laser, following the technique described in *York et al.* [1981], *Layer et al.* [1987] and *Layer* [2000]. Bulk furnace-run samples consisting

of ~5 K-spar crystals were loaded in aluminum packets and step-heated in a Modifications Ltd. low-blank furnace connected on-line to the mass spectrometer. Temperature was calibrated by means of a thermocouple and a maximum temperature in excess of 1,600 °C is achievable. Duplicated isothermal step-heating schedules were conducted on K-spar in order to retrieve diffusion characteristics, to apply diffusion models, and to calculate model thermal histories [*Harrison et al.*, 1994; *Lovera et al.*, 1993].

Argon purification was achieved using a liquid nitrogen cold trap and a SAES Zr-Al getter at 400 °C. The samples were analyzed with a VG-3600 mass spectrometer at the UAF Geophysical Institute. The argon isotopes measured were corrected for system blank and mass discrimination, as well as calcium, potassium and chlorine interference reactions following procedures outlined in *McDougall and Harrison* [1999]. System blanks were generally $2x10^{-16}$ mol ^{40}Ar and $2x10^{-18}$ mol ^{36}Ar, which are 10 to 50 times smaller than sample/standard volume fractions. Mass discrimination was monitored by running both calibrated air shots and a zero-age glass sample. These measurements were made on a weekly to monthly basis to check for changes in mass discrimination. A summary of all of the $^{40}Ar/^{39}Ar$ mica results are given in Table 3.1, with all ages quoted to the $\pm 1\sigma$ level and calculated using the constants of *Steiger and Jäger* [1977]. The integrated age is the age given by the total gas measured and is equivalent to a potassium-argon (K-Ar) age. The spectrum provides a true plateau age if three or more consecutive gas fractions

represent at least 50% of the total gas release and are within two standard deviations of each other (Mean Square Weighted Deviation less than ~2.7).

MDD thermochronology has proven to be a useful tool to examine orogenic development because of the wide closure-temperature window (~350 °C to ~150 °C) of the system [*McDougall and Harrison*, 1999]. K-spar MDD thermochronology is also useful because the depth for closure of the system minimizes the effect of topography and advection on the temperature field of the upper crust [*Ehlers*, 2005]. MDD thermal models were created using software developed by *Lovera et al.* [1993]. Low-temperature steps were adjusted to account for the likely presence of fluid-inclusion hosted excess Ar leading to older apparent ages. In many cases, the first step of an isothermal duplicate yielded a significantly older age than the second step, consistent with the presence of fluid-inclusion hosted excess Ar [*Harrison et al.*, 1994]. However, corrections using the equations from *Harrison et al.* [1994] did not yield usable results, similar to the findings of *Sanders et al.* [2006]. We used the isothermal correction technique outlined by *Sanders et al.* [2006], in which they took the average age of the step before and the step after an apparent old age as an estimate of the excess Ar correction.

We base our determination of initiation of rapid cooling and rapid cooling rate determination on the slope of the bottom line of the MDD best-fit thermal history for each sample (Figure 3R.1). Since there is no quantitative method to place an error on either initiation of rapid cooling or rapid cooling rate from an

MDD model, we chose an approximation of the minimum of the possible slopes. We used the 10 °C/Ma knick-points of the lower slope to determine when rapid cooling began and ended. This provides an estimate of the best-fit rapid cooling rate for each sample, allowing us to discuss overall variations in cooling rates for one or multiple samples.

We use the same general geothermal gradient, ~30 °C/km, used in many of the exhumation studies performed in southern Alaska to calculate exhumation rate [*O'Sullivan and Currie,* 1996; *Haeussler et al.,* 2008; *McAleer et al.,* 2009; *Benowitz et al.*, 2011]. This construct allows direct comparison of exhumation rates between southern Alaska regional exhumation studies. Presently, based on the maximum depth of aftershocks (~11 km), the geothermal gradient for the Denali Fault region is inferred to be ~30 °C/km [*Fisher et al.*, 2004]. We acknowledge that we have no actual constraints on the Denali Fault zone paleo-geothermal gradient or temporal and spatial variations of this gradient. However, $^{40}Ar/^{39}Ar$ K-spar has a closure temperature-window of ~350 °C to ~150 °C. This temperature zone is less affected by both heat advection and variations in isotherm depth linked to variations in surface topography compared to shallower temperature zones [e.g., *Braun et al.,* 2006]. In addition, there is no known history of extensional events, magmatic events, or hot spring activity along the Denali Fault during the Neogene that would dramatically alter regional geothermal gradients [*Plafker et al.,* 1994].

3.4.2 **Lateral Edge of Range Front and Deeper Indicators of Crustal Exhumation**

K-spar MDD modeling of sample 01KIM (Figure 3.1) was chosen to examine the exhumation rate adjacent to the Denali fault at the southeast edge of the region of high topography. Unaltered biotite from sample 01KIM was also dated using $^{40}Ar/^{39}Ar$ laser step heating to confirm the previous K-Ar emplacement age determined in the region. $^{40}Ar/^{39}Ar$ laser step heating of muscovite/biotite pairs from samples 26RAP and 28RAP (Figure 3.2) were used to constrain the exhumation rates above the K-spar closure temperature in the high peak region of the eastern Alaska Range. Biotite has been shown to be a potentially unreliable thermochronometer because of possible excess Ar affecting age determinations and instability during heating in vacuo [*McDougall and Harrison*, 1999]. However, biotite $^{40}Ar/^{39}Ar$ analysis can provide useful cooling-rate information if the range of possible closure temperatures (Tc; ~350 °C to ~300 °C) is taken into consideration, and it can be compared to muscovite, which has a better constrained closure temperature (~400 °C) [*Harrison et al.*, 2009].

3.4.3 **Stacked Multi-Domain Diffusion Modeling**

We offer a different approach to reconstructing the exhumation history of an orogen by vertically stacking the best-fit MDD thermal histories of eight bedrock samples collected along and across the strike of an orogen (Figure 3.2) [two new samples, 26RAP and 19BAL, as well as six others from *Benowitz et al.*,

2011]. The amount of cooling (inferred in terms of exhumation) recorded in each sample is complicated by differences in paleo-depth, present-day elevation, and location of an individual sample in relation to structures (e.g. the Denali fault). Stacking each MDD best-fit thermal history using an overall non-dimensional y-axis allows construction of a composite mosaic that shows slopes and trends in the thermal history that reflect long-term spatial variations in the rate of bedrock cooling along and across the strike of an orogen. Thus, by stacking the cooling histories of numerous samples, breaks in slope between samples reveal information about whether rapid exhumation within an entire orogen is episodic or persistent (Figure 3.3a, b).

3.5 **Results**

3.5.1 **Mica $^{40}Ar/^{39}Ar$ Ages**

Biotite from sample 01KIM has a plateau age of ~96 Ma (Figure 3.4, 3R.2 and Table 3.1) and an integrated (total fusion) age within error of the plateau age. The spectrum shows little evidence of extremely slow cooling or diffusion argon loss. Muscovite and biotite from samples 26RAP and 28RAP show simple spectra with well-defined plateaus and little or no argon loss (Figure 3R.3, 3R.4 and Table 3.1). The integrated and plateau ages are within error for both samples. Muscovite from sample 26RAP has a plateau age of ~24 Ma (Figure 3.5). Biotite from sample 26RAP has a plateau age of ~20 Ma (Figure 3.5). The time between closure of the two distinct mineral phases is ~4 Ma. Muscovite from sample 28RAP has a plateau

age of ~23 Ma (Figure 3.5) while biotite from 28RAP has a plateau age of ~19 Ma (Figure 3.5). The time between closure of the two distinct mineral phases is ~4 Ma.

3.5.2 **K-spar $^{40}Ar/^{39}Ar$ MDD Thermal Models**

All three bulk K-spar furnace step-heating experiments yielded diffusion patterns compatible with MDD modeling (Figure 3R.5, 3R.6, 3R.7 and Table 3R.2). The step-heating results yielded E=48.52 Kcal/mol and Do=7.97 cm^2/s for 01KIM, E=47.55 Kcal/mol and Do=7.97 cm^2/s for 26RAP, and E=47.45 Kcal/mol and Do=6.68 cm^2/s for 19BAL. Results are all within the ranges expected for K-spars [*McDougall and Harrison*, 1999]. The K-spar age spectra display complex thermal histories that reflect post-emplacement cooling (Figure 3.6). The thermal model from sample 01KIM demonstrates slow prolonged cooling starting at ~68 Ma with a long-term rate of ~4 °C/Ma (Figure 3.7). MDD models (Figure 3.8) from samples 26RAP and 19BAL show initiation of rapid cooling at ~12 Ma. This falls in the middle of the age range of rapid cooling initiation documented in previous MDD models from the high relief region of the eastern Alaska Range (Figure 3.8) [*Benowitz et al.*, 2011].

3.5.3 **Stacked K-spar $^{40}Ar/^{39}Ar$ MDD Thermal Models**

Most of the models (Figure 3.8) show nonsystematic short-term maximum cooling rates (~1 Ma) between ~30 °C/Ma and ~45 °C/Ma. Analysis of such short timescales is not relevant to our goal of understanding long-term cooling patterns and may over-interpret the T-t constraints provided by the MDD modeling

technique. Furthermore, it has been shown that long-term histories of cooling rate better reflect the effects of far-field driving forces than short-term, spatially limited thermal variations [*Bernet et al.*, 2009]. The eight samples all record periods of rapid cooling at an average rate of ~26 °C/Ma. The 90% confidence level of the median (best-fit) of K-spar thermal models from samples 26RAP and 19BAL were stacked with six previously published K-spar best-fit thermal models [*Benowitz et al.*, 2011] from the eastern Alaska Range (Figure 3.9). No single K-spar sample records rapid cooling for more than ~4 million years, but if the results are viewed collectively, rapid cooling occurred somewhere within the region throughout the entire time between ~21 Ma and ~6 Ma (Figure 3.9).

3.6 **Discussion**

We can infer the exhumation history of a rock by knowing the thermal history of a sample and assuming or modeling the regional geothermal gradient [see review by *Reiners and Brandon*, 2006]. An exhumation event is loosely defined as a change in inferred exhumation rate. In the literature, an exhumation event can be defined by a thermal history from a single rock, a single vertical transect from one mountain (several samples) or an extensive data set from an entire orogen. The looseness in both the semantic usage of the phrase "exhumation event" and variations in sampling strategy can lead to challenges in reconstructing the timing and spatial extent of deformation.

Poor constraints on a region's pre-orogenic background exhumation rate when defining initiation of rapid exhumation can be problematic. Thus, a limited T-t window approach can lead to the incorrect identification of the time of initiation of regional exhumation. Difficult terrain in active tectonic regions can also limit access for sampling, thereby biasing the thermal record of a region towards more accessible regions, which could very well be accessible because of different exhumation patterns. Part of an orogen's thermal record in bedrock samples can also be lost during unroofing because of erosion (*Clift and VanLaningham*, 2010). Both situations can lead to interpretations of episodic exhumation, because part of the thermal record is not represented. These issues of sample bias can also lead to an incorrect interpretation of the time of initiation of rapid exhumation.

To address these issues in sample bias in the use of thermochronology to study orogenic development, we used accomplished alpinists to collect samples (see acknowledgements) and assume we are constraining the minimum age for the initiation of rapid cooling and not the exact time of initiation of rapid cooling in the eastern Alaska Range. We will first constrain the background exhumation rate (inferred from the background cooling rate) for the eastern Alaska Range. Then we will demonstrate the minimum age for the start of Neogene rapid exhumation in the region. Next we will apply (and thus evaluate) the stacked thermochronology approach to eight best-fit MDD thermal models from the high peak region to determine whether exhumation has been episodic or persistent in the core of the

orogen since the initiation of rapid exhumation. Finally, we will discuss the large-scale regional tectonic implications of applying our stacked approach to thermochronology.

3.6.1 **Background Exhumation Rate**

The biotite age of 01KIM ($^{40}Ar/^{39}Ar$ age = ~96 Ma, Figure 3.4) is similar to the ~100 Ma emplacement age of plutons in the Kimball region [*Nokleberg et al.*, 1992]. The average rate of cooling between ~90 Ma and ~68 Ma based on K-spar from sample 01KIM is ~0.5 °C/Ma (Figure 3.7). From ~68 Ma to ~36 Ma the long-term average rate of cooling for sample 01KIM increases to ~4 °C/Ma. We do not make any tectonic interpretations based on the slightly higher (~6 °C/Ma) long term cooling rate between ~68 Ma and ~52 Ma, because we are not sure that ~2 °C/Ma is a significant rate change, but this may warrant further study. With that in mind, we interpret the K-spar MDD model for sample 01KIM (Figure 3.7) to reflect slow post-emplacement cooling until a change in tectonic environment at ~68 Ma led to an increase in cooling rate. Intrusion of alkaline dikes occurred in the Kimball region at approximately 68 Ma [*Foley*, 1985] and may have been related to a short-lived extensional event. The time of the change in cooling rate is also coincident with the interpreted start of movement along the western Denali fault at ~66 Ma [*Miller et al.*, 2002]. Thus, we infer that the change in cooling rate at ~68 Ma in sample 01KIM may be related to the onset of movement of the Denali fault in the region.

If the average cooling rate of sample 01KIM is projected past the closure age of K-spar to the present, the derived cooling rate of ~4 °C/Ma is the same average cooling rate demonstrated between ~68 Ma and ~36 Ma in the MDD modeling from 01KIM. *Fitzgerald et al.* [1995] infer a similar background cooling rate of ~3 °C/Ma for the central Alaska Range (i.e., Mount McKinley). We therefore assume any documented, well constrained, best-fit thermal model cooling rate change from slow (~5 °C/Ma) to rapid (≥~10 °C/Ma) represents a definitive increase in exhumation-related cooling (e.g., Figure 3R.1). We choose a rate of ~10 °C/Ma to avoid rate changes that are simply a reflection of the limitations in the T-t window of the thermochronometers/analytical methods used. Although arguably arbitrary, the use of a standard rapid-rate-change limit (≥~10 °C/Ma) allows us to compare cooling rate trends between samples from the high peak region of the eastern Alaska Range. Once individual samples (Figure 3.8) begin to cool at a rate greater than ~10 °C/Ma, most continue to cool at an equal or higher rate through the low end K-spar blocking temperature (~150°C). Sample 18BAL is an exception, where after a period of rapid cooling the sample records a period of slow cooling (<~10 °C/Ma).

3.6.2 **Initiation of Rapid Exhumation**

Based on the emplacement age (~70 Ma) of plutons in the Black Rapids Glacier region, the closure ages of 20-24 Ma for muscovite and biotite from samples 26RAP and 28RAP (Table 3.1 and Figure 3.5) reflect cooling related to

exhumation and not cooling related to initial pluton emplacement. Assuming an $^{40}Ar/^{39}Ar$ closure temperature of ~400 °C for muscovite [*Harrison et al.*, 2009] and ~350 °C to ~300 °C for biotite [*McDougall and Harrison*, 1999], the difference in muscovite and biotite closure ages for sample 26RAP (~4 Ma) indicates a cooling rate between ~24 °C/Ma and ~12 °C/Ma. The difference in muscovite and biotite closure ages for sample 28RAP (~4 Ma) reflects a cooling rate between ~27 °C/Ma and ~13 °C/Ma. Regardless of which biotite closure temperature is used for samples 26RAP and 28RAP, micas from these samples demonstrate rapid cooling. We infer that the cooling is related to rock uplift and that rapid exhumation in the eastern Alaska Range began by ~24 Ma.

3.6.3 **Standard Thermochronological Approach vs. the Vertically Stacked Approach**

If we apply standard "break in slope" exhumation analysis to the thermal history of sample 26BAL from the eastern Alaska Range (Figure 3.8), it appears that an exhumation "event" began at ~21 Ma. If we look at the thermal history of sample 22DEB from the eastern Alaska Range (Figure 3.8), 25 km to the west of sample 26BAL, it appears that a different exhumation "event" began at ~9 Ma. Applying the same approach to the remaining samples would suggest additional exhumation "events". Previous interpretation of the thermal history of the entire eastern Alaska Range from a few individual samples concluded that exhumation

was episodic in response to changes in Pacific plate motion [*Layer and Benowitz*, 2008].

Another common thermochronological method used to interpret an orgoen's exhumation history is to make a composite plot of the best-fit K-spar thermal model from numerous samples [e.g. *Metcalf et al.*, 2009]. When we perform this technique with the eight samples from the high-relief eastern Alaska Range, it appears that there is indeed an initiation of rapid exhumation, but the timing ranges from ~21 Ma to ~8 Ma (Figure 3.10). This result does not help to constrain the regional exhumation history, arguably because thermal histories of individual samples may reflect small-scale (km) variations in near-field conditions such as dip along the Denali fault [*Benowitz et al.*, 2011; *Mériaux et al.*, 2009].

The stacked approach presented here (Figure 3.9) reveals that, although the location of rapid exhumation varies over time, orogenesis has been occurring within the region quite persistently since ~24 Ma (K-spar and mica analysis combined). From these findings we now believe that our previous work [*Layer and Benowitz*, 2008] misinterpreted the lack of evidence for exhumation to conclude that no exhumation occurred. The stacked approach reveals a more complete and coherent story that indicates that the focus of rapid exhumation in the eastern Alaska Range varied spatially through time and reflects a long history of persistent deformation. We also believe that the stacked approach better constrains the initial

timing of rapid exhumation in the eastern Alaska Range and makes the case that there is no single all-encompassing uplift age for the entire region.

Thus, interpreting thermochronological data sets by classical means such as composite plots, a single vertical transect or single-sample thermochronological analyses is not an appropriate technique for the eastern Alaska Range. We suspect this may also be the case for many other orogens. We do appreciate that thermochronologic sampling that is limited in location or number provides initial control on the thermal evolution of an orogen, but once a large enough sample set is collected we recommend viewing the data as a continuum.

3.6.4 **A New View Of Eastern Alaska Range Exhumation Rates**

Assuming a geothermal gradient of ~30 °C/km [*Fisher et al.*, 2004], as discussed in the methods section, rapid exhumation has occurred in at least one location within the eastern Alaska Range at a persistent rate of ~0.9 km/Ma between ~24 Ma and ~6 Ma. This is roughly the same average exhumation rate from ~6 Ma to present as determined by apatite fission track work in the Nenana Glacier region [~1.0 km/Ma; *Perry et al.*, 2010], if calculated with the same 30 °C/km geothermal gradient applied in this study. It is not yet fully clear from the current low-temperature data [*Benowitz et al.*, 2011; *Perry et al.*, 2010; *Armstrong et al.*, 2007] whether there has been an overall increase in the regional extent of rapid exhumation since ~3 Ma in the eastern Alaska Range. At approximately 3 Ma there was a worldwide shift in global temperatures towards a cooler climate and the

onset of Northern Hemisphere Glaciation [*Zachos et al., 2001; Lisiecki and Raymo 2005*]. The coupling between climate instability and tectonics [*Molnar and England*, 1990; *Whipple*, 2009; *Clift*, 2010] is a subject of continued debate. Further research will investigate the climate-tectonic link in the sub-arctic eastern Alaska Range during the Pliocene-Quaternary transition with a focus on the spatial extent of changes in exhumation rate.

3.6.5 **Mechanism for Spatially Varying Exhumation Patterns**

Two distinct patterns are documented in biotite, K-spar minimum, AFT and AHe cooling ages in the eastern Alaska Range from previous work (Benowitz et al., 2011). Cooling ages on the north side of the Denali fault decrease towards the Fault and generally decrease from east to west adjacent to the north side of the Fault. The same general trends are documented in the MDD best-fit thermal models from the eastern Alaska Range (Figures 3.2, 3.8, 3.9, 3.11, 3.12). Both data sets document that the youngest cooling ages and youngest initiation of rapid cooling in thermal models occur adjacent to the north side of the Denali fault and generally decrease east to west (Figure 3.12).

A possible explanation for this unusual pattern of east to west variation in initiation of rapid cooling rates is focused deformation related to lateral migration of a short section of the southern Alaska block (south side of the Denali fault) [*St. Amand, 1957*; *Page et al.*, 1995; *Haeussler*, 2008] that has a non-vertical fault plane as suggested by *Benowitz et al.* [2011] and by *Mériaux et al.* [2009]. Based

on variations in paleo-slip rates, *Mériaux et al.* [2009] proposed that the southern Alaska block is moving to the northwest with no rotation. Our exhumation data in part supports their conclusions that the southern Alaska block is converging with stable North America and sections of the Denali fault have a non-vertical fault plane. The fact that initiation of rapid exhumation systematically migrated east to west along the Denali fault implies lateral migration of a fault asperity through time. The implication is that the asperity is on the southern Alaska block side of the Denali fault, and hence the southern Alaska block, has been moving west since at least ~24 Ma. In addition, the presence of contractional structures on the south side of the Denali fault, such as the Susitna thrust fault [*Crone et al.*, 2004] supports a rotating southern Alaska block. This differs from the *Mériaux et al.* [2009] model, which suggests no rotation. Further research is needed to constrain both the timing and extent of southern Alaska block rotation.

The decrease in cooling ages and initiation of rapid exhumation towards the Denali fault is a common pattern along transpressive strike-slip faults [e.g., *Little et al.*, 2005]. This pattern is most likely related to differential unroofing adjacent to the master strand of the Denali fault caused by a combination of a non-vertical fault dip as discussed above and erosional weakness of the fault zone (Figure 3.12).

3.6.6 **Alaska Range Deformation in Response to the Yakutat Collision**

The long-term occurrence of rapid exhumation in the eastern Alaska Range demands a long-term, continuous tectonic driving mechanism. The progressive

collision of the Yakutat microplate with south-central Alaska is an obvious candidate [*Plafker*, 1987; *Spotila and Berger*, 2010]. The Yakutat microplate is composed of crystalline crust that is 24–27 km thick and inferred to have an oceanic plateau origin [*Christeson et al.*, 2010]. The Yakutat microplate is currently undergoing flat-slab subduction beneath the Chugach-Saint Elias Mountains, with a northern edge 500 km inboard of the subduction zone at a depth of ~100 km, based on tomographic studies [*Eberhart-Phillips et al.*, 2006]. The arrival time of the Yakutat microplate into the southern Alaska subduction zone is thought to be ~25 Ma [*Plafker et al.*, 1994], yet it remains unclear when "collision" began [e.g. *Spotila and Berger*, 2010]. We define "collision" in this case as highly coupled flat-slab subduction. The stacked thermochronology data presented here demonstrate an increase in exhumation rate at ~24 Ma in the eastern Alaska Range, potentially in response to Yakutat collision.

Other regions of Alaska also show evidence of a late Oligocene/early Miocene rate change in regional tectonic forcing. *Ridgway et al.* [2007] suggested that the strata of the Tanana Basin encompass the entire Neogene and showed that the basin is genetically related to the formation of the Alaska Range. Thermochronological work in the Tordrillo Mountains [*Haeussler et al.*, 2008], ~50 km west-northwest of Anchorage, Alaska (Figure 3.1) indicates that rapid exhumation began there at ~23 Ma. Detrital zircon fission track work in the Chugach-St. Elias Range at Alaska's southern margin [*Enkelmann et al.*, 2008]

shows a pulse of exhumation beginning at ~25 Ma. Recent AFT work in southwestern Alaska indicates rapid cooling in both plutonic and meta-sedimentary samples between ~24 Ma and ~20 Ma, implying regional cooling due to exhumation during this time period (Figure 3.1) [*O'Sullivan et al.*, 2010]. Deformation and metamorphism was occurring on part of the far-eastern Denali fault by ~18 Ma (*Richter*, 1976). In addition, the Wrangell volcano field became active at ~26 Ma and is associated with convergence of the Yakutat microplate [*Richter et al.*, 1990]. It is clear that significant deformation across southern Alaska was initiated by ~24 Ma and continues today.

In terms of kinematics, *Koons et al.* [2010] use a three-dimensional thermal-mechanical numerical model to show that both near-field (i.e. Chugach/Saint Elias) and far-field (i.e. the Alaska Range) mountain ranges can develop from Yakutat microplate collision. An alternative model [*Soofi and Wu*, 2008] use a thin-viscous-sheet model to investigate the effect of the Yakutat microplate colliding with Alaska. The model predicts topographic development where the Alaska Range is located and demonstrates that lateral strength heterogeneities in the crust play a role in the location of deformation. The timing of deformation predicted by the models differs from our new geological constraints, but the general concepts of the models are still applicable.

An analog for the Yakutat collision is the India-Asia collision, where modeling predicts that intra-plate deformation in the Tibet region began soon after

collision and was caused by an indenting boundary concentrating strain along the southern edge of the strong Tarim Basin region [*Dayem et al.*, 2009]. Similarly, the deepest Neogene exhumation recorded in the Alaska Range is located at the apex of the curve in the Denali fault, with the late Paleozoic metamorphic Yukon- Tanana terrane to the north possibly acting as a strong backstop that concentrates strain from the Yakutat microplate collision. An alternative scenario is that the Hines Creek Fault (Figure 3.2), a major tectono-stratigraphic boundary that offsets the Moho, is acting like a backstop itself (Fig. 3.2) [*Veenestra et al.*, 2006].

Constraining the initial timing of tectonic plate collisions has proven problematic [*Zhu et al*, 2005]. Part of the issue is that a lack of thermochronological evidence is not clear-cut proof that rapid exhumation did not occur. As stated at the start of the discussion, exhumation data sets can be quite biased, because samples are difficult to acquire in rugged topography and high erosion rates remove the earliest bedrock record of exhumation, causing unroofing histories to be incomplete. The issue of along- and across-strike variations in focus of exhumation also makes interpretations difficult. Other records, like nearby basin depositional histories, other regional thermochronological data and the timing of associated magmatism can support a thermochronological interpretation. Indeed, the onset of eastern Alaska Range exhumation and arrival of the Yakutat microplate are coeval, around ~25 Ma. Geophysically plausible kinematic mechanisms have been proposed to drive coeval orogenesis in the Chugach-Saint Elias and Alaska

Ranges. During the Neogene, basin formation and regional magmatism also occurred concurrently in southern Alaska. Although we cannot definitively constrain the timing of the initial collision of the Yakutat microplate, we add the results of this paper to the growing evidence that collision was underway by ~24 Ma (Figure 3.12).

3.7 **Conclusions**

In this paper we investigated the spatially variable exhumation history of the eastern Alaska Range and the far-field driving mechanism for regional Neogene deformation in southern Alaska using a novel graphical approach for thermochronological analysis. We suggest that temporal and spatial variations in the focus of exhumation and thermochronologic data bias (sample collection/preservation) often lead to interpretations of episodic exhumation when in fact persistent exhumation may have been occurring. These problems can be addressed by stacking the thermal history curves of spatially diverse samples to examine the long-term history of an orogen.

Based on stacked K-spar MDD thermal models and mica $^{40}Ar/^{39}Ar$ thermochronology of samples collected over a ~100 km transect from the eastern Alaska Range, we show that sub-orogen scale regions have cooled rapidly at an average rate of ~26 °C/Ma between ~24 Ma and the present. Although the focus of exhumation varied over time, continual exhumation at a rate of ~0.9 km/Ma has occurred somewhere within the eastern Alaska Range since ~24 Ma.

The preponderance of evidence from thermochronology and basin analysis data shows initiation of rapid exhumation by ~24 Ma in southern Alaska that continues to the present. Collision of the Yakutat microplate is the most plausible far-field driving mechanism, and we suggest that it began at ~24 Ma, as was first proposed by *Plafker et al.* [*1994*]. We also postulate that progressive collision of the Yakutat block accounts for motion of the southern Alaska block, slip on the Denali fault and orogenesis throughout southern Alaska.

3.8 **Acknowledgements**

We thank Peter Haeussler, Paul Fitzgerald, and Stephanie Perry for helpful discussions on the Neogene tectonic history of Alaska. This project would not have been possible without the field-assistance from Sam Herreid, Andy Sterns, and Rob Wing. The manuscript benefited from a through pre-review by Wes Wallace. Support was provided by the National Science Foundation through grant EAR #0952793.

3.9 Figures

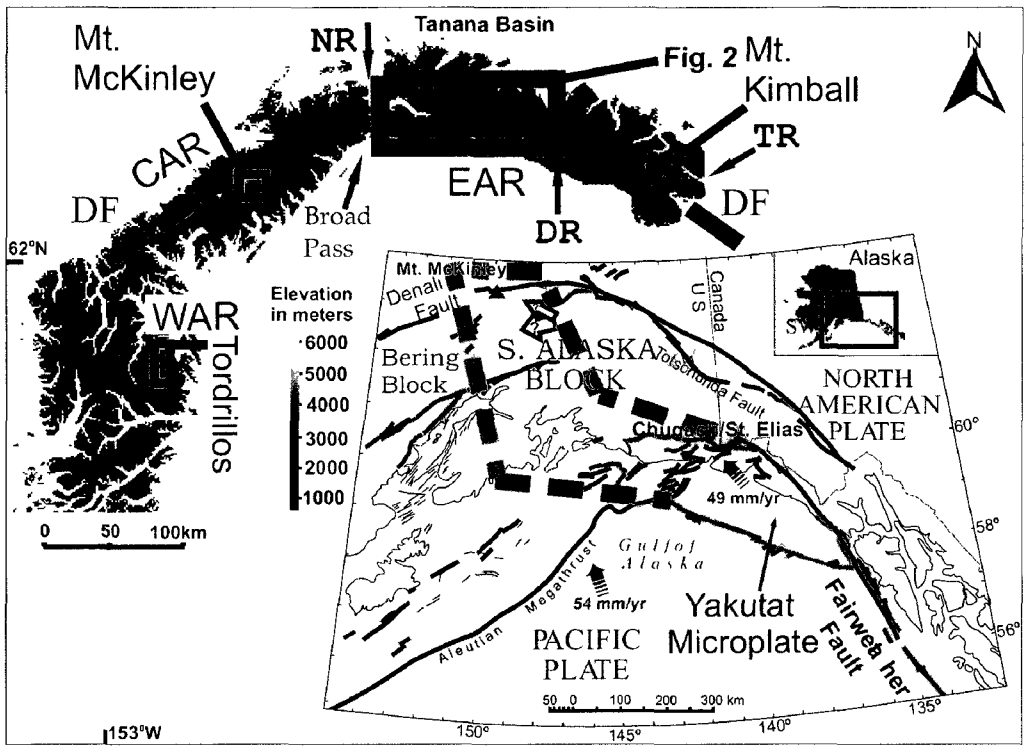

Figure 3.1: Tectonic map of southern Alaska. Modified from *Haeussler et al.*, 2000. Major faults, tectonic plates, and tectonic blocks are labeled. Yakutat–North America plate motion (solid arrow) is from *Fletcher and Freymueller* [2003]. The open arrows show the hypothesized direction of movement of the southern Alaska block with respect to North America. The present location of the subducted Yakutat slab beneath the continental margin is denoted [after *Eberhart-Phillips et al.*, 2006]. A detailed digital elevation model of the Alaska Range flooded to 1000 m is used to emphasize topography. The main topography of the western and central Alaska Range is south of the Denali fault. The main topography in the eastern Alaska Range is north of the Denali fault. The rectangle delineates the study area in the eastern Alaska Range along the Denali fault shown in Figure 3.2. WAR: Western Alaska Range; CAR: Central Alaska Range: EAR: Eastern Alaska Range; DF: Denali fault;NR: Nenana River; DR: Delta River. TR: Tok River. Mount Mckinley [Denali] and Mount Kimball locations noted. Small digital elevation model of all of Alaska. SW: Southwest Alaska samples.

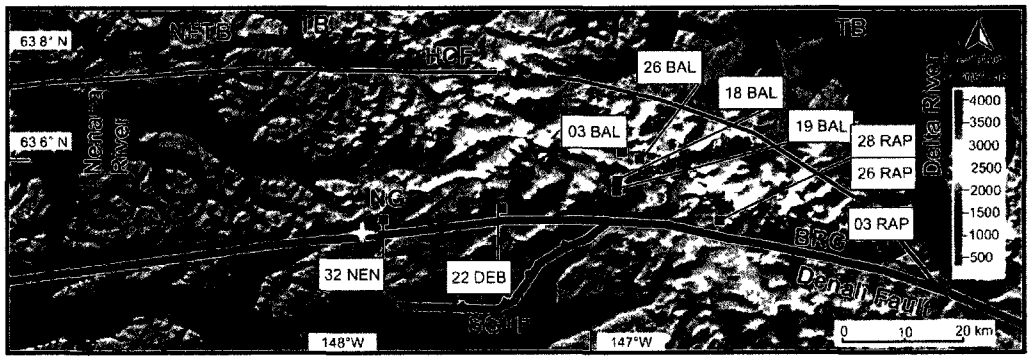

Figure 3.2: Colored digital elevation map of the eastern Alaska Range, showing labeled sample locations and major faults. Purple sample labels are new data. Black sample labels from Benowitz et al. [2011]. Sample 01KIM (Kimball) is located 90 km to the east of the Delta river. The red cross shows the epicenter of the November 2, 2002 **M**7.9 Denali Fault earthquake; the yellow cross the epicenter of the October 23, 2002 **M**6.7 Nenana Mountain earthquake. TB: Tanana Basin; NFTB: northern foothills thrust belt; HCF: Hines Creek fault; NG: Nenana Glacier; SGTF: Susitna Glacier thrust fault; BRG: Black Rapids Glacier. Red sample labels are new data. Black sample labels from *Benowitz et al.* [2011].

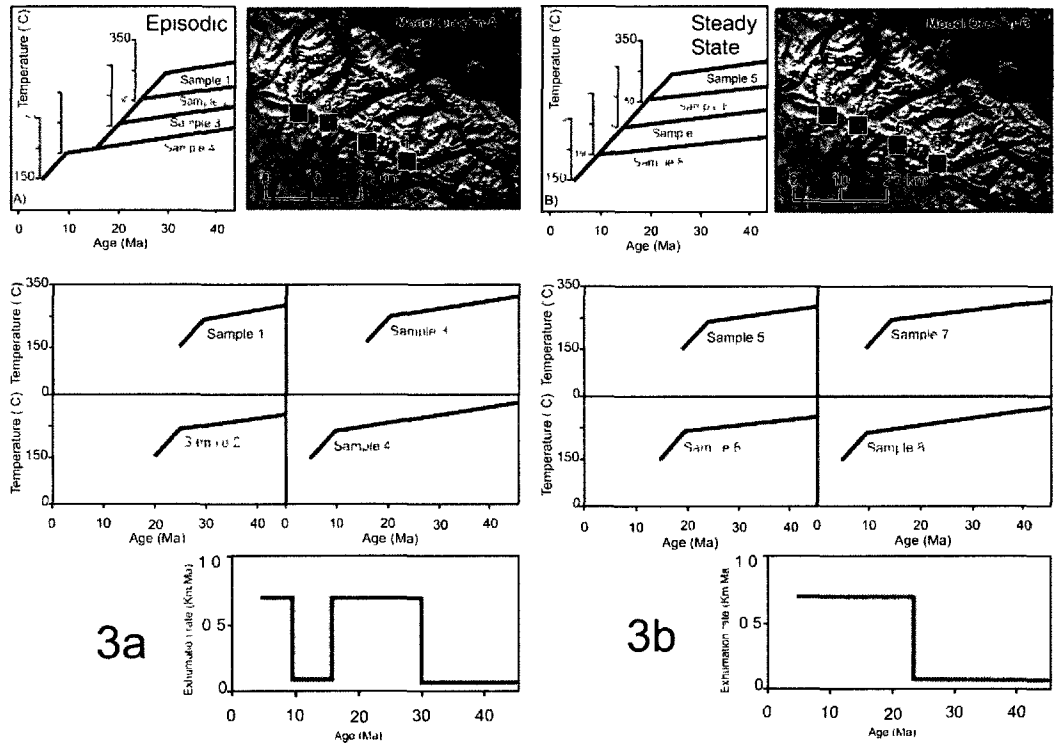

Figure 3.3: Conceptual schematic illustration of the stacked thermochronology approach. Given the assumption that each modeled orogen's complete thermal history is represented by four samples, these schematic figures illustrate two end-member scenarios for the stacking of K-spar MDD thermal models from an orogen experiencing a] Episodic exhumation and b] Persistent exhumation. For both scenarios, notice that if each sample set is viewed individually, it appears that each orogen experienced numerous discrete exhumation events. When the effect of spatial variations in the focus of exhumation is removed by stacking region-wide data, orogen "A" experienced two distinct exhumation events whereas orogen "B" experienced persistent rapid exhumation somewhere at a relatively constant rate after a single change in tectonic process and/or rate. Exhumation rate based on an assumed thermal gradient of 30 °C/ km.

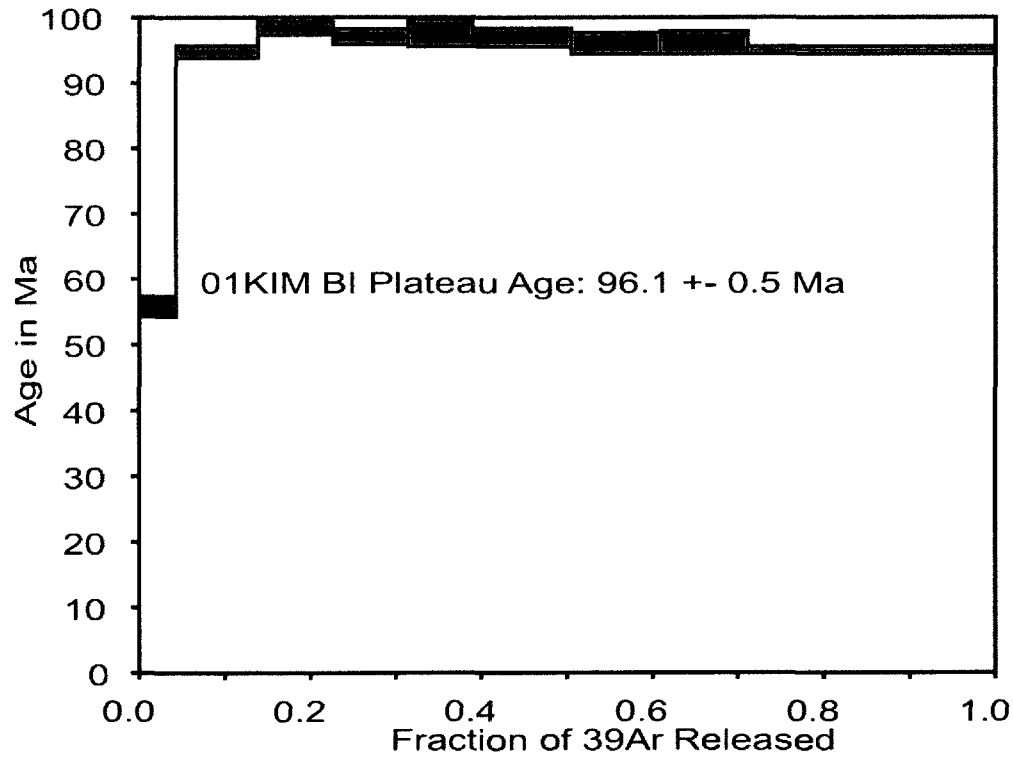

Figure 3.4: Biotite $^{40}Ar/^{39}Ar$ age spectrum for sample 01KIM. Showing a simple diffusional loss profile and a well-defined plateau.

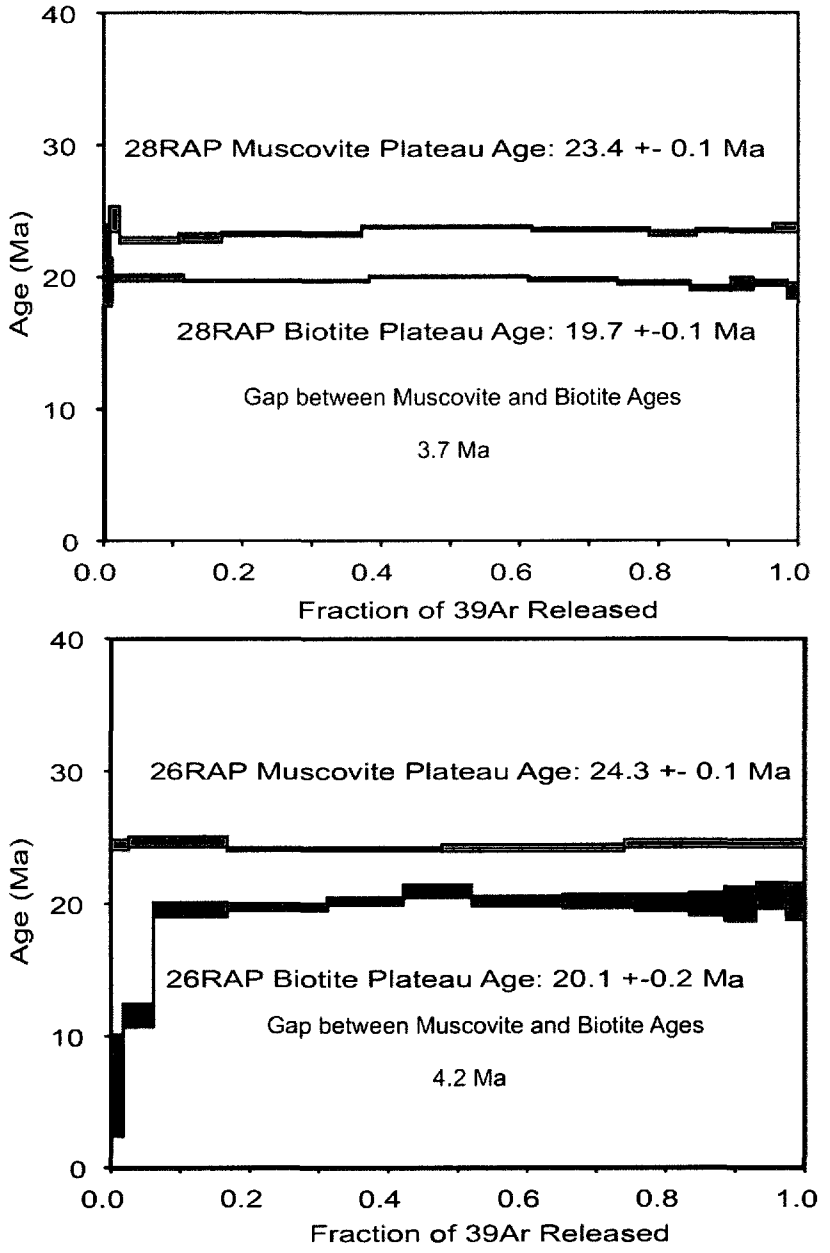

Figure 3.5: Muscovite/biotite $^{40}Ar/^{39}Ar$ age spectra pairs for sample 26 and 28 RAP. Showing a simple diffusional loss profile and a well-defined plateau. The "gap" represents the time between closure for the two distinct phases.

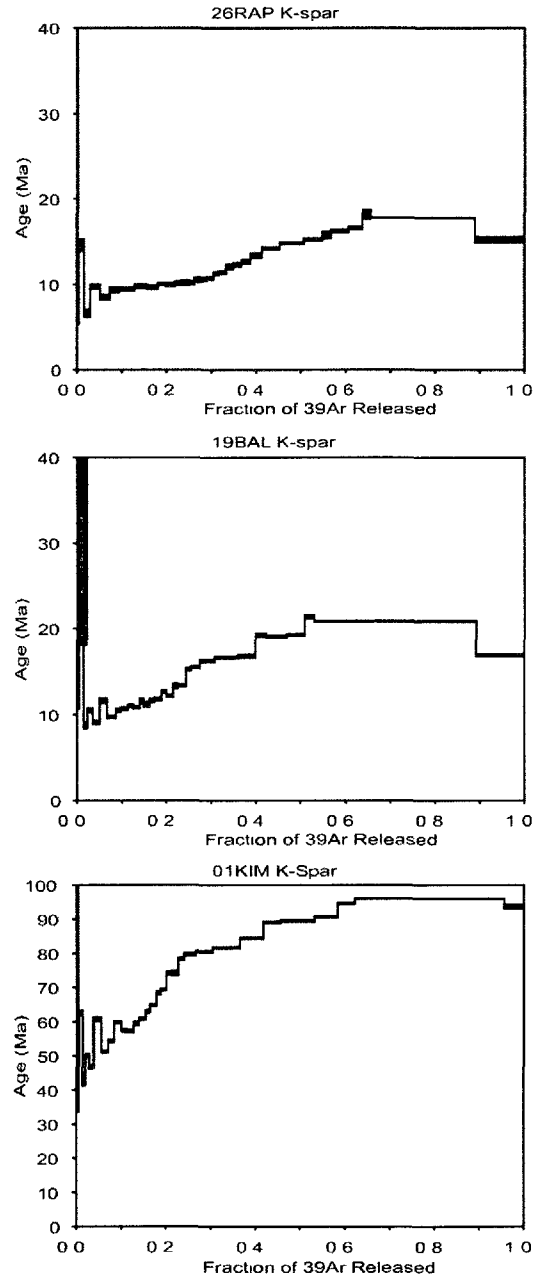

Figure 3.6: Complexly down-stepping K-spar $^{40}Ar/^{39}Ar$ age spectra. From samples 01KIM, 26RAP, and 19BAL.

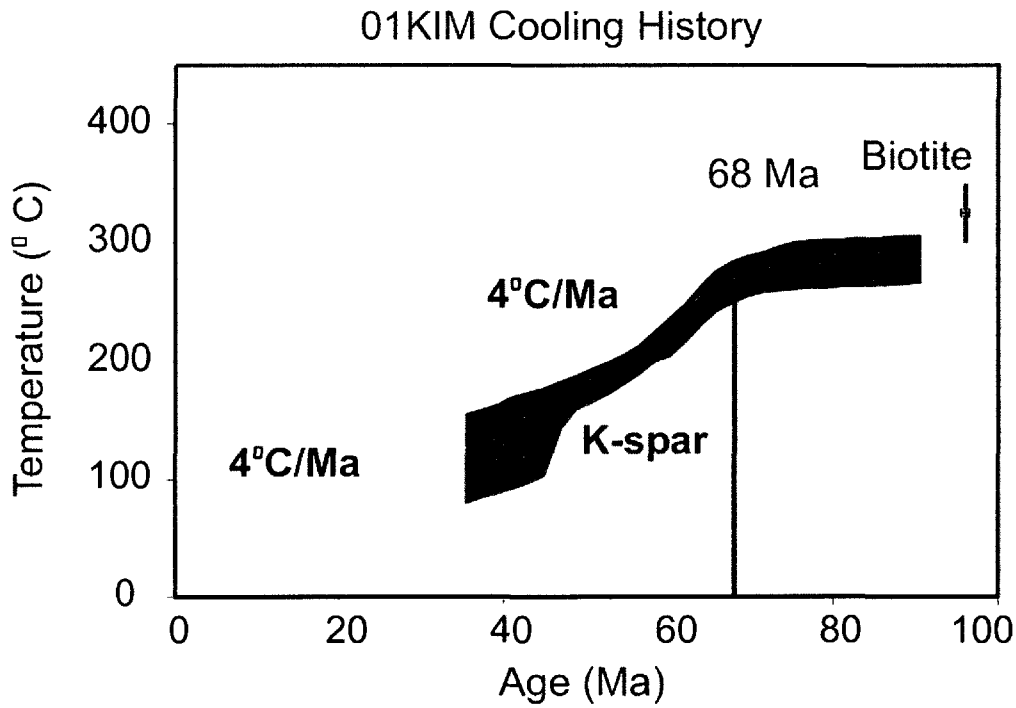

Figure 3.7: Monotonic multiple diffusion domain (MD) thermal model generated for K-spar and biotite ages from sample 01KIM. The MDD magenta band is the 90% confidence interval of the mean and the purple band is the 90% confidence of the distribution. The yellow bar is a projection of the long-term cooling rate past the closure temperature of K-spar to the present.

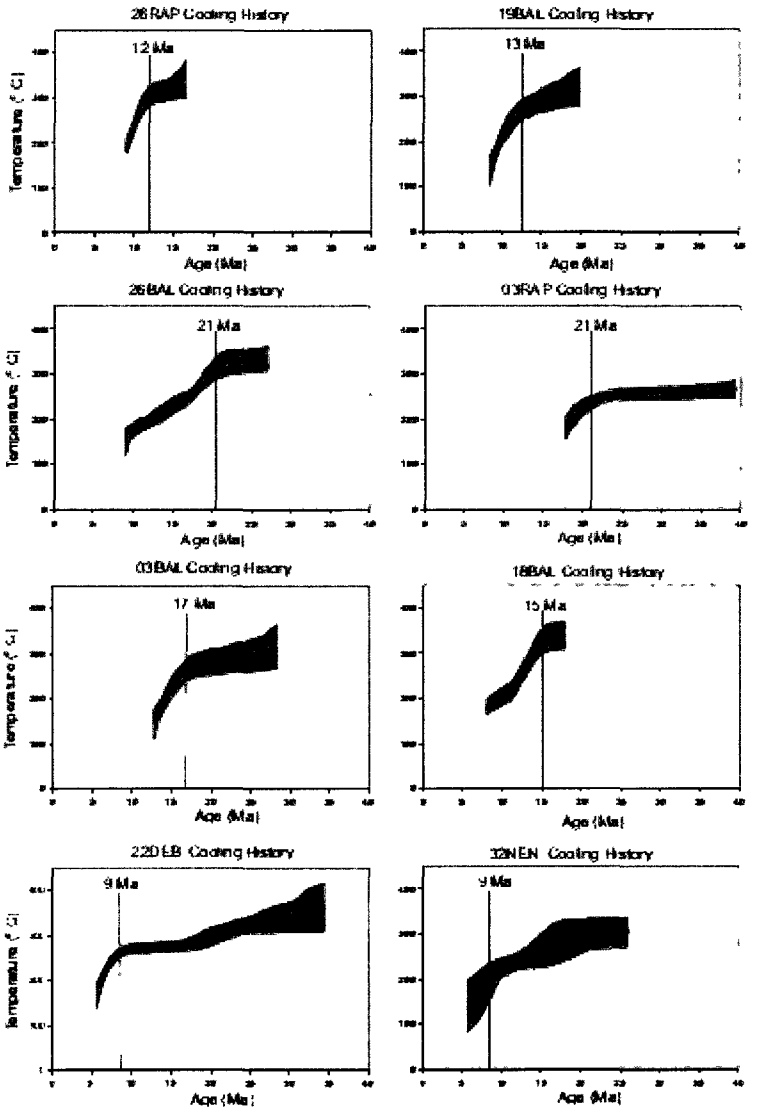

Figure 3.8: Monotonic multiple diffusion domain (MDD) thermal model generated for K-spar from samples 26RAP, 19BAL, 26BAL, 03RAP, 03BAL, 18BAL, 22DEB, and 32NEN. The MDD magenta band is the 90% confidence interval of the mean and the purple band is the 90% confidence of the distribution. Black lines mark exhumation rate knick points.

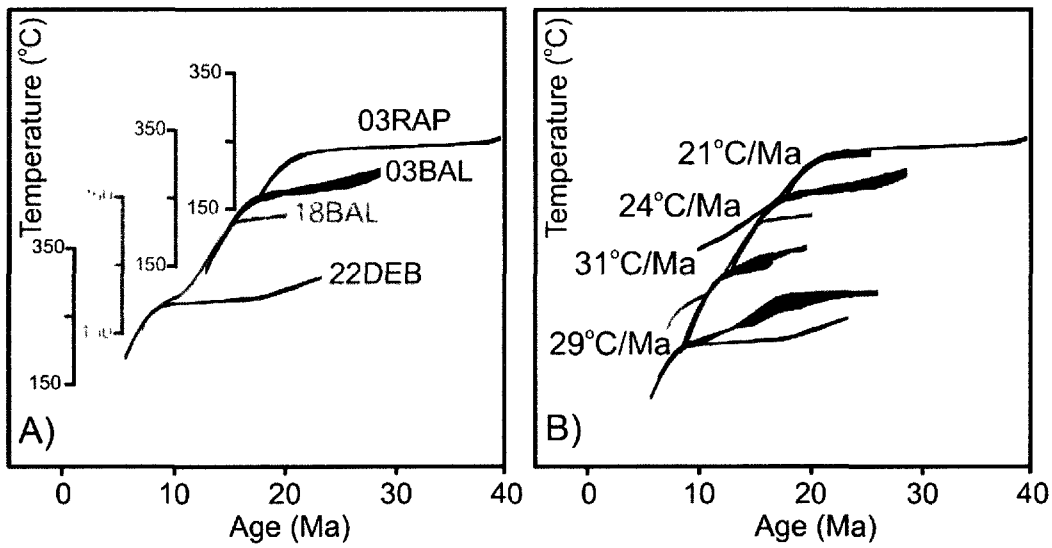

Figure 3.9: A) Example stacked MDD 90% confidence interval of the mean from samples 03 RAP, 03BAL, 18BAL, 22DEB from the high peak region of the eastern Alaska Range with temperature window shown for each sample. B) Stacked MDD 90% confidence interval of the mean of all the samples from the high peak region of the eastern Alaska Range (26RAP, 19BAL, 26BAL, 03RAP, 03 BAL, 18BAL, 22DEB, and 32NEN). Average rapid cooling rate labeled. Temperature windows removed for clarity.

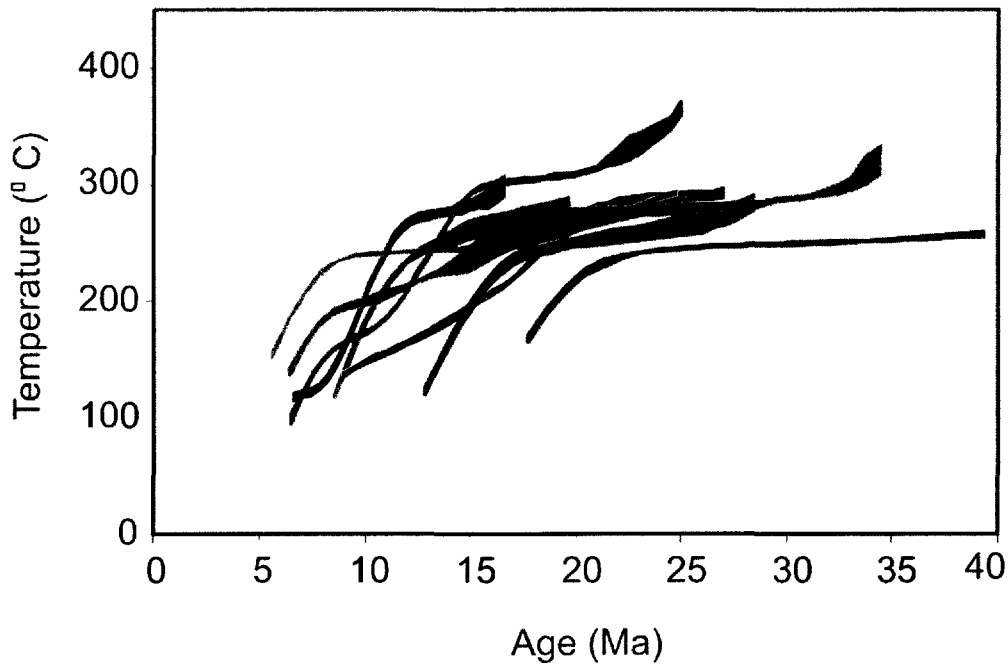

Figure 3.10: Standard composite of the MDD 90% confidence interval of the mean from samples from the high peak region of the eastern Alaska Range (26RAP, 19BAL, 26BAL, 03RAP, 03 BAL, 18BAL, 22DEB, and 32NEN).

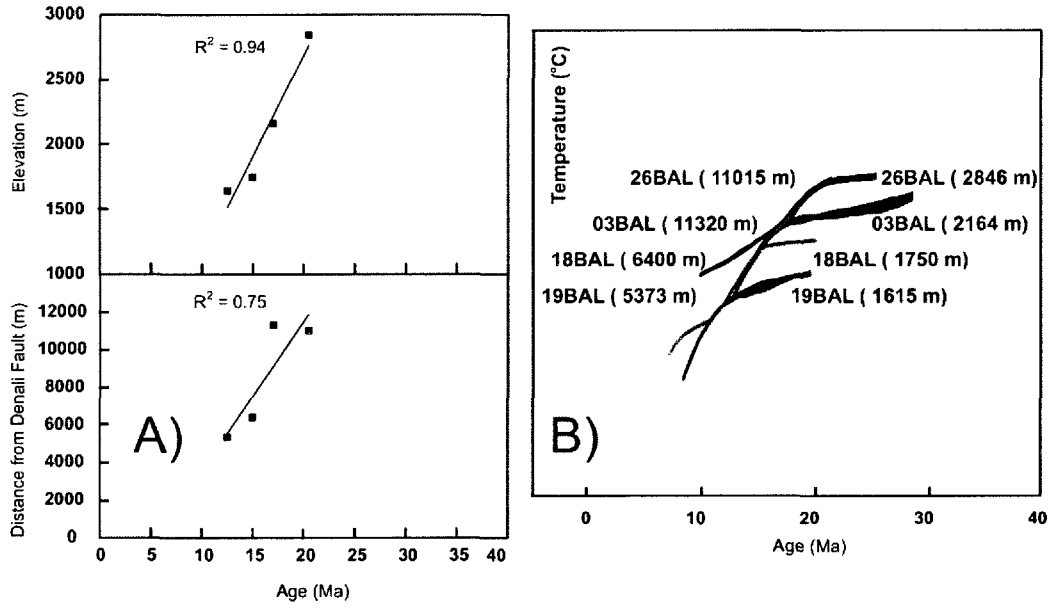

Figure 3.11: A) Age of initiation of rapid cooling versus distance from the Denali fault and elevation above sea level for all samples from the Balchen transect shown in figure 3.2. The Denali fault is interpreted to lie in the center of glacier in the study area. Lines show best linear fit to data points of same thermochronology method. Correlation coefficient is shown next to the best-fit lines. Although age of initiation of rapid cooling is correlated overall with both elevation and distance from the Denali fault, elevation is more significant. B) Stacked MDD 90% confidence interval of the mean of all four BAL (Balchen) samples with sample elevation and distance from the Denali fault in meters.

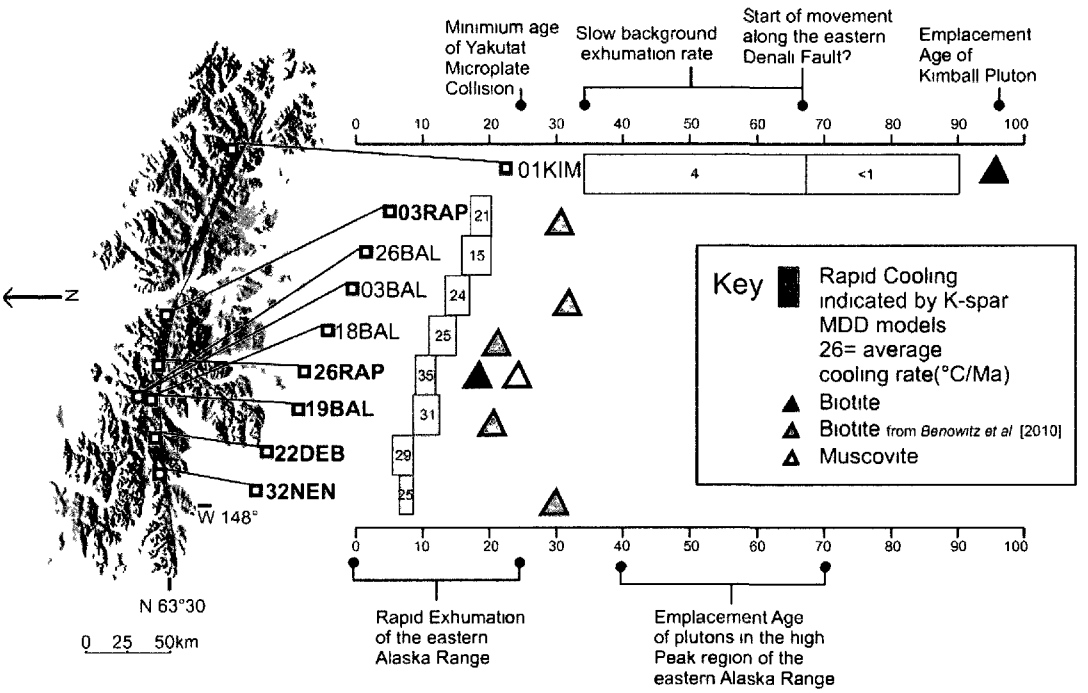

Figure 3.12: Summary figure of K-spar MDD thermal models and mica closure ages for the eastern Alaska Range. Base map is detailed digital elevation model of eastern Alaska Range flooded to 1000 m to emphasize topography. The thermal history of 01KIM on the southeast edge of the high peak region indicates slow post-emplacement cooling followed by slower background exhumation related to inferred movement along the Denali fault. Initiation of rapid cooling from samples from the high peak region is based on the well-constrained thermal model of each sample (Figure 3.8) at the initial point where cooling is > 10 °C/Ma. Average rapid cooling rate (°C/Ma) is a minimum time-averaged, long-term, rapid-cooling rate > 10 °C/Ma. Bold sample labels indicate close proximity to fault. Grey filled triangles are biotite cooling ages from *Benowitz et al.* [2011]. Error bars for the micas are smaller than the symbols used and so the symbols approximate the error.

3.10 **Tables**

Table 3.1: Sample location, rock type and age summary data for feldspars and micas.

Location	Elevation	Mineral	Integrated Age (Ma)	Plateau Age (Ma)	# of steps	MSWD	% of ^{39}Ar Release
01KIM granite							
63 1694°N	1420 m	K-spar	84 6±0 2	-	-	-	-
144 60362°W		biotite	94 8 ± 0 5	96 1 ± 0 5	8	1 87	95 4
19BAL granite							
63 5713°N	1615 m	K-spar	18 0 ±0 9	-	-	-	-
146 94813°W							
26RAP pegmatite granite							
63 519272°N	2076 m	K-spar	14 0±0 1	-	-	-	-
146 60105°W		biotite	19 5± 0 2	20 1 ± 0 2	11	0 61	93 8
		muscovite	24 3± 0 1	24 3 ± 0 1	4	1 52	97 5
28RAP pegmatite granite							
63 514757°N	2313 m	biotite	19 7 ± 0 1	19 7± 0 1	9	1 92	77 0
146 61361°W		muscovite	23 4 ± 0 1	23 4 ± 0 1	5	2 16	62 8

3.11 **References**

Aleinikoff, J.N., G.L. Farmer, R.O. Rye, and W.J. Nokleberg (2000), Isotopic evidence for the sources of Cretaceous and Tertiary granitic rocks, east-central Alaska: implications for the tectonic evolution of the Yukon–Tanana terrane. *Can. J. of Ear. Sci.*, v. 37: p. 945–956.

Armstrong, P, P. Haeussler, and J. Arkle (2007), Rapid Quaternary exhumation of the Eastern Alaska Range, *Geological Soc. Am. Abs. w. Progs*. V. 39(4), p. 71.

Benowitz, J., P.W. Layer, P. Armstrong, S. Perry, P.J. Haeussler, P.G. Fitzgerald, and S. Vanlaningham (2011), Spatial Variations in Focused Exhumation Along a Continental-Scale Strike-Slip Fault: the Denali Fault of the Eastern Alaska Range, *Geosphere,* v. 7; no. 2; p. 455-467; DOI: 10.1130/GES00589.1

Bernet M, M. Brandon, J. Garver, M.L. Balestieri, B. Ventura, M. Zattin (2009), Exhuming the Alps through time: clues from detrital zircon fission-track thermochronology. *Basin Res.* V. 21: p. 781–98

Berger, A. L., J. A. Spotila, J. B. Chapman, T. L. Pavlis, E. E. Enkelmann, N. A. Ruppert, and J. T. Buscher (2008), Architecture, kinematics, and exhumation of a convergent orogenic wedge: A thermochronological investigation of tectonic-climatic interactions in the central St. Elias orogen, Alaska, *Earth Planet. Sci. Lett.*, 270, 13 – 24, doi:10.1016/j.epsl.2008.02.034.

Braun, J.P. van der Beek, and G. Batt (2006), *Quantitative Thermochronology: Numerical methods for the interpretation of thermochronological data*. Cambridge University Press, Cambridge. 270 p.

Christeson, G.L., S.P.S. Gulick, H.J.A. van Avendonk, L. Worthington, R.S. Reece, and T.L. Pavlis (2010), The Yakutat terrane: Dramatic change in crustal thickness across the Transition fault, Alaska, *Geology*, v. 38; no. 10; p. 895-898; DOI: 10.1130/G31170.1

Clift, P. D. (2010), Enhanced global continental erosion and exhumation driven by Oligo-Miocene climate change, *Geophys. Res. Lett.*, v. 37, L09402, doi:10.1029/2010GL043067.

Clift, P. D. and S. VanLaningham (2010), A climatic trigger for a major Oligocene-Miocene unconformity in the Himalayan foreland basin, *Tectonics*, 29, TC5014, doi:10.1029/2010TC002711.

Crone, A.J., S. Personius, P.A. Craw, P.J. Haeussler, and L.A. Staft (2004), The Susitna Glacier thrust fault—characteristics of ruptures that initiated the 2002 Denali fault earthquake, *Bull. Seis. Soc. Amer.*, v. 94(6B), p. S5-S22.

Cross, R. S., and J. T. Freymueller (2008), Evidence for and implications of a Bering plate based on geodetic measurements from the Aleutians and western Alaska, *J. Geophys. Res.*, v. 113, B07405, doi:10.1029/2007JB005136.

Csejtey, B., Jr., M.W Mullen, D.P. Cox, and G.D. Stricker, (1992), Geology and geochronology of the Healy quadrangle, south-central Alaska: *U.S. Geological Survey Miscellaneous Investigation Map I-1961*, scale 1:250,000.

Dayem, K., P. Molnar, M. Clark, and G. Houseman (2009), Far-field lithospheric deformation in Tibet during continental collision, *Tectonics*, v. 28, TC6005, doi:10.1029/2008TC002344.

Eberhart-Phillips, D., D.H. Christensen, T.M. Brocher, R. Hansen, N.A. Ruppert, P.J. Haeussler, and G.A. Abers (2006), Imaging the transition from Aleutian subduction to Yakutat collision in central Alaska, with local earthquakes and active source data, *J. Geophys. Res.*, v. 111, B11303, doi:10.1029/2005JB004240

Eberhart-Phillips, D., P. J. Haeussler, J. T. Freymueller, A. Frankel, C. M. Rubin, P. Craw, N. A. Ratchkovski, G. Anderson, G. A. Carver, A. J. Crone, T. E. Dawson, H. Fletcher, R. Hansen, E. L. Harp, R. A. Harris, D. P. Hill, S. Hreinsdóttir, R. W. Jibson, L. M. Jones, R. Kayen, D. K. Keefer, C. F. Larsen, S. C. Moran, S. F. Personius, G. Plafker, B. Sherrod, K. Sieh, N. Sitar, and W. K. Wallace (2003), The 2002 Denali fault earthquake, Alaska: A large magnitude, slip-partitioned event, *Science*, v. 300(5622), p. 1113-1118.

Ehlers, T. A. (2005), Crustal thermal processes and the interpretation of thermochronometer data, in *Low Temperature Thermochronometry: Techniques, Interpretations, and Applications*, Rev. Mineral. Geochem., vol. 58, edited by T. Ehlers and P. W. Reiners, p. 315 – 350, Mineral. Soc. of Am., Washington, D. C.

Enkelmann, E., J.J. Garver, and T.L. Pavlis, (2008), Rapid exhumation of ice-covered rocks of the Chugach-St.Elias orogen, SE-Alaska. *Geology*, v 36, no. 12; p. 915-918 doi:10.1130/G2252A.1

Finzel, E., K. Ridgway, R. Reifenstuhl., R. Blodgett, J. White, P. Decker (2009), Stratigraphic framework and estuarine depositional environments of the Miocene Bear Lake Formation, Bristol Bay Basin, Alaska: Onshore equivalents to potential reservoir strata in a frontier gas-rich basin. *Am. Assoc. Pet. Geol. Bulletin*, v. 93, no. 3, p. 379–405.

Fisher, M. A., N. A. Ratchkovski,W. J. Nokleberg, L. Pellerin, and J. M. G. Glen (2004), Geophysical data reveal the crustal structure of the Alaska Range orogen within the aftershock zone of the Mw 7.9 Denali fault earthquake, *Bull. Seismol. Soc. Am.*, v. 94, p. S107–S131.

Fitzgerald, P.G., E. Stump, T.F. Redfield (1993), Late Cenozoic uplift of Denali and its relation to relative plate motion and fault morphology, *Science*, v. 259, p. 497-499.

Fitzgerald, P.G., R.B. Sorkhabi, T. F. Redfield, and E. Stump (1995), Uplift and denudation of the central Alaska Range: a case study in the use of apatite fission track thermochronology to determine absolute uplift parameters, *J. Geophys. Res.*, v. 100, p. 20,175-20,191.

Fletcher, H. J., and J. T. Freymueller (2003), New constraints on the motion of the Fairweather fault, Alaska, from GPS observations, *Geophys. Res. Lett.*, v. 30(3), p. 1139, doi:10.1029/2002GL016476.

Foley, J. (1985), Petrology, geochemistry, and geochronology of alkaline dikes and associated plutons in the eastern Mount Hayes and western Tanacross quadrangles, Alaska. M.S. Thesis, University of Alaska, Fairbanks.

Haeussler, P.J., R.L. Bruhn, and T.L. Pratt (2000), Potential seismic hazards and tectonics of upper Cook Inlet basin, Alaska, based on analysis of Pliocene and younger deformation, *Geol. Soc. Amer. Bull.*, v. 112, p. 1414-1429.

Haeussler, P. (2008), An Overview of the Neotectonics of Interior Alaska: Far- Field Deformation From the Yakutat Microplate Collision]: in *Active Tectonics and Seismic Potential of Alaska, Geophys. Monogr. Ser.*, edited by J.T. Freymueller, P.J. Haeussler, R. Wesson, and G. Ekstrom, Geophysical Monograph 179, AGU, Washington, D.C. p.83-108.

Haeussler, P., P. O'Sullivan, A. Berger, and J. Spotila (2008), Neogene exhumation of the Tordrillo Mountains, Alaska, and correlations with Denali [Mt. McKinley]: in *Active Tectonics and Seismic Potential of Alaska, Geophys. Monogr. Ser.*, edited by J.T. Freymueller, P.J. Haeussler, R. Wesson, and G. Ekstrom, Geophysical Monograph 179, AGU, Washington, D.C. p. 269-285.

Harrison, T. M., J. Celerier, A. B. Aikman, J. Hermann, M. T. Heizler (2009), "Diffusion of 40Ar in muscovite. *Geochim. Cosmochim. Acta*, v. 73, p. 1039-1051.

Harrison, T. M., M. T. Heizler, O. M. Lovera, W. Chen, and M. Grove (1994), A chlorine disinfectant for excess argon released from K-feldspar during step heating, *Earth Planet. Sci. Lett.*, v. 123, p. 95 – 104.

Ketcham, R.A. (2005), Forward and inverse modeling of low-temperature thermochronometry data, in Reiners, P.W., and Ehlers, T.A., eds., *Low Temperature Thermochronology: Techniques, Interpretations, and Applications: Reviews in Mineralogy and Geochemistry*, v. 58, p. 275–314, doi: 10.2138/rmg.2005.58.11.

Koons, P. O., B. P. Hooks, T. Pavlis, P. Upton, and A. D. Barker (2010), Three-dimensional mechanics of Yakutat convergence in the southern Alaskan plate corner, *Tectonics*, v. 29, TC4008, doi:10.1029/2009TC002463.

Lagoe, M. B., C. H. Eyles, N. Eyles, and C. Hale (1993), Timing of late Cenozoic tidewater glaciation in the far North Pacific, *Geol. Soc. Am. Bull.*, v. 105, p. 1542–1560, doi:10.1130/0016-7606(1993)105< 1542:TOLCTG>2.3.CO;2.

Lanphere, M. A., and G. B. Dalrymple (2000), First-principles calibration of 38Ar tracers: Implications for the ages of 40Ar/39Ar fluence monitors, U.S. Geol. Surv. Prof., 1621.

Layer, P.W. (2000), Argon-40/argon-39 age of the El'gygytgyn impact event, Chukotka, Russia, *Meteor and Planet Science*, v. 35, p. 591-599.

Layer, P. and J. Benowitz (2008), Prolonged Episodic Exhumation in the Eastern Alaska Range in Garver, J. I., and Montario, M., *International Fission-track Conference 2008 Extended Abstracts with Programs*, Anchorage, Alaska, p. 151.

Layer, P.W., C.M. Hall., and D. York (1987), The derivation of $^{40}Ar/^{39}Ar$ age spectra of single grains of hornblende and biotite by laser step heating, *Geophys. Res. Lett.*, v. 14, p. 757-760.

Lisiecki, L.E. and M.E. Raymo (2005), A Pliocene–Pleistocene stack of 57 globally distributed benthic d18O records. *Paleoceanography* 20, PA1003.

Little, T. A., S. Cox, J. K. Vry, and G. Batt (2005), Variations in exhumation level and uplift rate along the oblique-slip Alpine fault, central Southern Alps, New Zealand, *Geol. Soc. Am. Bull.*, v. 117, p. 707 – 723, doi:10.1130/B25500.1.

Lovera, O. M., M. Grove, and T. M. Harrison (2002), Systematic analysis of K-feldspar $^{40}Ar/^{39}Ar$ step heating results: II. Relevance of laboratory argon diffusion properties to nature, *Geochim. Cosmochim. Acta*, v. 66, p. 1237 – 1255.

Lovera, O. M., M. T. Heizler, and T. M. Harrison (1993), Argon diffusion domains in K-feldspar, II, Kinetic properties of MH-10, *Contrib. Mineral. P*etrol., v. 113, p. 381 – 393.

McAleer, R., Spotila, J., Enkelmann, E., Berger, A., 2009, Exhumation along the Fairweather fault, southeastern Alaska, based on low-temperature thermochronometry: Tectonics, v. 28, TC1007, doi:10.1029/2007TC002240.

McDougall, I., and T. M. Harrison (1999), Geochronology and Thermochronology by the $^{40}Ar/^{39}Ar$ Method, Oxford Univ. Press, New York.

Mériaux, A.-S., K. Sieh, R. C. Finkel, C. M. Rubin, M. H. Taylor, A. J. Meltzner, and F. J. Ryerson (2009), Kinematic behavior of southern Alaska constrained by westward decreasing postglacial slip rates on the Denali fault, Alaska, *J. Geophys. Res.*, v. 114, B03404, doi:10.1029/2007JB005053.

Metcalf, J., P. Fitzgerald, S. Baldwin, J. Munoz (2009), Thermochronology of a convergent orogen: Constraints on the timing of thrust faulting and subsequent exhumation of the Maladeta Pluton in the Central Pyrenean, *Earth Planet. Sci. Lett.*, doi:10.1016/j.epsl.2009.08.036.

Miller, M.L., D.C. Bradley, and T.K. Bundtzen, and W. McClelland (2002), Late Cretaceous through Cenozoic strike-slip tectonics of southwestern Alaska: *Journal of Geology*, v. 110, p. 247-270.

Molnar, P., and P. England (1990), Late Cenozoic uplift of mountain ranges and global climate change: Chicken or egg?, *Nature*, 346, 29–34, doi:10.1038/346029a0.

Nokleberg, W.J., J.N. Aleinikoff, J.T. Dutro Jr., M.A. Lanphere, N.J. Silberling, S.R. Silva, T.E. Smith, and D.L.Turner (1992), Map, tables, and summary of fossil and isotopic age data, Mount Hayes quadrangle, eastern Alaska Range, Alaska: *U.S. Geological Survey Miscellaneous Field Studies Map 1996-D*, scale 1:250,000.

O'Sullivan, P.B. and L.D. Currie (1996) Thermotectonic history of Mt. Logan, Yukon Territory, Canada; implications of multiple eposodes of middle to late Cenozoic denudation, *Earth Planet. Sci. Let.*, v. 144, p. 251–261.

O'Sullivan, P., M. Donelick, and R. Donelick (2010), Apatite Fission-Track Results From The Region of The Pebble Deposit, Southwest Alaska, Apatite to Zircon Report 950, *minerals.usgs.gov/mrerp/reports/O'Sullivan-08HQGR0061*.pdf, last accessed 5/5/2010.

Page, R.A., G. Plafker, and H. Pulpan (1995), Block rotation in east-central Alaska: A framework for evaluating earthquake potential?, *Geology,* v. 23, p. 629–632, doi: 10.1130/0091-7613

Perry, S., P. Fitzgerald, and J. Benowitz (2010), Thermotectonic evolution of the eastern Alaska Range: constraints from low-temperature thermochronology, *International Fission-track Conference 2010 Extended Abstracts with Programs*, Glasgow, Scotland.

Plafker, G., J. C. Moore, and G. R. Winkler (1994), Geology of the southern Alaska margin, in *The Geology of North America*, vol. G-1, The Geology of Alaska, edited by G. Plafker and H. C. Berg, p. 389 – 449, Geol. Soc. of Am., Boulder, Colo.

Plafker, G., C. W. Naeser, R. A. Zimmermann, J. S. Lull, and T. Hudson (1992), Cenozoic uplift history of the Mount McKinley area in the central Alaska Range based on fission-track dating, *U.S. Geol. Surv. Bull.*, v. 2041, p. 202-212.

Plafker, G. (1987), Regional geology and petroleum potential of the northern Gulf of Alaska continental margin, in Scholl, D.W., Grantz, A., and Vedder, J.G., eds., *Geology and Resource Potential of the Continental Margin of Western North America and Adjacent Ocean Basins, Beaufort Sea to Baja California*, Volume 6: Houston, Texas, Circum-Pacific Council for Energy and Mineral Resources, p. 229–268.

Reiners, P. W., and M. T. Brandon (2006), Using thermochronology to understand orogenic erosion, *Annu. Rev. Earth Planet. Sci.*, v. 34, p. 419 – 466, doi:10.1146/annurev.earth.34.031405.125202.

Reiners, P. W., T. A. Ehlers, and P. K. Zeitler (2005), Past, present, and future of thermochronology, in Low-Temperature Thermochronology, edited by P. W. Reiners and T. A. Ehlers, *Rev. Mineral. Geochem.*, v. 58, p. 1 – 18.

Richter, D. H., J. G. Smith, M. A. Lanphere, G. B. Dalrymple, B. L. Reed, and N. Shew (1990), Age and progression of volcanism, Wrangell volcanic field, Alaska, *Bull. Volcanol.*, v. 53, p.29–44.

Richter, D.H.(1976), Geologic map of the Nabesna quadrangle, Alaska: *U.S. Geological Survey Miscellaneous Investigations Series Map 1-932*, scale 1:250,000.

Ridgway, K.D., E.E. Thoms, P.W. Layer, M.E. Lesh, J.M. White, and S.V. Smith (2007), Neogene transpressional foreland basin development on the 39 north side of the central Alaska Range, Usibelli Group and Nenana Gravel, Tanana basin, in Tectonic growth of a collisional continental margin: crustal evolution of southern Alaska, *Geol. Soc. Amer. Spec. Pap. 431*, edited by K.D. Ridgway et al., p. 507-547, GSA, Boulder, Colo., doi: 10.1130/2007.2431(20).

Samson, S., and E. Alexander (1987), Calibration of the interlaboratory 40Ar-39Ar dating standard, MMhb-1, *Chem. Geol.*, v. 66, p. 27-34, doi:10.1016/0168-9622(87)90025-X.

Sanders, R.E., M.T. Heizler, and L.B. Goodwin (2006), $^{40}Ar/^{39}Ar$ thermochronology constraints on the timing of Proterozoic basement exhumation and fault ancestry, southern Sangre de Cristo Range, New Mexico: *Geological Society of America Bulletin*, v. 118, no. 11–12, p. 1489–1506, doi: 10.1130/B25857.1.

Seeber, L., Sorlien, C., Steckler, M. and Cormier, M. H. (2010), Continental transform basins: Why are they asymmetric? *EOS*, v. 91, no. 4, p. 29–30.

Soofi, M. and P. Wu (2008), Crustal deformation due to Alaska Yakutat collision, *Journal of Geodynamics*, v. 46, iss. 1-2, p. 38-47., doi:10.1016/j.jog.2008.04.006.

Spotila, J.A. (2005), Applications of lowtemperature thermochronometry to quantification of recent exhumation in mountain belts. In: in Low-Temperature Thermochronology, edited by P. W. Reiners and T. A. Ehlers, *Rev. Mineral. Geochem.*, v. 58.

Spotila, J.A. and A. Berger (2010), Exhumation at orogenic indentor corners under long-term glacial conditions: Example of the St. Elias orogen, Southern Alaska, Tectonophysics, v. 490, p. 241-256. doi:10.1016/j.tecto.2010.05.015.

St. Amand, P. (1957), Geological and geophysical synthesis of the tectonics of portions of British Columbia, the Yukon Territory, and Alaska, *Geol. Soc. Am. Bull.* V. 68, p. 1343–1370.

Steiger, R. H., and E. Jäger (1977), Subcommission on Geochronology: Convention on the use of decay constants in geo- and cosmochronology, *Earth Planet. Sci. Lett.*, v. 36, p. 359-362, doi:10.1016/0012- 821X(77)90060-7.

Stricker, G.D. and R.M. Flores (1996), Miocene fluvial-tidal sedimentation in a residual forearc basin of the northeast Pacific Rim: Cook Inlet, Alaska case study. *Am. Assoc. Petrol Geol. Natl. Meeting*, San Diego, CA, 243 pp.

Thoms, E.E. (2000), Late Cenozoic unroofing sequence and foreland basin developmentof the central Alaska Range: Implications from the Nenana Gravel [M.S. Thesis]:University of Alaska Fairbanks

Tricart, P., P. van der Beek, S. Schwartz, E. Labrin (2007), Diachronous late-stage exhumation across the Western Alpine arc: constraints from apatite fission track thermochronology between the Pelvoux and Dora-Maira Massifs. *Journal of the Geological Society*, London. V. 163, p. 1-12.

Wahrhaftig, C., S. Bartsch-Winkler, and G.D. Stricker, (1994) Coal in Alaska, in Plafker, G. and Berg, H.C., eds., *The Geology of Alaska: The Geology of North America*, G-1, Boulder, Colorado, Geological Society of America, p. 937–978.

Whipple, K. (2009), The influence of climate on the tectonic evolution of mountain belts. *Nature Geoscience,* v. 2, p. 97 – 104.

Veenstra, E., E.E. Christensen, G.A. Abers, A. Ferris (2006), Crustal thickness variation in south-central Alaska, *Geology*, v. 34, no. 9, p. 781–784; doi: 10.1130/G22615.1

Yin, A. (2006), Cenozoic tectonic evolution of the Himalayan orogen as constrained by along-strike variation of structural geometry, exhumation history, and foreland sedimentation, *Earth Sci. Rev.*, v. 76, p. 1– 131.

York, D., C. M. Hall, Y. Yanase, J. A. Hanes, and W. J. Kenyon (1981), 40Ar/39Ar dating of terrestrial minerals with a continuous laser, *Geophys. Res. Lett.*, v. 8, no.11, p. 1136–1138, doi:10.1029/GL008i011p01136.

Zachos, J. C., M. Pagani, L. Sloan, E. Thomas, and K. Billups (2001), Trends, rhythms, and aberrations in global climate 65 Ma to present, *Science*, v. 292, p. 686– 692, doi:10.1126/science.1059412.

Zhu, B., W. S. F. Kidd, D. B. Rowley, B. S. Currie, and N. Shafique (2005), Age of Initiation of the India-Asia collision in the east-central Himalaya, *J. Geol.*, v. 113, p. 265–285, doi:10.1086/428805

3.12 Repository Figures

Time (Ma)	Temp. °C
20	309
19.5	308
19	306
18.5	304
18	303
17.5	300
17	294
16.5	290
16	287
15.5	283
15	280
14.5	277
14	274
13.5	272
13	268
12.5	264
12	258
11.5	248
11	237
10.5	223
10	206
9 5	185
9	160
8 5	140

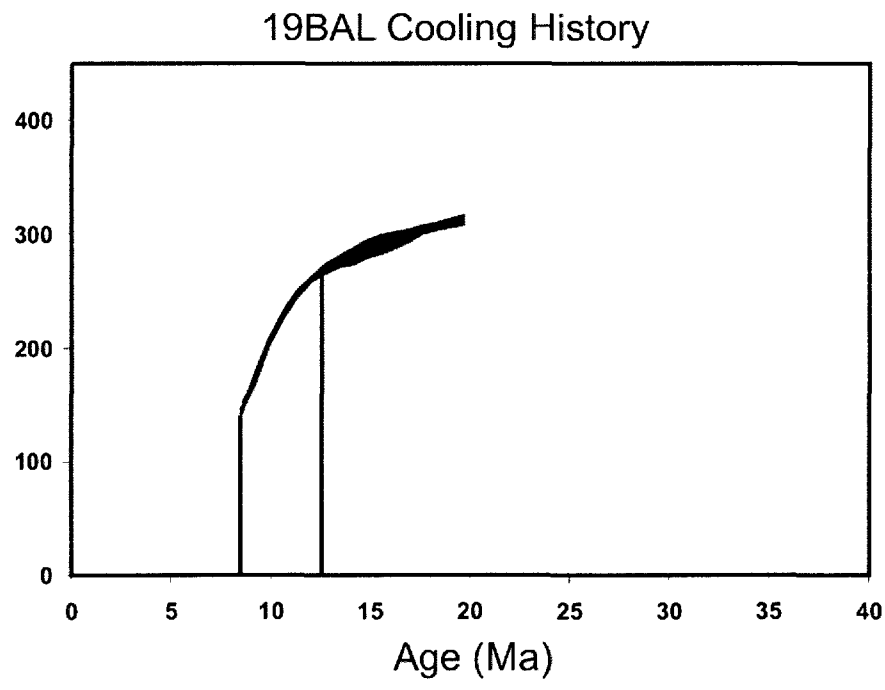

Figure 3R.1: Time-Temperature results from the lower line of best-fit thermal history of sample 19BAL derived from MDD modeling. Rate of $\geq$ 10 °C is used to define rapid-cooling rate knick point.

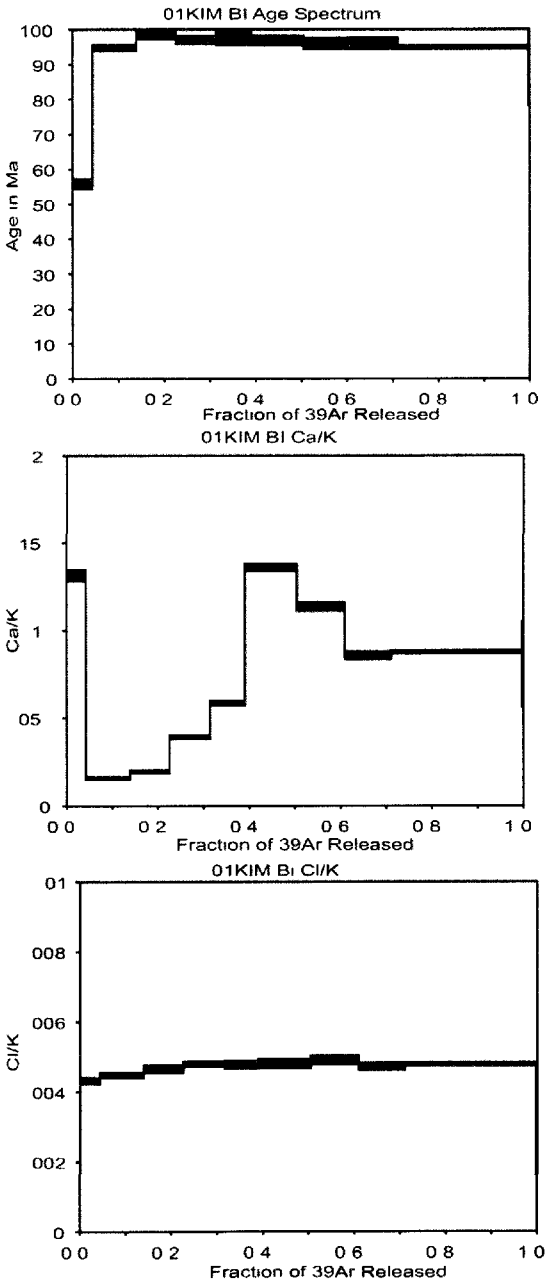

Figure 3R.2: $^{40}Ar/^{39}Ar$ age spectra for biotite from sample 01 KIM RAP.

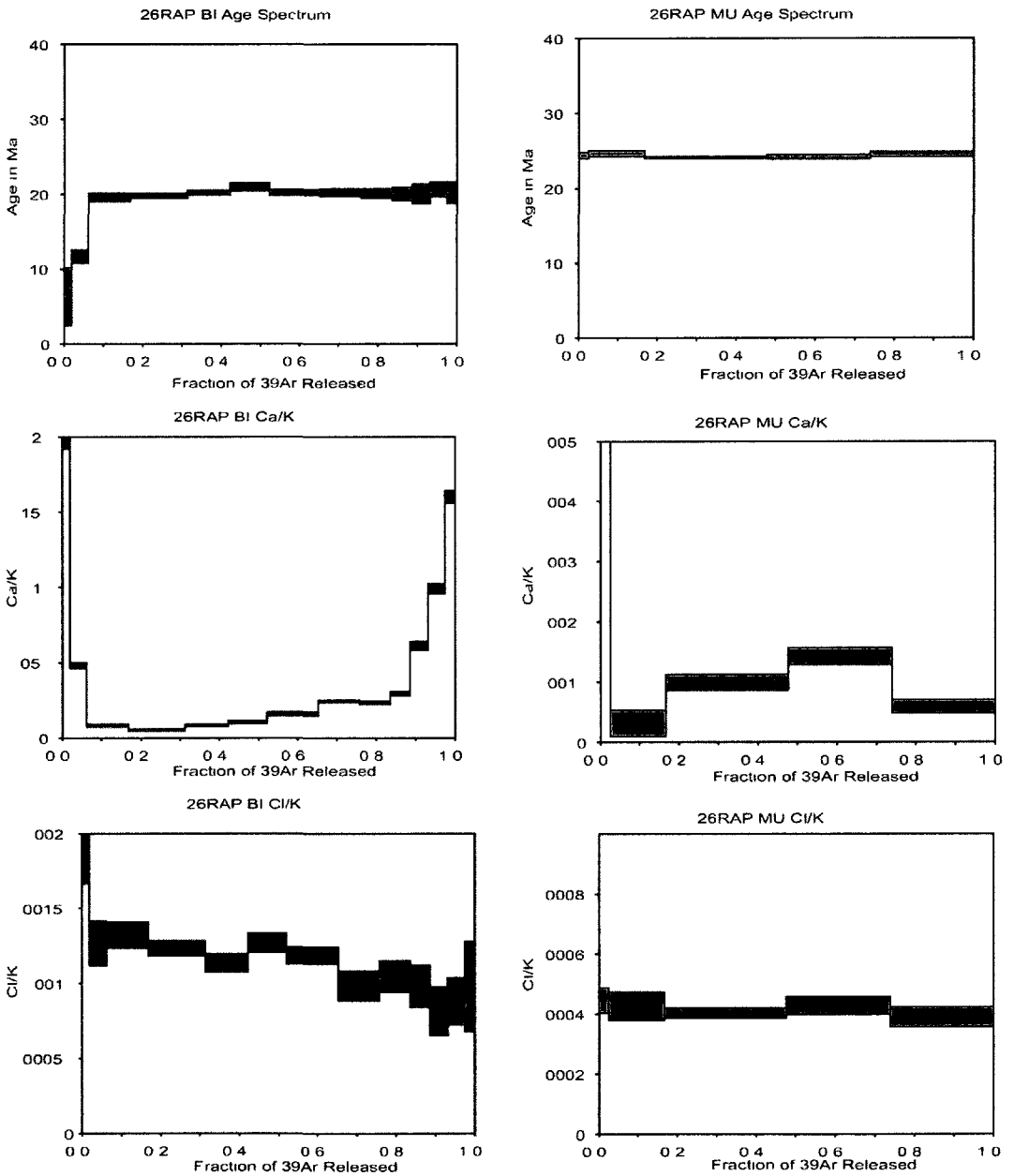

Figure 3R.3 $^{40}Ar/^{39}Ar$ age spectra for muscovite and biotite from sample 26 RAP

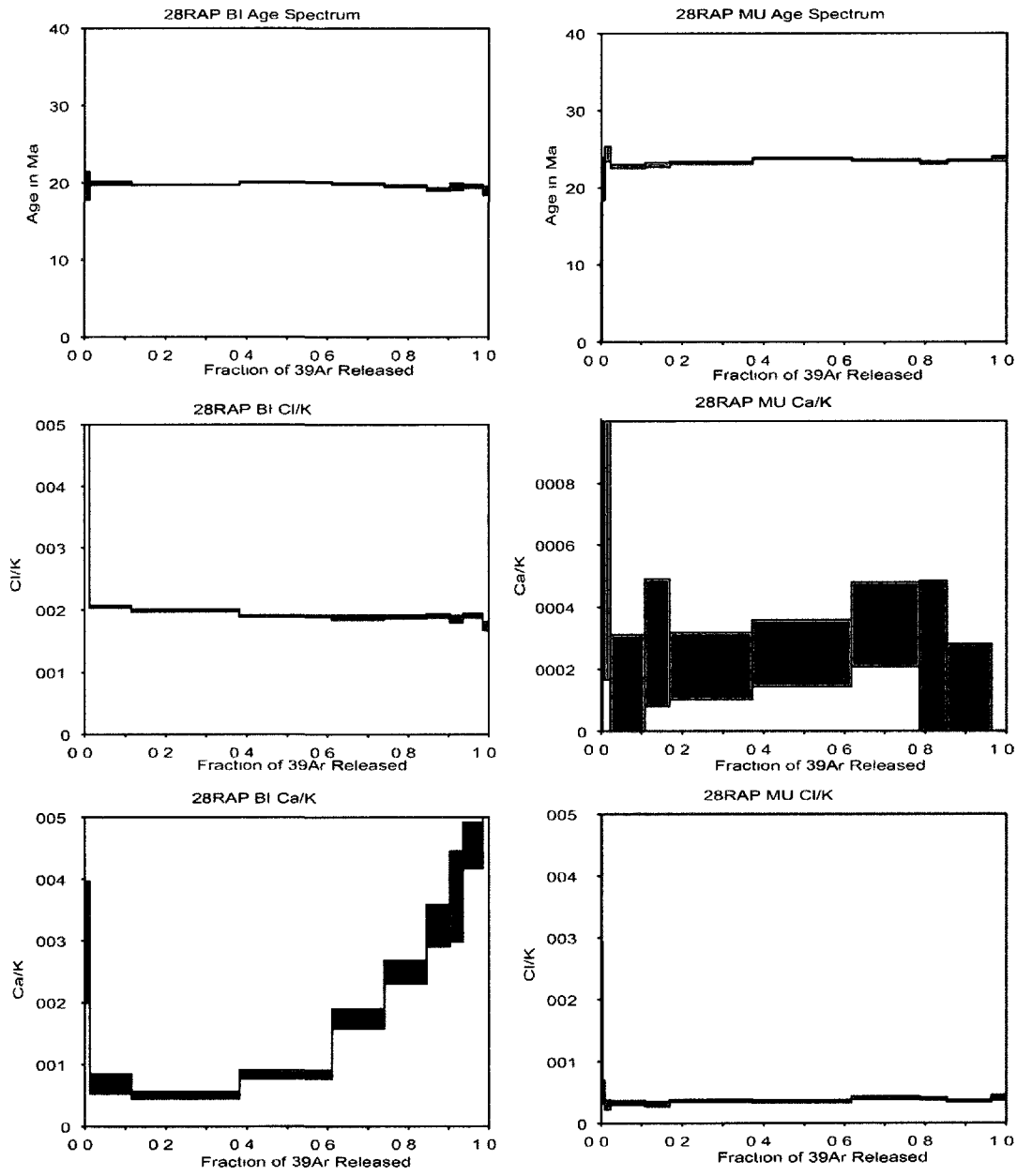

Figure 3R.4 $^{40}Ar/^{39}Ar$ age spectra for muscovite and biotite from sample 28 RAP.

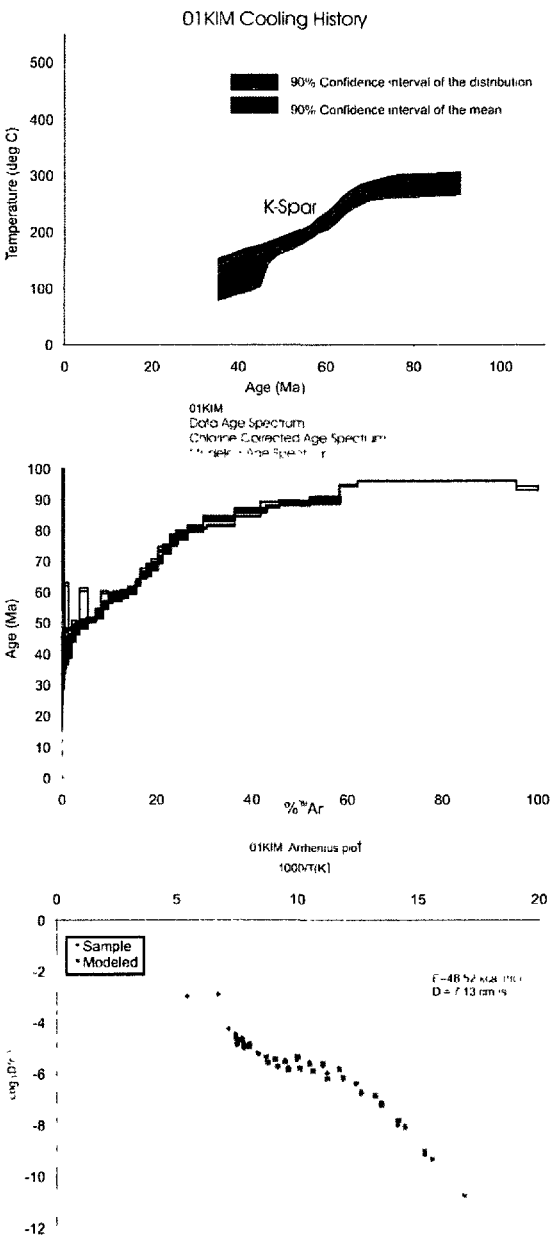

Figure 3R.5: Monotonic multiple diffusion domain (MDD) thermal models, measured, Cl corrected and modeled $^{40}Ar/^{39}Ar$ age spectra, and Arrhenius plot generated for K-spar from sample 01 KIM.

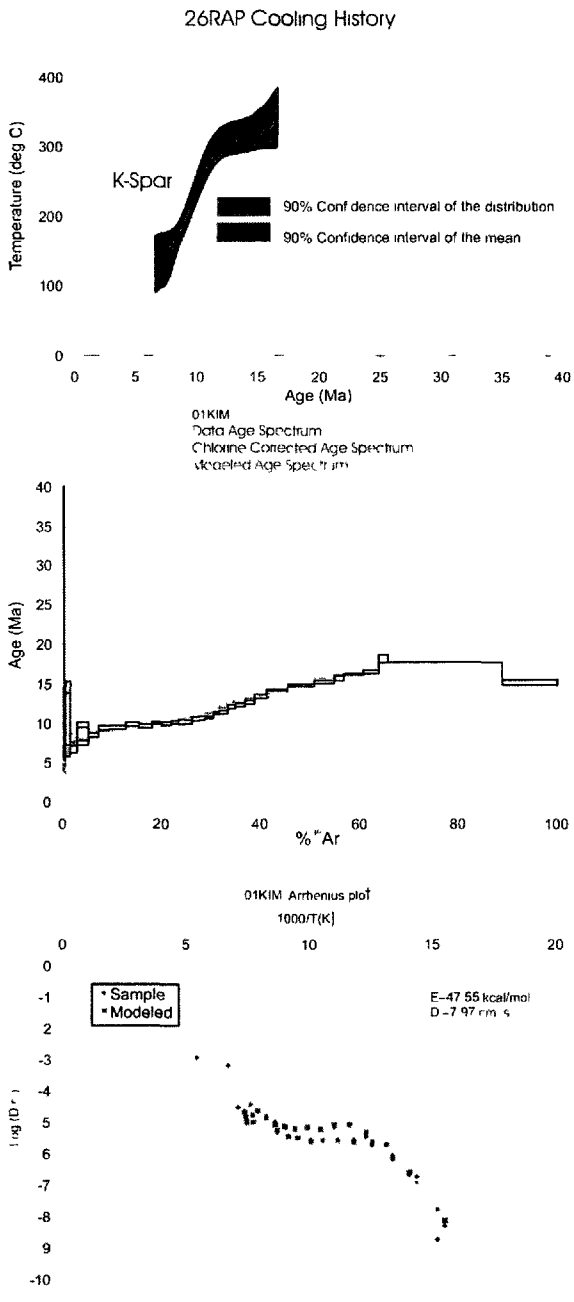

Figure 3R.6: Monotonic multiple diffusion domain (MDD) thermal models, measured, Cl corrected and modeled $^{40}Ar/^{39}Ar$ age spectra, and Arrhenius plot generated for K-spar from sample 26 RAP.

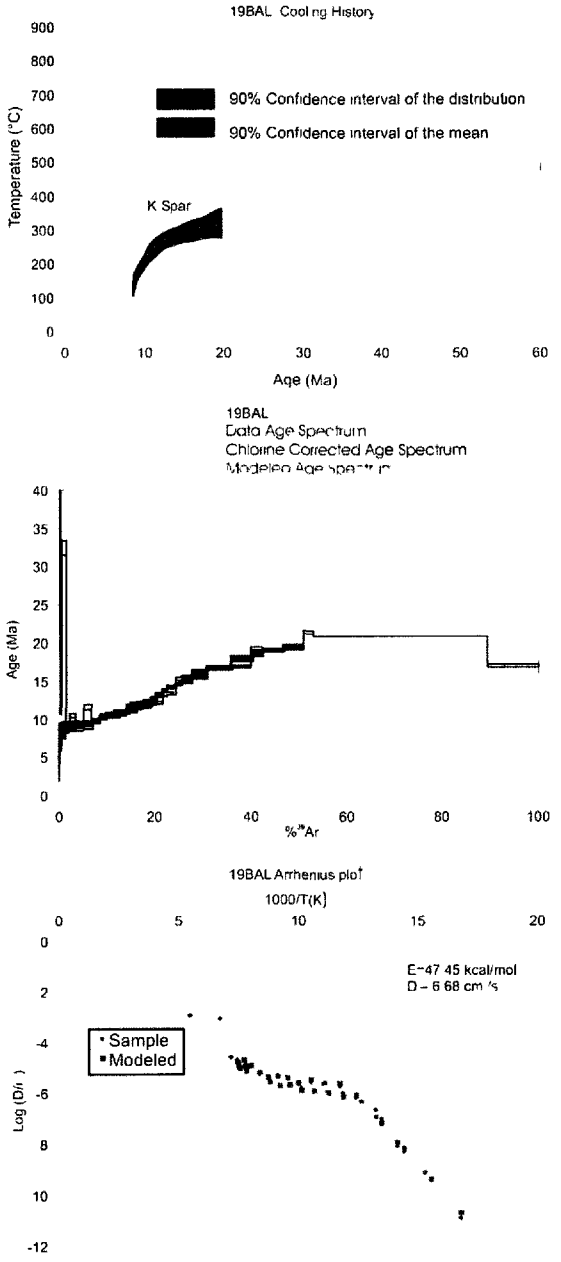

Figure 3R.7: Monotonic multiple diffusion domain (MDD) thermal models, measured, Cl corrected and modeled $^{40}Ar/^{39}Ar$ age spectra, and Arrhenius plot generated for K-spar from sample 19BAL.

3.13 Repository Tables

Table 3R.1: K-feldspar summary and model ages.

Step	T (°C)	t (min)	^{39}Ar (mol)	+/-	Cum ^{39}Ar	Age (Ma)	+/-	Model Age	Cl Age	+/-
01KIM K-Feldspar *Weighted average of J from standards = 7 125e-03 ± 1 903e-05*										
1	319	42	3 53E-13	3 36E-15	0 02423	536 40	18 65	18 65	34 97	1 38
2	382	14	9 41E-13	1 06E-14	0 08887	539 73	10 68	10 68	34 97	1 38
3	369	41	8 46E-13	9 25E-15	0 14699	62 16	7 98	7 98	34 97	1 38
4	434	13	2 95E-12	1 61E-14	0 34929	128 6	1 77	1 77	34 97	1 38
5	420	41	4 22E-12	3 42E-14	0 63919	34 97	1 38	1 38	34 97	1 38
6	484	13	9 75E-12	1 94E-14	1 30915	62 59	0 59	0 59	38 51	0 59
7	470	41	1 03E-11	3 69E-14	2 01548	42 04	0 72	0 72	42 04	0 72
8	533	13	1 13E-11	4 54E-14	2 79021	50 14	0 56	0 56	44 43	0 56
9	520	41	1 39E-11	3 70E-14	3 74297	46 82	0 52	0 52	46 82	0 52
10	582	13	2 48E-11	8 49E-14	5 44402	60 79	0 57	0 57	48 99	0 57
11	569	40	2 16E-11	4 47E-14	6 92741	51 16	0 28	0 28	51 16	0 28
12	632	13	1 89E-11	4 61E-14	8 22367	54 31	0 36	0 36	54 31	0 36
13	619	40	2 46E-11	7 30E-14	9 91150	59 83	0 34	0 34	55 89	0 34
14	680	13	1 85E-11	6 28E-14	11 18046	57 46	0 40	0 40	57 46	0 40
15	668	41	2 24E-11	6 52E-14	12 72034	57 21	0 35	0 35	57 21	0 35
16	731	12	1 65E-11	4 74E-14	13 85292	59 50	0 59	0 59	59 50	0 59
17	719	40	2 31E-11	7 48E-14	15 44251	60 83	0 38	0 38	60 83	0 38
18	782	13	1 39E-11	3 63E-14	16 39705	62 99	0 37	0 37	62 99	0 37
19	767	41	2 21E-11	5 09E-14	17 91277	64 82	0 32	0 32	64 82	0 32
20	830	12	1 37E-11	2 93E-14	18 85039	68 38	0 44	0 44	68 38	0 44
21	816	40	1 93E-11	3 18E-14	20 17510	69 40	0 32	0 32	69 40	0 32
22	877	13	1 50E-11	3 00E-14	21 20381	74 17	0 43	0 43	74 17	0 43
23	868	40	2 38E-11	1 30E-13	22 83903	74 24	0 67	0 67	74 24	0 67

Table 3R 1
Continued

24	926	13	1 81E-11	3 55E-14	24 08024	78 38
25	976	12	3 76E-11	1 19E-13	26 66536	79 65
26	1026	12	5 42E-11	1 73E-13	30 39085	80 46
27	1016	40	8 81E-11	2 04E-13	36 44467	81 64
28	1012	60	7 80E-11	1 71E-13	41 80144	84 47
29	1075	13	5 62E-11	1 09E-13	45 66318	89 19
30	1065	41	1 10E-10	3 59E-13	53 22715	89 52
31	1062	61	7 40E-11	1 13E-13	58 30899	90 75
32	1128	12	5 72E-11	8 68E-14	62 24121	94 67
33	1220	12	4 86E-10	3 50E-13	95 60395	95 99
34	1567	41	6 40E-11	3 07E-13	99 99999	93 65

Step	T (°C)	t (min)	^{39}Ar (mol)	+/-	Cum 39Ar	Age (Ma)
26RAP FS#F1, *Weighted average of J from standards = 3 411e-03 ± 1 051e-05*						
1	383	14	2 19E-12	1 73E-14	0 14131	50 37
2	370	41	4 28E-12	3 33E-14	0 41751	6 98
3	437	13	1 71E-11	8 29E-14	1 52357	14 58
4	421	41	2 07E-11	1 70E-13	2 86258	6 62
5	487	13	3 47E-11	2 85E-13	5 10372	9 73
6	472	41	3 29E-11	3 36E-13	7 23101	8 49
7	538	13	3 27E-11	3 08E-13	9 34269	9 34
8	521	41	5 41E-11	2 36E-13	12 83522	9 43
9	585	13	4 24E-11	2 36E-13	15 57613	9 79
10	571	40	3 91E-11	3 96E-13	18 09894	9 65
11	632	13	2 85E-11	1 38E-13	19 93964	10 02
12	621	40	3 15E-11	2 61E-13	21 97601	9 98
13	681	13	2 09E-11	6 06E-14	23 32589	10 12
14	670	41	2 52E-11	2 26E-13	24 95377	10 18
15	732	12	1 85E-11	3 31E-14	26 14824	10 17
16	718	40	2 38E-11	4 65E-14	27 68626	10 54
17	783	13	1 71E-11	3 64E-14	28 78850	10 62

0 40	0 40	78 38	0 40
0 38	0 38	79 65	0 38
0 30	0 30	80 46	0 30
0 22	0 22	81 64	0 22
0 21	0 21	84 47	0 21
0 20	0 20	89 19	0 20
0 30	0 30	89 52	0 30
0 18	0 18	90 75	0 18
0 18	0 18	94 67	0 18
0 10	0 10	95 99	0 10
0 67	0 67	93 65	0 67
+/-	Model Age	CI Age	+/-
3 52	3 52	6 5	0 70
1 62	1 62	6 5	0 70
0 68	*0 68*	*6 5*	*0 70*
0 47	0 47	6 62	0 47
0 29	0 29	7 555	0 29
0 29	0 29	8 49	0 29
0 30	0 30	9 34	0 30
0 2	0 2	9 43	0 2
0 23	0 23	9 79	0 23
0 23	0 23	9 65	0 23
0 15	0 15	10 02	0 15
0 22	0 22	9 98	0 22
0 21	0 21	10 12	0 21
0 31	0 31	10 18	0 31
0 21	0 21	10 17	0 21
0 26	0 26	10 54	0 26
0 22	0 22	10 62	0 22

Table 3R 1
Continued

18	771	41	2 59E-11	1 34E-13	30 46045	10 71
19	831	13	1 72E-11	3 47E-14	31 56995	11 26
20	817	40	2 77E-11	1 87E-13	33 35935	11 40
21	882	13	2 26E-11	1 55E-13	34 82133	12 07
22	871	40	3 04E-11	2 20E-13	36 78374	12 31
23	934	13	3 09E-11	2 59E-13	38 77853	12 68
24	982	12	3 88E-11	4 00E-13	41 28579	13 38
25	1031	12	6 28E-11	2 74E-13	45 34406	14 19
26	1016	40	8 38E-11	2 62E-13	50 75659	14 84
27	1013	60	6 35E-11	2 96E-13	54 85468	15 27
28	1076	13	2 91E-11	3 53E-13	56 73721	15 78
29	1069	40	6 05E-11	2 63E-13	60 64525	16 23
30	1061	61	4 93E-11	2 75E-13	63 82869	16 57
31	1125	12	2 81E-11	3 58E-13	65 64350	18 17
32	1216	12	3 60E-10	3 09E-13	88 90087	17 78
33	1565	41	1 72E-10	1 83E-12	99 99999	15 24

Step	T (°C)	t (min)	^{39}Ar (mol)	+/-	Cum 39Ar	Age (Ma)
19BAL FS#F1, *Weighted average of J from standards = 3 507e-03 ± 1 639e-05*						
1	321	42	3 32E-13	7 09E-15	0 02062	357 68
2	380	14	1 17E-12	1 24E-14	0 09367	430 06
3	369	41	8 57E-13	5 66E-15	0 14698	22 39
4	433	14	2 99E-12	4 67E-14	0 33268	83 86
5	420	41	3 00E-12	2 47E-14	0 51932	12 17
6	483	13	1 65E-11	1 78E-13	1 54477	32 5
7	469	41	1 23E-11	4 31E-14	2 30944	8 78
8	533	13	1 84E-11	2 98E-14	3 45236	10 53
9	519	41	2 56E-11	6 85E-14	5 04586	9 09
10	581	13	2 66E-11	8 88E-14	6 70244	11 65
11	571	40	3 09E-11	8 15E-14	8 62285	9 72
12	631	13	1 89E-11	5 77E-14	9 80121	10 53

0 16	0 16	10 71	0 16
0 19	0 19	11 26	0 19
0 18	0 18	11 40	0 18
0 26	0 26	12 07	0 26
0 21	0 21	12 31	0 21
0 23	0 23	12 68	0 23
0 27	0 27	13 38	0 27
0 12	0 12	14 19	0 12
0 12	0 12	14 84	0 12
0 15	0 15	15 27	0 15
0 38	0 38	15 78	0 38
0 15	0 15	16 23	0 15
0 19	0 19	16 57	0 19
0 49	0 49	18 17	0 49
0 04	0 04	17 78	0 04
0 31	0 31	15 24	0 31

+/-	Model Age	Cl Age	+/-
21 25	21 25	8 78	0 37
10 19	10 19	8 78	0 37
4 26	4 26	8 78	0 37
3 32	3 32	8 78	0 37
1 5	1 5	8 78	0 37
0 98	0 98	8 78	0 37
0 37	0 37	8 78	0 37
0 25	0 25	8 935	0 25
0 22	0 22	9 09	0 22
0 32	0 32	9 405	0 32
0 16	0 16	9 72	0 16
0 17	0 17	10 53	0 17

Table 3R 1
Continued

13	618	41	2 53E-11	6 40E-14	11 37204	10 73
14	679	13	1 91E-11	5 31E-14	12 56201	11 01
15	667	41	2 42E-11	6 59E-14	14 06924	10 85
16	729	13	1 28E-11	5 64E-14	14 86375	11 61
17	717	40	2 30E-11	1 75E-13	16 29512	11 19
18	778	13	1 65E-11	1 39E-13	17 32184	11 68
19	766	41	2 67E-11	8 37E-14	18 97984	11 8
20	827	12	1 83E-11	3 60E-14	20 11876	12 68
21	816	40	2 28E-11	4 48E-14	21 53725	12 19
22	876	13	1 63E-11	4 89E-14	22 55394	13 36
23	866	40	2 91E-11	5 51E-14	24 36218	13 4
24	925	13	1 84E-11	3 80E-14	25 50686	15 33
25	975	12	3 24E-11	5 19E-14	27 52242	15 55
26	1024	12	5 21E-11	2 61E-13	30 76434	16 3
27	1013	40	8 40E-11	3 16E-13	35 98828	16 69
28	1009	60	6 24E-11	2 09E-13	39 87080	16 88
29	1076	13	3 86E-11	2 24E-13	42 27010	19 26
30	1065	41	7 32E-11	2 86E-13	46 82338	19 06
31	1060	61	6 62E-11	2 00E-13	50 94446	19 28
32	1122	12	3 41E-11	1 57E-13	53 06703	21 36
33	1218	12	5 81E-10	3 98E-13	89 24210	20 87
34	1565	41	1 73E-10	1 04E-12	99 99999	16 96

0 17	0 17	10 73	0 17
0 19	0 19	10 79	0 19
0 16	0 16	10 85	0 16
0 3	0 3	11 02	0 3
0 32	0 32	11 19	0 32
0 21	0 21	11 68	0 21
0 17	0 17	11 8	0 17
0 18	0 18	11 995	0 18
0 15	0 15	12 19	0 15
0 27	0 27	13 36	0 27
0 15	0 15	13 4	0 15
0 18	0 18	15 33	0 18
0 11	0 11	15 55	0 11
0 16	0 16	16 3	0 16
0 12	0 12	16 69	0 12
0 19	0 19	16 88	0 19
0 2	0 2	19 26	0 2
0 13	0 13	19 06	0 13
0 1	0 1	19 28	0 1
0 18	0 18	21 36	0 18
0 03	0 03	20 87	0 03
0 15	0 15	16 96	0 15

Table 3R.2: 40Ar/39Ar data for step-heating analyses of micas

Laser (mW)	Cum ^{39}Ar	$^{40}Ar/^{39}Ar$ meas	+/-	$^{37}Ar/^{39}Ar$ meas	+/-	$^{36}Ar/^{39}Ar$ meas	+/-	% Atm ^{40}Ar	Ca/K	+/-	Cl/K	+/-	$^{40}Ar^*/^{39}Ar_K$	+/-	Age (Ma)	+/- (Ma)
28RAP MU								Weighted average of J from standards = 4 001e-03 +/- 1 478e-05								
300	0 0010	83 4972	1 1245	-0 00255	0 00691	0 28048	0 00873	99 3	-0 00468	0 01268	0 02517	0 00118	0 585	2 354	4 2	17 0
500	0 0028	23 7257	0 2161	0 00167	0 00654	0 07880	0 00407	98 3	0 00307	0 01200	0 00235	0 00058	0 412	1 206	3 0	8 7
750	0 0080	17 0426	0 1078	0 00216	0 00146	0 04758	0 00134	82 6	0 00396	0 00267	0 00051	0 00019	2 952	0 390	21 2	2 8
1000	0 0227	12 5200	0 0446	0 00074	0 00065	0 03076	0 00046	72 8	0 00135	0 00119	0 00029	0 00008	3 400	0 136	24 4	1 0
1250	0 1087	4 8502	0 0106	0 00007	0 00010	0 00558	0 00011	34 2	0 00013	0 00018	0 00033	0 00003	3 173	0 033	22 8	0 2
1500	*0 1694*	*5 4035*	*0 0092*	*0 00016*	*0 00011*	*0 00735*	*0 00015*	*40 4*	*0 00029*	*0 00020*	*0 00031*	*0 00004*	*3 201*	*0 045*	*23 0*	*0 3*
2000	0 3721	4 4060	0 0122	0 00011	0 00006	0 00385	0 00006	26 0	0 00021	0 00011	0 00036	0 00002	3 240	0 020	23 2	0 1
2500	0 6167	3 6140	0 0100	0 00014	0 00006	0 00090	0 00003	7 4	0 00025	0 00011	0 00035	0 00002	3 318	0 013	23 8	0 1
3000	0 7858	3 6306	0 0087	0 00019	0 00007	0 00105	0 00004	8 6	0 00034	0 00014	0 00041	0 00002	3 290	0 014	23 6	0 1
4000	0 8538	3 4270	0 0084	0 00011	0 00015	0 00052	0 00008	4 5	0 00020	0 00028	0 00039	0 00002	3 245	0 025	23 3	0 2
6000	0 9637	3 3753	0 0060	0 00005	0 00010	0 00023	0 00005	2 0	0 00009	0 00019	0 00036	0 00002	3 278	0 016	23 5	0 1
9000	1 0000	3 4223	0 0125	-0 00032	0 00029	0 00029	0 00015	2 5	-0 00059	0 00053	0 00041	0 00004	3 306	0 046	23 7	0 3
Integrated		4 2643	0 0043	0 00013	0 00004	0 00330	0 00003	23 0	0 00023	0 00007	0 00039	0 00001	3 260	0 009	23 4	0 1
28RAP BI								*Weighted average of J from standards = 4 001e-03 +/- 1 478e-05*								
300	0 0119	46 4904	0 1755	0 00162	0 00053	0 14799	0 00096	94 1	0 00298	0 00098	0 00622	0 00013	2 730	0 255	19 6	1 8
600	0 1155	5 2157	0 0182	0 00037	0 00009	0 00816	0 00010	46 5	0 00069	0 00016	0 00205	0 00002	2 775	0 033	19 9	0 2
900	0 3820	3 0554	0 0082	0 00028	0 00003	0 00095	0 00001	9 2	0 00051	0 00006	0 00199	0 00002	2 746	0 009	19 7	0 1
1200	0 6116	2 9779	0 0071	0 00046	0 00004	0 00053	0 00002	5 4	0 00084	0 00007	0 00190	0 00001	2 790	0 008	20 0	0 1
1500	0 7400	2 9522	0 0114	0 00095	0 00009	0 00055	0 00004	5 5	0 00174	0 00016	0 00188	0 00004	2 761	0 016	19 8	0 1
2000	0 8447	2 9774	0 0109	0 00136	0 00010	0 00077	0 00005	7 7	0 00249	0 00019	0 00189	0 00003	2 722	0 018	19 5	0 1
2500	0 9028	3 0338	0 0095	0 00177	0 00019	0 00115	0 00008	11 3	0 00324	0 00034	0 00191	0 00003	2 664	0 026	19 1	0 2
3000	0 9356	2 9883	0 0100	0 00203	0 00040	0 00083	0 00022	8 3	0 00372	0 00073	0 00185	0 00006	2 714	0 065	19 5	0 5
5000	0 9842	3 0098	0 0077	0 00247	0 00020	0 00087	0 00009	8 6	0 00454	0 00037	0 00191	0 00003	2 722	0 028	19 5	0 2
9000	1 0000	2 9648	0 0165	0 00370	0 00066	0 00100	0 00027	10 0	0 00679	0 00120	0 00174	0 00007	2 640	0 082	19 0	0 6
Integrated		3 7492	0 0044	0 00085	0 00003	0 00328	0 00002	26 1	0 00156	0 00006	0 00199	0 00001	2 750	0 007	19 7	0 1

Table 3R 2 Continued

Laser (mW)	Cum ^{39}Ar	$^{40}Ar/^{39}Ar$ measured	+/-	$^{37}Ar/^{39}Ar$ measured	+/-	$^{36}Ar/^{39}Ar$ measured	+/-	% Atm ^{40}Ar	Ca/K	+/-	Cl/K	+/-	$^{40}Ar^{*}/^{39}Ar_{K}$	+/-	Age (Ma)	+/- (Ma)
26RAP MU								*Weighted average of J from standards = 3 411e-03 +/- 1 051e-05*								
400	0 0009	52 9057	1 0794	-0 00957	0 01735	0 16363	0 00758	91 4	-0 01755	0 03184	-0 00050	0 00086	4 522	2 098	27 6	12 7
1000	0 0250	7 4660	0 0274	0 00396	0 00075	0 01191	0 00030	47 3	0 00727	0 00137	0 00049	0 00007	3 916	0 093	23 9	0 6
1500	0 1669	4 6685	0 0664	0 00017	0 00012	0 00205	0 00004	13 0	0 00031	0 00022	0 00043	0 00005	4 034	0 063	24 7	0 4
2000	0 4772	4 1358	0 0196	0 00054	0 00007	0 00055	0 00001	4 0	0 00099	0 00013	0 00040	0 00002	3 943	0 019	24 1	0 1
3000	0 7393	4 0616	0 0427	0 00078	0 00008	0 00026	0 00003	1 9	0 00143	0 00014	0 00043	0 00003	3 955	0 043	24 2	0 3
9000	1 0000	4 0861	0 0526	0 00032	0 00006	0 00016	0 00002	1 1	0 00059	0 00011	0 00039	0 00003	4 010	0 053	24 5	0 3
Integrated		4 3041	0 0213	0 00057	0 00004	0 00101	0 00002	7 0	0 00104	0 00008	0 00041	0 00001	3 977	0 021	24 3	0 2
01KIM BI								*Weighted average of J from standards = 7 125e-03 +/- 1 903e-05*								
500	0 0430	7 7282	0 0547	0 07161	0 00178	0 01115	0 00039	42 7	0 13140	0 00326	0 00431	0 00009	4 411	0 122	55 8	1 5
750	0 1385	7 7867	0 0629	0 00862	0 00047	0 00063	0 00014	2 4	0 01582	0 00087	0 00448	0 00007	7 571	0 074	94 8	0 9
1000	0 2264	8 0232	0 0639	0 01066	0 00036	0 00045	0 00016	1 7	0 01957	0 00066	0 00464	0 00011	7 862	0 080	98 3	1 0
1250	0 3143	8 0012	0 0824	0 02135	0 00054	0 00073	0 00014	2 7	0 03917	0 00100	0 00479	0 00007	7 758	0 092	97 1	1 1
1500	0 3898	7 8341	0 1597	0 03189	0 00068	0 00001	0 00018	0 0	0 05852	0 00125	0 00478	0 00012	7 805	0 169	97 6	2 1
2000	0 5043	7 8033	0 1132	0 07412	0 00118	0 00010	0 00008	0 3	0 13601	0 00217	0 00480	0 00013	7 750	0 115	97 0	1 4
2500	0 6087	7 7634	0 1291	0 06195	0 00133	0 00022	0 00011	0 8	0 11367	0 00244	0 00491	0 00012	7 674	0 133	96 0	1 6
3000	0 7109	7 7403	0 1366	0 04673	0 00123	0 00011	0 00012	0 4	0 08575	0 00226	0 00473	0 00010	7 681	0 141	96 1	1 7
5000	0 9974	7 6178	0 0435	0 04777	0 00049	0 00001	0 00005	0 0	0 08765	0 00089	0 00479	0 00005	7 588	0 046	95 0	0 6
9000	1 0000	7 2185	0 2295	0 04387	0 01326	-0 00202	0 00527	-8 4	0 08049	0 02433	0 00280	0 00117	7 791	1 575	97 5	19 2
Integrated		7 7723	0 0312	0 04266	0 00029	0 00069	0 00004	2 6	0 07827	0 00052	0 00473	0 00003	7 543	0 033	94 4	0 5

CHAPTER 4

CENOZOIC TECTONO-THERMAL HISTORY OF THE TORDRILLO MOUNTAINS, ALASKA: PALEO-EOCENE RIDGE-SUBDUCTION, DECREASING RELIEF, AND LATE NEOGENE FAULTING[1]

4.1 Abstract:

High temperature K-feldspar thermochronology (KFAT; Tc of ~350-150 °C) from bedrock samples from the Tordrillo Mountains in the western Alaska Range complement existing U-Pb, $^{40}Ar/^{39}Ar$ and AFT data to provide constraints on Paleocene pluton emplacement and cooling as well as Late Eocene to Miocene vertical movements and exhumation along fault-bounded blocks. Based on the KFAT analysis we also infer rapid exhumation-related cooling during the Eocene in the Tordrillo Mountains. Our KFAT cooling ages are coeval with the deposition of units in the Cook Inlet, Matanuska Valley and Tanana Basin which indicate high-energy depositional environments. They are also the same as cooling ages in the Iliamna Lake region, the Kichatna Mountains of the western Alaska Range and Mt. Logan in the Wrangell-St. Elias Mountains. We infer these cooling events and deposition of clastic rocks are related to the thermal effects of the passage of a slab window in Paleocene-Eocene time. In addition we conclude that the reconstructed $KFAT_{max}$ negative age-elevation relationship is likely related to a long period of decreasing relief in the Tordrillo Mountains. Old cooling ages in the Kichatna

[1]Benowitz, J., Haeussler, P.J., Layer, P.W., O'Sullivan, P.O., Wallace, W.K., Gillis, R., Cenozic Tectono-thermal History of the Tordrillo Mountains: Ridge-subduction, Decreasing Relief, and Neogene Faulting, prepared for submission to *Geochemistry, Geophysics and Geosystems*.

(AFT; Tc of ~120 °C; ~50 Ma to ~30 Ma) and the Kenai Mountains regions (AHe; Tc of ~70 °C; ~25 Ma to ~15 Ma) and similar negative age-elevation relations support this interpretation of overall long-term slow erosion rates and a period of decreasing paleorelief in the western Alaska

4.2 **Introduction**

The topographically segmented, ~700 km long Alaska Range can be divided into the eastern, central and western Alaska Ranges by regions of high and low topography (Figure 4.1). The eastern Alaska Range follows the curve of the Denali Fault strike-slip system, forming an arc of high topography across southern Alaska. The majority of the topography in the eastern Alaska Range lies north of the Fault. A region of low topography separates the eastern Alaska Range from the central Alaska Range, where the majority of high topography lies south of the Denali Fault. To the west, there is a restraining bend in the Fault northwest of Mt. McKinley. Southwest of the bend, the north-south trending western Alaska Range takes an abrupt 90 degree turn away from the Denali Fault.

The relationship between the Denali Fault system and the central and eastern Alaska Range has been documented through past thermochronology research [*Fitzgerald et al.*, 1995; *Haeussler, 2008*; *Benowitz et al.*, 2011; *Chapter 3*]. The majority of the topography of the western Alaska Range is not spatially correlated with the Denali Fault system. However, it has been suggested that counter-clockwise rotation of the southern Alaska Block along the curved Denali

Fault system may be responsible for deformation in the western Alaska Range (Figure 4.2) [*Haeussler et al.*, 2008]. Besides the distinctive north-south topographic signature of the western Alaska Range, the region can be divided into subranges (e.g., Tordrillo, Revelation, and Kichatna Mountains; Figures 4.1 and 4.2). These subranges have a predominately domal topographic expression. To the south of the Tordrillo Mountains, the Neacola Mountains of the Aleutian Range also have a domal topographic expression (Figure 4.1).

We applied K-feldspar $^{40}Ar/^{39}Ar$ thermochronology (KFAT, Tc of ~350 °C to ~150 °C) to 10 previously collected bedrock samples from the Tordrillo Mountains of the western Alaska Range to further examine both the overall exhumation history of the region and possible mechanisms responsible for the region's subrange-scale domal topography. In addition, we used the new western Alaska Range KFAT data to expand on a previous interpretation of unmapped faults by *Haeussler et al.* [2008] that was based on an AFT inverse age-elevation relationship.

4.3 **Tordrillo Mountains (Western Alaska Range) Physiography**

Numerous Late Cretaceous to Paleocene granitic plutons are found in the Tordrillo Mountains region [*Reed and Lanphere*, 1973; *Magoon et al.*, 1976], with $^{40}Ar/^{39}Ar$ and U/Pb ages of ~85 Ma to ~ 55 Ma [*Haeussler et al.*, 2009]. A ~58 Ma to ~51 Ma mafic dike swarm also exists in the region [*Haeussler et al.*, 2009]. There is a large gap between the age of the dikes and the next oldest dated igneous

rocks in the Tordrillo Mountains region. These are associated with the active Spurr Volcano and have ages of ~1.8 Ma [*Haeussler et al.*, 2009]. The Quaternary Hayes Volcano [*Riehle et al.*, 1990] is located 2.5 km west of sample 03PH401A (Figures 4.2 and 4.3). The well-constrained magmatic history of the Tordrillo Mountains makes the region a prime natural laboratory for the application of thermochronological techniques to reconstruct the region's topographic development.

The western Alaska Range has a present average elevation of ~1300 m, with an area of high peaks above 2500 m in the Tordrillo Mountains (Fig. 4.1). A previous AFT study from the Tordrillo Mountains [*Haeussler et al.*, 2008] found a complex age-elevation relationship that led to an interpretation of unmapped thrust faults and proposed cooling events at ~35 Ma, ~23 Ma and ~6 Ma (Fig. 4.4, Table 4.1). The events at ~23 Ma and ~6 Ma were inferred to reflect cooling related to exhumation. The ~35 Ma cooling event was recorded by only one sample and thus was not well documented.

South of the Tordrillo Mountains region, the Lake Clark Fault has undergone ~26 km of right-lateral offset since the late Eocene [*Haeussler and Saltus*, 2004]. Therefore, the sediment source in the Tordrillo Mountains has moved only a short distance relative to Cook Inlet basin between the Eocene and the present. The thick Miocene Tyonek Formation and Pliocene Sterling Formation in the neighboring Cook Inlet Basin (Fig. 4.2) [*Fisher and Magoon*, 1978] are

consistent with the thermochronologic reconstruction of Mio-Pliocene uplift in the region [*Fitzgerald et al.*, 1995; *Haeussler et al.*, 2008].

Whether surface uplift in the Tordrillo Mountains is purely related to Neogene tectonic processes is not clear from the current thermochronological data. Further constraints (this study) on the thermal history of the region from higher-temperature thermochronometers (KFAT) provide insight into the tectonic history of the region from initial melt emplacement to closure through the AFT system.

4.4 **Methods: Sampling and Analytical Techniques**

We applied high-temperature feldspar thermochronology to 10 bedrock samples previously collected along a north to south transect of the spine of the Tordrillo Mountains [*Haeussler et al.*, 2008] to better constrain the tectono-thermal history of the region. Samples were analyzed using $^{40}Ar/^{39}Ar$ thermochronology on potassium feldspar (K-spar) degassed using an argon laser (8 samples) or a resistance furnace (2 samples) at the University of Alaska Fairbanks geochronology facility (data repository table 4R.1). See *Benowitz et al.* [2011] and chapter 3 for detailed discussions of the University of Alaska Fairbanks Geochronology $^{40}Ar/^{39}Ar$ dating procedures and methods.

We examine the resulting age spectra using a multi-domain diffusion modeling (MDD) approach (e.g., *Lovera et al.*, 2002) to determine thermal histories. However, we do not model the complete time-temperature history of the KFAT analyzed samples. The short duration of the cooling age span (~4 Ma)

exhibited by almost all of the Tordrillo Mountains samples limits the usefulness of the time and efforts of the full furnace iso-thermal duplicate heating schedule approach (*Lovera et al.*, 2002). Due to the rapid cooling of the samples, timeTime-temperature models for the majority of samples would produce a steep straight line between ~350 °C and ~150 °C and would not provide additional information. Instead of a thermal modeling approach, we look at the time span between closure of the high-temperature (~350 °C) and low-temperature (~150 °C) domains for K-spar [*Ridgway et al.*, 2007; *Thoms*, 2000; *McDougall and Harrison*, 1999; *Copeland and Harrison*, 1990]. We interpret the KFAT thermal histories in relation to the timing of regional pluton and dike emplacement to distinguish between cooling related to magmatism, exhumation and thermal relaxation. We use the KFAT data to interpret fault blocks based on inferred cooling history parameters (timing and cause) and compare the new structural interpretation with the previous interpretation of unmapped thrust faults in the Tordrillo Mountains [*Haeussler et al.*, 2008]. The new KFAT data permit us to reconstruct the original relative positions of the inferred structural blocks. In addition, we used the KFAT maximum closure temperature age data ($KFAT_{max}$) to evaluate the overall Tordrillo Mountains relief history since $KFAT_{max}$ closure. *Benowitz et al.* [2011] provide further details of the K-spar mineral separation and $^{40}Ar/^{39}Ar$ methods used at the University of Alaska Fairbanks geochronological facility.

4.5 **Results**

Samples from the northeast edge of the Tordrillo Mountains (01PH426A and 02PH332A) yielded K-spar analyses with well-defined $^{40}Ar/^{39}Ar$ age plateaus with flat age spectra (Figure 4.5, Table 4.2, Figures 4R.1 and 4R.2 and Table 4R.1 in data repository). These samples are the only two out of the 10 analyzed that provided plateau ages. The age span between the high- and low-temperature closure domains for the samples was less than one million years, demonstrated by the high concordance between integrated ages (whole gas) and plateau ages for these samples (Table 4.2). Thus the inferred cooling rate between ~350 °C and ~150 °C for these two samples was geologically instantaneous. Samples 03PH407A and 03PH408A (Figure 4.5, Table 4.2, Figures 4R.3 and 4R.4 and Table 4R.1 in data repository) are located farther within the Tordrillo batholith than 01PH426A and 02PH332A. These samples produced similar down-stepping age spectra and closure spans (~4 Ma), indicating rapid cooled at a rate of ~55 °C/Ma.

Samples 03PH402A, 03PH403A, 03PH404A, 03PH405A, and 03PH406A (Figure 4.5, Table 4.2, Figures 4R.5, 4R.6, 4R.7, 4R.8 and 4R.9 and Table 4R.1 in data repository) have down-stepping age spectra indicative of more complex thermal histories. Closure spans vary from ~10 Ma to ~4 Ma, with all samples cooling through the ~150 °C isotherm by ~40 Ma and recording rapid cooling rates between ~20 °C/Ma to ~50 °C/Ma. Sample 03PH401A was the sample collected closest to the Hayes volcano (Figures 4.3 and 4.5, Table 4.2, Figures 4R.5, 4R.6,

4R.7, 4R.8 and 4R.9 and Table 4R.1 in data repository). The $^{40}Ar/^{39}Ar$ analyses produced a multi-humped age spectrum for the less retentive, lower temperature domains that is indicative of excess argon or alteration [*McDougall and Harrison*, 1999]. The more retentive, higher temperature domains of sample 03PH401A produced an undisturbed age spectrum.

4.6 **Discussion**

Thermochronology provides information on the temperature history of a rock through time. From cooling ages and cooling age patterns we infer whether cooling or reheating was related to burial, rock uplift, surface lowering, magmatic events, or relaxation of isotherms. A geothermal gradient needs to be determined to quantify the amount of exhumation once additional constraints suggest that cooling resulted from rock uplift and exhumation. We have no measurements of the paleogeothermal gradient in the Tordrillo Mountains, so we made no attempts to quantify the total amount of exhumation or exhumation rates. However we used rock cooling and petrological observations to investigate whether an unusually high geothermal gradient may have been present. We used evidence of a high, standard, or low regional geothermal gradient to evaluate the possible far-field tectonic process responsible for exhumation in the western Alaska Range.

4.6.1 **Mechanisms for Rock Cooling in the Tordrillo Mountains**

Samples 01PH426A and 02PH332A cooled quickly (<~1 Ma) through the high temperature and low temperature closure domains for the KFAT system and

have ages similar to the ~60 Ma crystallization age of the pluton. We infer that cooling was related to thermal relaxation following melt emplacement (Table 4.2). Alternatively, the samples may have cooled due to thermal relaxation after being heated by coeval dike emplacement. Regardless, the cooling measured in the KFAT data does not indicate cooling related to exhumation. We infer that the samples were emplaced at shallow depth above the ~150 °C isotherm, which is the lowest temperature for Ar retention in KFAT.

Samples 03PH407A and 03PH408A cooled quickly (~55 °C/Ma) between ~55 Ma to ~51 Ma, but not instantaneously. We interpret the rapid cooling of both samples as cooling related to thermal relaxation after crystallization deeper within the pluton than samples 01PH426A and 02PH332A. Alternatively, the samples may have cooled due to thermal relaxation after being reheated by coeval dike emplacement during this time period. Once again, we infer that the samples were emplaced at shallow depth above the ~150 °C degree isotherm.

Samples 03PH402A, 03PH404A, 03PH405A, and 03PH406A all underwent rapid cooling long after initial crystallization (~60 Ma) and long after the end of dike emplacement in the region (~51 Ma). These samples record rapid cooling (20 °C/Ma to 50 °C/Ma) between ~50 Ma and ~40 Ma which we attribute to rock uplift and exhumation. This interpretation is supported by the deposition of sediment in the West Foreland Formation during this time period [*Flores et al.*, 2004]. Sample 03PH403A also most likely cooled as a result of exhumation based on its proximity

to samples 03PH402A, 03PH404A, 03PH405A, and 03PH406A, but we cannot rule out the possibility that some of the higher temperature cooling is due to thermal relaxation after heating by dike emplacement at ~51 Ma.

Sample 03PH401A most likely has been altered and affected by fluids from the Hayes volcano or other Quaternary igneous activity. Excess argon from fluids is known to produce irregular age spectra and geologically meaningless ages [*Kelley*, 2002; *McDougall and Harrison*, 1999]. Alternatively, sample 03PH401A may have undergone a short period of reheating, because the AFT age (~22 Ma) of the sample is older than the minimum K-spar closure age (~8.5 Ma) [*Reiners*, 2009]. The higher temperature and thus more retentive closure age (~33.2 Ma) for sample 03PH401A probably records the time the sample was exhumed through the ~350 °C isotherm. There is no kinetic information (rate of cooling) associated with this age because of the altered low temperature release. The higher temperature age of sample 03PH401A is similar to the ~35 Ma AFT rapid cooling age for sample 03PH332A [*Haeussler et al.*, 2008]. In addition, a large bedrock sample set from the Iliamna Lake region has a peak of rapidly cooled AFT ages at ~ 35 Ma (Figures 4.2 and 4.6) [*O'Sullivan et al.*, 2010]. AFT data from the Kichatna Mountains (Figure 4.1) also have ~35 Ma ages [*Ward*, 2010]. We infer that rapid exhumation was occurring over a large region of southern Alaska at around 35 Ma.

4.6.2 **Tordrillo Mountains Eocene Regional Cooling Rates, Total Rock Uplift, Cooling Amount, and Depth of Emplacement**

The amount of Eocene exhumation-related cooling (~200 °C) documented by the KFAT span of the Tordrillo Mountains samples, assuming a standard continental geothermal gradient of ~25 °C/km, would indicate ~8 km of exhumation. Furthermore, using a ~25 °C/km thermal gradient would imply that the Tordrillo Mountains pluton samples require at least ~14 km of total exhumation. This is based on the fact that samples 03PH402A, 03PH404A, 03PH405A, and 03PH406A have been exhumed through the KFAT and AFT thermal systems (~350 °C and ~120 °C isotherms) and are now at the surface (~0 °C isotherm). The presence of numerous miarolitic cavities in the region of the Tordrillo sample traverse places petrological limits on the amount of exhumation in the region. Miarolitic cavities are not limited to, but are a strongly indicative of epizonal granite [*Candela*, 1997]. Epizonal granites by definition are emplaced ~6 km from the surface [*Buddington*, 1959]. The fine to intermediate grain size of the samples also points to a shallow depth of emplacement. A higher than normal geothermal gradient could account for the discrepancy between the total cooling history and petrological evidence of limited exhumation.

4.6.3 **Tordrillo Mountains Block Boundaries Defined by KFAT Thermochronology Results**

Samples 01PH426A, 02PH332A, 03PH407A, and 03PH408A all record rapid cooling related to post-crystallization thermal relaxation inferred from the KFAT data. As noted in section 4.5, the samples further with in the pluton cooled slightly later and slower. Samples 03PH404A, 03PH405A, and 03PH406A have similar high temperature closure ages and all indicate rapid exhumation-related cooling. Samples 03PH403A and 03PH402A have similar high domain closure ages and may represent a distinct population of samples based on the KFAT minimum ($KFAT_{min}$) and $KFAT_{max}$ age-elevation pattern for all of the samples (Figures 4.7, 4.8). The uppermost sample, 03PH401A, records a different thermal history than all of the other samples, as demonstrated by its hump-shaped, less retentive phase age spectrum and discordant AFT closure age.

Based on the inferred mechanism for cooling (post-emplacement thermal relaxation), AFT data, $KFAT_{min}$ and $KFAT_{max}$ ages, we assign samples 01PH426A, 02PH332A, 03PH407A, and 03PH408A to Block "A." We assign samples 03PH404A, 03PH405A, and 03PH406A to Block "B" based on the inferred mechanism for cooling (exhumation), AFT data, similar $KFAT_{min}$ and $KFAT_{max}$ ages and the intra-block $KFAT_{max}$ negative age-elevation pattern. For the same set of reasons, we assign samples 03PH403A and 03PH402A to Block "C." We assign

sample 03PH401A to Block "D" based on the inferred mechanism for cooling (exhumation), AFT data and inferred altered low-temperature KFAT closure age.

4.6.4 **Tordrillo Mountains Age-elevation Relation Reconstruction and Block Model**

We will postpone discussion of Block A, because the AFT (~35 Ma exhumation event) and KFAT (emplacement cooling) data from the block imply a different thermal history than Blocks B, C, and D. Whereas the AFT age-elevation relationship within blocks is positive, the expected pattern for both relief production and constant topographic relief over time (Figures 4.4 and 4.8a) [*Braun et al.*, 2006; *Braun*, 2002a,b; e.g., *Fitzgerald et al.*, 1995], the AFT data and KFAT higher temperature closure age data between Blocks B, C, and D show a general inverse age-elevation relationship. The youngest ages are at higher elevations. *Haeussler et al.* [2008] inferred thrust faults between what we refer to as sample Blocks A, B, C and D to explain the overall inverse AFT age-elevation relationship (Figures 4.4 and 4.8a).

When we consider the sample sets from Blocks B, C, and D as a whole (Figure 4.8a), the $KFAT_{max}$ data have a slightly negative age-elevation relationship Interestingly, the $KFAT_{max}$ age-elevation relationship within blocks is also negative. If we assume the intra-block pattern for the $KFAT_{max}$ ages mirrors the overall pattern prior to block motion, we can reconstruct the original pre-displacement age-elevation relationship. The three samples in Block B have a

$KFAT_{max}$ age-elevation lapse rate of ~200 m/Ma. Applying this elevation/age lapse rate to Blocks C and D returns the AFT data to a highly correlated positive age-elevation relationship. Block D is moved up ~1794 m relative to Block B and Block C is moved down ~1340 m relative to Block B (Figure 4.8b).

We do not attempt to reconstruct Block A's original position relative to Block B. The KFAT data from Block A likely document cooling related to a magmatic process and not an exhumation event and thus are not equivalent. In addition, sample 02PH332A indicates a different exhumation history (e.g., rapid cooling at ~35 Ma) than neighboring samples in the region. This may reflect translation along a strike-slip fault that has been documented adjacent to the sample location [*Haeussler et al.*, 2008].

If we apply standard methodology to interpret a break in slope defined by the AFT age-elevation relationship [e.g., *Fitzgerald et al.*, 1995], the reconstructed Block B, C, and D vertical transect is consistent with the previous track-length modeling of sample 03PH401A from Block D, which suggested the sample underwent rapid cooling at ~23 Ma [*Haeussler et al.*, 2008]. We agree with this interpretation and infer ~2000 m of exhumation of block D at ~23 Ma (Figure 4.9). In addition, Block A, if one discounts outlier sample 02PH332A, underwent at least 1000 m of exhumation at ~23 Ma, which is also consistent with previous AFT modeling of sample 03PH401A (Block D) [*Haeussler et al.*, 2008]. We infer that this exhumation event occurred in Blocks B and C also, but it is not captured by the

available data due to unroofing and paleo-location of samples below the Tc for AFT during that pulse of rock uplift.

Using the elevations reconstructed from the KFAT and AFT data, we can restore the relative sample elevations through time and construct a plausible block model for the Tordrillo Mountains (Figure 4.10). The restored negative $KFAT_{max}$ age/elevation relationship suggests exhumation resulting from domal uplift in the Tordrillo Mountains between ~50 to 35 Ma. The inferred fault between Block A and Blocks B, C and D was active during the initial Eocene exhumation event. This is inferred from the fact that samples from Block A do not record exhumation-related cooling during this time period compared samples from Blocks B, C, and D, which do. The inferred fault between Block A and Blocks B, C, and D was also likely active during the ~23 Ma event. This is based on the fact that samples across the Block A/Block B, C, D boundary exhibit a distinictive break in AFT age patterns (Fig. 4.7 and 4.9, Table 4.1) [*Haeussler et al.*, 2008].

Based on the available data, it is not possible to constrain the exact timing of movement along the inferred fault between Block D and Block C, but movement must be more recent than the ~23 Ma exhumation event. Movement along the inferred fault between Block C and Blocks B and D must have occurred during or after the ~6 Ma exhumation event.

There is not enough available information to determine whether the inferred blocks are separated by normal or reverse faults. It is possible that the bounding

faults may have slipped in different directions to accommodate changing tectonic stresses (e.g., extension vs. contraction; north-south vs. east-west) over the last ~50 Ma.

4.6.5 $KFAT_{max}$ Negative Age-elevation Relationship

The unusual negative age-elevation relationship of the $KFAT_{max}$ ages deserves discussion in depth. The two most likely explanations for a negative age-elevation relationship are displacement along faults or decreasing relief with time [*Haeussler* et al., 2008; *Reiners, 2007*; *Braun,* 2002a,b]. The negative age-elevation relation in the $KFAT_{max}$ ages within Blocks B and C discounts a structural explanation. How decreasing relief over time can lead to a negative age-elevation relationship is clarified by a short review of age-elevation plots and paleotopographic reconstruction.

Historically, age-elevation plots have been used to quantify exhumation history and rates. Exhumation histories were inferred from the slope of an age-elevation plot of cooling ages from the same thermochronometric system collected using a vertical profile sampling approach [e.g., *Fitzgerald et al., 1995*]. Both breaks in slope and the slope itself were commonly used to constrain exhumation rates and the start and end of exhumation events.

More recent work has demonstrated that surface topography can perturb subsurface temperature fields [e.g., *Braun et al.*, 2006; *Braun*, 2002a,b]. The perturbation of temperature isotherms by surface topography is dependent on the

wavelength of topography and the depth of the isotherm. The bending of isotherms can lead to a negative age-elevation relationship in a region of decreasing relief due to the vertical trajectory of rocks towards the surface (Cecil et al., 2006). Compared to constant relief, relief reduction leads to a shortening of the distance traveled from the time a rock sample crossed a closure temperature isotherm until the rock reached the surface on a ridge top (Figures 4.8 and 4.11). Conversely, the isotherm to surface distance will increase for rocks found at valley bottoms or lower elevation compared to a constant relief scenario. This leads to younger ages higher and older ages lower on age-elevation profiles (Figures 4.9 and 4.11) [*Braun*, 2002b].

The wavelength, amplitude, and geothermal gradient must be high to perturb isotherms deeper than a few kilometers [*Braun,* 2002a,b]. Therefore, low-temperature thermochronometers such as AHe are normally used to examine paleotopography [*Reiners*, 2007]. When the wavelength of topography is long (~≥50km) [*Reiners*, 2007], surface topography will perturb subsurface temperature fields deep enough to be recorded in high temperature thermochronometers like $KFAT_{max}$. The current wavelength of topography in the Tordrillo Mountains is over ~50 km both along and across trend (Figure 4.3). The Tordillo Mountains currently have a relief, or amplitude, of ~2 km, but paleorelief may have been higher (Figures 4.3, 4.10 and 4.11).

The amount that long wavelength topography perturbs subsurface temperature fields is strongly controlled by geothermal gradient [*Reiners*, 2007; *Braun et al.*, 2006]. The ~50 km wave length of the Tordrillo Mountains could only significantly deflect high temperature isotherms if the geothermal gradient was unusually high (≥~40°C /km) [*Braun*, 2002b]. We have no local constraints on the geothermal gradient in the Tordrillo Mountains during the time of closure for $KFAT_{max}$ (~50 Ma to ~33 Ma). We infer that the geothermal gradient must have been higher than a standard continental geothermal gradient of ~25°C during this time period, based on the negative age-elevation relationship shown by the $KFAT_{max}$ cooling age data, petrological indicators of relatively shallow emplacement depth, and the total amount of cooling related to rock uplift and exhumation.

It is important to note that once a column of rock has passed through the ~350 °C isotherm, the inverse age-elevation pattern would remain in the KFAT record even if the geothermal gradient changed over time. Therefore, $KFAT_{max}$ closure ages and KFAT cooling span data likely reflect the creation of Eocene topography under a high geothermal gradient regime.

The $KFAT_{max}$ age-elevation relationship likely reflects decreasing relief of paleotopography through time and does not reflect the original exhumation event (Figure 4.11). The Neogene AFT data records younger pulses of exhumation (~23

Ma and ~6 Ma) under a different, though still high, geothermal gradient of ~35°C/km [this study; *Haeussler et al.*, 2008].

One implication of Eocene formation and subsequent decrease of relief in the Tordillo Mountains is that long-term erosion rates were slow in this region. If erosion rates were high, the record of the Eocene cooling event and paleotopography would have been removed through the process of unroofing. Slow erosion rates over ~50 Ma time scales have been documented in other granitic orogenic belts [*House et al.*, 2001]. Additional thermochronological evidence from the western Alaska Ranges provides supporting evidence for slow erosion and Eocene paleorelief. Samples from the Kichatna Mountains of the northern western Alaska Range (Figure 4.1) have AFT ages in the range of ~52 Ma to ~35 Ma, reflecting over-all slow exhumation (~0.08 km/yr) since the Eocene [*Ward*, 2010]. The Kichatna Mountain negative AFT age-elevation relationship further implies a long-term trend of decreasing paleorelief [*Ward*, 2010]. The Kenai and Chugach Mountains (Figure 4.2) southeast of the Tordrillo Mountains also experienced relatively slow erosion (~0.2 km/Ma) during the last ~25 Ma based on available AHe data [*Buscher et al.*, 2008]. These data also have complex age-elevation relationships, implying a possible trend of decreasing relief over time in the Kenai and Chugach Mountains.

4.6.6 **Southern Alaska Paleocene-Eocene Tectonic Reconstruction: Ridge Subduction and Slab Window Migration**

Near-trench plutons in the southern Alaska accretionary prism show an eastward progression in the age of magmatism in southern Alaska from 62 to 50 Ma that reflects both subduction of an oceanic spreading center subparallel with the trench and eastward migration of the subducting ridge (Figure 4.12) [*Farris and Paterson*, 2009; *Bradley et al.*, 2003]. This Paleocene–Eocene ridge subduction event is also associated with cessation of Cretaceous arc magmatism in the region [*Ridgway et al.*, 2011].

A currently favored model for the configuration of oceanic plates in the North Pacific includes the existence of a Resurrection oceanic plate between the Kula and Farallon plates (Figure 4.12), which allows synchronous interaction of two trench-ridge-trench triple junctions at two widely separated locations along the northern Cordilleran margin during Paleocene-Eocene time [*Farris*, 2010; *Madsen et al.*, 2006; *Haeussler et al.*, 2003; *Bradley et al.,* 2003].

Ridge subduction results in the formation of a gap between the two subducting plates, or slab window, which leads to upwelling of asthenospheric mantle beneath the upper plate. Slab windows are linked to geochemically distinctive magmatism and surface uplift [*Groome and Thorkelson*, 2009; *Thorkelson*, 1996]. Based on geochemical and petrologic investigations, Paleocene-Eocene volcanic and intrusive rocks in south-central Alaska have been interpreted

to be derived from depleted basaltic magmatic sources related to a slab window (Figure 4.12) [*Cole and Layer*; 2002; *Cole et al.*, 2006; *Thorkelson et al., 2011*]. *Cole et al.* [2006] proposed that a slab window associated with subduction of the Resurrection-Kula ridge affected magmatic processes for ~20 Ma after the initial ridge-subduction event (at ~60 Ma). More recently, *Thorkelson et al.* [2011] proposed that a large swath of southern Alaska was affected by Cenozoic slab window events.

Paleocene-Eocene spreading ridge subduction in Alaska was also coeval with widespread mafic dike swarms and mafic volcanic rocks throughout southern Alaska. Between ~57 Ma and ~52 Ma, dike swarms intruded Mesozoic accretionary prism strata along the Border Ranges Fault system [*Little and Naeser*, 1989]. Dike swarms also intruded a large portion of the western Alaska Range. A dike swarm in the Tordrillo Mountains region has whole rock $^{40}Ar/^{39}Ar$ ages that range between ~58 Ma and ~51 Ma [*Haeussler et al.*, 2009]. To the west in the Revelation Mountains region, mafic dikes and extrusive rocks have K-Ar ages between ~55 Ma and ~42 Ma [*Solie et al.*, 1991]. In the Yukon Territory of Canada, magmatic evidence also exists for a slab-window event during the Paleocene-Eocene [*Miskovic and Francis*, 2006].

Correlating surface uplift to Paleocene-Eocene ridge subduction in southern Alaska presents several challenges. For instance, lack of constraints on regional elevations before ridge subduction limits the ability to tie topographic development

directly to ridge subduction. An additional challenge to tectonic reconstruction is the possibility of surface uplift and translation related to movement on any of the numerous strike-slip faults in the region [Lake Clark Fault, *Haeussler and Saltus*, 2004; Border Ranges Fault, *Roeske et al.*, 2003; Denali Fault, *Miller et al.*, 2002]. Local structural settings may also play a role in the exhumation history of southern Alaska during thise time period [*Gasser et al.*, 2011]. Changes in the obliquity of convergence between the subducting oceanic plate and North America may also be responsible for surface uplift [~56 Ma to ~43 Ma; *Doubrovine and Tarduno*, 2008; *Engebretson et al.*, 1985; *Stock and Molnar*, 1988]. In addition, a slab window would lead to both high and perturbed geothermal gradients, which complicates attempts to infer amount of exhumation from thermochronologic cooling-age constraints [*Groome and Thorkelson*, 2009]. The time-progressive spatial widening and thermally evolving nature of slab windows makes tectonic reconstruction from cooling ages and patterns after ridge subduction a five-degree problem [x, y, z location, time, and temperature; *Groome and Thorkelson*, 2009, *Madsen et al.*, 2006; *Thorkelson*, 1996]. Furthermore, the relaxation of elevated isotherms to pre-slab window conditions could result in rock cooling, when in fact no rock uplift took place. Possible regional subsidence related to thermal-relaxation after the passage of a slab window is yet another complication to topographic reconstruction.

Caveats aside, thermochronology results from across southern Alaska [western Chugach Mountains, *Little and Naeser*, 1989; St. Elias Mountains of Alaska/Yukon, *O'Sullivan and Currie*, 1996;Yukon-Tanana Upland, *Dusel-Bacon and Murphy*, 2001; eastern Chugach Mountains, *Enkelmann et al., 2008, 2009, 2010]* have been interpreted as evidence of widespread exhumation-related rapid cooling between ~43 Ma and ~32 Ma (Figure 4.12). In particular, a well-constrained period of rapid cooling is documented at Mount Logan between ~43 Ma and ~36 Ma [*O'Sullivan and Currie*, 1996]. The authors concluded that ~200 °C of rock cooling occurred in ~8 Ma and inferred a high geothermal gradient of 50 °C /km based on the thermochronological analysis. Herein, we correlate rapidly cooled bedrock indicated by AFT data from the Iliamna Lake region with the Tordrillo Mountains Eocene exhumation event (Figure 4.6) [*O'Sullivan et al.*, 2010]. In addition, the Kichatna Mountains have surface AFT ages from ~51 Ma to ~35 M,a implying that this was a period of rapid exhumation in the region.

Regional basin analysis also supports the occurrence of surface uplift in southern Alaska during this time period. Paleocene-Eocene deposits from Cook Inlet [West Foreland Formation; *Flores et al.*, 2004], Matanuska Valley [Wishbone Formation; *Trop and Ridgway*, 2007], the Cantwell basin [Teklanika Formation, *Gilbert et al.*, 1976] and the Amphitheater Formation near the Canada/Alaska border [*Sweet and Cameron*, 1991] all provide evidence of Paleocene-Eocene high-energy depositional environments (Figure 4.12).

Extensive new basin reconstruction work by *Ridgway et al.* [in press] concludes that the Paleogene-Eocene ridge subduction event led to intrabasinal topographic highs with adjacent depocenters across southern Alaska. Their tectonic reconstruction infers that uplift and subsidence were spatially diachronous related to the progression of flat-slab subduction of the spreading ridge and an associated slab window. West to east time-progression of an unconformity in Paleogene southern Alaska forearc basins [*White et al.,* 2006] is in agreement with this ridge-subduction model.

If the high topography of the western Alaska Range, and the Tordrillo Mountains in particular, are related to a slab window event, then the effects of slab windows deserve further discussion. To summarize, slab window events are associated with domal uplift, mantle derived magmatic rocks, time progressive spatially diachronous surface uplift, basin development and a high geothermal gradient [e.g., *Rosenbaum and Mo*, in press; *Guenthner et al.,* 2010; *Cole and Stewart*, 2009; *Bradley et al.*, 2006; *Sisson et al.,* 2003; *Hole and LeMasurier*, 1994].

The basaltic trachyandesite dikes of the Tordrillo Mountains [*Haeussler et al.*, 2009] are associated as products of a slab window events [*Ickert et al.*, 2009; *Cole et al.*, 2006]. The chemistry of the mafic dike swarms in the northern western Alaska Range [*Solie et al.*, 1991] is not known, but the age of the dikes is coeval with the suggested time of the ridge-subduction event. We have already discussed

the domal topography of the sub-ranges of the western Alaska Range: Tordrillo Mountains, Revelation Mountains, the Kichatna Mountains and the Neacola Mountains of the Aleutian Range (Figures 4.1, 4.3 and 4.10) and basin formation [e.g., *Ridgway et al.*, in press]. Data are limited, but the available constraints indicate that Eocene uplift in southern Alaska began to the west and migrated to the east [this study, *Garver et al.*, 2010; *Enkelmann et al.*, 2010; *White et al.,* 2006; *O'Sullivan and Currie*, 1996], in broad agreement with the timing of near-trench magmatism related to eastward migration of ridge subduction [*Farris and Paterson;* 2009*; Bradley et al.,* 2003].

The process of ridge subduction and related slab windows can lead to high geothermal gradients [50 °C/km to 100 °C/km; *Groome and Thorkelson*, 2009]. We have already discussed new evidence for a high geothermal gradient during the Eocene in the Tordrillo Mountains and existing paleogeothermal constraints for the Mount Logan region. In addition, *Dusel-Bacon and Murphy* [2001] infer an Eocene geothermal gradient of ~45 °C/km for the Yukon-Tanana Upland based on an intraplate magmatic episode in the region, possibly related to ridge subduction. Hence, a growing body of magmatic and thermochronological data indicate that a large portion of southern Alaska had a high geothermal gradient during the Eocene. We can not determine whether surface uplift was purely related to a thermal event, but both high geothermal gradients and domal uplift are associated with thermal uplift events [*Taylor and Fitzgerald*, 2011].

A consideration of the regional tectonic history suggests that the likely cause for the ~50 Ma to ~35 Ma rock uplift event in the western Alaska Range is the thermal effects of the passage of Paleocene-Eocene slab window. Thermal uplift related to a slab window can be a dynamic process, with uplift followed quickly by subsidence. The tectono-thermal record indicates sustained relief, albeit decreasing with time. Injection of magma into the crust most likely led to crustal thickening and an isostatic response that limited post-thermal relaxation subsidence [e.g., *Taylor and Fitzgerald*, 2011]. Inferred sustained surface uplift is substantiated by the fact that the lower temperature KFAT domains have not been reset in any of the samples, except possibly the altered sample (03PH401A) in Block D.

Alternatively, the ~35 Ma event seen in the Tordrillo Mountain AFT data, Kichatna Mountain AFT data and Iliamna Lake region AFT data could be related to predicted thermal relaxation after the passage of a slab window. Thermal relaxation of isotherms may be responsible for part of the measured cooling, in association with limited rock uplift and exhumation. We discount this possibility because of the aforementioned unreset KFAT data, the negative age-elevation relationship of the $KFAT_{max}$ data which implies sustained, albeit decreasing relief and the inferred high Neogene geothermal gradient [*Haeussler et al.*, 2008].

Based on the available thermochronometric data, we propose the presence of more than one slab window under southern Alaska [*Madsen et al.*, 2006] or a single slab window with a complex geometry. The second scenario could result

from non-orthogonal intersection of a trench with a segmented ridge-transform system along the subducting Kula-Resurrection ridge [*Farris and Paterson*; 2009; *Thorkelson,* 1996]. Use of thermochronology to investigate the Antarctica-Phoenix ridge subduction event has demonstrated that each type of slab window should produce a unique style of uplift that reflects the geometry and evolution of the window [*Guenthner et al.*, 2010]. In addition, the unusual high topography of the western Alaska Range may also be affected by location above the edge of a slab-window [*Guillaume et al.*, 2010].

~50 Ma to ~35 Ma was a dynamic time in Alaskan tectonics. Coeval with the slab window event is the possibility of thermal uplift related to proposed ~68 Ma to ~44 Ma oroclinal bending in southern Alaska [*Hillhouse and Coe,* 1994]. It is plausible that part of the magmatic activity in southern Alaska during this time period is related to this bending (Cole et al., 2006), but the regional extent and timing of the thermal event in the western Alaska Range and the Mount Logan region discounts oroclinal bending as the main contributor to surface uplift in southern-Alaska during this time period. Oblique subduction following plate reorganization at ~52 Ma and associated strike-slip faulting [*Miller et al.*, 2002] may also have contributed to surface uplift in southern Alaska, but in itself would not lead to a regionally high geothermal gradient, thermally related uplift or mantle derived magmatic events.

4.7 **Conclusions**

KFAT data provided an expanded view of the thermal history of the Tordrillo Mountains. The KFAT data also support structural interpretations made using AFT data alone. Interpretation of cooling history was facilitated by using the thermochronology data to identify displaced structural blocks. KFAT and AFT data document rapid Eocene cooling (~50 Ma to ~35 Ma) in the Tordrillo Mountains, and we infer that this cooling was related to exhumation. AFT age-elevation profile reconstruction supports previous AFT constraints indicating significant exhumation at ~23 Ma in the Tordrillo Mountains (Figure 4.13). Since the Eocene, we infer a general trend of decreasing relief in the Tordrillo Mountains from the reconstructed negative $KFAT_{max}$ age-elevation profile. This conclusion is in agreement with thermochronological constraints from the Kichatna and Kenai Mountains. We thus infer that a large portion of the relief in the western Alaska Range was formed during the Eocene.

The amount of Eocene cooling indicated by the Tordrillo Mountain samples demands either a large amount of rock uplift, for which supporting data is lacking, or an unusually high geothermal gradient. A high geothermal gradient is in agreement with previous thermochronology work at Mount Logan. We infer a high geothermal gradient (~50 °C/km to ~100 °C/km) and deflected isotherms at depth for the Eocene Tordrillo Mountains based on evidence of a slab window. Overall spatial resolution of Paleocene-Eocene thermochronological data in southern

Alaska is limited, but a trend of initiation of exhumation progressing from west to east coincides with the progression of ridge-subduction related neartrench plutonism during this time period.

Southern Alaska Paleocene-Eocene ridge subduction, associated flat-slab subduction, and related slab window evolution has led to asymmetric and diachronous topographic development, magmatism, and basin subsidence and inversion across southern Alaska. Further research is needed to better constrain the geometry and location of slab window(s) under southern Alaska during this time period.

4.8 **Acknowledgements**

This manuscript has benefited greatly from fruitful discussions with Sarah Roeske in the field, over the phone and at conferences.

4.9 Figures

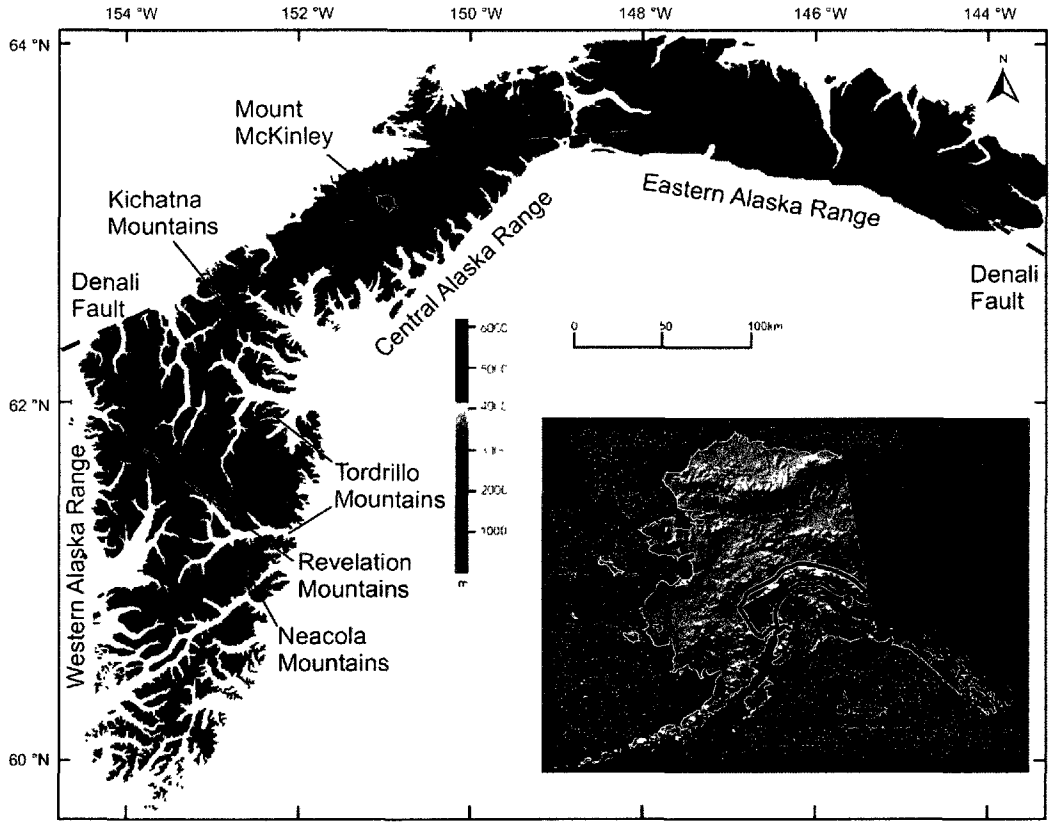

Figure 4.1: Digital elevation map of the topographically segmented Alaska Range flooded to 795 m to emphasize high topography. Denali Fault noted by long-dashed black lines. Inset digital elevation map of Alaska with Alaska Range outlined.

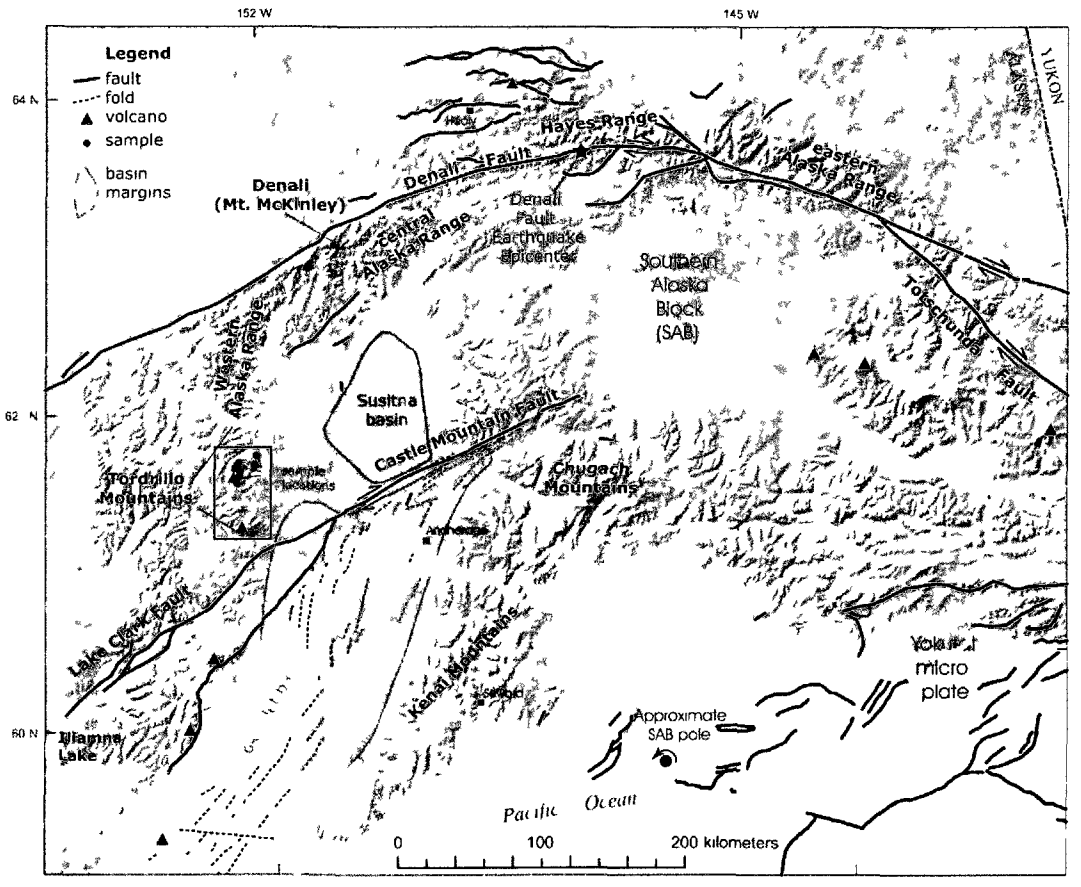

Figure 4.2: Map of south central Alaska. Triangles show active volcanoes. Figure from *Haeussler et al.* [2008]. Location of Tordrillo Mountains samples indicated by black circles. Major faults labeled.

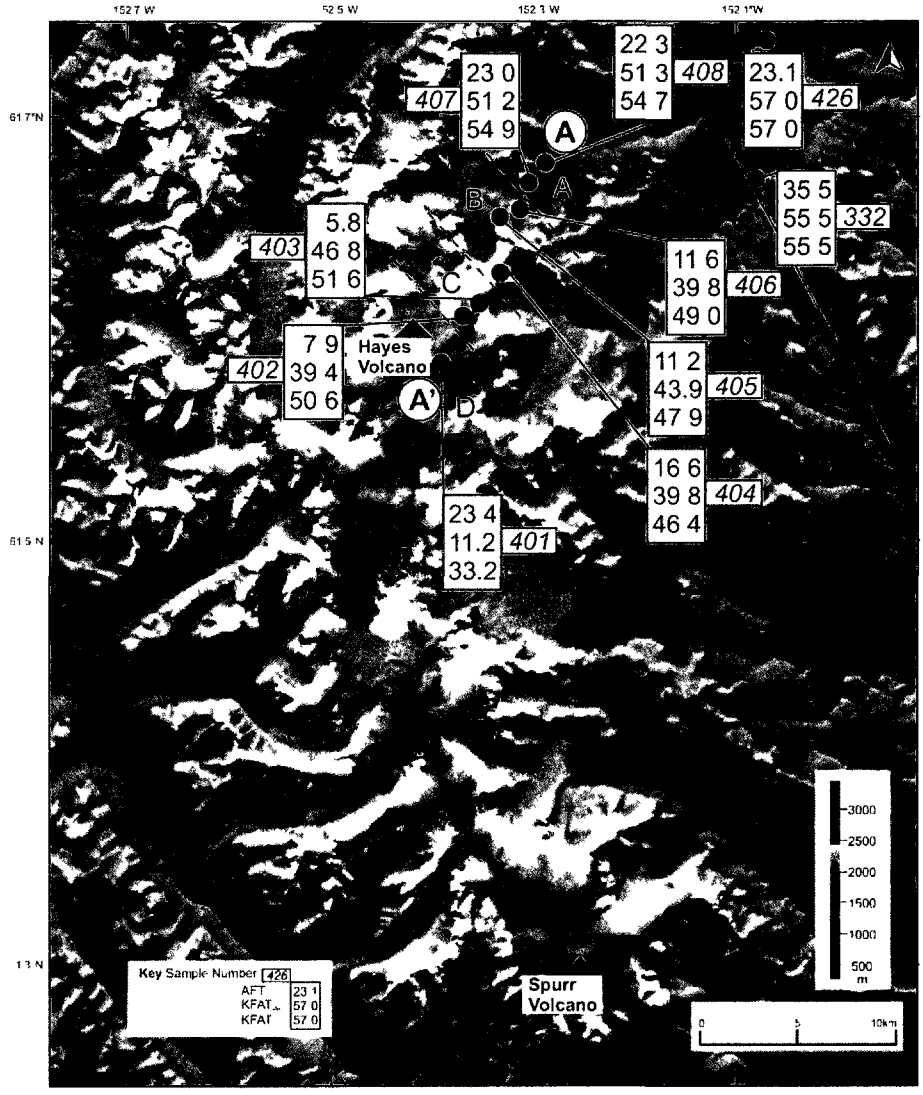

Figure 4.3: Digital elevation map of Tordrillo Mountains of western Alaska. Sample locations denoted by red circles. Sample names shortened to number for figure clarity (e.g., 426 is 03PH426). KFAT maximum and minimum ages and AFT ages are presented. Dashed lines represent boundaries of "blocks" inferred from the AFT data and the KFAT data. AFT data from *Haeussler et al.* [2008]. Profile for figure 4.10 shown by A - A'.

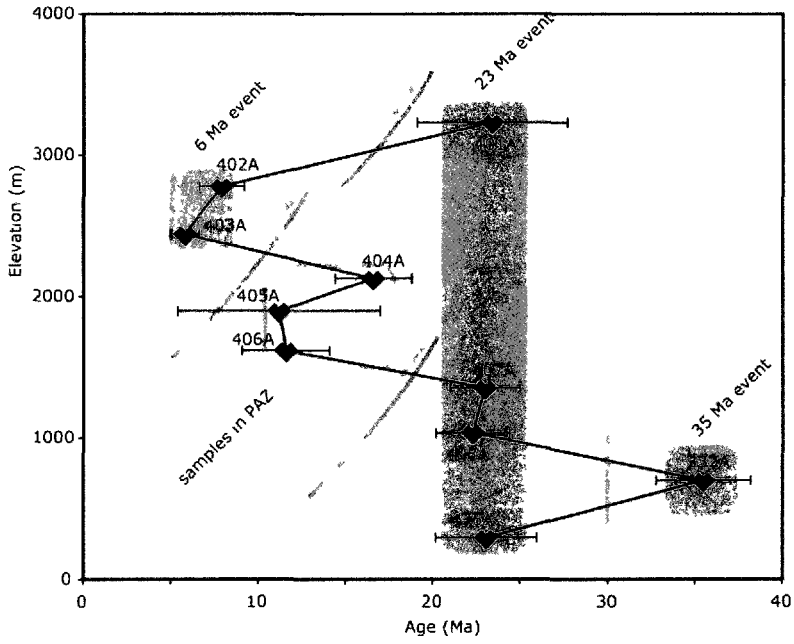

Figure 4.4: Age-elevation plot of AFT dates with two sigma errors. From the Tordrillo Mountains *Haeussler et al.* [2008]. Sample names shortened to number for figure clarity. Sample numbers are indicated next to data points. Interpreted cooling events at ~6, ~23, and ~35 Ma are noted. Samples 404, 405, and 406, within grey box, are interpreted to have been in a partial annealing zone and cooled slowly. Because age does not increase with increasing elevation between samples 407 and 406 and between 404 and 403A *Haeussler et al.* [2008], thrust or reverse faults are inferred between the sample pairs, as shown with grey fault symbols. These faults could also be normal faults. A northwest striking strike-slip fault separates sample 332 from the other samples, and may be the cause of the age discrepancy.

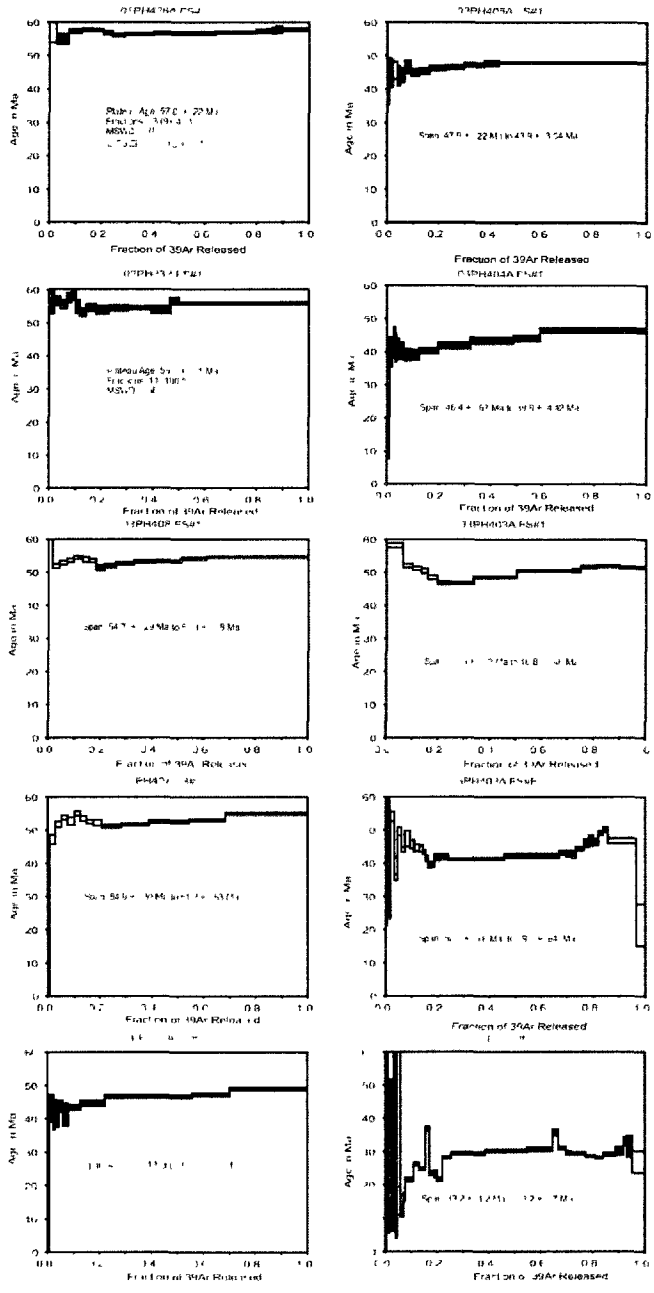

Figure 4.5: $^{40}Ar/^{39}Ar$ age K-spar spectra for the ten Tordrillo Mountains samples. Previously dated with AFT thermochronology [*Haeussler et al.*, 2008]. Plateau ages are given for samples 01PH426Aand 02PH332A, which experienced rapid post-emplacement cooling. Span ages (KFAT maximum and KFAT minimum ages) are given for all other samples.

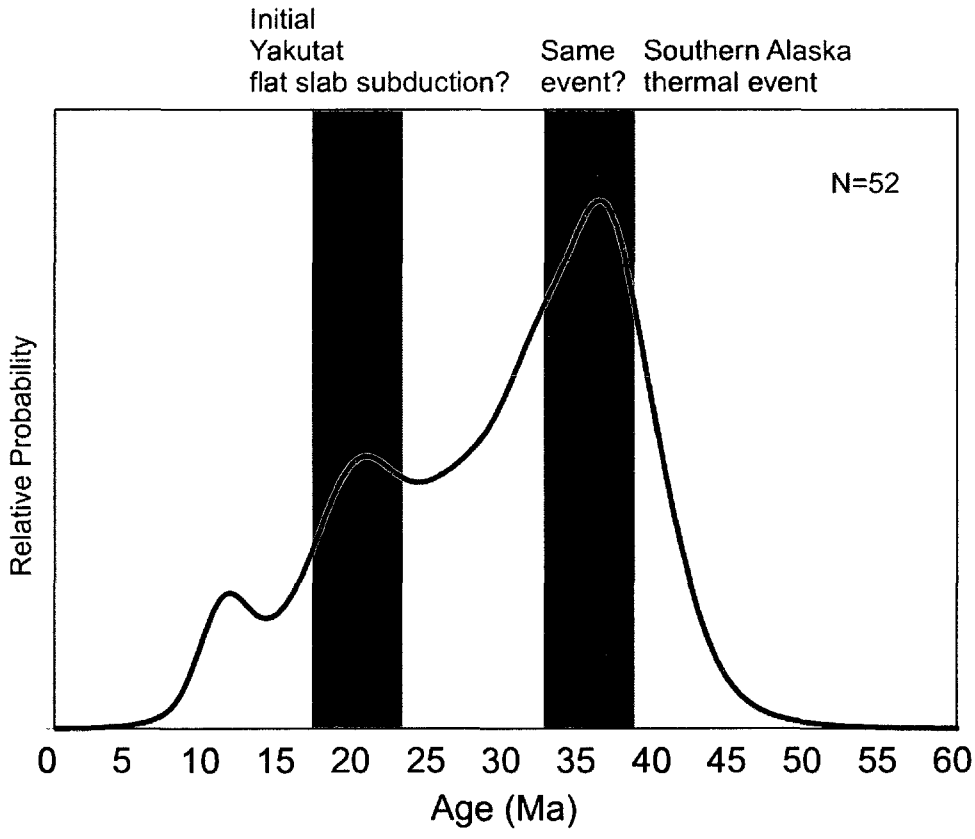

Figure 4.6: Probability plot of AFT ages from igneous, metamorphic, and sedimentary units in the area of the Pebble deposit (~200 km south-southwest of Tordrillo Mountains) [compiled from *O'Sullivan et al.*, 2010] that record rapid cooling. A population peak at ~35 Ma may be related to the same thermal event as seen in the Tordrillo Mountains AFT and KFAT data (Figures 4.4 and 4.5) and Kichatna Mountains AFT data [*Ward*, 2010]. The population peak around ~23 Ma may be related to ~23 Ma cooling event in the Tordrillo Mountains (Figure 4.4) that is correlated with the initiation of Yakutat microplate flat slab subduction [*Benowtiz et al.*, 2011; *Haeussler et al.*, 2008].

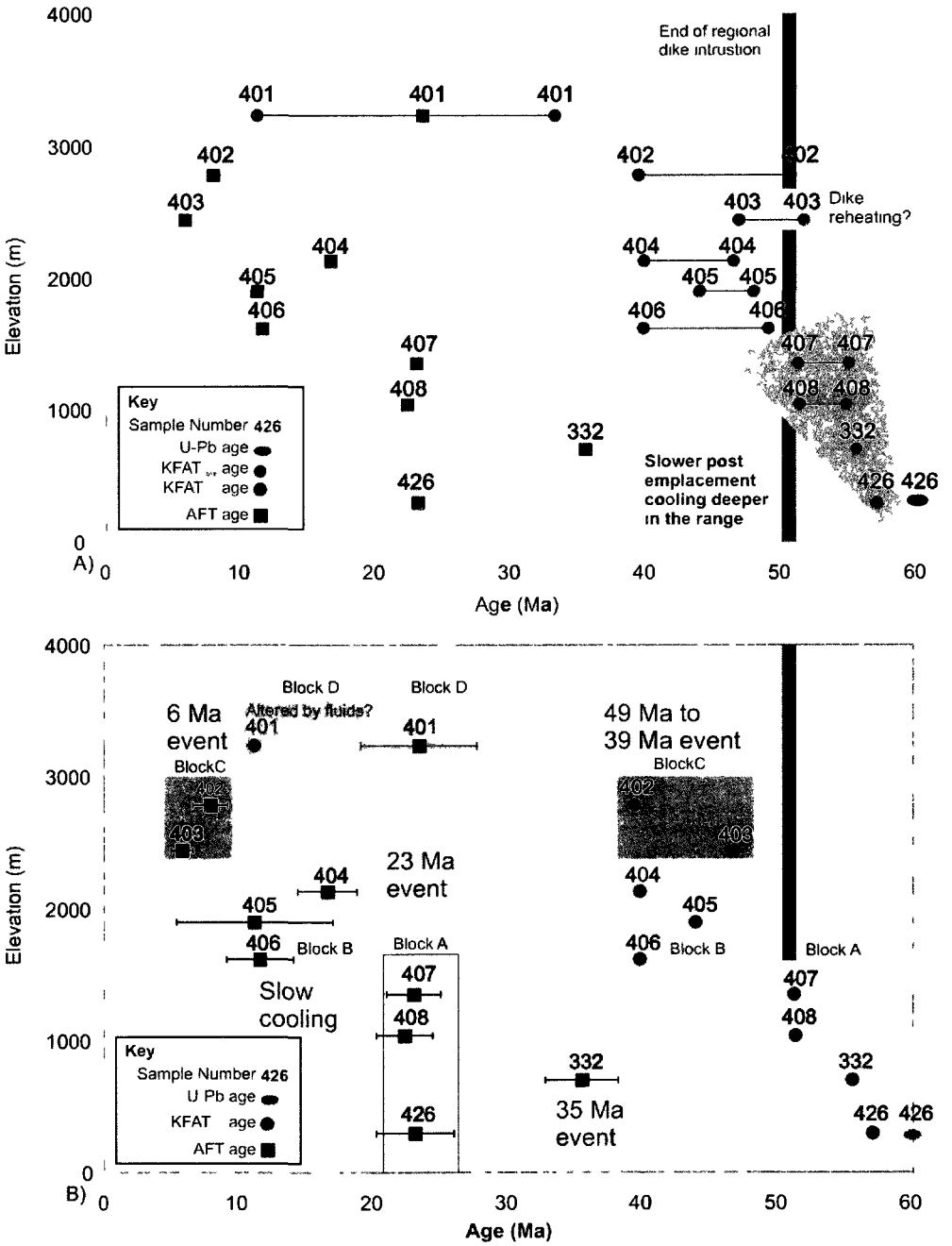
A)
Elevation (m)
Age (Ma)
End of regional dike intrusion
Dike reheating?
Slower post emplacement cooling deeper in the range
Key
Sample Number 426
U-Pb age
KFAT age
KFAT age
AFT age
B)
6 Ma event
Altered by fluids?
Block D
Block C
Block B
Block A
23 Ma event
Slow cooling
49 Ma to 39 Ma event
35 Ma event

Figure 4.7: A) AFT and KFAT span ages plotted vs. elevation. Along a general northeast to southwest sampling transect in the Tordrillo Mountains. Sample names shortened to number for figure clarity. Part of sample 403 cooling history may have been affected by reheating and then cooling related to thermal relaxation following dike emplacement in the region between ~58 Ma and ~51 Ma. Samples 426, 322, 408, and 407 most likely record cooling related to thermal relaxation after initial magma crystallization.
B) AFT and KFAT minimum ages plotted vs. elevation along a general northeast to southwest sampling transect in the Tordrillo Mountains. Sample names shortened to number for figure clarity. Exhumation events were interpreted from the AFT data at ~35 Ma, ~23 Ma, and ~6 Ma. The KFAT minimum ages from the same samples can also be divided into four distinct blocks, inferred to be fault-bounded. Note that the AFT data also show similar groupings and relations. Block A, based on new KFAT data and previous U-Pb data, records post-emplacement rapid cooling between ~57 Ma and ~51 Ma. Block B and Block C indicate rapid exhumation-related cooling between ~49 Ma and ~39 Ma based on the KFAT data for these samples and because the thermal event occurred after pluton (~60 Ma) and dike (~51 Ma) emplacement in the region. Block D is the closest sample to an active volcano (Hayes) and the young/discordant KFAT data from sample 401 may reflect partial resetting due to heating by fluids combined with possible excess Ar that is commonly associated with fluids. Thus, the KFAT minimum age data from sample 03PH401A may be useful for defining a fault-block boundary, but not in deciphering the thermal history of the region. Note that sample 332 with an AFT age of ~35 Ma is anomalous relative to neighboring samples, and may have been displaced to its current position by possible strike-slip faulting.

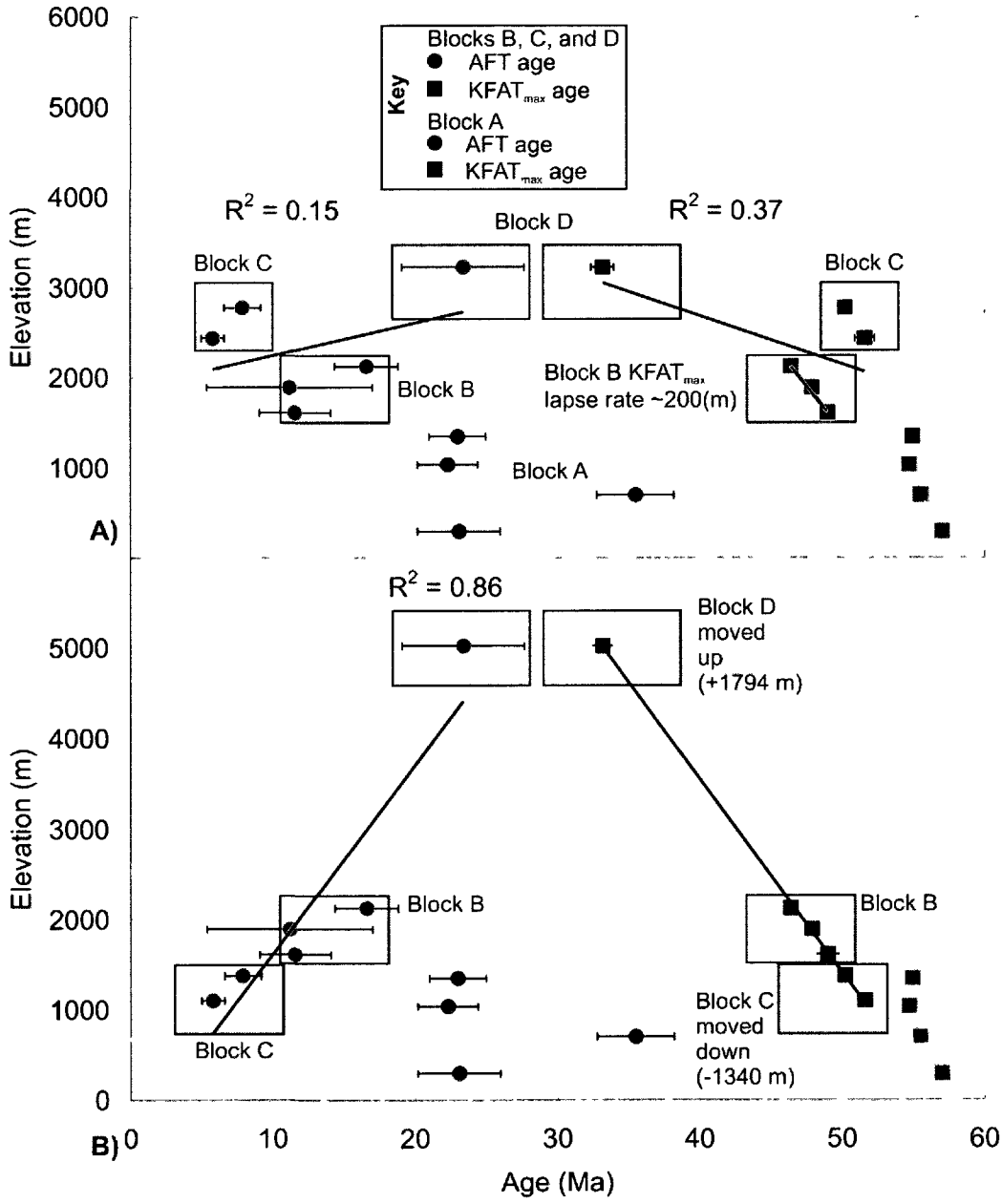
Key
Blocks B, C, and D
AFT age
KFAT$_{max}$ age
Block A
AFT age
KFAT$_{max}$ age
R^2 = 0.15
R^2 = 0.37
Block D
Block C
Block C
Block B
Block B KFAT$_{max}$ lapse rate ~200(m)
Block A
A)
R^2 = 0.86
Block D moved up (+1794 m)
Block B
Block B
Block C
Block C moved down (-1340 m)
Elevation (m)
6000
5000
4000
3000
2000
1000
0
B)
0
10
20
30
40
50
60
Age (Ma)

Figure 4.8: A) $KFAT_{max}$ and AFT cooling ages plotted vs. elevation. Defined structural blocks noted. Both $KFAT_{max}$ and AFT cooling ages have general negative age-elevation relationships with younger ages at higher elevations. Intra-block AFT cooling ages in Blocks B and C have a positive age-elevation relationship while intra-block $KFAT_{max}$ ages in Blocks B and C have a negative age-elevation relationship. The elevation/age lapse rate for $KFAT_{max}$ is ~200 m/Ma for Block B (blue line).
B) Reconstructed Block C and Block D positions relative to Block B based on the $KFAT_{max}$ lapse rate. Block A is not moved because we infer $KFAT_{max}$ ages for these samples records magmatic cooling. We infer that $KFAT_{max}$ ages for Blocks B, C, and D record rock uplift cooling. Block D is moved up 1794 m and Block C is moved down 1340 m. The AFT data age-elevation relation before fault displacement is independently reconstructed.

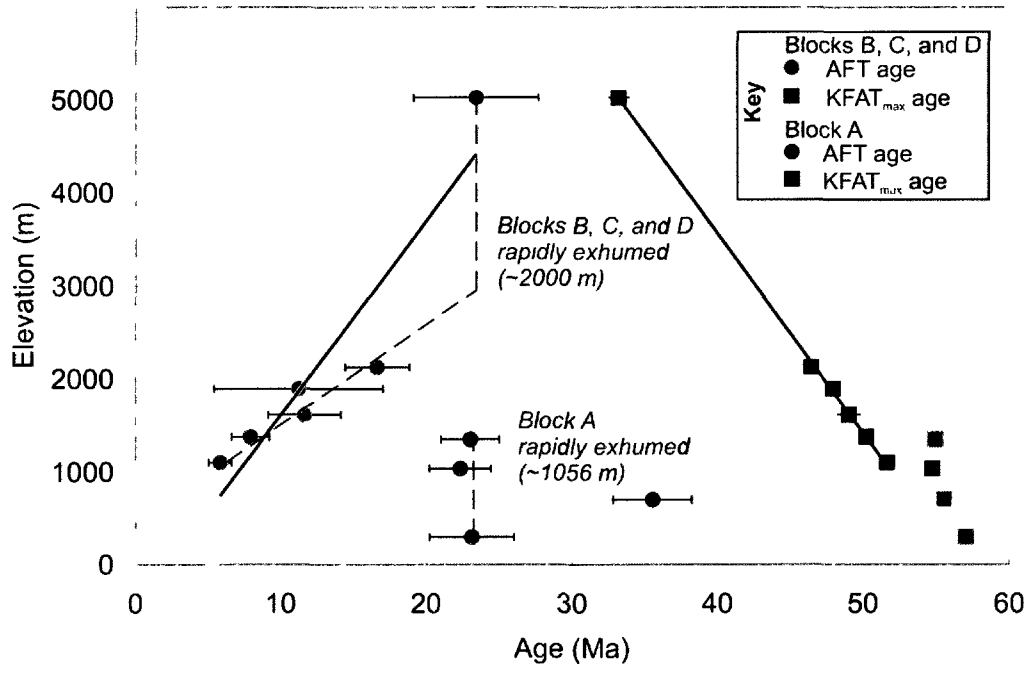

Figure 4.9: Reconstructed AFT age-elevation relationship for Blocks B, C and D. The reconstructed AFT age-elevation relationship is strongly correlated with a positive age-elevation trend. The reconstructed AFT age-elevation relationship documents ~2000 m of exhumation at ~23 Ma for Blocks B, C, and D. Block A experienced at least ~1000 m of rapid exhumation during this same time period.

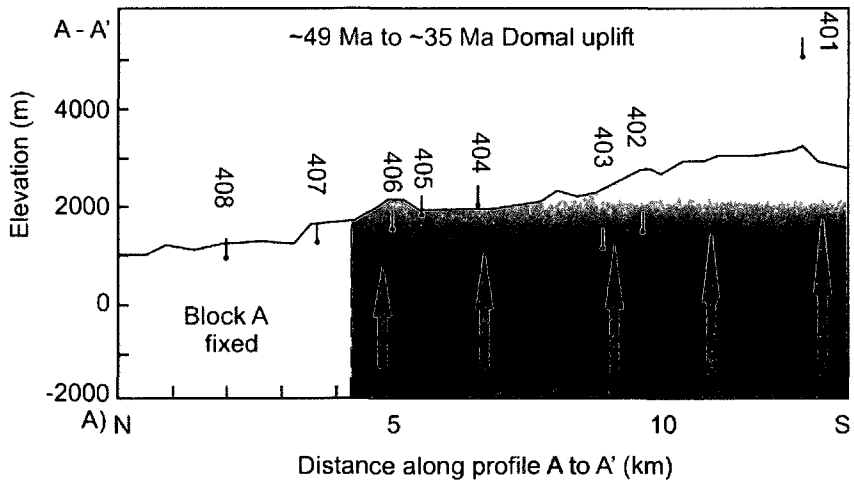
A - A'
~49 Ma to ~35 Ma Domal uplift
Elevation (m)
4000
2000
0
-2000
401
402
403
404
405
406
407
408
Block A
fixed
A) N
5
10
S
Distance along profile A to A' (km)

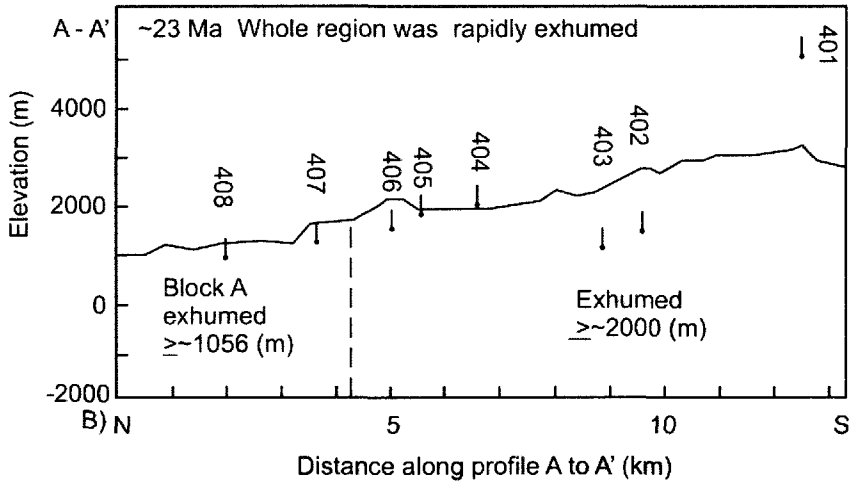
A - A'
~23 Ma Whole region was rapidly exhumed
Elevation (m)
4000
2000
0
-2000
401
402
403
404
405
406
407
408
Block A
exhumed
≥~1056 (m)
Exhumed
≥~2000 (m)
B) N
5
10
S
Distance along profile A to A' (km)

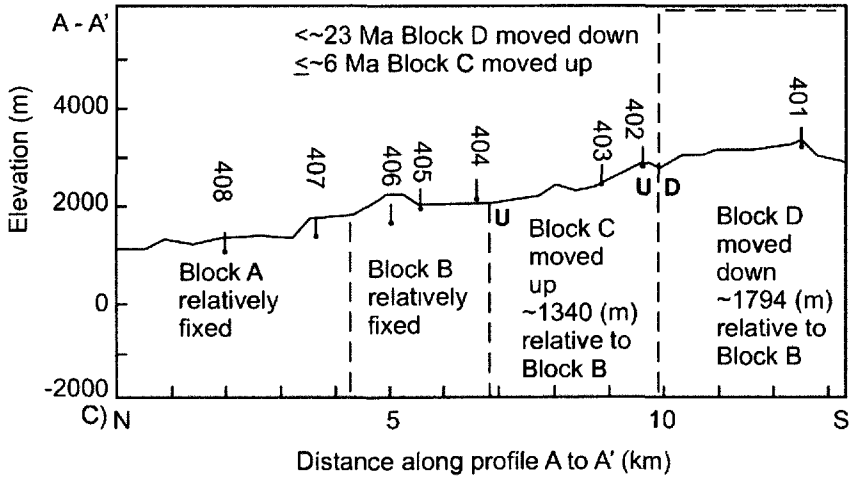
A - A'
≤~23 Ma Block D moved down
≤~6 Ma Block C moved up
Elevation (m)
4000
2000
0
-2000
401
402
403
404
405
406
407
408
U
U
D
Block A
relatively
fixed
Block B
relatively
fixed
Block C
moved
up
~1340 (m)
relative to
Block B
Block D
moved
down
~1794 (m)
relative to
Block B
C) N
5
10
S
Distance along profile A to A' (km)

Figure 4.10: Block diagrams of the Tordrillo Mountains through time based on the AFT and KFAT data. Topographic profile is north to south along profile A to A' (Figure 4.3, 4.13). Samples are projected onto the profile line. Bulb on end of sample's hash mark is real elevation of samples. Sample names shortened to number for figure clarity.
A) Samples in Blocks C and D are moved to pre-faulting position relative to Block B. Red color denotes region with inferred thermally related rock uplift between ~49 Ma and ~35 Ma.
B) At ~23 Ma the entire sampled Tordrillo Mountains region was rapidly exhumed (Figure 4.4 and 4.9). The minimum amount of documented exhumation is different for Blocks A and D. The AFT data from samples in Blocks B and C do not document the ~23 Ma event, likely due to erosion of the thermal record or paleo-location of samples below the Tc for AFT.
C) Block D moved down relative to Block B after ~23 Ma. Block C moved up either during or after the ~6 Ma exhumation event.

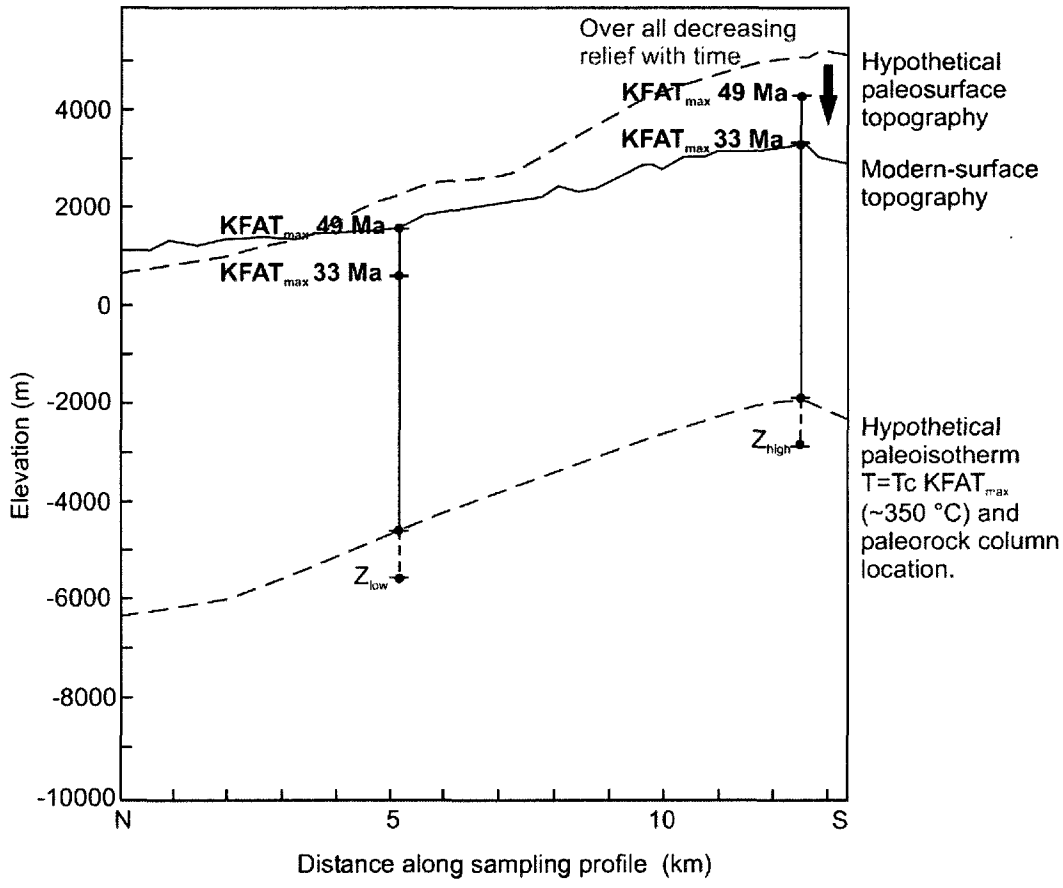

Figure 4.11: Conceptual cross section of the Tordrillo Mountains explaining the negative $KFAT_{max}$ age-elevation relationship. Diagram details how long wavelength, high amplitude topography with a high geothermal gradient during a period of decreasing relief can lead to a $KFAT_{max}$ negative age-elevation relationship in samples from the Tordrillo Mountains (Figure 4.8). Samples after $KFAT_{max}$ closure in the column of rock Z_{low} would take longer to reach the surface than sample in column of rock Z_{high}. This is due to both isothermal bending and differential unroofing at higher elevations during a period of decreasing relief. This scenario is likely responsible for the $KFAT_{max}$ negative age-elevation relationship in the Tordrillo Mountain samples. Samples 03PH406A (49 Ma $KFAT_{max}$) and 03PH401A (33 Ma $KFAT_{max}$) are shown with real elevations as an example.

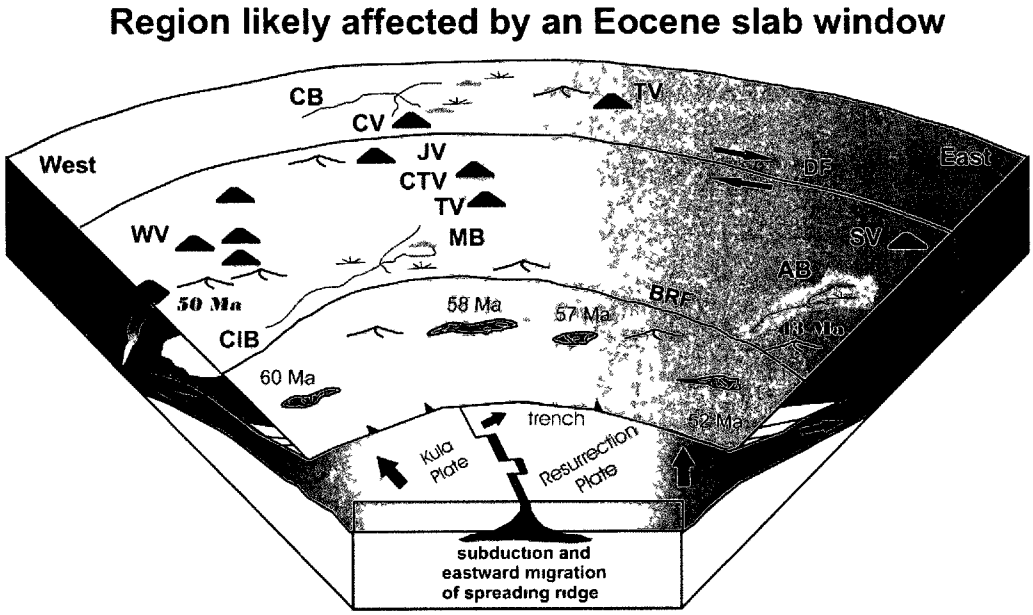

Figure 4.12: Eocene slab window summary figure. Showing near-trench pluton emplacement ages, ages of near-trench initiation of rapid exhumation, basin formation and regional magmatism across the region of Alaska affected by the Paleocene-Eocene ridge subduction-related slab window. Basins: Cook Inlet Basin; CIB, Matanuska Basin; MB, Cantwell Basin; CB, Amphitheater Basin; AB. Western Alaska Range Volcanics: WV; Jack River Volcanics: JV, Central Talkeetna Volcanics: CTV; Caribou Hill Volcanics: CV; Tanana Valley Volcanics: TV; Sifton Volcanics: SV. Denali Fault system: DF; Border Ranges Fault system: BRF are also shown. Modified from *Ridgway et al.* [in press]

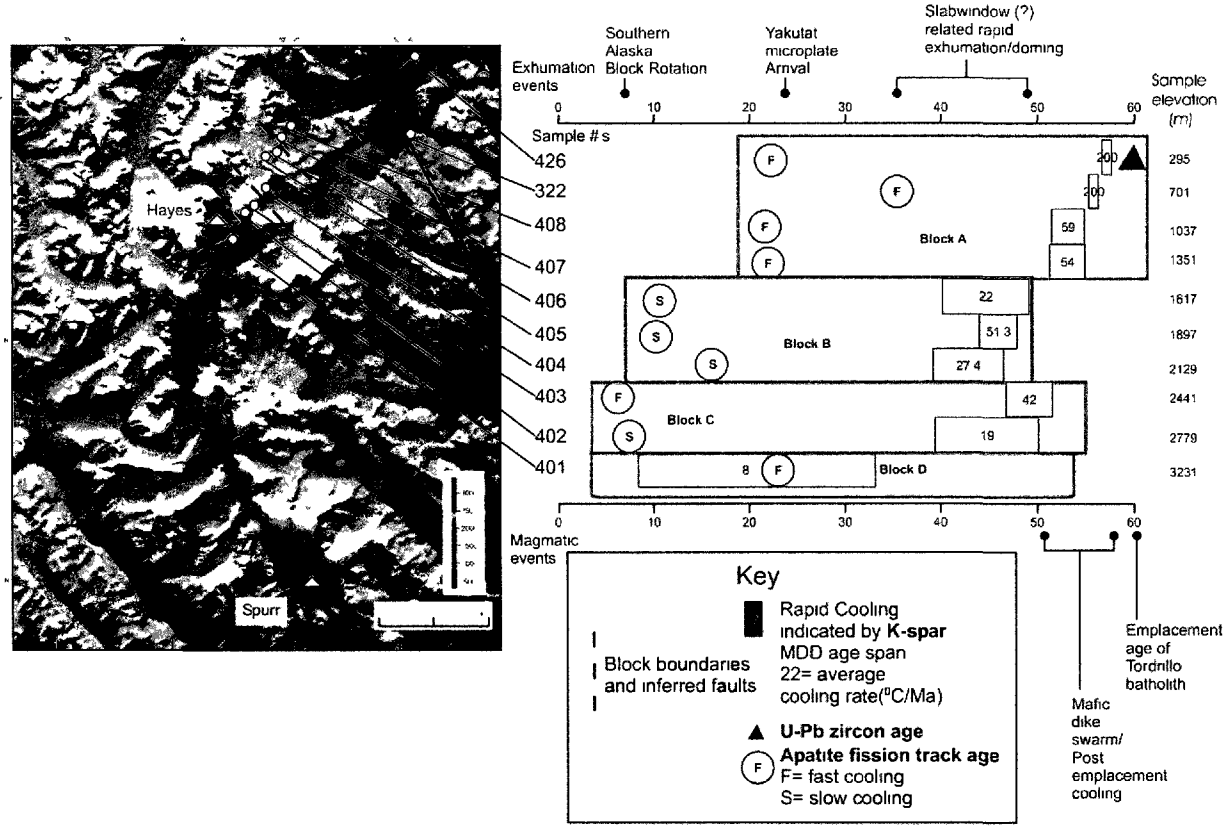

Figure 4.13: Summary of the Cenozoic history of the Tordrillo Mountains. Sample KFAT cooling rate based on the gap between $KFAT_{max}$ and $KFAT_{min}$ ages/200 °C. AFT age are circles with "F" and "S" to designate slow or fast cooling based on track length modeling. Exhumation events and magmatic events noted. AFT data and ~6 Ma interpretation from *Haeussler et al.* [2008].

4.10 **Tables**

Table 4.1: Samples, locations, FT age summary

sample	latitude (°N)	longitude (°W)	elevation (m)	elev. diff btwn samples (m)	fission track mineral	pooled FT age (Ma)	pooled FT age err (Ma)	AHe average corr. Age (Ma)
03PH401A	61 58353	152 39147	3231	---	apatite	23 4	4 3	7 9
03PH402A	61 60664	152 36806	2779	452	apatite	7 9	1 3	6 1
03PH403A	61 61096	152 35458	2441	338	apatite	5 8	0 8	15 8
03PH404A	61 62679	152 33105	2129	312	apatite	16 6	2 2	–
03PH405A	61 65242	152 33069	1897	232	apatite	11 2	5 8	19 9
03PH406A	61 65546	152 31454	1617	280	apatite	11 6	2 5	–
03PH407A	61 66690	152 30583	1351	266	apatite	23 0	2 0	39 7
03PH408A	61 67676	152 28687	1037	314	apatite	22 3	2 1	37 3
02PH332A	61 66985	152 08268	701	336	apatite	35 5	2 7	48 0
01PH426A	61 73477	152 07037	295	406	apatite	23 1	2 9	74 8

NAD27 datum

(F) Furnace

(L) Laser

Table 4.2: Summary of K-Spar $^{40}Ar/^{39}Ar$ results.

Sample name	Latitdude (N)	Longitude (W)	Elev (m)	Intergrated age (Ma)	Plataeu age (Ma)	Span (Ma)	Total span (Ma)	Cooling rate (C/Ma)	Cooling Interpertation
03PH401A(F)	61 58353	152 39147	3231	30 0+-0 3	--	33 2+-1 2 to 8 5 +-2 2	24 7	8 1	Altered or reheated?
03PH402A(F)	61 60664	152 36806	2779	43 5+-0 3	--	50 2+-0 8 to 39 5+-0 7	10 7	18 7	Exhumation
03PH403A(L)	61 61096	152 35458	2441	50 5+-0 2	--	51 6+-0 4 to 46 8+-0 5	4 8	41 7	Dike emplacement?
03PH404A(L)	61 62679	152 33105	2129	47 3+-0 4	--	46 4+-0 7 to 39 1+-1 2	7 3	27 4	Exhumation
03PH405A(L)	61 65242	152 33069	1897	47 2+-0 2	--	47 9+-0 2 to 44 0 +-1 7	3 9	51 3	Exhumation
03PH406A(L)	61 65546	152 31454	1617	46 6+-0 3	--	49 0+-0 4 to 40 0 +-2 3	9	22 2	Exhumation
03PH407A(L)	61 66690	152 30583	1351	52 8+-0 2	--	54 9+-0 3 to 51 2 +-0 5	3 7	54 1	Slow emplacement
03PH408A(L)	61 67676	152 28687	1037	54 2+-0 2	--	54 7+-0 3 to 51 3 +-0 8	3 4	58 8	Slow emplacement
02PH332A(L)	61 66985	152 08268	701	55 5+-0 3	55 5+-0 3	--	--	200	Rapid emplacement
01PH426A(L)	61 73477	152 07037	295	57 1+- 4	57 0+-0 2	--	--	200	Rapid emplacement

NAD27 datum

4.11 **References:**

Benowitz, J.A., P.W. Layer, P. Armstrong, S. Perry, P.J. Haeussler, P.G. Fitzgerald, and S. VanLaningham (2011), Spatial variations in focused exhumation along a continental-scale strike-slip fault: the Denali fault of the eastern Alaska Range. *Geosphere*, v. 7; no. 2; p. 455-467; DOI: 10.1130/GES00589.1.

Bradley, D., R. Friedman, P.W. Layer, P.J. Haeusslle r, A.B. Till, S.M. Roeske, and M.L. Miller (2006), Far-field effects of early tertiary ridge subduction in Alaska *Geological Society of America Abstracts with Programs*, Specialty Meeting No. 2, p. 91.

Bradley, D.C., T.M. Kusky, P.J. Haeussler, R.J. Goldfarb, M.L. Miller, J.A. Dumoulin, S.W. Nelson, and S.M. Karl (2003), Geologic signature of early Tertiary ridge subduction in Alaska; Geology of a transpressional orogen developed during ridge-trench interaction along the North Pacific margin, *Special Paper - Geological Society of America, vol. 371*, pp. 19-49.

Braun, J. (2002a), Estimating exhumation rate and relief evolution by spectral analysis of age elevation datasets. *Terra Nova*, 14:210–214.

Braun, J. (2002b), Quantifying the effect of recent relief changes on age-elevation relationships. *Earth and Planetary Sciences Letters*, 200:331–343.

Braun, J.P. van der Beek, and G. Batt (2006), *Quantitative Thermochronology: Numerical methods for the interpretation of thermochronological data*. Cambridge University Press, Cambridge. 270 p.

Buddington, A. F. (1959), Granite emplacement with special reference to North America: *Geological Society of America Bulletin*, v. 70, p. 671-747.

Buscher, J. T., A. L. Berger, and J. A. Spotila (2008), Exhumation in the Chugach-Kenai mountain belt above the Aleutian subduction zone, southern Alaska, in *Active Tectonics and Seismic Potential of Alaska, Geophysics Monograph Series,* vol. 179, edited by J. Freymueller et al., pp. 151 – 166, AGU, Washington, D. C.

Candela, P.A. (1997) A review of shallow, ore-related granites: textures, volatiles, and ore metals. *Journal of Petrology* 38, 1619-1633.

Cecil, M.R., M.N. Ducea, P.W. Reiners, and C.G., Chase, (2006), Cenozoic exhumation of the northern Sierra Nevada, California, from (U-Th)/ He thermochronology: *Geological Society of America Bulletin*, v. 118, p. 1481–1488, doi: 10.1130/B25876.1.

Cole, R.B., and P.W. Layer (2002), Stratigraphy, age, and geochemistry of Tertiary volcanic rocks and associated synorogenic deposits, Mount McKinley quadrangle, Alaska, in Wilson, F.H., and Galloway, J.P., eds., Studies by the U.S. Geological Survey in Alaska, 2000: *U.S. Geological Survey Professional Paper 1662*, p. 19–43.

Cole, R.B., and B.B. Stewart (2009), Continental margin volcanism at sites of spreading ridge subduction: Examples from southern Alaska and western California, *Tectonophysics*, 464, 118-136, doi:10.1016/j.tecto.2007.12.005.

Cole, R.B., S.W. Nelson, P.W. Layer, and P.J. Oswald (2006), Eocene volcanism above a depleted mantle slab window in Southern Alaska. *Geological Society of America Bulletin* 118 (1–2), 140–158.

Copeland, P. and T.M. Harrison (1990), Episodic rapid uplift in the Himalaya revealed by 40Ar/ 39Ar analysis of detrital K-feldspar and muscovite, Bengal fan. *Geology* 18, 354– 357.

Doubrovine, P.V., and J.A. Tarduno (2008), A revised kinemtaic model for the relative motion between Pacific oceanic plates and North America since Late Cretaceous: *Journal of Geophysical Research-Solid Earth*, v. 113, doi:10.1029/2008JB005585.

Dusel-Bacon, C., and J.M. Murphy (2001), Apatite fission-track evidence of widespread Eocene heating and exhumation in the Yukon-Tanana Upland, interior Alaska: *Canadian Journal of Earth Sciences*, v. 38, no. 8, p. 1191–1204.

Engebretson, D.C., A. Cox, and R.G. Gordon (1985), Relative motions between oceanic and continental plates in the Pacific Basin, *Special Paper - Geological Society of America*, vol. 206, pp. 59.

Enkelmann, E., P.K. Zeitler, J.I. Garver, T.L. Pavlis, and B.P. Hooks (2010), The thermochronological record of tectonic and surface process interaction at the YakutatNorth American collision zone in southeast Alaska. *American Journal of Science* 310, 231-260.

Enkelmann, E., P.K. Zeitler, T.L. Pavlis, J.I. Garver, and K.D. Ridgway (2009), Intense localized rock uplift and erosion in the St Elias orogen of Alaska, *Nature Geoscience*, 2, 360-363.

Enkleman, E., J.I. Garver, and T.L. Pavlis (2008), Rapid exhumation of ice-covered rocks of the Chugach-St.Elias orogen, SE-Alaska. *Geology*, 36, no. 12; 915-918 doi:10.1130/G2252A.1

Farris, D. W., and S. R. Paterson (2009), Subduction of a segmented ridge along a curved continental margin: Variations between the western and eastern Sanak Baranof belt, southern Alaska, *Tectonophysics*, 464, 100-117.

Farris, D. W. (2010), Tectonic and petrologic evolution of the Kodiak batholith and the trenchward belt, Kodiak Island, AK: Contact fault juxtaposition?, *Journal of Geophysics Research*, 115, B07208, doi:10.1029/2009JB006434.

Fisher, M.A., and L.B. Magoon (1978), Geologic framework of lower Cook Inlet, Alaska: *American Association of Petroleum Geologists Bulletin*, v. 62, p. 373–402.

Fitzgerald, P. G., R. B. Sorkhabi, T. F. Redfield, and E. Stump (1995), Uplift and denudation of the central Alaska Range – a case-study in the use of apatite fission-track thermochronology to determine absolute uplift parameters: *Journal of Geophysical Research-Solid Earth*, v. 100, p. 20175-20191.

Flores, R. M., G. D. Stricker, and S. A. Kinney (2004), Alaska coal geology, resources, and coalbed methane potential, *U.S. Geological Survey DDS-77*, 125 p., 3 sheets.

Garver, J.I., E. Enkelmann, and K.J. Kveton (2010), Uplift and exhumation of the Chugach-Prince William Terrane, Alaska, revealed through variable annealing of fission tracks in detrital zircon; *Geological Society of America Abstracts with Programs*, vol. 42, no. 4, p. 46

Gasser, D., E. Bruand, K. Stüwe, D. A. Foster, R. Schuster, B. Fügenschuh, and T. Pavlis (2011), Formation of a metamorphic complex along an obliquely convergent margin: Structural and thermochronological evolution of the Chugach Metamorphic Complex, southern Alaska, *Tectonics*, 30, TC2012, doi:10.1029/2010TC002776.

Gilbert, W.G., V.M. Ferrell, and D.L. Turner (1976), The Teklanika Formation—A new Paleocene volcanic formation in the central Alaska Range: *Alaska Division of Geological and Geophysical Survey, Geology Report 47,* scale 1:63,360, 16 p.

Groome, W.G., and D.J. Thorkelson (2009), The three-dimensional thermomechanical signature of ridge subduction and slab window migration, *Tectonophysics*, 464, 70-83.

Guenthner, W.R., D.L. Barbeau Jr., P.W. Reiners, and S.N. Thomson (2010), Slab window migration and terrane accretion preserved by low-temperature thermochronology of a magmatic arc, northern Antarctic Peninsula, *Geochem. Geophys. Geosyst.*, 11, Q03001, doi:10.1029/2009GC002765.

Guillaume, B., M. Moroni, F. Funiciello, J. Martinod, and C. Faccenna (2010), Mantle flow and dynamic topography associated with slab window opening: Insights from laboratory models, *Tectonophysics*, Volume 496, Issues 1-4, 13 December 2010, Pages 83-98, ISSN 0040-1951, DOI: 10.1016/j.tecto.2010.10.014.

Haeussler, P.J., D.C. Bradley, R.E. Wells, and M.L. Miller (2003), Life and death of the Resurrection Plate; evidence for its existence and subduction in the northeastern Pacific in Paleocene-Eocene time, *Geological Society of America Bulletin*, vol. 115, no. 7, pp. 867-880.

Haeussler, P.J., D. Bradley, R., Ayuso, P.W. Layer, R. Friedman, P. O'Sullivan, M. Miller, and S. Karl (2009), The new USGS Western Alaska Range Project and precursory results from the Tyonek Quadrangle, *Abstracts with Programs*, Alaska Miners Association.

Haeussler, P.J. (2008), An overview of the neotectonics of interior Alaska; far-field deformation from the Yakutat Microplate collision. in *Active Tectonics and Seismic Potential of Alaska, Geophysics Monograph Series*, edited by J.T. Freymueller, P.J. Haeussler, R. Wesson, and G. Ekstrom, Geophysical Monograph 179, AGU, Washington, D.C. p. 269-285.

Haeussler, P.J., P. O'Sullivan, A. Berger, and J. Spotila (2008), Neogene exhumation of the Tordrillo Mountains, Alaska, and correlations with Denali [Mt. McKinley]: in *Active Tectonics and Seismic Potential of Alaska, Geophysics Monograph Series*, edited by J.T. Freymueller, P.J. Haeussler, R. Wesson, and G. Ekstrom, Geophysical Monograph 179, AGU, Washington, D.C. p. 269-285.

Haeussler, P. J., and R.W. Saltus (2004), 26 km of offset on the Lake Clark fault since Late Eocene time: *U.S. Geological Survey Professional Paper 1709- A*, 4 p.

Hillhouse, J.W., and R.S. Coe, (1994) Paleomagnetic data from Alaska, in Plafker, G., and Berg, H.C., eds., *The geology of Alaska: Boulder*, Colorado, Geological Society of America, The Geology of North America, v. G-1, p. 797–812.

Hole, M.J. and W.E. LeMasurier, (1994) Tectonic controls on the geochemical composition of Cenozoic, mafic alkaline volcanic rocks from West Antarctica. *Contributions to Mineralogy and Petrology* 117, 187–202.

House, M.A., B.P. Wernicke, and K.A. Farley (2001), Paleogeomorphology of the Sierra Nevada, California, from the (U-Th)/He ages in apatite: *American Journal of Science*, v. 301, p. 77–102.

Ickert, R.B., D.J. Thorkelson, D.D. Marshall, and T.D. Ullrich (2009), Eocene adakitic volcanism in southern British Columbia: Remelting of arc basalt above a slab window: *Tectonophysics*, v. 464, p. 164–185, doi: 10.1016/j.tecto.2007.10.007.

Kelley, S. (2002), Excess argon in K-Ar and Ar-Ar geochronology, *Chemical Geology*, v. 188, p. 1 – 22.

Little, T.A., and C.W. Naeser (1989), Tertiary tectonics of the Border Ranges fault system, Chugach Mountains, Alaska – deformation and uplift in a fore-arc setting: *Journal of Geophysical Research-Solid Earth and Planets*, v. 94, p. 4333-4359.

Lovera, O.M., M. Grove, and T.M. Harrison (2002), Systematic analysis of K-feldspar $^{40}Ar/3^{9}Ar$ step heating results: II. Relevance of laboratory argon diffusion properties to nature, *Geochimical. Cosmochimical. Acta*, v. 66, p. 1237 – 1255.

Madsen, J.K., D.J. Thorkelson, R.M. Friedman, and D.D. Marshall (2006), Cenozoic to Recent plate configurations in the Pacific Basin: ridge subduction and slab window magmatism in western North America. *Geosphere* v.1, p. 11–34.

Magoon, L. B., W.L. Adkison, and R.M. Egbert (1976), Map showing geology, wildcat wells, Tertiary plant fossil localities, K-Ar age dates, and petroleum operations, Cook Iulet area, Alaska. *U.S. geological Survey Miscellaneous investigations Series Map 1-1019*, scale 1:250,000.

McDougall, I., and T. M. Harrison (1999), Geochronology and Thermochronology by the $^{40}Ar/^{39}Ar$ Method, 212 pp., *Oxford Univ. Press*, New York.

Miller, M.L., D.C. Bradley, and T.K. Bundtzen, and W. McClelland (2002), Late Cretaceous through Cenozoic strike-slip tectonics of southwestern Alaska: *Journal of Geology*, v. 110, p. 247-270.

Miskovic, A., and D., Francis (2006), Interaction between mantle-derived and crustal calc-alkaline magmas in the petrogenesis of the Paleocene Sifton Range volcanic complex, Yukon, Canada. *Lithos* 87 (1–2), 104–134.

O'Sullivan, P.B. and L.D. Currie (1996), Thermotectonic history of Mt. Logan, Yukon Territory, Canada; implications of multiple eposodes of middle to late Cenozoic denudation, *Earth Planetary Science Letters*, 144, pp. 251–261.

O'Sullivan, P., M. Donelick, and R. Donelick (2010), Apatite Fission-Track Results From The Region of The Pebble Deposit, Southwest Alaska, Apatite to Zircon Report 950, *minerals.usgs.gov/mrerp/reports/O'Sullivan-08HQGR0061*.pdf, last accessed 5/5/2010.

Reed, B.L., and M.A. Lanphere (1973), Alaska-Aleutian Range batholith; geochronology, chemistry, and relation to circum-Pacific plutonism, *Geological Society of America* Bulletin v. 84, p. 2583–2609.

Reiners **P**.W. (2009), Nonmonotonic thermal histories and contrasting kinetics of multiple thermochronometers. *Geochemical Cosmochemical Acta* 73:3612-3629.

Reiners, P. W. (2007), Thermochronologic approaches to paleotopography, in *Paleoaltimetry: Geochemical and Thermodynamic Approaches*, Rev. Mineral. Geochem., vol. 66, edited by M. J. Kohn, pp. 243–267, Mineral. Society of America, Chantilly, Va.

Ridgway, K.D., J.M. Trop, and E.S., Finzel, Modification of continental forearc basins by spreading ridge subduction and flat-slab subduction processes: a case study from southern Alaska: submitted to *Recent Advances in Tectonics of Sedimentary Basins*, book volume edited by C. Busby and A. Azor., in press.

Ridgway, K.D., E.E. Thoms, P.W. Layer, M.E. Lesh, J.M. White, and S.V. Smith (2007), Neogene transpressional foreland basin development on the 39 north side of the central Alaska Range, Usibelli Group and Nenana Gravel, Tanana basin, in Tectonic growth of a collisional continental margin: crustal evolution of southern Alaska, *Geological Society of America. Special Paper 431*, edited by K.D. Ridgway et al., pp. 507-547, GSA, Boulder, Colo., doi: 10.1130/2007.2431(20).

Riehle, J.R., P.M. Bowers, P.M., and T.A. Ager (1990), The Hayes tephra deposits, an upper Holocene marker horizon in south-central Alaska. *Quaternary Research* 33, 276–290.

Roeske, S.M., L.W. Snee, and T.L. Pavlis (2003), Dextral-slip reactivation of an arc–forearc boundary during Late Cretaceous–Early Eocene oblique convergence in the northern Cordillera. In: Sisson, V.B., Roeske, S.M., Pavlis, T.L. (Eds.),Geology of a Transpressional Orogen Developed During Ridge–Trench Interaction Along the North Pacific Margin. *Geological Society of America Special Paper,* vol. *371*, pp. 141–170.

Rosenbaum, G., and W. Mo, Tectonic and magmatic responses to the subduction of high bathymetric relief, *Gondwana Research*, in press.

Sisson, V.B., T.L. Pavlis, S.M. Roeske, and D.J. Thorkelson (2003), An overview of ridge–trench interactions in modern and ancient settings. In: Sisson, V.B., Roeske, S., Pavlis, T.L. (Eds.), *Geology of a Transpressional Orogen Developed During Ridge–Trench Interaction Along the North Pacific Margin, Special Paper*, vol. 371. Geological Society of America, Boulder, CO, p. 1 –18.

Solie, D. N., T.K. Bundtzen, and W.G. Gilbert (1991), K/Ar ages of igneous rocks in the McGrath quadrangle, Alaska. *Alsk. Div. Geology Geophysics Survey Public Data File 91-23*, 8 p., scale, I: 63,360.

Stock, J. and P. Molnar (1988), Uncertainties and implications of the Late Cretaceous and Tertiary position of North America relative to the Farallon, Kula, and Pacific plates, *Tectonics*, vol. 7, no. 6, pp. 1339-1384.

Sweet, A.R., and A.R. Cameron (1991), Palynofacies, coal petrographic facies and depositional environments: Amphitheatre Formation (Eocene to Oligocene) and Ravenscrag Formation (Maastrichtian to Paleocene), Canada. *International Journal of Coal Geology*, 19: 121–144.

Taylor, J.P. and P.G. Fitzgerald (2011), Low-temperature thermal history and landscape development of the eastern Adirondack Mountains, New York; constraints from apatite fission-track thermochronology and apatite (U-Th)/He dating, *Geological Society of America Bulletin*, v. 123(3-4), p. 412-426.

Thoms, E.E. (2000), Late Cenozoic unroofing sequence and foreland basin development of the central Alaska Range: implications from the Nenana Gravel: *M.S. thesis*, 215 pp., Univ. Alaska Fairbanks.

Thorkelson, D., J. Madsen, and C. Slugget (2011), Mantle flow through the Northern Cordilleran slab window revealed by volcanic geochemistry, *Geology*, v., 39; no. 3; p. 267–270; doi: 10.1130/G31522.1.

Thorkelson, D. J. (1996), Subduction of diverging plates and the principles of slab window formation, *Tectonophysics*, 255, 47-63, doi:10.1016/0040-1951(95)00106-9.

Trop, J. M., and K. D. Ridgway (2007), Mesozoic and Cenozoic tectonic growth of southern Alaska: a sedimentary basin perspective, in K. D. Ridgway, J. M. Trop, J. M. G. Glen, and J. M. O'Neill, eds., Tectonic growth of a collisional margin: crustal evolution of southern Alaska: *Geological Society of America Special Paper 431,* p. 55-94.

Ward, D. (2010), The effects of lithology on glacial landscape evolution, paced using terrestrial cosmogenic nuclides: Examples from the Colorado Rocky Mountains and the Kichatna Mountains, Alaska Range, Alaska. *Ph.D. dissertation*, University of Colorado, Boulder, CO.

White, T., D. Bradley, and R. Friedman (2006), Stratigraphic model for the development of a time-transgressive unconformity during Paleocene Ridge Subduction, South Costal Alaska. *Geological Society of America Abstracts with Programs*, Vol. 38, No. 7, p. 387

4.12 Repository Figures

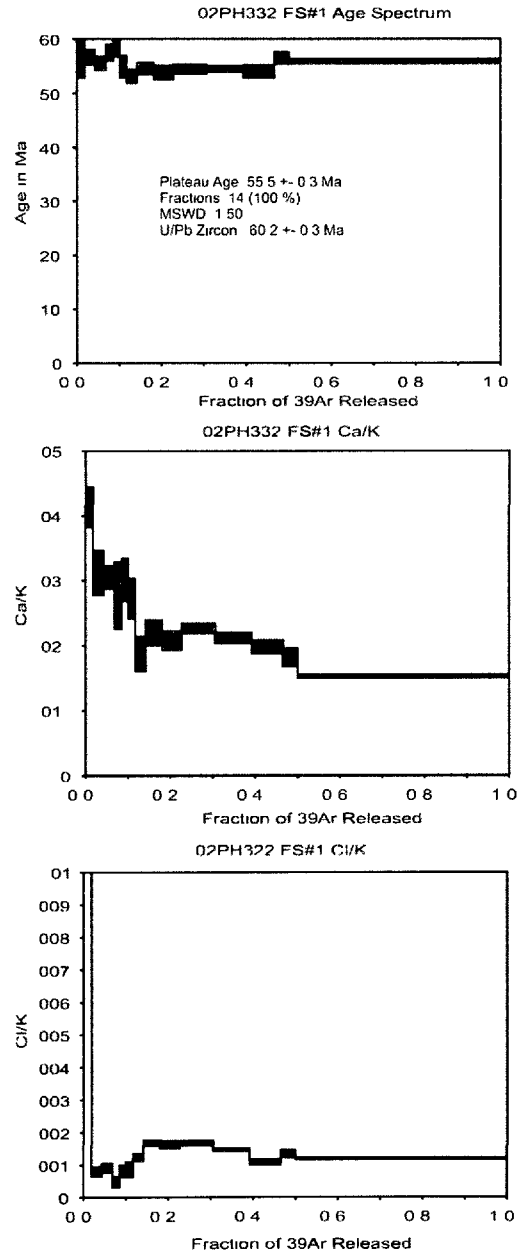

Figure 4R.1: $^{40}Ar/^{39}Ar$ age spectra for K-spar from Tordrillo Mountains sample 02PH322.

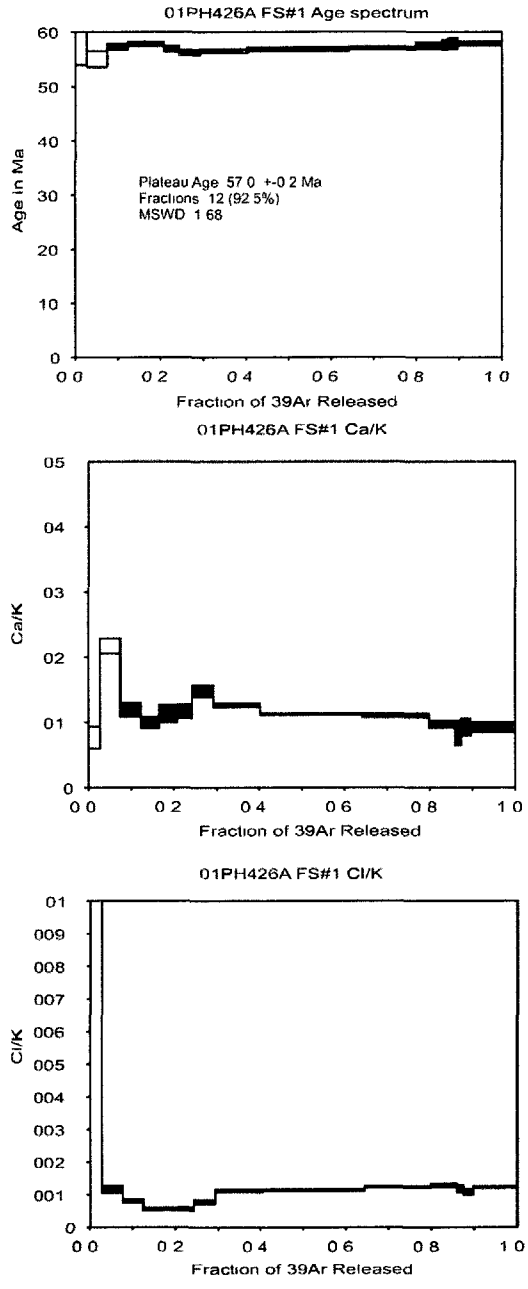

Figure 4R.2: $^{40}Ar/^{39}Ar$ age spectra for K-spar from Tordrillo Mountains sample 01PH426A.

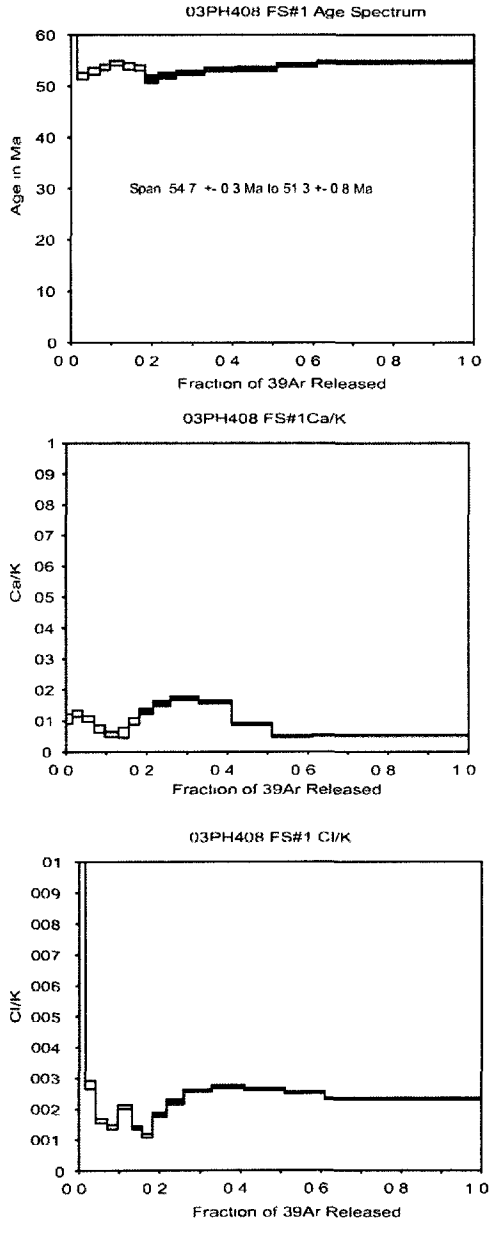

Figure 4R.3: $^{40}Ar/^{39}Ar$ age spectra for K-spar from Tordrillo Mountains sample 03PH408.

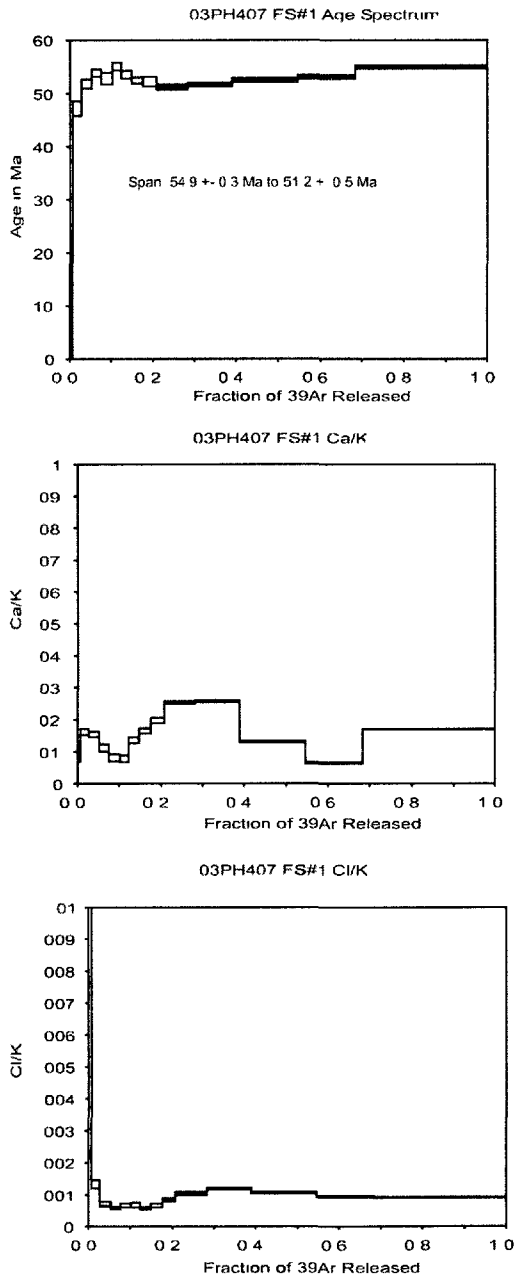

Figure 4R.4: $^{40}Ar/^{39}Ar$ age spectra for K-spar from Tordrillo Mountains sample 03PH407.

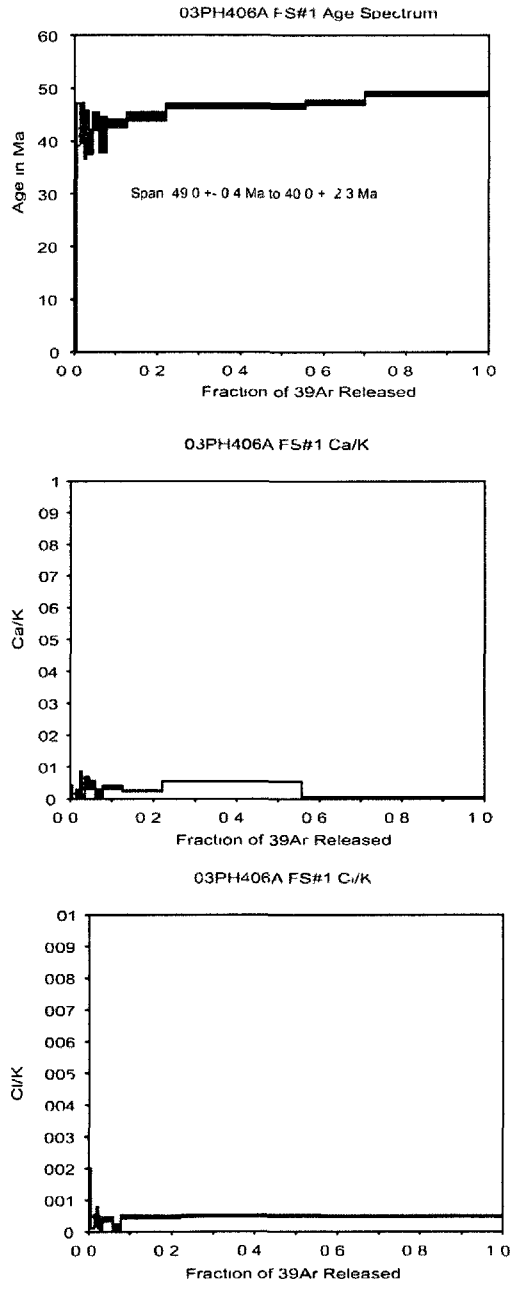

Figure 4R.5: $^{40}Ar/^{39}Ar$ age spectra for K-spar from Tordrillo Mountains sample 03PH406A.

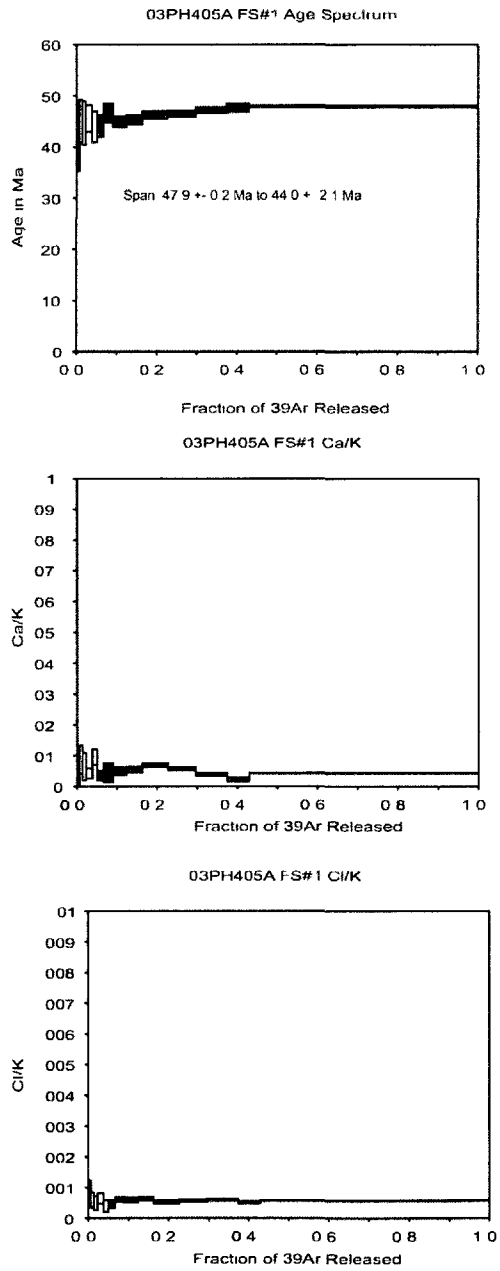

Figure 4R.6: $^{40}Ar/^{39}Ar$ age spectra for K-spar from Tordrillo Mountains sample 03PH405A.

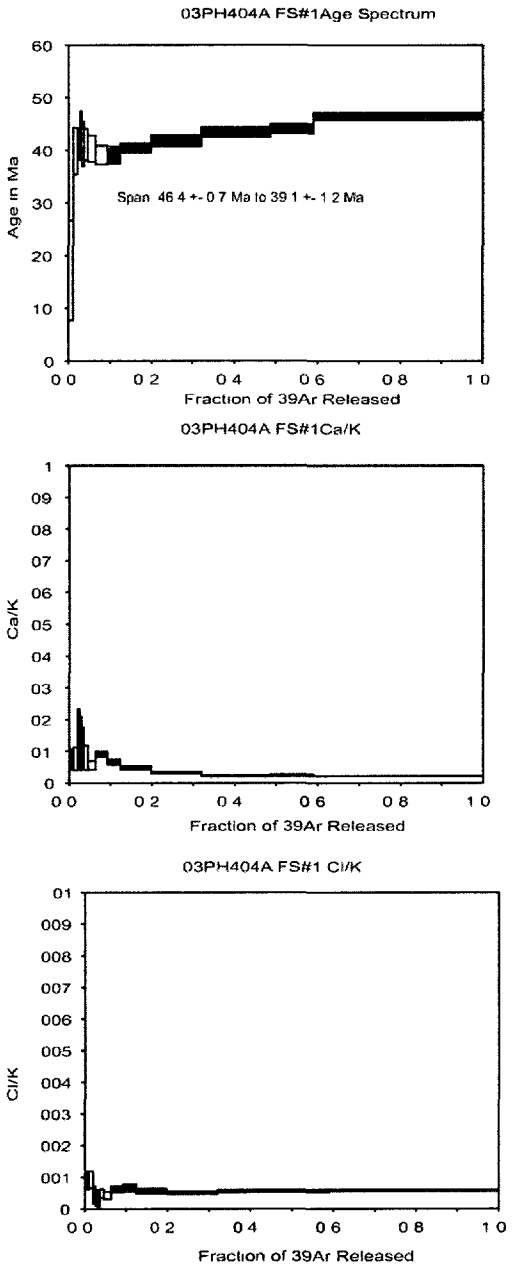

Figure 4R.7: $^{40}Ar/^{39}Ar$ age spectra for K-spar from Tordrillo Mountains sample 03PH404A.

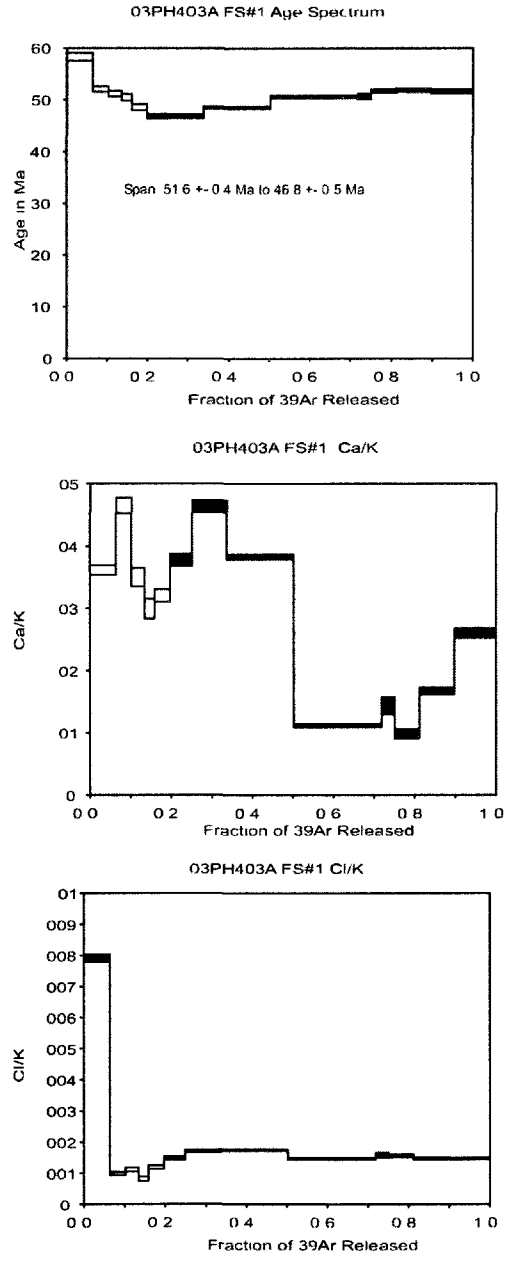

Figure 4R.8: $^{40}Ar/^{39}Ar$ age spectra for K-spar from Tordrillo Mountains sample 03PH403A.

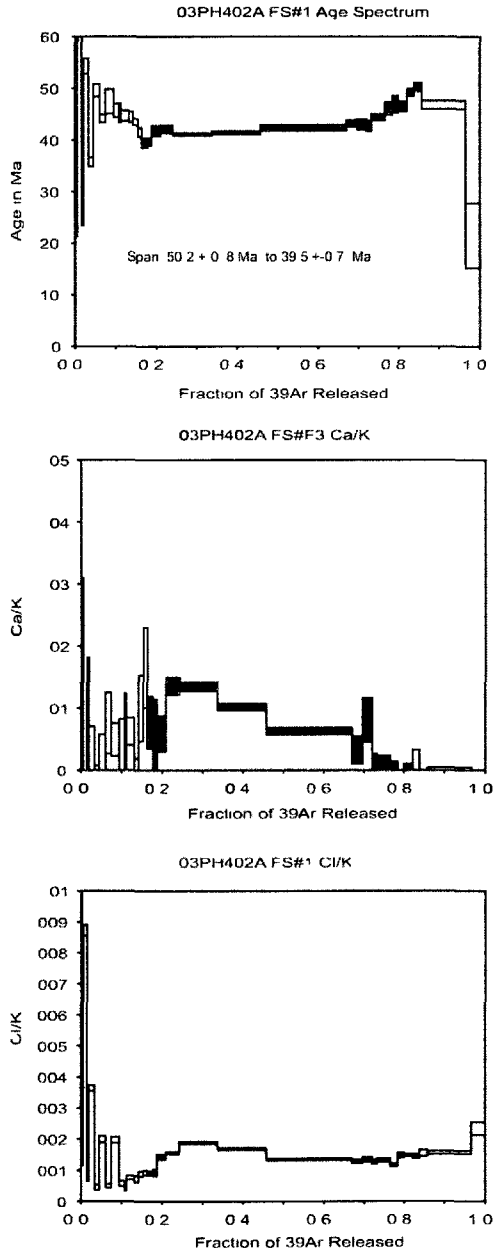

Figure 4R.9: $^{40}Ar/^{39}Ar$ age spectra for K-spar from Tordrillo Mountains sample 03PH402A.

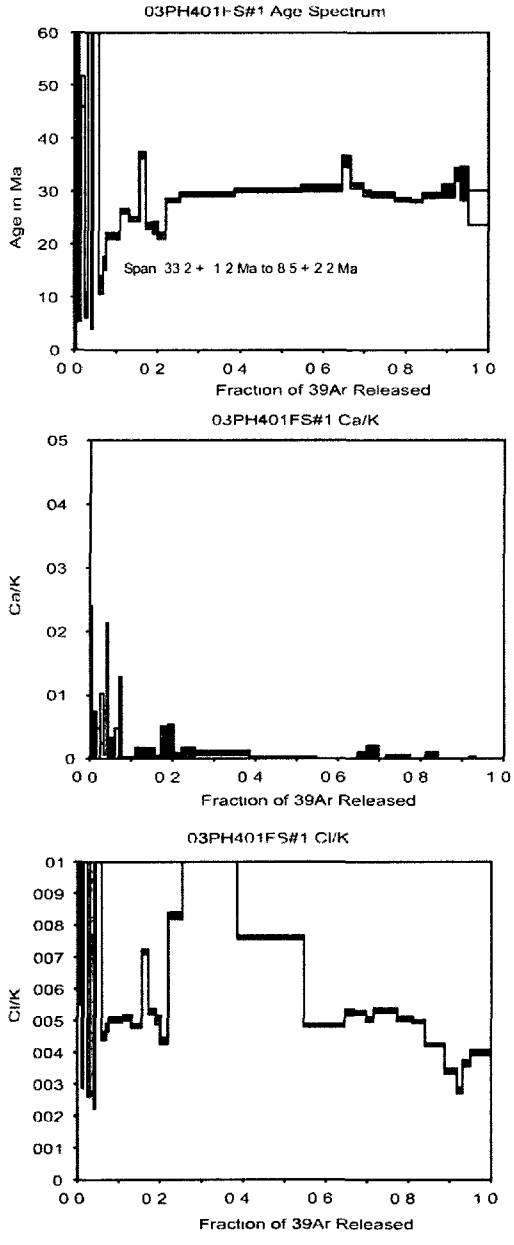

Figure 4R.10: $^{40}Ar/^{39}Ar$ age spectra for K-spar from Tordrillo Mountains sample 03PH401.

4.13 Repository Tables

Table 4R.1: $^{40}Ar/^{39}Ar$ data for K-spar from the Tordrillo Mountains.

01PH426A FS#1 Tordrillo Mountains

Weighted average of J from standards = 3 585e-03 +/- 1 017e-05

Laser Power (mW)	Cumulative 39Ar	40Ar/39Ar measured	+/-	37Ar/39Ar measured	+/-	36Ar/39Ar measured	+/-	% Atmospheric 40Ar
400	0 0264	560 9484	1 8018	0 0042	0 0009	1 8642	0 0069	98 2065
600	0 0746	21 9498	0 1727	0 0118	0 0006	0 0450	0 0007	60 6086
800	0 1233	14 3705	0 0847	0 0065	0 0006	0 0181	0 0002	37 2679
1000	0 1659	11 7681	0 0500	0 0054	0 0005	0 0090	0 0002	22 6739
1300	0 2078	11 6033	0 0487	0 0062	0 0007	0 0085	0 0001	21 6617
1600	0 2427	11 2729	0 0681	0 0064	0 0006	0 0078	0 0002	20 5389
2000	0 2917	12 0673	0 0589	0 0081	0 0005	0 0109	0 0002	26 7437
2500	0 4040	13 4751	0 0483	0 0069	0 0002	0 0155	0 0002	34 0367
3000	0 6424	13 5542	0 0671	0 0061	0 0001	0 0156	0 0002	34 0584
4000	0 7978	13 1530	0 0554	0 0060	0 0002	0 0141	0 0001	31 8215
5000	0 8590	12 8784	0 0862	0 0053	0 0003	0 0130	0 0002	29 7913
6000	0 8735	12 5446	0 0857	0 0046	0 0010	0 0117	0 0004	27 7254
9000	0 8966	12 9083	0 0852	0 0051	0 0007	0 0128	0 0005	29 4183
9001	1 0000	12 6657	0 0400	0 0050	0 0004	0 0120	0 0002	28 0838
Integrated		27 9047	0 0478	0 0063	0 0001	0 0640	0 0002	67 8001

02PH322 FS#1 Tordrillo Mountains

Weighted average of J from standards = 3 585e-03 +/- 1 017e-05

Laser Power (mW)	Cumulative 39Ar	40Ar/39Ar measured	+/-	37Ar/39Ar measured	+/-	36Ar/39Ar measured	+/-	% Atmospheric 40Ar
400	0 0186	69 2344	0 5325	0 0226	0 0017	0 2039	0 0022	87 0676
600	0 0429	26 2599	0 1296	0 0170	0 0019	0 0586	0 0006	66 0385
800	0 0688	28 0249	0 1259	0 0166	0 0010	0 0652	0 0006	68 8100
1000	0 0855	18 8324	0 1311	0 0151	0 0028	0 0330	0 0008	51 9244
1300	0 1009	21 9916	0 1356	0 0164	0 0018	0 0433	0 0008	58 2429
1600	0 1170	18 8742	0 1062	0 0148	0 0017	0 0346	0 0011	54 1887
2000	0 1419	19 7871	0 1367	0 0102	0 0014	0 0386	0 0006	57 7302
2500	0 1814	21 1976	0 1243	0 0120	0 0010	0 0426	0 0005	59 5084
3000	0 2276	22 2844	0 1445	0 0113	0 0008	0 0467	0 0006	61 9876
4000	0 3062	19 5217	0 1168	0 0123	0 0004	0 0370	0 0004	56 0969
5000	0 3923	19 0206	0 0746	0 0115	0 0004	0 0353	0 0002	54 8954

Ca/K	+/-	Cl/K	+/-	40*/39K	+/-	Age (Ma)	+/- (Ma)
0 0077	0 0017	0 0189	0 0004	10 0602	1 5996	63 92	9 99
0 0217	0 0011	0 0012	0 0001	8 6347	0 2316	55 00	1 45
0 0119	0 0011	0 0008	0 0001	8 9964	0 0972	57 27	0 61
0 0099	0 0009	0 0005	0 0001	9 0769	0 0706	57 77	0 44
0 0114	0 0014	0 0006	0 0000	9 0666	0 0600	57 71	0 38
0 0117	0 0010	0 0006	0 0001	8 9340	0 0893	56 88	0 56
0 0148	0 0009	0 0008	0 0001	8 8183	0 0708	56 15	0 44
0 0126	0 0003	0 0011	0 0000	8 8691	0 0540	56 47	0 34
0 0112	0 0001	0 0012	0 0000	8 9183	0 0635	56 78	0 40
0 0111	0 0003	0 0012	0 0000	8 9473	0 0503	56 96	0 31
0 0097	0 0005	0 0013	0 0001	9 0209	0 0934	57 42	0 58
0 0084	0 0019	0 0012	0 0001	9 0451	0 1414	57 58	0 89
0 0093	0 0013	0 0011	0 0001	9 0900	0 1619	57 86	1 01
0 0092	0 0008	0 0012	0 0000	9 0873	0 0660	57 84	0 41
0 0115	0 0002	0 0015	0 0000	8 9758	0 0489	57 14	0 35

Ca/K	+/-	Cl/K	+/-	40*/39K	+/-	Age (Ma)	+/- (Ma)
0 0414	0 0031	0 0182	0 0004	8 9499	0 6498	56 98	4 07
0 0312	0 0034	0 0008	0 0002	8 9083	0 2160	56 72	1 35
0 0305	0 0018	0 0009	0 0001	8 7318	0 2048	55 61	1 28
0 0277	0 0052	0 0005	0 0002	9 0396	0 2370	57 54	1 48
0 0301	0 0033	0 0008	0 0002	9 1708	0 2498	58 36	1 56
0 0272	0 0031	0 0009	0 0002	8 6330	0 3207	54 99	2 01
0 0187	0 0027	0 0012	0 0001	8 3515	0 2002	53 22	1 26
0 0219	0 0019	0 0017	0 0001	8 5713	0 1719	54 60	1 08
0 0207	0 0015	0 0016	0 0001	8 4596	0 2049	53 90	1 29
0 0226	0 0008	0 0017	0 0001	8 5577	0 1373	54 52	0 86
0 0212	0 0008	0 0015	0 0000	8 5658	0 0891	54 57	0 56

Table 4R 1
continued

6000	0 4655	19 3235	0 1425	0 0108	0 0006	0 0366	0 0005
9000	0 4994	19 5854	0 1200	0 0099	0 0008	0 0361	0 0005
9001	1 0000	18 6978	0 0807	0 0083	0 0001	0 0335	0 0002
Integrated		20 5786	0 0484	0 0105	0 0002	0 0401	0 0001

03PH408 FS#1 Tordnllo Mountains

Weighted average of J from standards = 3 585e-03 +/- 1 017e-05

Laser Power (mW)	Cumulative 39Ar	40Ar/39Ar measured	+/-	37Ar/39Ar measured	+/-	36Ar/39Ar measured	+/-
400	0 0154	162 4893	0 5389	0 0058	0 0009	0 5054	0 0022
600	0 0417	13 1009	0 0916	0 0067	0 0006	0 0167	0 0003
800	0 0704	11 3643	0 0765	0 0058	0 0005	0 0103	0 0003
1000	0 0964	10 7315	0 0712	0 0041	0 0007	0 0077	0 0002
1300	0 1304	11 9808	0 0704	0 0031	0 0004	0 0115	0 0002
1600	0 1561	10 8485	0 0659	0 0034	0 0009	0 0080	0 0003
2000	0 1823	10 7609	0 0559	0 0054	0 0006	0 0079	0 0002
2500	0 2162	11 1030	0 0769	0 0071	0 0005	0 0102	0 0004
3000	0 2590	11 7531	0 0777	0 0085	0 0005	0 0120	0 0002
4000	0 3294	11 7202	0 0618	0 0094	0 0003	0 0116	0 0002
5000	0 4101	11 2011	0 0503	0 0088	0 0002	0 0095	0 0002
6000	0 5102	10 6149	0 0663	0 0049	0 0002	0 0075	0 0001
9000	0 6094	10 4164	0 0554	0 0027	0 0002	0 0064	0 0001
9001	1 0000	10 5216	0 0520	0 0029	0 0001	0 0065	0 0001
Integrated		13 2416	0 0287	0 0047	0 0001	0 0159	0 0001

03PH407 FS#1 *Tordnllo Mountains*

Weighted average of J from standards = 3 585e-03 +/- 1 017e-05

Laser Power (mW)	Cumulative 39Ar	40Ar/39Ar measured	+/-	37Ar/39Ar measured	+/-	36Ar/39Ar measured	+/-
400	0 0068	585 2155	1 7711	0 0056	0 0018	1 9775	0 0101
600	0 0272	48 6219	0 2548	0 0088	0 0005	0 1394	0 0010
800	0 0528	24 1779	0 1468	0 0084	0 0005	0 0542	0 0003
1000	0 0754	17 9820	0 1091	0 0061	0 0006	0 0322	0 0003
1300	0 1018	21 2566	0 0895	0 0044	0 0006	0 0438	0 0006
1600	0 1237	17 4961	0 1020	0 0043	0 0006	0 0298	0 0003
2000	0 1484	18 3053	0 0746	0 0073	0 0005	0 0334	0 0003
2500	0 1756	16 3486	0 0836	0 0090	0 0005	0 0274	0 0002
3000	0 2073	18 9446	0 1089	0 0108	0 0005	0 0363	0 0004

56 0416	0 0198	0 0011	0 0011	0 0001	8 4813	0 1889	54 04	1 19
54 5542	0 0182	0 0014	0 0013	0 0001	8 8873	0 1711	56 59	1 07
52 9415	0 0153	0 0002	0 0012	0 0000	8 7850	0 0639	55 94	0 40
57 6247	0 0193	0 0003	0 0016	0 0000	8 7077	0 0429	55 46	0 31

% Atmospheric 40Ar	Ca/K	+/-	Cl/K	+/-	40*/39K	+/-	Age (Ma)	+/- (Ma)
91 9302	0 0106	0 0016	0 0611	0 0005	13 1102	0 5656	82 86	3 49
37 6486	0 0123	0 0010	0 0028	0 0001	8 1501	0 1085	51 96	0 68
26 7865	0 0106	0 0009	0 0016	0 0001	8 2985	0 1025	52 89	0 64
21 3109	0 0075	0 0012	0 0014	0 0001	8 4212	0 0834	53 66	0 52
28 4558	0 0056	0 0008	0 0021	0 0001	8 5504	0 0754	54 47	0 47
21 8948	0 0062	0 0017	0 0014	0 0001	8 4501	0 1092	53 84	0 69
21 6563	0 0099	0 0011	0 0011	0 0001	8 4073	0 0797	53 57	0 50
27 2911	0 0130	0 0009	0 0018	0 0001	8 0513	0 1251	51 34	0 79
30 3464	0 0156	0 0009	0 0022	0 0001	8 1658	0 0914	52 06	0 57
29 3943	0 0173	0 0006	0 0026	0 0000	8 2542	0 0762	52 61	0 48
25 2128	0 0161	0 0004	0 0027	0 0001	8 3549	0 0669	53 25	0 42
20 9366	0 0090	0 0004	0 0026	0 0000	8 3690	0 0745	53 33	0 47
18 1892	0 0049	0 0003	0 0025	0 0000	8 4975	0 0607	54 14	0 38
18 2064	0 0053	0 0001	0 0023	0 0000	8 5817	0 0458	54 67	0 29
35 5715	0 0087	0 0001	0 0032	0 0000	8 5122	0 0249	54 23	0 22

% Atmospheric 40Ar	Ca/K	+/-	Cl/K	+/-	40*/39K	+/-	Age (Ma)	+/- (Ma)
99 8552	0 0102	0 0032	0 0125	0 0006	0 8474	2 8996	5 47	18 70
84 7859	0 0162	0 0010	0 0013	0 0001	7 3929	0 2194	47 19	1 38
66 3615	0 0154	0 0009	0 0007	0 0001	8 1232	0 1362	51 79	0 86
52 9678	0 0112	0 0012	0 0006	0 0001	8 4434	0 1087	53 80	0 68
60 9878	0 0081	0 0011	0 0007	0 0001	8 2811	0 1801	52 78	1 13
50 4845	0 0078	0 0011	0 0007	0 0001	8 6486	0 1094	55 09	0 69
54 0286	0 0135	0 0009	0 0006	0 0000	8 4016	0 1143	53 54	0 72
49 5673	0 0165	0 0008	0 0007	0 0001	8 2301	0 0917	52 46	0 58
56 7143	0 0197	0 0008	0 0008	0 0000	8 1875	0 1428	52 19	0 90

Table 4R 1
continued

4000	0 2832	20 6192	0 0778	0 0138	0 0002	0 0425	0 0003
5000	0 3900	18 5881	0 0729	0 0140	0 0002	0 0354	0 0002
6000	0 5447	15 2935	0 0650	0 0071	0 0001	0 0238	0 0002
9000	0 6830	14 4707	0 0573	0 0035	0 0001	0 0207	0 0001
9001	1 0000	17 6796	0 0563	0 0092	0 0001	0 0305	0 0001
Integrated		21 9661	0 0313	0 0086	0 0001	0 0462	0 0001

03PH406A FS#1 Tordrillo Mountains

Weighted average of J from standards = 3 585e-03 +/- 1 017e-05

Laser Power (mW)	Cumulative 39Ar	40Ar/39Ar measured	+/-	37Ar/39Ar measured	+/-	36Ar/39Ar measured	+/-
400	0 0056	323 8739	1 4863	0 0012	0 0011	1 0967	0 0080
600	0 0131	65 8774	0 4039	0 0004	0 0005	0 2000	0 0021
800	0 0189	51 9891	0 4806	0 0010	0 0007	0 1531	0 0015
1000	0 0228	36 5118	0 2135	0 0000	0 0013	0 0999	0 0016
1300	0 0278	41 5676	0 3965	0 0032	0 0016	0 1195	0 0018
1600	0 0340	43 8066	0 4213	0 0008	0 0009	0 1254	0 0014
2000	0 0438	37 9937	0 2711	0 0027	0 0010	0 1074	0 0011
2500	0 0586	35 3027	0 2071	0 0024	0 0007	0 0962	0 0009
3000	0 0777	32 1927	0 1427	0 0009	0 0008	0 0870	0 0018
4000	0 1262	27 4593	0 1074	0 0020	0 0002	0 0699	0 0004
5000	0 2200	26 0515	0 1516	0 0014	0 0001	0 0644	0 0005
6000	0 5576	22 8794	0 0744	0 0030	0 0000	0 0526	0 0002
9000	0 7010	22 8086	0 0904	0 0003	0 0001	0 0520	0 0002
9001	1 0000	24 1017	0 0880	0 0003	0 0000	0 0555	0 0002
Integrated		26 7214	0 0455	0 0015	0 0000	0 0657	0 0001

03PH405A FS#1 Tordrillo Mountains

Weighted average of J from standards = 3 585e-03 +/- 1 017e-05

Laser Power (mW)	Cumulative 39Ar	40Ar/39Ar measured	+/-	37Ar/39Ar measured	+/-	36Ar/39Ar measured	+/-
400	0 0061	131 9272	1 0432	-0 0025	0 0027	0 4245	0 0041
600	0 0137	49 0946	0 5024	0 0048	0 0025	0 1422	0 0024
800	0 0221	48 1155	0 3698	0 0036	0 0024	0 1390	0 0022
1000	0 0379	50 2639	0 3396	0 0024	0 0009	0 1458	0 0014
1300	0 0497	46 8417	0 3424	0 0053	0 0014	0 1352	0 0016
1600	0 0662	38 6431	0 2567	0 0020	0 0008	0 1073	0 0010

61 0065	0 0253	0 0004	0 0010	0 0001	8 0287	0 0838	51 20	0 53
56 3513	0 0257	0 0003	0 0012	0 0000	8 1006	0 0574	51 65	0 36
46 0037	0 0131	0 0002	0 0011	0 0000	8 2419	0 0638	52 54	0 40
42 3588	0 0064	0 0002	0 0009	0 0000	8 3240	0 0532	53 05	0 33
51 1077	0 0170	0 0002	0 0009	0 0000	8 6295	0 0481	54 97	0 30
62 2068	0 0158	0 0001	0 0010	0 0000	8 2905	0 0308	52 84	0 24

% Atmospheric 40Ar	Ca/K	+/-	Cl/K	+/-	40*/39K	+/-	Age (Ma)	+/- (Ma)
100 0675	0 0022	0 0020	0 0015	0 0005	-0 2187	2 0798	-1 41	13 46
89 7404	0 0008	0 0008	0 0003	0 0002	6 7557	0 6416	43 18	4 05
87 0836	0 0017	0 0012	0 0004	0 0002	6 7113	0 5085	42 89	3 21
80 9375	0 0001	0 0024	0 0005	0 0003	6 9544	0 4535	44 43	2 86
85 0108	0 0058	0 0029	0 0003	0 0002	6 2262	0 5072	39 83	3 21
84 6458	0 0014	0 0016	0 0000	0 0001	6 7216	0 4503	42 96	2 84
83 5623	0 0050	0 0019	0 0004	0 0001	6 2404	0 3675	39 92	2 33
80 5636	0 0044	0 0012	0 0004	0 0001	6 8558	0 2716	43 81	1 71
79 9646	0 0016	0 0015	0 0002	0 0001	6 4440	0 5339	41 21	3 38
75 2491	0 0037	0 0004	0 0005	0 0001	6 7891	0 1235	43 39	0 78
73 1129	0 0025	0 0002	0 0005	0 0000	6 9965	0 1376	44 70	0 87
67 9712	0 0055	0 0001	0 0005	0 0000	7 3185	0 0680	46 73	0 43
67 4557	0 0006	0 0001	0 0005	0 0000	7 4132	0 0685	47 32	0 43
68 0810	0 0005	0 0001	0 0005	0 0000	7 6836	0 0649	49 02	0 41
72 6857	0 0027	0 0001	0 0005	0 0000	7 2907	0 0390	46 55	0 28

% Atmospheric 40Ar	Ca/K	+/-	Cl/K	+/-	40*/39K	+/-	Age (Ma)	+/- (Ma)
95 1106	0 0045	0 0049	0 0010	0 0003	6 4490	0 9316	41 24	5 89
85 6193	0 0087	0 0046	0 0006	0 0003	7 0559	0 6719	45 07	4 24
85 4440	0 0066	0 0045	0 0005	0 0002	6 9994	0 6758	44 71	4 26
85 7809	0 0043	0 0017	0 0007	0 0002	7 1429	0 4116	45 62	2 60
85 3098	0 0097	0 0026	0 0004	0 0002	6 8768	0 4822	43 94	3 04
82 1254	0 0036	0 0015	0 0005	0 0001	6 9020	0 3356	44 10	2 12

Table 4R 1
continued

2000	0 0901	27 4156	0 1601	0 0025	0 0017	0 0680	0 0010
2500	0 1236	22 3911	0 1241	0 0027	0 0007	0 0519	0 0005
3000	0 1629	21 3536	0 1089	0 0031	0 0005	0 0481	0 0004
4000	0 2269	19 2716	0 0934	0 0038	0 0004	0 0406	0 0004
5000	0 2963	16 9082	0 0980	0 0031	0 0003	0 0324	0 0002
6000	0 3741	15 9857	0 0861	0 0022	0 0002	0 0290	0 0002
9000	0 4297	15 3256	0 0713	0 0013	0 0004	0 0265	0 0004
9001	1 0000	17 7104	0 0478	0 0024	0 0001	0 0344	0 0001
Integrated		20 4124	0 0342	0 0025	0 0001	0 0440	0 0001

03PH404A FS#1 Tordrillo Mountains

Weighted average of J from standards = 3 585e-03 +/- 1 017e-05

Laser Power (mW)	Cumulative 39Ar	40Ar/39Ar measured	+/-	37Ar/39Ar measured	+/-	36Ar/39Ar measured	+/-
400	0 0103	200 3153	0 9670	0 0040	0 0017	0 6688	0 0053
600	0 0202	59 1234	0 3521	0 0041	0 0020	0 1789	0 0024
800	0 0264	39 3741	0 3308	0 0091	0 0035	0 1114	0 0014
1000	0 0308	43 5192	0 2986	0 0068	0 0046	0 1236	0 0014
1300	0 0365	47 2112	0 4251	0 0063	0 0032	0 1379	0 0022
1600	0 0460	57 1754	0 4354	0 0043	0 0021	0 1717	0 0017
2000	0 0646	49 9240	0 2699	0 0030	0 0007	0 1475	0 0013
2500	0 0930	46 9340	0 2147	0 0049	0 0005	0 1381	0 0010
3000	0 1243	40 6251	0 1628	0 0035	0 0005	0 1167	0 0009
4000	0 1977	34 6307	0 1721	0 0026	0 0003	0 0957	0 0005
5000	0 3202	29 7821	0 1514	0 0017	0 0001	0 0786	0 0006
6000	0 4874	27 5406	0 1473	0 0012	0 0001	0 0701	0 0005
9000	0 5892	25 7660	0 1191	0 0013	0 0002	0 0638	0 0005
9001	1 0000	26 3513	0 1084	0 0011	0 0000	0 0645	0 0003
Integrated		31 6683	0 0635	0 0018	0 0001	0 0840	0 0002

03PH403A FS#1 Tordrillo Mountains

Weighted average of J from standards = 3 585e-03 +/- 1 017e-05

Laser Power (mW)	Cumulative 39Ar	40Ar/39Ar measured	+/-	37Ar/39Ar measured	+/-	36Ar/39Ar measured	+/-
400	0 0640	35 7123	0 1164	0 0197	0 0004	0 0898	0 0004
600	0 1024	9 9075	0 0658	0 0254	0 0007	0 0058	0 0002
800	0 1349	9 3960	0 0652	0 0191	0 0008	0 0045	0 0002

73 3189	0 0045	0 0030	0 0006	0 0001	7 3069	0 2982	46 65	1 88
68 5228	0 0050	0 0012	0 0006	0 0001	7 0388	0 1719	44 96	1 08
66 6865	0 0056	0 0009	0 0006	0 0001	7 1038	0 1471	45 37	0 93
62 3206	0 0069	0 0006	0 0005	0 0001	7 2503	0 1275	46 30	0 80
56 7944	0 0058	0 0005	0 0006	0 0000	7 2925	0 0985	46 56	0 62
53 6115	0 0040	0 0004	0 0006	0 0000	7 4018	0 0909	47 25	0 57
51 1256	0 0023	0 0007	0 0005	0 0000	7 4758	0 1308	47 72	0 82
57 4913	0 0043	0 0001	0 0006	0 0000	7 5159	0 0351	47 97	0 22
63 7088	0 0046	0 0002	0 0006	0 0000	7 3972	0 0305	47 22	0 23

% Atmospheric 40Ar	Ca/K	+/-	Cl/K	+/-	40*/39K	+/-	Age (Ma)	+/- (Ma)
98 6689	0 0074	0 0031	0 0009	0 0003	2 6661	1 4789	17 16	9 48
89 4656	0 0076	0 0036	0 0009	0 0003	6 2252	0 6993	39 82	4 42
83 6914	0 0167	0 0065	0 0004	0 0003	6 4166	0 4550	41 03	2 88
83 9551	0 0125	0 0084	0 0004	0 0003	6 9779	0 4463	44 58	2 82
86 3456	0 0116	0 0059	0 0001	0 0003	6 4424	0 6747	41 20	4 27
88 7619	0 0079	0 0039	0 0005	0 0001	6 4221	0 4732	41 07	2 99
87 3804	0 0056	0 0013	0 0004	0 0001	6 2965	0 3926	40 27	2 48
86 9849	0 0090	0 0009	0 0006	0 0001	6 1047	0 2799	39 06	1 77
84 9587	0 0065	0 0009	0 0007	0 0001	6 1061	0 2593	39 07	1 64
81 7549	0 0048	0 0005	0 0006	0 0001	6 3130	0 1394	40 38	0 88
78 0187	0 0032	0 0002	0 0005	0 0000	6 5400	0 1657	41 81	1 05
75 2805	0 0022	0 0002	0 0006	0 0000	6 8006	0 1453	43 46	0 92
73 2079	0 0023	0 0003	0 0006	0 0000	6 8953	0 1406	44 06	0 89
72 3706	0 0021	0 0001	0 0006	0 0000	7 2725	0 1061	46 44	0 67
78 4121	0 0032	0 0001	0 0006	0 0000	6 8301	0 0609	43 64	0 40

% Atmospheric 40Ar	Ca/K	+/-	Cl/K	+/-	40*/39K	+/-	Age (Ma)	+/- (Ma)
74 3436	0 0361	0 0008	0 0079	0 0001	9 1550	0 1230	58 26	0 77
17 3324	0 0465	0 0012	0 0010	0 0001	8 1659	0 0871	52 06	0 55
14 2935	0 0350	0 0015	0 0011	0 0001	8 0276	0 0853	51 19	0 54

Table 4R 1
continued

1000	0 1597	8 9494	0 0658	0 0163	0 0009	0 0034	0 0003	11 2842	0 0299
1300	0 1977	9 1863	0 0649	0 0175	0 0005	0 0052	0 0003	16 9092	0 0320
1600	0 2504	9 6233	0 0471	0 0206	0 0006	0 0077	0 0002	23 5432	0 0378
2000	0 3356	9 5844	0 0573	0 0253	0 0005	0 0075	0 0001	23 3027	0 0464
2500	0 5024	9 1601	0 0408	0 0209	0 0002	0 0052	0 0000	16 7504	0 0383
3000	0 7185	8 8714	0 0323	0 0061	0 0002	0 0031	0 0001	10 2937	0 0112
4000	0 7496	9 1827	0 0753	0 0078	0 0008	0 0041	0 0002	13 2618	0 0144
5000	0 8110	9 0225	0 0458	0 0054	0 0004	0 0030	0 0001	9 8433	0 0099
6000	0 8972	9 1164	0 0494	0 0091	0 0003	0 0032	0 0001	10 4350	0 0168
9001	1 0000	9 2650	0 0587	0 0142	0 0004	0 0039	0 0001	12 3863	0 0260
Integrated		10 8881	0 0169	0 0148	0 0001	0 0100	0 0000	27 0933	0 0271

03PH402A FS#1 Tordrillo Mountains

Weighted average of J from standards = 3 585e-03 +/- 1 017e-05

Step	T (C)	t (min)	39Ar (mol)	+/-	Cum 39Ar	Age (Ma)	+/-	Model Age
1	300	12	3 01E-13	3 48E-15	0 0532	-74 78	112 39	112 39
2	300	40	4 67E-13	3 23E-15	0 1359	154 77	23 88	23 88
3	350	12	1 10E-12	1 03E-14	0 3312	167 1	11 86	11 86
4	350	40	1 00E-12	6 54E-15	0 5085	27 3	6 05	6 05
5	400	12	5 54E-12	2 17E-14	1 4893	92 39	2 48	2 48
6	400	40	2 73E-12	7 91E-15	1 9717	25 7	2 34	2 34
7	450	12	7 61E-12	2 91E-14	3 319	54 23	1 48	1 48
8	450	40	6 55E-12	2 15E-14	4 4779	35 77	0 87	0 87
9	500	12	8 95E-12	3 88E-14	6 0629	49 62	1 24	1 24
10	500	40	7 61E-12	2 91E-14	7 4094	44 16	0 76	0 76
11	550	12	1 15E-11	6 71E-14	9 4376	47 45	2 38	2 38
12	550	40	7 02E-12	8 26E-14	10 68	45 69	1 32	1 32
13	600	12	2 84E-12	1 10E-14	11 182	45 24	1 79	1 79
14	600	40	1 13E-11	1 03E-13	13 182	44 68	1 05	1 05
15	650	12	6 07E-12	2 29E-14	14 258	44 46	0 96	0 96
16	650	40	6 48E-12	3 14E-14	15 405	43 46	0 65	0 65
17	700	12	5 40E-12	1 53E-14	16 361	41 48	0 88	0 88
18	700	40	8 32E-12	6 86E-14	17 833	39 43	0 94	0 94
19	750	12	5 45E-12	1 65E-14	18 797	39 65	0 73	0 73
20	750	40	1 22E-11	9 33E-14	20 962	41 75	1	1
21	800	12	1 82E-11	6 48E-14	24 183	42 05	0 75	0 75
22	800	40	5 38E-11	2 28E-13	33 704	41 08	0 23	0 23
23	850	12	6 80E-11	3 03E-13	45 741	41 37	0 29	0 29
24	850	40	1 20E-10	3 54E-13	67 061	42 33	0 59	0 59
25	900	12	1 44E-11	5 26E-14	69 604	43 19	0 65	0 65
26	950	12	1 36E-11	5 86E-14	72 002	42 99	0 99	0 99
27	1000	12	7 15E-12	3 54E-14	73 269	42 72	1 02	1 02

0 0016	0 0008	0 0001	7 9133	0 1043	50 47	0 66
0 0010	0 0012	0 0001	7 6084	0 0957	48 55	0 60
0 0010	0 0015	0 0001	7 3351	0 0728	46 83	0 46
0 0010	0 0017	0 0001	7 3283	0 0567	46 79	0 36
0 0004	0 0017	0 0000	7 6011	0 0373	48 51	0 23
0 0003	0 0015	0 0000	7 9316	0 0373	50 59	0 23
0 0014	0 0016	0 0001	7 9392	0 0890	50 63	0 56
0 0007	0 0016	0 0000	8 1076	0 0578	51 69	0 36
0 0006	0 0015	0 0000	8 1386	0 0541	51 89	0 34
0 0008	0 0015	0 0000	8 0914	0 0604	51 59	0 38
0 0002	0 0019	0 0000	7 9166	0 0180	50 49	0 18

CI age	+/-
-74 78	112 39
154 77	23 88
167 1	11 86
27 3	6 05
92 39	2 48
25 7	2 34
54 23	1 48
35 77	0 87
49 62	1 24
44 16	0 76
47 45	2 38
45 69	1 32
45 24	1 79
44 68	1 05
44 46	0 96
43 46	0 65
41 48	0 88
39 43	0 94
39 65	0 73
41 75	1
42 05	0 75
41 08	0 23
41 37	0 29
42 33	0 59
43 19	0 65
42 99	0 99
42 72	1 02

Table 4R 1
continued

28	1000	40	1 87E-11	7 04E-14	76 573	44 35	0 62
29	1000	60	1 01E-11	3 91E-14	78 357	46 05	1 23
30	1050	12	8 73E-12	7 19E-14	79 902	46 93	1 62
31	1050	40	1 21E-11	3 58E-14	82 048	46 45	0 99
32	1050	60	9 75E-12	1 61E-14	83 774	49 17	0 69
33	1100	12	1 12E-11	4 34E-14	85 763	50 23	0 78
34	1200	12	6 09E-11	3 18E-13	96 542	46 82	0 78
35	1600	40	1 95E-11	5 12E-14	99 99	21 48	6 28

03PH401FS#1 Tordrillo Mountains

Weighted average of J from standards = 3 585e-03 +/- 1 017e-05

Step	T (C)	t (min)	39Ar (mol)	+/-	Cum 39Ar	Age (Ma)	+/-
1	300	12	7 30E-13	4 65E-15	0 0729	19 87	22 29
2	300	40	4 07E-13	4 10E-15	0 1136	33 57	41 13
3	350	12	2 11E-12	3 29E-14	0 3245	81 11	25 02
4	350	40	1 10E-12	9 56E-15	0 4348	10 52	16 53
5	400	12	5 43E-12	4 90E-14	0 9773	63 38	10 08
6	400	40	4 78E-12	2 86E-14	1 4549	8 83	3 35
7	450	12	9 63E-12	6 50E-14	2 4178	48 88	2 86
8	450	40	7 50E-12	5 05E-14	3 1676	8 55	2 41
9	500	12	8 34E-12	4 28E-14	4 0009	66 44	2 41
10	500	40	4 01E-12	4 38E-14	4 4016	8 53	4 44
11	550	12	1 49E-11	1 28E-13	5 8941	77 25	4 29
12	550	40	1 07E-11	1 10E-13	6 9655	12 26	1 74
13	600	12	6 61E-12	6 93E-14	7 6262	16 37	1 23
14	600	40	3 30E-11	1 54E-13	10 923	21 58	0 58
15	650	12	2 15E-11	1 21E-13	13 076	26 24	0 5
16	650	40	2 44E-11	9 16E-14	15 518	24 78	0 42
17	700	12	1 53E-11	6 29E-14	17 049	36 85	0 66
18	700	40	1 84E-11	1 28E-13	18 891	23 5	0 6
19	750	12	1 20E-11	1 41E-13	20 091	23 14	1 11

Table 4R 1
continued

20	750	40	1 88E-11	1 43E-13	21 969	21 63	0 64
21	800	12	3 37E-11	1 58E-13	25 337	28 29	0 35
22	800	40	1 32E-10	1 45E-12	38 481	29 43	0 44
23	850	12	1 61E-10	5 47E-13	54 583	30 22	0 33
24	850	40	1 01E-10	3 07E-13	64 629	30 63	0 58
25	900	12	2 07E-11	1 18E-13	66 698	35 73	1 03
26	950	12	3 03E-11	1 44E-13	69 724	31 07	0 47
27	1000	12	1 84E-11	1 04E-13	71 562	29 65	0 55
28	1000	40	5 70E-11	3 04E-13	77 263	29 41	0 45
29	1000	60	3 85E-11	1 95E-13	81 112	28 51	0 28

0 62	44 35	0 62
1 23	46 05	1 23
1 62	46 93	1 62
0 99	46 45	0 99
0 69	49 17	0 69
0 78	50 23	0 78
0 78	46 82	0 78
6 28	21 48	6 28

Model Age	CI age	+/-
22 29	19 87	22 29
41 13	33 57	41 13
25 02	81 11	25 02
16 53	10 52	16 53
10 08	63 38	10 08
3 35	8 83	3 35
2 86	48 88	2 86
2 41	8 55	2 41
2 41	66 44	2 41
4 44	8 53	4 44
4 29	77 25	4 29
1 74	12 26	1 74
1 23	16 37	1 23
0 58	21 58	0 58
0 5	26 24	0 5
0 42	24 78	0 42
0 66	36 85	0 66
0 6	23 5	0 6
1 11	23 14	1 11

0 64	21 63	0 64
0 35	28 29	0 35
0 44	29 43	0 44
0 33	30 22	0 33
0 58	30 63	0 58
1 03	35 73	1 03
0 47	31 07	0 47
0 55	29 65	0 55
0 45	29 41	0 45
0 28	28 51	0 28

Table 4R I
continued

30	1050	12	2 93E-11	6 83E-14	84 037	28 17	0 25	0 25	28 17	0 25
31	1050	40	4 72E-11	2 14E-13	88 752	29 22	0 49	0 49	29 22	0 49
32	1050	60	3 05E-11	1 80E-13	91 799	30 13	1 27	1 27	30 13	1 27
33	1100	12	1 36E-11	6 75E-14	93 156	33 15	1 2	1 2	33 15	1 2
34	1200	12	1 98E-11	4 67E-14	95 135	31 46	3 2	3 2	31 46	3 2
35	1600	40	4 87E-11	9 53E-14	99 99	26 84	3 25	3 25	26 84	3 25

CHAPTER 5

CONCLUSION: OROGENIC HISTORY OF THE TOPOGRAPHICALLY SEGMENTED ALASKA RANGE

5.1 **Introduction**

Orogenesis, also known as mountain building, is ultimately driven by far-field (plate scale) tectonic processes. For example, the textbook case for mountain building is the continent-continent plate collision that resulted in the formation of the Himalayas. When one continental land mass collides with another, there is substantial shortening accompanied by surface uplift, because both plates are too buoyant to fully undergo subduction. Thermal perturbations, like migrating hotspots (Taylor and Fitzgerald, 2011) and ridge-subduction related slab windows (Thorkelson, 1996), can also lead to surface uplift.

Another driver of mountain building is oblique convergence between plates that can result in the formation of large scale strike-slip fault systems. Strike-slip fault systems like the San Andreas transform fault of California have associated mountain belts due to transpression (a component of shortening along with strike-slip shear). Interestingly, topographic development along strike-slip faults can vary along and across strike (e.g., Buscher and Spotila, 2007). This behavior is not always correlated with the degree of obliquity of the plate motion vector with respect to the fault trace or composition of juxtaposed rocks. This phenomenon is

referred to as strain-partitioning and can result in asymmetric topographic development.

Strain-partitioning along strike-slip faults has been correlated with near-field boundary conditions (within ~20 km of the fault zone) such as structural irregularities: for example, restraining bends and variations in master strand fault dip. Climate regime also can play a role in strain-partitioning and associated asymmetrical topographic development. Surface processes can also have a first order effect on the structural evolution of an orogenic belt (Whipple, 2009) and affect relief through isostatic response to focused valley erosion (Molnar and England, 1990).

5.2 **Discussion**

The topographically segmented, ~700 km long Alaska Range is a classic example of topographic development related to both far-field driving mechanisms and near-field boundary conditions. The central and eastern Alaska Range follows the curve of the Denali Fault strike-slip system. Areas of high peak elevation (e.g., 6194 m in the central Alaska Range and 4216 m in the eastern Alaska Range) are separated by broad regions of low topography (e.g., Broad Pass, ~700 m, separating the central Alaska Range from the eastern Alaska Range).

To the west, there is a restraining bend in the Fault, and ~6,000 m Mount McKinley lies within the south side of the bend. Southwest of the bend the main topography of the western Alaska Range takes an abrupt 90 degree turn away from

the Denali Fault. This north-south limb of the Alaska Range is known as the western Alaska Range. The western Alaska Range lies at the junction between the southern Alaska block (Page et al., 1995) and the Bering block (Freymueller et al., 2008). The western Alaska Range has few peaks over ~2,500 m and a regional average elevation of ~1300 m. The topographically high Tordillo Mountains, with ~3,500 m peaks is an exception to this general western Alaska Range trend of ~2500 m peak heights.

Understanding whether the Alaska Range formed synchronously or diachronously is key to deciphering both the far-field plate-tectonics mechanism(s) and the near-field boundary conditions that actuated the stress inboard into deformation and rock uplift. Based on new $^{40}Ar/^{39}Ar$, apatite fission track and (U-Th)/He cooling ages (this study) and existing apatite fission track work (Fitzgerald et al., 1995; Haeussler et al., 2008) the general Eocene to present thermal history of the Alaska Range can be constrained. The exhumation history of the Alaska Range can be inferred from the constrained thermal history of the region.

5.2.1 **Eocene Slab Window**

Rock cooling (~50 Ma to ~ 35 Ma) and associated topographic development of the western Alaska Range is predominately driven by the thermal affects of an Eocene slab window (Chapter 4, this study). The slab window was related to the subduction of the Resurrection Plate-Kula Plate ridge (Haeussler et al., 2003). The migrating and thermally evolving slab-window affected a broad expanse of

southern Alaska (O'Sullivan et al., 2010; Enkelmann et al., 2010). The available evidence indicates that the central (West, 1994; Fitzgerald et al., 1995) and eastern Alaska Range (Chapter 2; Chapter 3) were not strongly affected by the slab window event.

5.2.2 **Neogene Yakutat Flat Slab Subduction**

There is general agreement that the Yakutat microplate is the main far-field driver of Neogene deformation in southern Alaska (Plafker, 1987; Eberhart-Phillips et al., 2006; Haeussler, 2008; Christeson et al., 2010; Benowitz et al., 2011; Finzel et al., 2011; Chapter 3). The timing of the initiation of flat slab subduction of the Yakutat microplate is still controversial. Apatite fission track work in the Tordrillo Mountains and rapid deposition of the Tyonek Formation in Cook Inlet (Haeussler et al., 2008) indicates that rapid Miocene exhumation began at ~23 Ma. Detrital zircon fission track work in the Chugach-St. Elias Range at Alaska's southern margin (Enkelmann et al., 2008) show a pulse of exhumation beginning by ~25 Ma. Apatite fission track work in southwestern Alaska indicates rapid cooling in both plutonic and meta-sedimentary samples between ~24 Ma and ~20 Ma, implying regional cooling due to exhumation occurred during this time period (O'Sullivan et al., 2010). Deformation and metamorphism was occurring on the far-eastern Denali Fault by ~18 Ma (Ritcher, 1976).

In addition, the Wrangell volcano field became active at ~26 Ma and is associated with the Yakutat microplate convergence (Richter et al., 1990). The

eastern Alaska Range was undergoing rapid exhumation by ~24 Ma that continues to the present (Benowitz et al., 2011; Chapter 3). It is clear that significant deformation across southern Alaska began by ~24 Ma and continues today. Long-term occurrence of rapid exhumation in the eastern Alaska Range demands a continuous tectonic driving mechanism. Flat slab subduction of the Yakutat microplate under south-central Alaska is an obvious candidate.

5.2.3 ~6 Ma: Fault Reorganization and Block Rotation

The coeval ~6 Ma cooling events at Mount McKinley (Fitzgerald et al., 1995), the Tordrillo Mountains, and the southeastern corner of Alaska (Enkelmann et al., 2010) deserve further discussion. It is generally accepted that the Bering Strait (Fig. 5.1) opened ~6 Ma to ~5 Ma (Gladenkov et al., 2002). This is correlated with increased tectonism in the Bering Strait region related to the formation of the Bering block (Mackey et al., 1997). At the same time, initial glaciation in the southeastern corner of Alaska is associated with increased production of relief, preceding a world-wide change in climatic forcing (Zachos et al., 2001; Enkelmann et al., 2010; Arnaud and Enkin, 2010). The time of formation of a hypothesized tectonic aneurism in the southeastern corner of Alaska is also ~6 Ma (Enkelmann et al., 2010). By definition, tectonic aneurisms demand strong tectonic forcing (Zeitler et al., 2001). The Fairweather Fault region experienced an increase in rock uplift rates at ~5 Ma (McAleer et al., 2009). Furthermore, ~5 Ma is

the time of a change in the magmatic composition of the Wrangell volcanic belt (Preece and Hart, 2004).

Interestingly, no region-wide change in exhumation rate of the high peak region of the eastern Alaska Range north of the Denali fault has been documented during this time period. The eastern Alaska Range aside, it is widely agreed that ~6 Ma to ~5 Ma was the time of a change in tectonic process across southern Alaska, but no general agreement exists regarding the cause of the change in tectonic process.

Fitzgerald et al. (1995) suggested that a plate motion change was responsible for the change in exhumation rates in the McKinley region (37% increase in convergence rate; Engebretson et al., 1985). Haeussler et al. (2008) discounted the plate motion change argument because it is not clear if the plate motion change happened before, after, or during the McKinley exhumation event (~8 Ma: Atwater and Stock, 1998; ~ 4 Ma: Harbert and Cox; 1989; ~ 5 Ma: Engebretson et al., 1985). Haeussler et al. (2008) suggested that contractional response to the rotation of the southern Alaska block was responsible for deformation in the Tordrillo Mountains at ~ 6 Ma. Haeussler et al. (2008) linked to the progressive subduction of the Yakutat microplate as the far-field driving mechanism for a change in block rotation during this time period. As I discuss below, recent exhumation constraints from north of the Denali fault in the eastern Alaska Range (Benowitz et al., 2011; Chapter 3) and seismic imaging of the

Yakutat microplate along the costal margin of Alaska support this interpretation (Christeson et al., 2010; Worthington et al., 2009).

A 37% increase in convergence rate should result in a region-wide increase in exhumation rates in the eastern Alaska Range. This is because deformation in the region is in part driven by the northwest migration of the southern Alaska block (Chapter 3; Benowitz et al., 2011). As stated above, no region-wide increase in exhumation rates has been identified along the north side of the Denali fault between ~6 and ~5 Ma, implying that plate motion change is probably not primarily responsible for the southern Alaska ~6 Ma tectonic event.

With new seismic constraints on the thickness/shape of the Yakutat microplate, we can refine the proposed progressive Yakutat subduction as driver/mechanism for the ~ 6 Ma southern Alaska tectonic event of Haeussler et al. (2008). We suggest that reorganization of slip partitioning on the Denali Fault system was driven by the progressive increase in thickness of the subducting Yakutat microplate in the indenter corner (Worthington et al., 2009; Christeson et al., 2010;). The unsubducted part of the Yakutat microplate progressively thickens from west (~15 km) to east (~30 km) along the southern Alaska margin (Christenson et al., 2010; Worthington et al., 2009). As the thicker, unsubductable part of the Yakutat block was transported up the Queen Charlotte-Fairweather transform system into the southern margin of mainland Alaska, increased coupling and transfer of stress inboard would be expected (Yorath and Hyndman, 1983;

Cloos, 1993; McAleer et al., 2009). This, in turn, may have resulted in displacement on the Totschunda strand of the Denali Fault. A transfer of slip from the eastern Denali Fault onto the Totschunda Fault would lead to a smaller radius for the outer arcuate boundary of the rotating southern Alaska block (Lahr and Plafker, 1980; Page et al., 1995). A change in the geometry and rotation of the southern Alaska block may have affected deformation along the western edge of the southern Alaska block. Using current plate motion rates (Elliott et al., 2010), the ~30 km thick unsubductable section of the Yakutat microplate would have been located at the junction of the Denali Fault and Queen Charlotte Fault at ~6 Ma, resulting in more coupling westward of the master strand of the Denali Fault. Testing of the hypothesis that progressive increase of Yakutat thickness led to onset of rotation of the southern Alaska block at ~6 Ma is hampered by lack of constraints on the history of the Totschunda Fault and the long-term displacement history of the Denali Fault.

5.2.4 **Near Field Boundary Conditions: The Geometry of the Denali Fault**

The asymmetrical topographic signature of the Alaska Range is not solely related to variations in large-scale tectonic forcing or to block rotation reference frame (Fig. 5.2) (Benowitz et al., 2011; Chapter 3; Chapter 4). The Denali Fault itself plays an important role in topographic development in response to the Yakutat microplate collision. The Denali Fault is a major intracontinental right-lateral strike-slip fault that is still active, as demonstrated by the 2002 **M**7.9 Denali

Fault earthquake (Eberhart-Phillips et al., 2003). High topography is located primarily to the north of the Denali Fault in the eastern Alaska Range. To the west in the central Alaska Range, high topography is primarily south of the Denali Fault. If the dip of the Fault changes from north dipping along the eastern Alaska Range, to vertical at Broad Pass, to south dipping in the central Alaska Range, that fault geometry configuration would in part explain the north-south asymmetric topographic signature of the Alaska Range.

5.2.5 **Late Cenozoic Climatic Forcing: Tecono-Glacial Interactions**

The average elevation within the eastern, central, and western segments of the Alaska Range is only ~1300 m. Along the whole range front, high topographic regions are only ~2500 m. Conversely, the relief and verticality of the range from the tundra (~700 m) to glacier capped peaks (up to ~6000 m) is quite dramatic over a short horizontal distance (<20 km). The topographic signature we see today is the result of a pre-existing landscape modified by Plio-Quaternary surface processes. Though there is no singular tectonic driver or uplift age for the Alaska Range, it is clear that the orogenic belt as a whole has been affected by the late Cenozoic worldwide trend in increased erosion rates related to global cooling and climatic instability (Chapter 2 and 3).

5.3 **Figures**

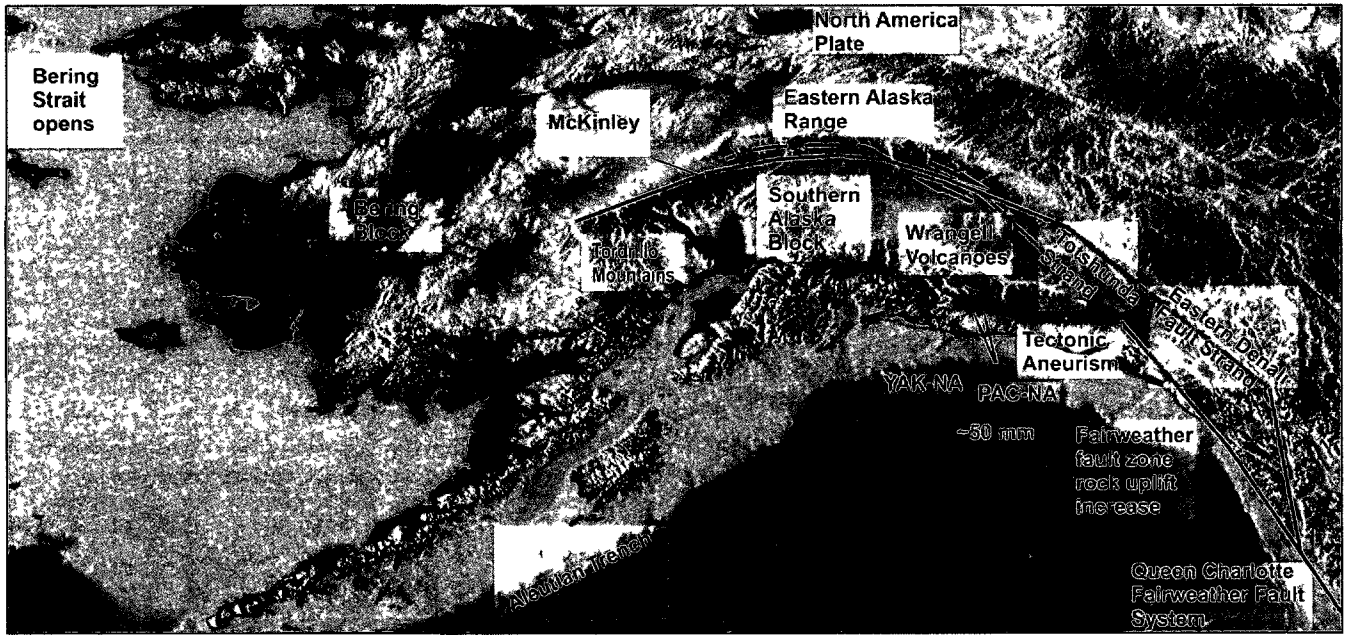

Figure 5.1: Coastal relief model of southern Alaska. From Lim and Wigley (2009). ~6 Ma tectonic events across southern Alaska discussed in detail in the text. Yakutat–North America and Pacific-North America plate motion is from Elliott et al. (2010).

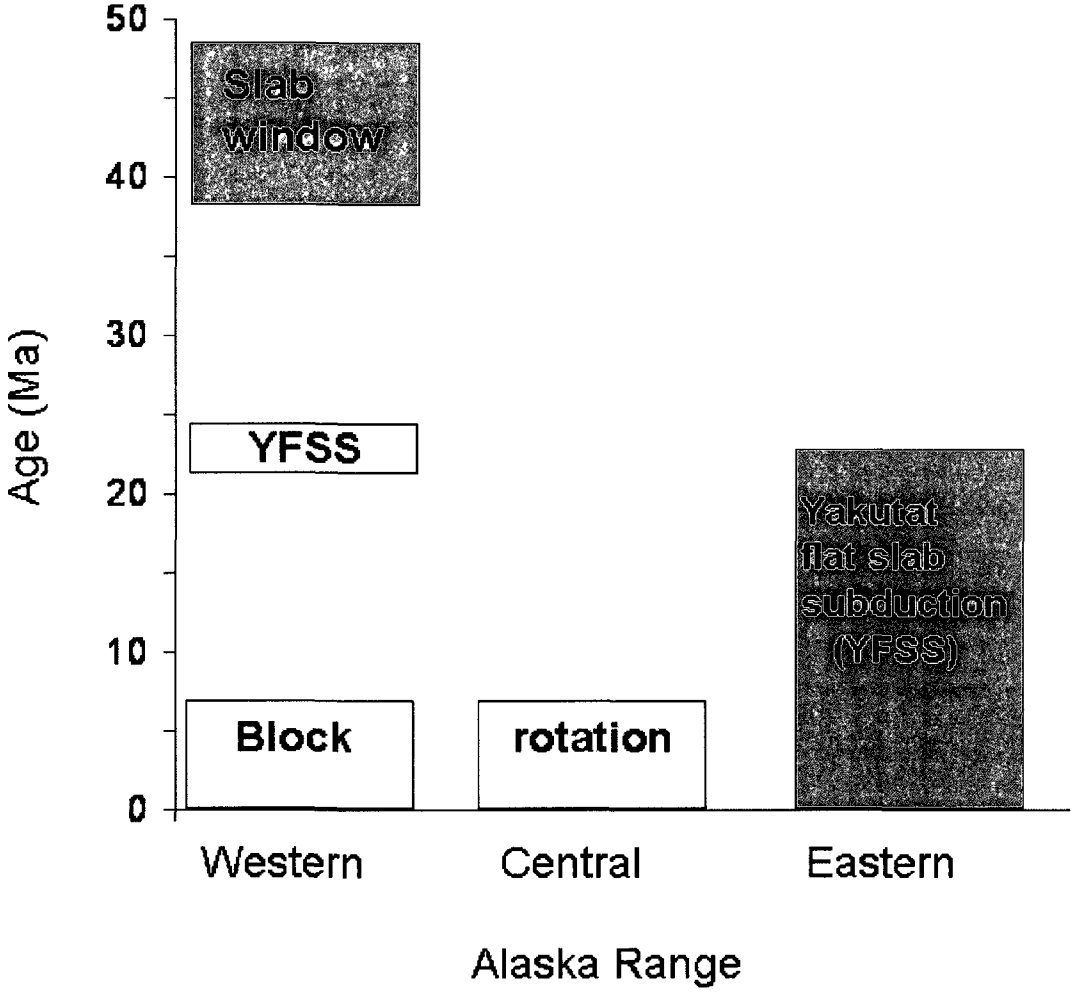

Figure 5.2: Summary of timing and tectonic cause of surface uplift events in the Alaska Range since ~50 Ma to present. The gaps in surface uplift may be real periods of tectonic quiescence or may simply reflect insufficient data collection.

5.4 **References:**

Arnaud, E. and Enkin, R., 2010, On set of Late Cenozoic Glaciation in the Gulf of Alaska, Geol. Soc. of Am. Abstracts with Programs v. 42. no.5, p. 361.

Atwater, T., and Stock, J.M., 1998, Pacific-North America plate tectonics of the Neogene Southwestern United States: An Update, International Geology Review, v. 40, p. 375–402.

Benowitz, J.A., Layer, PW.. Armstrong, P. Perry, S. Haeussler, P.J., Fitzgerald, P.G. and Vanlaningham, S., 2011, Spatial Variations in Focused Exhumation Along a Continental-Scale Strike-Slip Fault: the Denali Fault of the Eastern Alaska Range, Geosphere, v. 7; no. 2; p. 455-467; DOI: 10.1130/GES00589.1

Buscher, J. T., and Spotila, J.A., 2007, Near-field response to transpression along the southern San Andreas Fault, based on exhumation of the northern San Gabriel Mountains, southern California, Tectonics, v. 26, TC5004, doi:10.1029/2006TC002017.

Christeson, G.L., Gulick, S.P.S., van Avendonk, H.J.A., Worthington, L.L., Reece, R.S., and Pavlis, T.L., 2010, The Yakutat terrane: Dramatic change in crustal thickness across the Transition fault, Alaska. Geology v. 38, p. 895-898.

Cloos, M., 1993. Lithospheric buoyancy and collisional orogenesis: Subduction of oceanic plateaus, continental margins, island arcs, spreading ridges and seamounts, Geol. Soc. Am. Bull. V. 105, p. 715-737.

Eberhart-Phillips, D., Christensen, D.H., Brocher, T.M., Hansen, R., Ruppert, N.A., Haeussler, P.J., and Abers, G.A., 2006, Imaging the transition from Aleutian subduction to Yakutat collision in central Alaska, with local earthquakes and active source data, Journal of Geophysical Research, v. 111, B11303.

Eberhart-Phillips, D., Haeussler, P.J., Freymueller, J.T., Frankel, A., Rubin, C.M., Craw, P., Ratchkovski, N.A., Anderson, G., Carver, G.A., Crone, A.J., Dawson, T.E., Fletcher, H., Hansen, R., Harp, E.L., Harris, R.A., Hill, D.P., Hreinsdóttir, S., Jibson, R.W., Jones, L.M., Kayen, R., Keefer, D.K., Larsen, C.F., Moran, S.C., Personius, S.F., Plafker, G. Sherrod, B., Sieh, K., Sitar, N. and Wallace, W.K., 2003, The 2002 Denali fault earthquake, Alaska: A large magnitude, slip-partitioned event, Science, v. 300(5622), p. 1113-1118.

Elliott, J. L., Larsen, C. F., Freymueller, J. T. and Motyka, R. J., 2010, Tectonic block motion and glacial isostatic adjustment in southeast Alaska and adjacent Canada constrained by GPS measurements, J. Geophys. Res., v. 115, B09407, doi:10.1029/2009JB007139.

Engebretson, D.C., Cox, A., and Gordon, R.G. 1985, Relative motions between oceanic and continental plates in the Pacific Basin, Special Paper – Geol. Soc. of Am., v. 206, p. 59.

Enkelmann, E., Zeitler, P.K., Garver, J.I., Pavlis, T.L., Hooks, B.P., 2010, The thermochronological record of tectonic and surface process interaction at the YakutatNorth American collision zone in southeast Alaska. American Journal of Science v. 310, p. 231-260.

Enklemann, E., Garver, J.I. Pavlis, T.L., 2008, Rapid exhumation of ice-covered rocks of the Chugach-St.Elias orogen, SE-Alaska. Geology, v. 36, p. 915-918 doi:10.1130/G2252A.1

Finzel, E., Trop, J., Ridgway, K., and Enkelmann, E., 2011, Upper-plate proxies for flat-slab subduction processes in southern Alaska, ESPL in press.

Fitzgerald, P.G., Sorkhabi, R.B., Redfield, T.F., Stump, E., 1995, Uplift and denudation of the central AlaskaRange – a case-study in the use of apatite fission-track thermochronology to determine absolute uplift parameters. Journal of Geophysical Research-Solid Earth v. 100, p. 20175-20191.

Freymueller, J.T., Woodard, H., Cohen, H.S., Cross, R., Elliott, J., Larsen, C., Hreinsdottir, S., Zweck, C., 2008, Active deformation processes:in Active Tectonics and Seismic Potential of Alaska, Geophys. Monogr. Ser., edited by J.T. Freymueller, P.J. Haeussler, R. Wesson, and G. Ekstrom, Geophysical Monograph 179, AGU, Washington, D.C. p. 269-285.

Gladenkov, A.Y., Oleinik, A.E., Marincovich, L., Barinov, K.B., 2002, A new age for the earliest opening of Bering Strait, Palaeogeogr. Palaeoclimatol. Palaeoecol. w. 183 (3–4), p. 321–328.

Haeussler, P.J., 2008, An overview of the neotectonics of interior Alaska; far-field deformation from the Yakutat Microplate collision:in Active Tectonics and Seismic Potential of Alaska, Geophys. Monogr. Ser., edited by J.T. Freymueller, P.J. Haeussler, R. Wesson, and G. Ekstrom, Geophysical Monograph 179, AGU, Washington, D.C. p. 269-285.

Haeussler, P., O'Sullivan, P., Berger, A., and Spotila, J., 2008, Neogene exhumation of the Tordrillo Mountains, Alaska, and correlations with Denali (Mt. McKinley): in Active Tectonics and Seismic Potential of Alaska, Geophys. Monogr. Ser., edited by J.T. Freymueller, P.J. Haeussler, R. Wesson, and G. Ekstrom, Geophysical Monograph 179, AGU, Washington, D.C. p. 269-285.

Haeussler, P.J., Bradley, D.C., Wells, R.E. & Miller, M.L., 2003, Life and death of the Resurrection Plate; evidence for its existence and subduction in the northeastern Pacific in Paleocene-Eocene time, Geological Society of America Bulletin, vol. 115, no. 7, p. 867-880.

Harbert, W. and Cox, A., 1989. Late Neogene motion of the Pacific Plate, J. geophys. Res., v. 94, p. 3052–3064.

Lahr, J. C. and Plafker, G., 1980, Holocene Pacific–North American Plate interaction in southern Alaska; implications for the Yakataga seismic gap. Geology, v. 8, p. 483–486.

Mackey, K.G., Fujita, K., Gunbina, L.V., Kovalev, V.N., Imaev, V.S., Koz' min, B.M., Imaeva, L.P., 1997, Seismicity of the Bering Strait region: Evidence for a Bering block. Geology v. 25, p. 979-982.

McAleer, R. J., Spotila, J. A., Enkelmann, E., and Berger, A.L., 2009, Exhumation along the Fairweather fault, southeastern Alaska, based on low-temperature thermochronometry, Tectonics, v. 28, TC1007, doi:10.1029/2007TC002240.

Molnar, P., and England, P., 1990, Late Cenozoic uplift of mountain ranges and global climate change: Chicken or egg?, Nature, v. 346, p. 29–34, doi:10.1038/346029a0.

O'Sullivan, P., Donelick, M., and Donelick, R., 2010, Apatite Fission-Track Results From The Region of The Pebble Deposit, Southwest Alaska, Apatite to Zircon Report 950, minerals.usgs.gov/mrerp/reports/O'Sullivan-08HQGR0061.pdf, last accessed 5/5/2010.

Page, R.A., Plafker, G., and Pulpan, H., 1995, Block rotation in east-central Alaska: A framework for evaluating earthquake potential?, Geology, v. 23, p. 629–632, doi: 10.1130/0091-7613

Plafker, G., 1987, Regional geology and petroleum potential of the northern Gulf of Alaska continental margin, in Scholl, D.W., Grantz, A., and Vedder, J.G., eds., Geology and Resource Potential of the Continental Margin of Western North America and Adjacent Ocean Basins, Beaufort Sea to Baja California, v. 6: Houston, Texas, Circum-Pacific Council for Energy and Mineral Resources, p. 229–268.

Preece, S.J., and Hart, W.K., 2004, Geochemical variations in the <5 Ma Wrangell Volcanic Field, Alaska: Implications for the magmatic and tectonic development of a complex continental arc system, Tectonophysics, v. 392, p. 165–191, doi: 10.1016/j.tecto.2004.04.011.

Richter, D. H., Smith, J.G., Lanphere, M.A., Dalrymple, G.B., Reed, B.L., and Shew, N.,1990, Age and progression of volcanism, Wrangell volcanic field, Alaska, Bull. Volcanol., v. 53, p. 29–44.

Richter, D.H., 1976, Geologic map of the Nabesna quadrangle, Alaska: U.S. Geological Survey Miscellaneous Investigations Series Map 1-932, scale 1:250,000.

Taylor, J.P. and Fitzgerald, P.G., 2011, Low-temperature thermal history and landscape development of the eastern Adirondack Mountains, New York; constraints from apatite fission-track thermochronology and apatite (U-Th)/He dating, Geol. Soc. of Am. Bull., v. 123(3-4), p. 412-426.

Thorkelson, D. J., 1996, Subduction of diverging plates and the principles of slab window formation, Tectonophysics, v. 255, p. 47-63, doi:10.1016/0040-1951(95)00106-9.

West, A.W., 1994, A petrologic and geochronologic study of the McKinley Pluton, Alaska, M.S. thesis, 181 pp., Univ. Alaska Fairbanks.

Whipple, K., 2009, The influence of climate on the tectonic evolution of mountain belts. Nature Geoscience v. 2, p. 97 – 104.

Worthington, L. L., Christeson, G. L., van Avendonk, H. J.; Gulick, S. P., 2009, Crustal Structure of the Yakutat Microplate: New Parameters for Understanding the Evolution of the Chugach-St.Elias Orogeny, Am. Geophys. U., Fall Meeting, abstract in programs.

Yorath, C.J., Hyndman, R.D., 1983, Subsidence and thermal history of Queen Charlotte Basin. Can. J. Earth Sci v. 20, p. 135–159.

Zachos, J., Pagani, M., Sloan, L., Thomas, E., and Billups, K., 2001, Trends, rhythms, and aberrations in global climate 65 Ma to present, Science, v. 292, p. 686-693.

Zeitler, P. K., Koons, P. O., Bishop, M. P., Chamberlain, C. P., Craw, D., Edwards, M. A., Hamidullah, S., Jan, M. Q., Khan, M. A., Khattak, M. U. K., Kidd, W. S. F., Mackie, R. L., Meltzer, A. S., Park, S. K., Pecher, A., Poage, M. A. Sarker, G., Schneider, D. A., Seeber, L., and Shroder, J. F., 2001, Crustal reworking at Nanga Parbat, Pakistan: Metamorphic consequences of thermal-mechanical coupling facilitated by erosion, Tectonics, v. 20, p. 712–728, doi:10.1029/2000TC001243.